Coherent dynamics, relaxation and fragmentation of a spinor Bose-Einstein condensate

Bertrand Evrard

PSL UNIVERSITÉ PARIS

THÈSE DE DOCTORAT
DE L'UNIVERSITÉ PSL

Préparée au Collège de France

Dynamique cohérente, relaxation et fragmentation d'un condensat de Bose-Einstein spinoriel

Soutenue par

Bertrand Evrard

Le 18 Septembre 2020

École doctorale n° 564

Physique en Île-de-France

Spécialité

Physique quantique

Composition du jury :

Isabelle Bouchoule Directrice de recherche, Institut d'optique	*Rapporteur*
Markus Oberthaler Professeur, Université de Heidelberg	*Rapporteur*
Jean-François, Roch Professeur des universités, ENS-P-S	*Examinateur*
Gwendal, Fève Professeur des universités, ENS	*Président du Jury*
Fabrice, Gerbier Directeur de recherche, ENS	*Directeur de thèse*
Jean, Dalibard Professeur au Collège de France	*Codirecteur de thèse*

COLLÈGE DE FRANCE
1530

La Nature est un temple où de vivants piliers
Laissent parfois sortir de confuses paroles;
L'homme y passe à travers des forêts de symboles
Qui l'observent avec des regards familiers.

Baudelaire
Correspondances

Résumé

Dans cette thèse, nous présentons des expériences réalisé avec des gaz d'atome de sodium ultrafroids, piégés à l'intersection de deux faisceaux laser. A très basse température, discrétisation de l'énergie et indiscernabilité des particules conduisent à un nouvel état de la matière, un condensat de Bose-Einstein. Ce phénomène remarquable à d'abords été décrit pour un gaz idéal, c'est à dire sans interaction entre ses constituants. Ici, nous nous intéressons aux effets des interactions entre atomes. Plus précisément, nos atomes possèdent un spin 1, et nous nous interessont à l'état spinoriel collectif, dans un régime ou les degrées de liberté spatiaux sont gelés.

Deux résultats importants que nous présentons ont été obtenus en plongeant le condensat dans un champ magnétique quasi-nul. Dans ce régime, les interactions dominent et favorisent l'émergence d'états fortement corrélés. Dans une première série d'expériences, le champ est soudainement réduit, et le système se retrouve hors-équilibre. Il s'ensuit une dynamique de relaxation, qui mène à un état stationnaire bien décrit par un ensemble de Gibbs. Dans une seconde expérience, le champ est progressivement réduit, de façon à suivre l'état fondamental du système. Nous réalisons ainsi un condensat fragmenté, dont une remarquable propriété est l'invariance sous rotations des spins. La restauration de cette symétrie, toujours brisée par les condensat "simple" (i.e. non-fragmenté), se fait grâce à l'appariement des atomes en état singulet.

Abstract

In this thesis, we present some experiments realized with ultracold gases of sodium atoms, trapped at the intersect between two laser beams. At very low temperature, the discretization of energy and the indistinguishability of particles, lead to a new state of matter, a Bose-Einstein condensate. This remarkable phenomenon was initially introduced to describe an ideal gas, that is to say with no interactions between its constituents. Here, we are interested in the effects of the interactions between the atoms. More precisely, our atoms carry a spin 1, and we focus on the collective spin state, in a regime where the spatial degrees of freedom are frozen.

Two important results that we present were obtained by embedding the condensate in a nearly vanishing magnetic field. In that regime, interactions dominate and favor the emergence of strongly correlated states. In a first series of experiment, the magnetic field is suddenly decreased to bring the system out-of-equilibrium. The ensuing relaxation dynamics leads to a stationnary state that can be well described by a Gibbs ensemble. In a second experiment, the field is slowly reduced, in order to follow the ground state of the system. We thereby produce a fragmented condensate, which possesses the remarkable feature of being invariant upon spin rotations. The restoration of this symmetry, always broken by single (i.e. non-fragmented) condensates, is driven by the pairing of atoms in singlet states.

Remerciement

Les microcondensats spinoriels fortement corrélés, voici ce sur quoi Fabrice et Jean m'ont proposé de faire une thèse. Sans y voir tout à fait clair (bel euphémisme!), mais bien inspiré, j'ai rejoint l'équipe et le reste de l'aventure est raconté dans ce manuscrit. Mais d'abord, ces quelques lignes pour remercier celles et ceux qui m'ont accompagné.

Je voudrais remercier les membres de mon jury de thèse, pour le temps qu'ils ont consacré à me lire et m'écouter, et pour les questions et remarques qui suivirent la soutenance. Je remercie en particulier les rapporteurs pour avoir accepté de rédiger un compte rendu.

Tout au long de ma thèse, j'ai pu compter sur l'aide précieuse des membres du laboratoire Kastler-Brossel et de l'institut de physique du collège de France. Je tiens à remercier le directeur du LKB, Antoine Heidmann, ainsi que mes tuteur et parrain, Dominique Delande et Quentin Glorieux. Je suis également reconnaissant envers les personnels administratifs et techniques du LKB et de l'IPCDF.

Au sein de l'équipe "Sodium", j'ai été chaleureusement accueilli par Camille, Andrea et Karina, qui m'ont enseigné, avec patience, les rouages de l'expérience. Enfin, j'ai eu la chance d'avoir An à mes coté pour une bonne partie de ma thèse. Je les remercie tous les quatres, ainsi que les membres de l'équipe qui m'ont précédés et qui ont laissé derrière eux une très belle machine à refroidir des atomes.

Pendant ces années, j'ai aussi pu compter en permanence sur mes encadrants Jean Dalibard et Fabrice Gerbier, toujours disponible pour discuter de problèmes techniques ou de physique. Je veux leur exprimer à tous les deux mes remerciements les plus sincères. Leur rigueur scientifique restera pour moi un modèle à suivre.

J'ai passé les derniers mois de ma thèse à Chicago, dans le groupe de Cheng Chin. Bien que cette visite ait été fortement impactée par la pandémie, je tiens à remercier Cheng pour son accueil (et je suis une nouvel fois redevable à Jean et Fabrice pour avoir proposé et soutenu cette visite).

J'ai évolué dans une ambiance formidable à l'IPCDF et je veux remercier toutes les personnes que j'ai côtoyées au jour le jour, et parfois hors du labo, au zig-zag ou au piano-vache, à la montagne ou à Barcelone... J'en garderais de très bon souvenirs.

J'ai la chance de pouvoir compter sur des amis fidèles, Vianney (après toutes ces années...), Jaouad (je salue ton sens aigu de l'absurde), Romain, Hugo (I'm starving), Guillaume, Raphaël (les quantum beer), Olivier (tu connais), le Merlin, Stéphane, Emmanuelle, mon cher colloc Louis et les soirées Zen, et les vieux camarades, perdu dans les montagnes ou au saint Hilaire, Steph, Jérémie-Luc, Robbie, Vince, Vivek, Boris.

Enfin, tout ce qui me reste de reconnaissance va à ma famille, et en particulier à mes parents.

Contents

Chapter 1

Introduction

Quantum mechanics is often thought as a description of nature at the microscopic scale, typically the size of a molecule or smaller. From the early days and the Bohr model of the atom, to modern quantum electrodynamics, the theory has indeed been extremely successful at this scale, and remained up to this day in perfect agreement with ever more accurate measurements. On the experimental side, novel methods, to a large extent enabled by the invention of the laser, have allowed for an exquisite control over the internal and external states of individual particles [1]. These progresses have contributed to revolutionize the field of fundamental metrology. Indeed, single particles have "god given" properties which can serve as universal references, for instance of time [2]. Atomic clocks have technological and fundamental applications, and as an exciting prospective, we can mention the possibility to track an hypothetical time dependence of the fundamental constants by comparing the beat of two clocks made of different atoms.

The exploration of quantum phenomena at a larger scale has also been very fruitful, both theoretically and experimentally. Important experimental milestones are the discovery of superconductivity, superfluidity and more recently the realization of gazeous Bose-Einstein condensates. Common to all these systems, is the behavior of a macroscopic number of particles in phase. Let us focus on the Bose-Einstein condensation of ultracold gases [3, 4]. A direct manifestation of the phase coherence is the interference pattern formed at the overlap of two condensates [5]. We can also mention the tunneling in phase of thousands of atoms through a potential barrier, observed in reference [6]. This experiment reproduces with atoms the celebrated Josephson effect, in which a macroscopic current flows through a thin insulating layer separating two superconductors. In these set-ups, a quantum effect usually occurring at a microscopic scale, here tunneling, is amplified and manifests itself on a much larger scale, thanks to the synchronized motion of a macroscopic number of atoms or Cooper pairs. Addressing simultaneously and coherently large ensembles of independent particles is clearly favorable for metrology, as a larger signal can be obtained. This approach is pursued in state-of-the-art, optical lattice clocks [2].

The key features of quantum theory which underlie the phenomenon of macroscopic coherence are the quantization of energy and the particles indistinguishability. Despite the spectacular consequences mentioned above, mere macroscopic coherence remains far from revealing the full potential of a strict application at the macroscopic scale of the laws of quantum mechanics [7]. For instance, the superposition principle allows *a priori* for the existence of "Schrödinger cat" states, that is to say, superposition of distinguishable many-body states. "Cat states" are characterized by the existence of non-classical correlations between the particles. They belong to the vast category of entangled states. Beyond their fundamental interest (whether the superposition principle holds at a macroscopic scale remains to be proven [8]), entangled states can be used as a new resource in various domains, and as an illustration we can turn again to the field of metrology. A fundamental limit of interferometers, the shot-noise, arises from the granular nature of matter or light. For N independent particles, the relative error scales as $1/\sqrt{N}$. With appropriate correlations, one can reach the so-called Heisenberg scaling $1/N$, hence a gain in sensitivity by a potentially very large factor $\sqrt{N}$ [9]. However, we now reach the limit of current technology. On the one hand, the realization of highly correlated states usually requires strong interactions between particles, and on the other hand, entangled states are known to be fragile against "measurements" performed by the environment (ie decoherence). The difficulty thus resides in combining substantial interactions within the system, together with a good isolation from the environment. In that respect, ultracold atoms constitute a promising platform. Proof-of-principle experiments have already demonstrated the generation of highly correlated states of atomic ensembles with potential metrological application [10–16].

Highly correlated states of large ensembles of electrons can be found in condensed matter systems such as unconventional supraconductors or spin-liquids [17]. The description of such materials is frequently out of the reach of current theoretical methods, either analytical or numerical. A telling example is given in reference [17]: it takes the most powerful computers we currently have to compute the ground state wavefunction of the Beryllium dimer's eight electrons. As an alternative to classical computers, one could use analog quantum simulators. In that respect, ultracold atom experiments may help to tackle the "many-body problem" [18, 19]. Indeed, idealized Hamiltonian can be implemented, where atoms mimic electrons in solids or complex molecules. Optical standing waves can be used to create periodic potentials, of various geometries, which reproduce a crystal potential [20]. The transition from the Mott insulator to the superfluid phase in such an optical lattice was observed in [21]. Various experimental techniques have been developed to simulate condensed matter systems with neutral atoms, for instance synthetic magnetic

fields [22] and spin-orbit coupling [23] can be realized using tailored light-matter interactions [24]. Another great asset of cold atom experiments is the possibility to tune the interaction strength using Feshbach resonances [25]. Finally, compared to solid-state systems, ultracold atomic ensembles benefit from alternative and powerful diagnostic possibilities, for instance the momentum distribution can be accessed from a so-called time-of-flight measurement [26], while the real-space density distribution can be measured on in-situ images. In particular, for atoms in a two dimensional lattice, single site resolution has been achieved in several experiments [27].

Ultracold gases also offer the opportunity to synthesize and study new quantum fluids, which do not necessarily have an analogous in condensed matter systems. A particularly fruitful field of research looks at so-called spinor Bose-Einstein condensates (BEC), where atoms can be in different internal states [28, 29]. The latter can for instance be the three Zeeman sublevels of the $F = 1$ hyperfine manifold of alkali atoms (BECs with two to seventeen components have also been realized). This additional degree of freedom opens the door to the exploration of interesting phenomena at the interface of superfluidity and magnetism. Formally, spinor BECs are described by a vector order parameter, breaking both gauge and spin rotational symmetries. This rich structure can host a large variety of topological excitations, for instance spin vortices, observed in [30] or Skyrmions, observed in [31]. Spinor BECs are also ideal candidates regarding the generation of correlated states. For instance, out of equilibrium spin-mixing dynamics have been used to produce spin squeezing, relevant for quantum-enhanced interferometry [10–15]. The microscopic mechanism is analogous to parametric down-conversion in optics. For a spin-1, spin-changing collisions of the type

$$2 \times |m = 0\rangle \to |m = +1\rangle + |m = -1\rangle \,, \tag{1.1}$$

correlates the $m = \pm 1$ modes. Starting with all atoms in $m = 0$, this process produces coherent superposition of states having each mode $m = \pm 1$ equally populated. More precisely, at short-time, the dynamics creates a so-called two-mode squeezed vacuum state [32, 33]. The equilibrium state of spinor BEC has been less studied experimentally than the dynamics, partly because of the long time (sometime comparable to the condensate lifetime) required to reach equilibrium [34]. Yet, this situation is certainly worth exploring, especially in a regime where spin-dependent interactions prevail. As in condensed matter systems, different ordering can be realized depending on the nature, ferromagnetic or antiferromagnetic, of the interactions [29, 35–38]. A generic Hamiltonian for the interaction of two spin-1 atoms is

$$\hat{H}_{\text{int}} = \frac{U_s}{2} \hat{\mathbf{s}}_1 \hat{\mathbf{s}}_2 \,, \tag{1.2}$$

$$= \frac{U_s}{4} (\hat{\mathbf{s}}_1 + \hat{\mathbf{s}}_2)^2 + \text{constant} \,. \tag{1.3}$$

Ferromagnetic interactions ($U_s < 0$) favor the "quintet" manifold, *ie* the states of total spin $S = 2$, whereas for antiferromagnetic interactions ($U_s > 0$) the ground state is the singlet expressed as (in the basis $|m_1, m_2\rangle$)

$$|S = 0\rangle = \frac{1}{\sqrt{3}} (|0, 0\rangle - |+1, -1\rangle - |-1, +1\rangle) \,. \tag{1.4}$$

In our experiments, the condensed atoms occupy the same spatial wave function, independently on the spin state, and thus are interacting "all-to-all" via the Hamiltonian

$$\hat{H}_{\text{int}} = \frac{U_s}{N} \sum_{i,j=1}^{N} \hat{\mathbf{s}}_i \hat{\mathbf{s}}_j \,, \tag{1.5}$$

$$= \frac{U_s}{2N} \hat{\mathbf{S}}^2 + \text{constant} \,, \tag{1.6}$$

where $\hat{\mathbf{S}}$ is the total spin. In the antiferromagnetic case, the ground state is a "macroscopic singlet", which can be seen as a condensate of singlet pairs [39–41]. Note that the state (1.4) is entangled, which fundamentally distinguishes a condensate of such pairs from the mere accumulation of atoms in a unique single particle state occurring for the ideal (non-interacting) gas. Instead, the BEC is fragmented [42–44].

The observation of condensate fragmentation was one of the long term goals of our group, and a motivation for using Sodium atoms, with an hyperfine spin $F = 1$ and antiferromagnetic interactions. In this thesis, we present experiments where the atoms are tightly confined, so that to a good approximation, the motional degree of freedom is frozen, and we explore physical phenomena that only involve the spin. This is a considerable simplification of the system. For instance, within this approximation, the effective Hamiltonian can be numerically diagonalized, and even analytically in various regimes. Yet, we will show that this simple configuration is sufficient to explore new and interesting many-body quantum phenomena.

In Chapter 2, we present some important aspects of the physics of spin-1 BECs. We review the relevant contributions to the Hamiltonian, in particular the Zeeman effect and the antiferromagnetic interactions. We then focus on the spin degree of freedom, study the ground state in various regimes, and pay particular attention to the emergence of entanglement.

In Chapter 3 we present the experimental apparatus. The latter was already built when I arrived, so the preparation of the BEC is only described briefly, for completeness. I have contributed to the implementation of a new imaging method, which is presented in detail.

In Chapter 4, we revisit the so-called internal Josephson effect, in which spin-changing coherent collisions lead to oscillation of the Zeeman populations. We explore the effect of a parametric excitation, and observe resonances reminiscent of the "Shapiro steps" in a Josephson junction. We study the relaxation dynamics and find non-trivial steady states, bistability and hysteresis in this system. For this Chapter, we reproduce the article published in [45].

Although the results of Chapter 4 can be understood using a mean-field picture, spin-changing collisions naturally generate correlations between the atoms. In the remaining Chapters, we present various experiments where we created entangled states starting from a so-called nematic state, where all the atoms are in the $m = 0$ Zeeman sublevel.

In Chapter 5, we build on the work of Chapter 4 and use a parametric excitation to destabilized the initial nematic state and trigger the generation of correlated pairs of atoms in the $m = \pm 1$ Zeeman states. We measure "spin-squeezing", and discuss its relation to entanglement and metrology. We then turn to the study of the dynamics in a stable regime, realized in a static magnetic field, and where the evolution is reversible. This gives further insight on the nature of the state produced by the spin-changing collisions, demonstrating the coherence between the spin modes. Finally, we investigate the effect of a seed on the dynamics to emphasize on the role played by quantum fluctuations in initiating the dynamics.

In Chapter 6 we carry on with similar experiments, *ie* quenches of the magnetic field, but down to even lower fields, such that the Zeeman effect becomes negligible. Despite the system being to a good approximation isolated and under unitary evolution, we observe the relaxation to a steady state. We discuss the mechanism underlying this behavior and show how the steady state can be described by a generalized Gibbs ensemble.

In Chapter 7, we report on our observation of a condensate of singlet pairs. We use a slow ramp of the magnetic field to populate the lowest energy states. At the end of the ramp, we measure a very small (microscopic) collective spin, indicating that most atoms are involved in singlet pairs. This constitutes the first observation of a condensate of this kind. From a complete reconstruction of the many-body spin state we find a significant overlap with the macroscopic singlet, for which the total spin exactly vanishes.

Chapter 2

Spin-1 Bose-Einstein condensates

We review in this Chapter the theoretical elements required for the understanding of the experiments presented in the rest of this manuscript. We try to make the experimental Chapters self consistent, and recall when needed the relevant theoretical background. The reader can find here a general discussion, and more complete reviews in [28, 29].

The experiments realized in this thesis were all performed on spinor Bose-Einstein condensates (BEC) of Sodium atoms confined in an optical dipole trap. In a spinor BEC, Zeeman effect and spin-dependent interactions compete to determine the dynamics and equilibrium state. They can yield magnetic ordering, much like what can be observed in metals, for instance. However, while strong electron exchange interactions can lead $e.g.$ to ferromagnetism in Iron at room temperature, in dilute gases, the energy scale for the spin-dependent interactions is on the order of a few nano Kelvin, quite smaller than the typical temperatures achieved in ultracold gases (~ 100 nK). Yet, when a BEC is produced, a macroscopic number of atoms occupy the single-particle ground state, which has a magnetic structure, even though the thermal cloud remains essentially disordered. This is often refereed to as Bose-enhanced magnetism [28]. For this reason, we can focus our study on the ground state.

In our system, the spins carried by the atoms are delocalized and interact collectively. This situation is analogous to that of electronic spins in transition metals, such as Iron, and is called itinerant magnetism. The interplay between spatial and spin degrees of freedom is in general very complex. However, we realized our experiments in a regime where the orbital and spin modes are weakly coupled and can be treated independently. Within this approximation, we will first determine the spatial wave function before deriving an effective spin-only Hamiltonian. The latter is used to described all experiments presented in Chapter 4 to 7 and is studied in the second half of the present Chapter. Starting with a mean-field treatment, we identify two magnetic phases accessible to our system. In the vicinity of the phase transition, quantum fluctuations play an important role, and deplete the BEC. The regime of small depletion can be captured by Bogoliubov theory. Closer to the phase transition, the depletion becomes macroscopic, and the many-body state can no longer be seen as a condensate of atoms in a single-particle state. We pay particular attention to the onset of entanglement, and its characterization in the critical regime, near the phase transition.

2.1 Hamiltonian of a spin-1 Bose-Einstein condensates

2.1.1 Internal degree of freedom

Sodium is an alkali metal with a unique valence electron. The electronic ground state has a spin $s = \frac{1}{2}$ and vanishing angular momentum $l = 0$. The nuclear spin is $i = \frac{3}{2}$, and hence the hyperfine spin is $F = 1$ or $F = 2$ [46]. The hyperfine splitting is much larger than the typical energies so that the atoms remain in the $F = 1$ manifold. In all of our experiments, we apply a bias magnetic field B. To a very good approximation this field is uniform over the size of the clouds. We set the z axis as the direction of B. It serves as a quantization axis to define the three Zeeman states $m = 0, \pm 1$.

Bloch-Rabi representation of a spin-1 We introduce here a geometrical representation that helps visualizing the symmetries of spin-1 states. A spin $1/2$ can be conveniently represented by a unit vector n with spherical coordinates (θ, φ) as $|\psi_{\frac{1}{2}}(\mathrm{n})\rangle = \alpha|\uparrow\rangle + \beta|\downarrow\rangle$, with $\alpha = \cos\left(\frac{\theta}{2}\right) e^{i\varphi/2}$ and $\beta = \sin\left(\frac{\theta}{2}\right) e^{-i\varphi/2}$. The Bloch sphere representation for a spin $1/2$ is generalized by thinking of a spin-1 as a symmetric composition of two spin-$1/2$

$$|+1\rangle = |\uparrow\rangle|\uparrow\rangle\,, \qquad |0\rangle = \frac{1}{\sqrt{2}}(|\uparrow\rangle|\downarrow\rangle + |\downarrow\rangle|\uparrow\rangle)\,, \qquad |-1\rangle = |\downarrow\rangle|\downarrow\rangle\,, \tag{2.1}$$

We introduce two unit vectors n_1 and n_2. With the same definition of $\theta_{1,2}$, $\varphi_{1,2}$ and $\alpha_{1,2}$, $\beta_{1,2}$ as above, the state of a spin-1 is parametrized as

$$|\psi(\mathrm{n}_1, \mathrm{n}_2)\rangle = \frac{1}{2}\left(\alpha_1|\uparrow\rangle_1 + \beta_1|\downarrow\rangle_1\right) \otimes \left(\alpha_2|\uparrow\rangle_2 + \beta_2|\downarrow\rangle_2\right) + 1 \leftrightarrow 2\,, \tag{2.2}$$

where $1 \leftrightarrow 2$ indicates permutation of the indexes 1 and 2, in order to satisfy the exchange symmetry. Using Eq. (2.1) we obtain

$$|\psi(\mathrm{n}_1, \mathrm{n}_2)\rangle = \frac{1}{\sqrt{\mathcal{N}}}\left(\alpha_1\alpha_2|+1\rangle + \frac{\alpha_1\beta_2+\alpha_2\beta_1}{\sqrt{2}}|0\rangle + \beta_1\beta_2|-1\rangle\right) . \tag{2.3}$$

with $\mathcal{N} = \frac{3+\mathrm{n}_1\cdot\mathrm{n}_2}{4}$. With this parametrization, rotation in spin space maps onto simultaneous rotation of n_1 and n_2. Moreover, the mean spin takes a simple form $\langle\hat{\mathrm{s}}\rangle = \frac{\mathrm{n}_1+\mathrm{n}_2}{2}$. The states with $\mathrm{n}_1 = \mathrm{n}_2$ have a net spin and are called oriented. The unpolarized state, with $\mathrm{n}_1 = -\mathrm{n}_2$ are sometimes called nematic state, in analogy with liquid crystals where molecules are aligned but have no particular orientation. The Zeeman states $|m = \pm 1\rangle$ are oriented (along $\pm e_z$). On the other hand, $|m = 0\rangle$ is the nematic state align along z. Those three states are represented in figure 1.

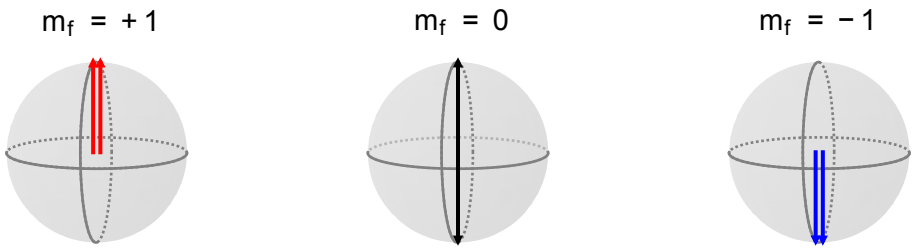

Figure 1: Bloch rabi represention of the spin states $|F = 1, m = +1\rangle$ (a), $|F = 1, m = 0\rangle$ (b) and $|F = 1, m = -1\rangle$ (c).

Zeeman Effect Sodium atoms have a nuclear and an electronic spin that both couple to a magnetic field, but with different magnetic moments (the nuclear contribution is much smaller due to the larger nucleus mass). For low enough magnetic fields, the effect of the nuclear spin can be treated as a perturbation. In this approximation, F remains a good quantum number. After an expansion up to the second order in B one obtains the following Hamiltonian [46]

$$\hat{h}_Z = p\hat{s}_z + q\hat{s}_z^2 , \tag{2.4}$$

$\hat{s}_{x,y,z}$ are the spin-1 matrices

$$s_x = \frac{1}{\sqrt{2}}\begin{pmatrix} 0 & 1 & 0 \\ 1 & 0 & 1 \\ 0 & 1 & 0 \end{pmatrix} , \qquad s_y = \frac{i}{\sqrt{2}}\begin{pmatrix} 0 & -1 & 0 \\ 1 & 0 & -1 \\ 0 & 1 & 0 \end{pmatrix} , \qquad s_z = \begin{pmatrix} 1 & 0 & 0 \\ 0 & 0 & 0 \\ 0 & 0 & 1 \end{pmatrix} . \tag{2.5}$$

The first term of Eq. (2.4) is the linear Zeeman shift, $p = g\mu_B\|\mathrm{B}\|$ with $g \simeq \frac{1}{2}$ the Landé hyperfine g-factor and $\mu_B = e\hbar/(2m_e)$ the Bohr magneton. The second term is the quadratic Zeeman shift (QZE), $q = \alpha\mathrm{B}^2$, with $\alpha = (g\mu_B)^2/\Delta E_{\mathrm{hf}}$ where ΔE_{hf} is the hyperfine energy splitting.

The expansion leading to Eq. (2.4) is legitimate only for $q \ll p$. In practice, $g\mu_B/h \simeq 700\,\mathrm{kHz/G}$ and $\alpha/h \simeq 277\,\mathrm{Hz/G}^2$. We typically use field below a few G, so that $q/p < 10^{-3}$. Although the QZE may seem negligible, it is in fact in many situations the relevant term. Indeed, we will see in Sec. 2.1.2 that owing to the isotropy of the interaction in spin space, the magnetization $\hat{S}_z$, defined as the component of the collective spin along the magnetic field axis, is conserved in a static field. The linear Zeeman shift is then simply a constant in the Hamiltonian and plays no role in the dynamics or the equilibrium state.

We often apply time-dependent, or spatially dependent magnetic fields to perform spin rotation or apply spin-dependent forces. These are used as experimental tools and will be described in Chapter 3.

2.1.2 Interactions

Scattering potential Neutral atoms interact strongly at short distances and weakly at larger distances via van der Waals interactions. Several simplifications arise in ultra-cold dilute gases because of the very low temperature and density. First, because the interaction range is much smaller than the inter-atomic distance, it is sufficient to consider only two-body interactions, described in the framework of quantum scattering theory. Second, the interaction range is also much smaller than the de Broglie wavelength. This restricts the possible collisions to those with vanishing total orbital angular momentum (s-wave collisions). It also allows us to conveniently replace the complex interaction potential by a contact interaction (for scalar atoms)

$$\hat{U}_{\mathrm{ext}}(\mathrm{r}) = g\delta(\mathrm{r}) , \tag{2.6}$$

depending on a unique parameter g, related to the s-wave scattering length a by $g = \frac{4\pi\hbar^2}{M}a$. In our situation, the atoms have a spin $F = 1$, and can occupy the three Zeeman states. A similar pseudo-potential can be used irregardless of the internal state of the colliding atoms, such that the scattering potential becomes

$$\hat{U}_{\mathrm{scat}} = \hat{U}_{\mathrm{spin}} \otimes \delta(\mathrm{r}) . \tag{2.7}$$

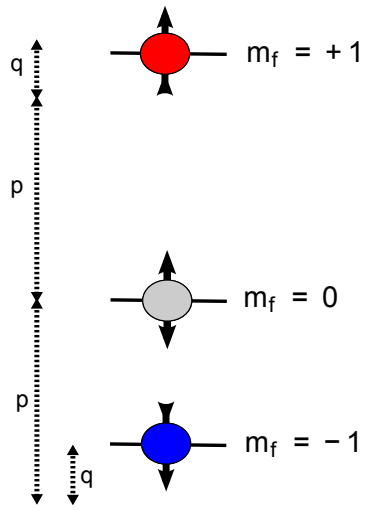

Figure 2: Left: linear and quadratic Zeeman shifts. Right: owing to the conservation of the magnetization, the linear Zeeman shift is a constant and only the quadratic Zeeman shift matters.

This delta potential is rotationally invariant in real space. Isotropy of the interaction[1] then requires $\hat{U}_{\text{spin}}$ to be rotationally invariant in spin space. Let $\hat{\mathcal{F}}$ be the total angular momentum of the colliding pair and $\hat{P}_{\mathcal{F}} = \sum_{|M|\leq\mathcal{F}} |\mathcal{F}, M\rangle\langle\mathcal{F}, M|$ the projectors on the subspace of total spin $\mathcal{F}$. The commutation relations $[\hat{U}_{\text{spin}}, \hat{\mathcal{F}}_{x,y,z}] = 0$ impose (Shur's lemma)

$$\hat{U}_{\text{spin}} = \sum_{\mathcal{F}=0}^{2} g_{\mathcal{F}} \hat{P}_{\mathcal{F}} \,, \tag{2.8}$$

where $g_{\mathcal{F}} = \frac{4\pi\hbar^2}{M} a_{\mathcal{F}}$ and $a_{\mathcal{F}}$ is the scattering length in the channel $\mathcal{F}$. Because of the exchange symmetry, the total spin of the colliding pair cannot be equal to 1. Furthermore, using $(\hat{\mathrm{s}}_1 + \hat{\mathrm{s}}_2)^2 = 2(1 + \hat{\mathrm{s}}_1 \cdot \hat{\mathrm{s}}_2) = 6\hat{P}_2$ and $\sum \hat{P}_{\mathcal{F}} = I$, one can rewrite $\hat{U}_{\text{spin}}$ as a familiar spin exchange interaction [29]

$$\hat{U}_{\text{spin}} = \overline{g} I + g_s \hat{\mathrm{s}}_1 \cdot \hat{\mathrm{s}}_2 \,. \tag{2.9}$$

Here we introduced $\overline{g} = \frac{4\pi\hbar^2}{M}\overline{a}$, $\overline{a} = \frac{a_0+2a_2}{3}$ and $g_s = \frac{4\pi\hbar^2}{M} a_s$, $a_s = \frac{a_2-a_0}{3}$. In practice, the scattering lengths are determined experimentally. In [47] the values $a_2 \simeq 2.80$ nm and $a_0 \simeq 2.51$ nm were measured ($\overline{a} = 2.7$ nm, $a_s \simeq 0.097$ nm). We point out that $\overline{a} > 0$ indicates repulsive interactions and that $a_s > 0$ favors anti-alignment of the spins and indicates antiferromagnetic interaction (AFI). Finally, we have $a_s \ll \overline{a}$, so that the scattering potential is in fact mostly spin-independent. However, thanks to Bose-Einstein condensation, we are able to probe very low energy scales, where the spin dependent interaction plays a crucial role.

A popular atom in spinor BEC experiments is Rubidium. The interactions in the $F = 1$ manifold are ferromagnetic (and significantly weaker) than for Sodium. At low magnetic fields, this yields BECs with very different magnetic order. This was one of the original motivations for the choice of Sodium in our experiment.

2.1.3 Many-body Hamiltonian

Interaction The many-body Hamiltonian is most conveniently written in second quantization. We introduce the atomic field operators $\hat{\Psi}^\dagger_m(\mathrm{r})$ that create an atom at position r in the Zeeman state $m = 0, \pm 1$. The interaction Hamiltonian is

$$\hat{H}_{\text{int}} = \frac{\overline{g}}{2} \sum_{i,j=1}^{N} \int d^3\mathrm{r} \Psi^\dagger_i(\mathrm{r})\Psi^\dagger_j(\mathrm{r})\Psi_i(\mathrm{r})\Psi_j(\mathrm{r}) + \frac{g_s}{2} \sum_{i,j,k,l=1}^{N} \int d^3\mathrm{r} \Psi^\dagger_i(\mathrm{r})\Psi^\dagger_j(\mathrm{r})\mathrm{s}_{ik} \cdot \mathrm{s}_{jl} \Psi_k(\mathrm{r})\Psi_l(\mathrm{r}) \,, \tag{2.10}$$

where s_{ik} are the spin-1 matrix elements. Introducing the density operator $\hat{\rho} = \sum_i \hat{\Psi}^\dagger_i(\mathrm{r})\hat{\Psi}_i(\mathrm{r})$ and the spin density operator $\hat{\mathcal{S}}(\mathrm{r}) = \sum_{i,j} \hat{\Psi}^\dagger_i(\mathrm{r})\mathrm{s}_{ij}\hat{\Psi}_i(\mathrm{r})$, the Hamiltonian Eq. (2.12) can be conveniently rewritten as

$$\hat{H}_{\text{int}} = \frac{1}{2} \int d^3\mathrm{r} \left(\overline{g}\hat{\rho}^2(\mathrm{r}) + g_s \hat{\mathcal{S}}^2(\mathrm{r}) \right) \,. \tag{2.11}$$

[1] neglecting the very small effect of an applied magnetic field on the electronic cloud, and other symmetry breaking fields.

We have omitted constant terms $\propto \int d^3\mathrm{r}\rho(\mathrm{r}) = N$. Using the expression of the spin-1 (2.5), we can develop the Hamiltonian and obtain (omitting the r dependence of the field and density operators)

$$\begin{aligned}\hat{H}_{\text{int}} = \frac{1}{2}\int d^3\mathrm{r}(\overline{g}+g_s)(:\hat{\rho}_{+1}\hat{\rho}_{+1}: + :\hat{\rho}_{-1}\hat{\rho}_{-1}:) + \overline{g} :\hat{\rho}_0\hat{\rho}_0: \\ + 2(\overline{g}+g_s)(\hat{\rho}_{+1}\hat{\rho}_0 + \hat{\rho}_{-1}\hat{\rho}_0) + 2(\overline{g}-g_s)\hat{\rho}_{+1}\hat{\rho}_{-1} \\ + 2g_s(\hat{\Psi}^\dagger_{+1}\hat{\Psi}^\dagger_{-1}\hat{\Psi}_0\hat{\Psi}_0 + \hat{\Psi}^\dagger_0\hat{\Psi}^\dagger_0\hat{\Psi}_{+1}\hat{\Psi}_{-1})\,. \end{aligned} \tag{2.12}$$

We use the symbol ": :" to indicate normal ordering of the field operators. The first line corresponds to spin-conserving collisions between atoms in the same Zeeman state, the second line to spin-conserving collisions between atoms in different Zeeman state, and the last line to the only spin-changing collision allowed by spin rotational symmetry.

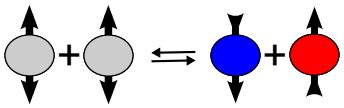

Figure 3: Spin changing collision.

Full Hamiltonian Let us conclude by writing the full Hamiltonian, including the Zeeman and interaction terms described above, plus the kinetic energy term, and the trapping potential V_{trap}. The latter is modeled as a harmonic trap, with frequencies $\omega_{x,y,z}$. The Hamiltonian is then

$$\hat{H} = \int d^3\mathrm{r}\left[\hat{\mathbf{\Psi}}^\dagger(\mathrm{r})\left(-\frac{\hbar\nabla^2}{2M} + V_{\text{trap}}(\mathrm{r})\right)\hat{\mathbf{\Psi}}(\mathrm{r}) + \frac{\overline{g}}{2}\rho^2(\mathrm{r}) + \frac{g_s}{2}\hat{\mathcal{S}}^2(\mathrm{r})\right] + p\hat{S}_z - q\hat{N}_0\,, \tag{2.13}$$

where we used the integrated quantities

$$\hat{N}_i = \int d^3\mathrm{r}\hat{\Psi}^\dagger_m\hat{\Psi}_m\,, \tag{2.14}$$

$$\hat{S}_z = \int d^3\mathrm{r}\hat{\mathcal{S}}_z = \hat{N}_{+1} - \hat{N}_{-1}\,. \tag{2.15}$$

As mentioned earlier, owing to the revolution symmetry around the z-axis, the magnetization $\hat{S}_z$ commutes with the Hamiltonian and is a conserved quantity.

2.2 Single Mode Approximation

We present in this Section an approach that considerably simplifies the study of the Hamiltonian Eq. (2.13), namely the single mode approximation (SMA) [48–50]. It assumes that all atoms occupy the same spatial mode, irregardless of their spin state. This is motivated by the following observations. Let us rewrite the Hamiltonian as $\hat{H} = \hat{H}_1 + \hat{H}_2$, with

$$\hat{H}_1 = \int d^3\mathrm{r}\left[\hat{\mathbf{\Psi}}^\dagger(\mathrm{r})\left(-\frac{\hbar\nabla^2}{2M} + V_{\text{trap}}(\mathrm{r})\right)\hat{\mathbf{\Psi}}(\mathrm{r}) + \frac{\overline{g}}{2}\rho^2(\mathrm{r})\right]\,, \tag{2.16}$$

$$\hat{H}_2 = \int d^3\mathrm{r}\left[\frac{g_s}{2}\hat{\mathcal{S}}^2(\mathrm{r})\right] + p\hat{S}_z - q\hat{N}_0\,. \tag{2.17}$$

The contribution $\hat{H}_1$ depends only on the spatial degree of freedom, and its energy scale (~ 1 kHz) is typically much larger than that of $\hat{H}_2$ (~ 10 Hz), which can thus be treated as a perturbation. More precisely, we first find the ground state of $\hat{H}_1$ and then derive an effective Hamiltonian for the spin degree of freedom. Finally we verify the self consistency of the procedure.

2.2.1 Spatial degree of freedom

Gross-Pitaevskii equation Given the previous discussion, we take the following ansatz:

$$\hat{\mathbf{\Psi}}(\mathrm{r}) = \psi_{\text{SMA}}(\mathrm{r})\hat{\zeta}\,, \tag{2.18}$$

where $\hat{\zeta} = (\hat{a}_{+1}, \hat{a}_0, \hat{a}_{-1})^T$. We first focus on the spatial mode, purposely written as a classical field $\psi_{\text{SMA}}(\mathrm{r})$ (normalized to 1). This is known as the Hartree-Fock (or mean field) approximation, and it is widely used to describe ultra-cold Bose gases, where a

large number of particles occupy the same single particle state [26]. Minimization of the energy under the constraint of conserved atom number (taken into account by introducing a Lagrange multiplier μ, the chemical potential) yields the Gross-Pitaevskii equation

$$\left(-\frac{\hbar^2\nabla^2}{2M} + V_{\text{trap}}(\mathrm{r}) + \bar{g}N|\psi_{\text{SMA}}|^2\right))\psi_{\text{SMA}} = \mu\psi_{\text{SMA}}\,. \tag{2.19}$$

Kinetic energy and repulsive interactions compete against the trapping potential.

Solutions We can distinguish two limiting cases

- For non-interacting particles, the solution is the ground state of the trapping potential ($\mu = \frac{\hbar}{2}(\omega_x + \omega_y + \omega_z)$) [51]

$$\psi_{\text{id}}(\mathrm{r}) = \prod_{\nu=x,y,z}\left(\frac{M\omega_\nu}{\pi\hbar}\right)^{\frac{1}{4}}\exp\left(-\frac{M\omega_\nu}{2\hbar}\nu^2\right)\,. \tag{2.20}$$

- In the other limit, known as Thomas-Fermi, the quantum pressure can be neglected and the density is an inverted parabola [26]

$$\psi_{\text{TF}}(\mathrm{r}) = \sqrt{\frac{1}{g}(\mu_{\text{TF}} - V_{\text{trap}}(\mathrm{r}))}\,, \tag{2.21}$$

  where $V_{\text{trap}}(\mathrm{r}) < \mu_{\text{TF}}$, and zero elsewhere. The chemical potential is computed to ensure proper normalization, $\mu_{\text{TF}} = \frac{\hbar\omega_{\text{ho}}}{2}\left(\frac{15N\bar{a}}{a_{\text{ho}}}\right)^{\frac{2}{5}}$, with $\omega_{\text{ho}} = (\omega_x\omega_y\omega_z)^{\frac{1}{3}}$ and $a_{\text{ho}} = \sqrt{\hbar/(m\omega_{\text{ho}})}$.

The relative effect of the kinetic energy and the interactions can be quantified using the healing length

$$\bar{\xi} = \sqrt{\frac{h^2}{2M\bar{g}n}}\,, \tag{2.22}$$

where n is the mean density. For a system of typical size L, the ratio between kinetic and interaction energy is $\sim \bar{\xi}^2/L^2$. In practice, we perform experiments with a wide range of parameters. Two typical situations are

- $N \sim 100$ and $\omega_{\text{ho}} \sim 2\pi \times 2\,\text{kHz}$. This situation is closer to the ideal-gas regime, with $L \sim a_{\text{ho}} \sim 0.5\,\mu\text{m}$ and $\bar{\xi} \sim 1\,\mu\text{m}$.
- $N \sim 10^4$ and $\omega_{\text{ho}} \sim 2\pi \times 300\,\text{Hz}$. This situation is closer to the Thomas-Fermi regime, with $L \sim R_{TF} \sim 2\,\mu\text{m}$ and $\bar{\xi} \sim 0.8\,\mu\text{m}$.

In general, we have to solve Eq. (2.19) numerically to get accurate predictions for the density profile. However, this is often of little importance to us, since we mostly focus on spatially averaged quantities, depending only on the spin degree of freedom.

2.2.2 Spin Hamiltonian

We now turn to the spin degree of freedom. Injecting the SMA ansatz in the Hamiltonian Eq. (2.17) we obtain an effective Hamiltonian for the spin degree of freedom

$$\hat{H}_{\text{spin}} = \frac{U_s}{2N}\hat{\mathbf{S}}^2 + p\hat{S}_z - q\hat{N}_0\,. \tag{2.23}$$

Here $U_s = Ng_s\int d^3\mathrm{r}|\psi_{\text{SMA}}(\mathrm{r})|^4$. In practice, $U_s/\hbar \sim 20\,\text{Hz}$ is calibrated experimentally (see chapter 4 and 5). We also introduced the total spin operator $\hat{\mathbf{S}} = \hat{S}_z\mathbf{e}_z + \hat{\mathbf{S}}_\perp$ with $\hat{\mathbf{S}}_\perp = \hat{S}_x\mathrm{e}_x + \hat{S}_y\mathrm{e}_y$ the transverse spin operator. Using the expression of the spin-1 matrices (2.5), we find

$$\hat{\mathbf{S}}_\perp^2 = N + \hat{N}_0 + 2\hat{N}_0(N - \hat{N}_0) + 2(\hat{a}_{+1}^\dagger\hat{a}_{-1}^\dagger\hat{a}_0^2 + \hat{a}_0^{\dagger 2}\hat{a}_{+1}\hat{a}_{-1})\,. \tag{2.24}$$

Let us remark once again that $[\hat{H}_{\text{spin}}, \hat{S}_z] = 0$. A unitary transform $\hat{U} = \exp(i\frac{pt}{\hbar}\hat{S}_z)$ allows us to get rid of the linear Zeeman term. We then obtain (we use the same notation for $\hat{H}_{\text{spin}}$ with a slight abuse of notation):

$$\hat{H}_{\text{spin}} = \frac{U_s}{2N}\hat{\mathbf{S}}^2 - q\hat{N}_0\,. \tag{2.25}$$

As mentioned in Sec. 2.1.2, for Sodium, the spin-dependent interaction energy U_s is positive, corresponding to AFI and $q \propto B^2 > 0$. This Hamiltonian governs most of the physics behind the experiments presented in this manuscript. We will discuss the ground state in the next Section.

2.2.3 Validity of the single-mode approximation

Let us consider a cloud with $S_z > 0$ (we use the notation $O = \langle \hat{O} \rangle$). The QZE is minimized by having as many atoms as possible in the $m = 0$ state. On the other hand, a quick estimate using Eq. (2.24) shows that a cloud with $m = +1$ and $m = 0$ atoms has a transverse spin $\sim N^2$, while a cloud with $m = \pm 1$ atoms has a transverse spin $\sim N$. Their is thus a competition between the QZE that favors a $m = 0, m = +1$ mixture and the AFI that prefers a $m = \pm 1$ mixture. However, if we relax the single-mode constraint, the transverse spin density $\langle \mathcal{S}_{\mathrm{perp}}(\mathrm{r}) \rangle$ could be kept equal to zero everywhere, providing the wave functions for the $m = 0$ and $m = +1$ states do not overlap. Hence, one may expect the AFI to lead to the formation of spin-domains, which obviously violates the SMA. However, the creation of such spin domains comes with an increase of the kinetic energy as each spin component is confined in a smaller volume. In sufficiently tight traps, this effect enforces the SMA.

In a same way that a healing length was defined to quantify the effect of the spin-independent interactions, we can define a spin healing length associated to the AFI

$$\xi_s = \sqrt{\frac{h^2}{2Mg_s n}}, \tag{2.26}$$

such that $E_{\mathrm{kin}}/E_{\mathrm{sp.int.}} \sim \xi_s^2/L^2$. The spin healing length gives an order of magnitude of the smallest size of a possible spin domain. We compute ξ_s for different experimental configurations, characterized by the atom number N and the trap frequencies, and we report the values in table 2.1.

Geometry	N	Trap. freq.	L	ξ_s
CDT	100	$\sim 2\,\mathrm{kHz}$	$\sim 0.5\,\mu\mathrm{m}$	$\sim 5\,\mu\mathrm{m}$
CDT	10^4	$\sim 300\,\mathrm{Hz}$	$\sim 2\,\mu\mathrm{m}$	$\sim 4.5\,\mu\mathrm{m}$
SBT	10^4	$\sim 300\,\mathrm{Hz}$ and $3\,\mathrm{Hz}$	$\sim 60\,\mu\mathrm{m}$	$\sim 10\,\mu\mathrm{m}$

Table 2.1: The first two situations correspond to a roughly isotropic, tight crossed dipole trap (CDT). In the first case, the cloud is deep in the SMA, the AFI are two orders of magnitude below the kinetic energy. From this simple estimate, we can expect small deviations to the SMA in the second case. This is one of the reasons why we tend to work with small BECs. The last situation corresponds to an elongated, single-beam trap (SBT), with a very weak confinement along one axis, and where we observe the appearance of spin domains.

To be more quantitative, it is possible to find numerically the ground state of Eq. (2.13) in the mean-field approximation. One has to solve three coupled Gross-Pitaevksii equations to obtain the wave function of each Zeeman state. Results for our typical experimental conditions are reported in [52]. The fidelity with the SMA solution is larger than 0.99 for $N < 10^4$ in a crossed dipole trap, with $\omega_{\mathrm{ho}} = 2\pi \times 600\,\mathrm{Hz}$.

Spin domain formation in an elongated trap We show in figure 4a a typical picture, of a BEC with magnetization $\langle \hat{S}_z \rangle \simeq N/2$, in an elongated trap and in a large bias field. This picture is taken after having separated the Zeeman state using a Stern-Gerlach set-up, described in Chapter 3. We see a domain with $m = 0$ atoms, surrounded by $m = +1$ atoms. This configuration maximizes the quadratic Zeeman energy under the constraint $\langle \hat{S}_z \rangle \simeq N/2$. Moreover, thanks to the spatial separation of the $m = 0$ and $m = \pm 1$ states, the transverse spin vanishes almost everywhere (up to quantum corrections discussed later on). Finally, the domain $m = +1$, which has non-zero magnetization density, and therefore larger interaction energy is located on the edge of the trap, where the particle density is smaller. Neglecting the kinetic energy, a spatially separated configuration with sharp domain walls minimizes the energy. As the confinement increases, so does the kinetic energy, and the domain starts to overlap. For strong enough confinement, the three Zeeman states are forced to overlap. We show in figure 4b an image of a BEC in such conditions, realized in practice in a tight cross dipole trap.

Experiments in the 1D regime were carried on during the first year of my PhD and are presented in details in [53], and in Andrea Invernizzi's thesis [54]. I will not discuss them further, and I will rather focus on experiments accomplished during the rest of my PhD. Those were realized using tight cross dipole traps, and are all well described within the SMA.

2.3 Mean field approximation

We carry on with the investigation of the ground state property of the Hamiltonian (2.25). We first use a mean-field treatment, similar to the one used for the spatial mode. It is a variational method, and we start by introducing trial states, the so-called coherent spin states.

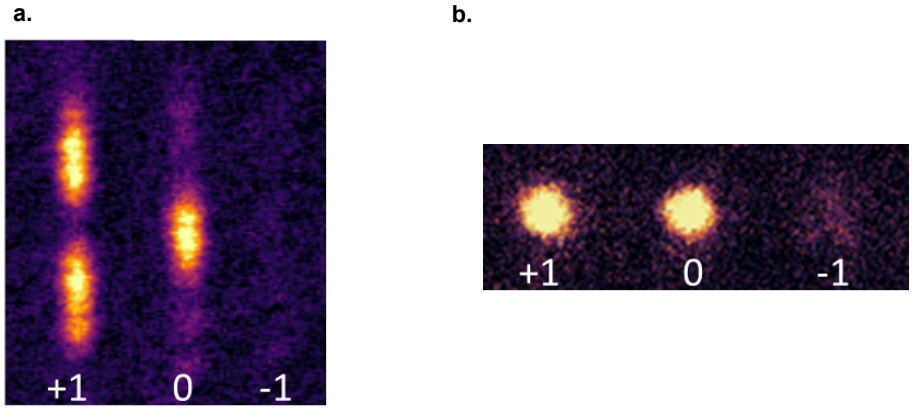

Figure 4: Clouds after Stern-Gerlach separation of the Zeeman states confined in (a) a single beam elongated trap and (b) a cross-dipole trap. In latter case, the SMA appears to be well verified. In the former, the spontaneous formation of spin domains constitutes a dramatic deviation.

2.3.1 Coherent spin states

General case Let us consider a general spin-1 state defined in the standard basis as $|\boldsymbol{\zeta}\rangle = \sum_m \zeta_m |m\rangle$, with $\boldsymbol{\zeta}$ a complex unit vector define by three real variable n_0, s_z and $\varphi_{\pm 1}$ as

$$\boldsymbol{\zeta} = \begin{pmatrix} \sqrt{\frac{1-n_0+s_z}{2}} e^{i\varphi_{+1}} \\ \sqrt{n_0} \\ \sqrt{\frac{1-n_0-s_z}{2}} e^{i\varphi_{-1}} \end{pmatrix} . \tag{2.27}$$

We have chosen the phase φ_0 to be equal to 0. We will often use the relative phases

$$\eta = \frac{\varphi_{+1} - \varphi_{-1}}{2} \qquad \text{and} \qquad \vartheta = \varphi_{+1} + \varphi_{-1} - 2\varphi_0 . \tag{2.28}$$

A coherent state where all atoms occupy the same single particle state describes a perfect BEC and can be written as

$$|N : \boldsymbol{\zeta}\rangle = \frac{1}{\sqrt{N!}} (\boldsymbol{\zeta} \cdot \hat{\mathbf{a}}^\dagger)^N |\text{vac}\rangle , \tag{2.29}$$

with $\hat{\mathbf{a}}^\dagger = (\hat{a}^\dagger_{+1}, \hat{a}^\dagger_0, \hat{a}^\dagger_{-1})^T$. Here, $n_0 = \langle \hat{N}_0 \rangle / N$ is the reduced population in the state $m = 0$ and $s_z = \langle \hat{S}_z \rangle / N$ is the reduced magnetization.

Nematic state We now introduce the family of nematic, or polar coherent states, which plays an important role in the description of antiferromagnetic spinor BECs. The nematic coherent state aligned along z, is the state with all atoms in $m = 0$. By spin rotation of this state, one obtains the family of nematic coherent state aligned along $\boldsymbol{\Omega} = (\sin\theta\cos\phi, \sin\theta\sin\phi, \cos\theta)$. They can be expressed as

$$|N : \boldsymbol{\Omega}\rangle = \frac{1}{\sqrt{N!}} \left(-\frac{1}{\sqrt{2}} \sin\theta e^{-i\phi} \hat{a}^\dagger_{+1} + \cos\theta \hat{a}^\dagger_0 + \frac{1}{\sqrt{2}} \sin\theta e^{i\phi} \hat{a}^\dagger_{-1} \right)^N |\text{vac}\rangle . \tag{2.30}$$

By comparison with Eq. (2.27), we identify $n_0 = \cos^2\theta$, $s_z = 0$, $\vartheta = \pi$ and $\eta = -\phi + \frac{\pi}{2}$.

2.3.2 Mean-field ground state

Mean-field energy The mean field energy per atom $\varepsilon_{\text{spin}} = \langle \hat{H}_{\text{spin}} \rangle / N$, where $\hat{H}_{\text{spin}}$ is given by Eq. (2.25) and the expectation value is taken for a general spin coherent state given by Eq. (2.29), is

$$\varepsilon_{\text{spin}} = \frac{U_s}{2} (\mathbf{s}_\perp^2 + s_z^2) - q n_0 . \tag{2.31}$$

Here $\mathbf{s}_\perp$ is the (reduced) transverse spin of a coherent state

$$\mathbf{s}_\perp = \|\mathbf{s}_\perp\| \left(\cos\eta \mathbf{e}_x + \sin\eta \mathbf{e}_y \right) , \tag{2.32}$$

with

$$\|\mathbf{s}_\perp\|^2 = 2n_0\left(1 - n_0 + \sqrt{(1-n_0)^2 - s_z^2}\cos\vartheta\right) + \mathcal{O}\left(\frac{1}{N}\right). \tag{2.33}$$

Because the mean magnetization s_z is a conserved quantity, it should be thought of as an experimental parameter. More precisely, the relation $[\hat{S}_z, \hat{H}_{\text{spin}}] = 0$ implies the conservation of the whole distribution of magnetization, not only the mean value. Consistency with the mean field ansatz imposes a Poissonian distribution, fully characterized by the mean value s_z. In the next Section, when we derive the ground state with no assumption on the nature of the many-body state, we will have to specify the whole magnetization distribution.
For now, we investigate the mean-field ground state as a function of s_z and q (of any sign). It is studied theoretically in [28,29,55] and experimentally in [37,56,57].

Phase diagram The minimization of $\varepsilon_{\text{spin}}$ for a given q and s_z leads to different phases characterized by the order parameter $\|\mathbf{s}_\perp\|$. We use the same notation as in [29].

AF. The *antiferromagnetic* phase, with vanishing transverse spin, exists for $q < q_c = U_s(1-\sqrt{1-s_z})$. When $s_z \neq 0$, $s_\perp = 0$ when the $m = 0$ state is not populated. For $0 < q < q_x$, this is driven by the AFI, which competes against the QZE.

BA. The *broken-axisymmetry* phase exists for $q > q_c$. It is characterized by a non-vanishing transverse spin $\mathbf{s}_\perp > 0$ (except along the lines $s_z = 0$ and $s_z = \pm 1$), which breaks the rotational symmetry around the z-axis. The phase ϑ is locked to π in order to minimize the AFI (this has been observed in [37]).

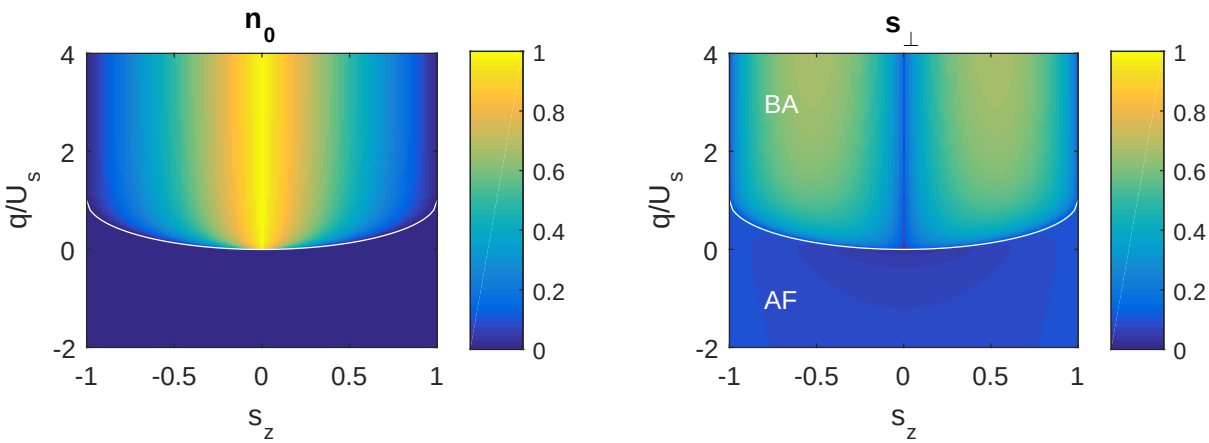

Figure 5: Relative population in the state $m = 0$ (left plot) and order parameter $\mathbf{s}_\perp$ (right plot) in the ground state, versus the reduced magnetization s_z and q/U_s. The white line delimits the phase transition determined from a mean field treatment.

The mean-field approximation has been successful in describing numerous experiments, either looking at the equilibrium state [37,56,57], or the dynamics of a spinor BEC [58–61]. Yet, recent experiments [10,62–67] (mostly focusing on the dynamics) cannot be understood within this simple picture. A hint of the failure of the mean field treatment to precisely describe the ground state comes from the symmetry breaking. Indeed, because $[\hat{H}_{\text{spin}}, \hat{S}_z] = 0$, the eigenstates of $\hat{H}_{\text{spin}}$ are eigenstates of $\hat{S}_z$, which are invariant under rotation around the z-axis. The mean field states do not belong to that family (except when there is only one Zeeman state populated).

2.4 Beyond the mean-field approximation

We now look for the ground state beyond the mean-field ansatz. This opens the possibility of entangled states as will be discussed in Section 2.5. Before we proceed, we need to specify the constraint on the magnetization. For mean field states, which have a Poissonian distribution of S_z, we only need to constrain the mean value. For more general states we have to constrain the whole distribution. We will first focus on the simple case, where the magnetization is *exactly* zero (*i.e.* we take a centered delta distribution). This corresponds to the experimental situation explored in Chapter 5 to 7. We will see that for antiferromagnetic interactions, it includes the unconstrained ground state.

2.4.1 Bogoliubov approximation

Bogoliubov Hamiltonian When $q \to \infty$, one can neglect the AFI and the exact ground state is the nematic state $|N : \mathbf{e}_z\rangle$, with all atoms in $m = 0$. For large and positive q (the range of validity will be determined to ensure self-consistency) we thus expect $N_0 \simeq N \gg N_{\pm 1}$. In that situation, the system should be fairly insensitive to small fluctuations of N_0. This motivates a Bogoliubov ansatz,

$$\hat{\mathbf{a}} = (\hat{a}_{+1}, (N - \hat{N}_{+1} - \hat{N}_{-1})^{\frac{1}{2}}, \hat{a}_{-1})^T \,, \tag{2.34}$$

where the mode $m = 0$ is taken as a classical field, but the $m = \pm 1$ modes are treated quantum mechanically. The SMA Hamiltonian Eq. (2.25) is approximated by the quadratic Hamiltonian

$$\hat{H}_B = (q + U_s)\left(\hat{N}_{+1} + \hat{N}_{-1}\right) + U_s\left(\hat{a}_{+1}\hat{a}_{-1} + \hat{a}^\dagger_{+1}\hat{a}^\dagger_{-1}\right) \,, \tag{2.35}$$

up to a constant and neglecting terms of order $1 \ll N$. Using the Bogoliubov transformation [68],

$$\begin{aligned} \hat{\alpha} &= \cosh(\theta)\hat{a}_{+1} - \sinh(\theta)\hat{a}^\dagger_{-1} \,, \\ \hat{\beta} &= \sinh(\theta)\hat{a}^\dagger_{+1} - \cosh(\theta)\hat{a}_{-1} \,, \end{aligned} \tag{2.36}$$

with $\tanh(2\theta) = -\frac{U_s}{q+U_s}$, the Hamiltonian is diagonalized

$$\hat{H}_B = \hbar\omega_B(\hat{\alpha}^\dagger\hat{\alpha} + \hat{\beta}^\dagger\hat{\beta}) \,, \tag{2.37}$$

up to constant terms, and with the Bogoliubov energy

$$\hbar\omega_B = \sqrt{q(q + 2U_s)} \,. \tag{2.38}$$

The longitudinal spin is $\hat{S}_z = \hat{N}_{+1} - \hat{N}_{-1} = \hat{\alpha}^\dagger\hat{\alpha} - \hat{\beta}^\dagger\hat{\beta}$.

Ground state The ground state is the vacuum of Bogoliubov excitations. It satisfies the constraint of exactly vanishing magnetization. Let $\hat{N}_p = \frac{\hat{N}_{+1}+\hat{N}_{-1}}{2}$ be the operator "number of $m = \pm 1$ pairs". We can compute the mean value and variance of $\hat{N}_p$ in the ground state of the Hamiltonian $\hat{H}_B$ (for $q \ll U_s$):

$$\langle\hat{N}_p\rangle_B \simeq \sqrt{\frac{U_s}{8q}} \,, \tag{2.39}$$

$$\Delta\hat{N}^2_{p,B} = \langle\hat{N}_p\rangle_B(1 + \langle\hat{N}_p\rangle_B) \,. \tag{2.40}$$

Eq. (2.40) is characteristic of a thermal Bose-Einstein distribution [26]. We show in the appendix C that this is an exact result. In the number basis $|N_{+1}, N_{-1}\rangle$ the many-body state is

$$|\text{TMSV}\rangle = \frac{1}{\sqrt{\mathcal{N}}}\sum_{n=0}^{\infty}\zeta^n|n, n\rangle \,, \tag{2.41}$$

with $\mathcal{N} = 1 + \langle\hat{N}_p\rangle$ and $\zeta^2 = \langle\hat{N}_p\rangle/(1 + \langle\hat{N}_p\rangle)$. This state is sometimes called a two-mode squeezed vacuum state (TMSV). Its most distinctive feature is the wide distribution of the atoms number in mode $m = \pm 1$, in contrast with the perfect correlation with the atoms number in the other mode $m = \mp 1$. This remarkable property cannot be realized with a mean-field state, nor with any separable states, as will be shown in Section 2.5. The TMSV can be used for instance, to perform metrology beyond the standard quantum limit (see App. D). We will come back to this in Chapter 5 when discussing the dynamical production and characterization of a TMSV.

The depletion of the $m = 0$ mode results in an increase of the QZE, compensated by a reduction of the AFI energy. This effect can be identified computing the total spin

$$\langle\hat{\mathbf{S}}^2\rangle_B = \frac{2Nq - U_s}{\hbar\omega_B} \,. \tag{2.42}$$

When $q \gg U_s$, $\langle\hat{\mathbf{S}}^2\rangle_B = 2N$, the shot noise value in the nematic state. Indeed, in first quantization, the total spin can be written as

$$\hat{\mathbf{S}}^2 = \sum_{i=1}^{N}\hat{\mathbf{s}}_i^2 + 2\sum_{i=1,j>i}^{N}\hat{\mathbf{s}}_i\hat{\mathbf{s}}_j \,, \tag{2.43}$$

where $\hat{\mathbf{s}}_i$ is the spin of the atom i. For spin 1, $\langle \hat{\mathbf{s}}_i^2 \rangle = 2$. Furthermore, for a separable state, if $i \neq j$, $\langle \hat{s}_i \hat{s}_j \rangle = \langle \hat{\mathbf{s}}_i \rangle \langle \hat{\mathbf{s}}_j \rangle$, and for indistinguishable atoms $\langle \hat{s}_i \rangle = \langle \hat{s}_1 \rangle$. These considerations yields for separable states

$$\langle \hat{\mathbf{S}}^2 \rangle = 2N + N(N-1)\langle \hat{s}_1 \rangle^2 \,. \tag{2.44}$$

Hence, for separable states the minimal value of the spin fluctuations is obtain for nematic states, which verifies $\langle \hat{\mathbf{s}}_1 \rangle = 0$, and $\langle \hat{\mathbf{S}}^2 \rangle = 2N$.

Bosonic amplification Let us consider the evolution of the ground state in the range $\frac{U_s}{N} \ll q \ll U_s$. According to Eq. (2.39), we have $1 \ll \langle \hat{N}_p \rangle \ll N$. The ratio between the total spin and its shot noise value is

$$\frac{\langle \hat{\mathbf{S}}^2 \rangle_B}{2N} \simeq \frac{1}{4\langle \hat{N}_p \rangle} \ll 1 \,. \tag{2.45}$$

In words, the fluctuation of the spins are reduced well below the shot noise level. This is quite a surprising result: a microscopic (independent on N) depletion of the condensate, still leads to a significant decrease of the spin fluctuations. This counterintuitive phenomenon can be understood as an effect of bosonic amplification [41].
The microscopic mechanism that leads to reduction of the collective spin below the shot noise value is the association of two spins to form a singlet state, with zero total spin:

$$|\text{sing}\rangle = \frac{1}{\sqrt{3}}(|0,0\rangle - |+1,-1\rangle - |-1,+1\rangle) \,. \tag{2.46}$$

Naively (and wrongly), one could reason as follows. We assume that the cloud can be divided into two independent groups, N_{singlet} atoms forming singlet pairs, and $N - N_{\text{singlet}}$ atoms remaining in the $m = 0$ Zeeman state. We then compute the mean values of observables by summing the contribution of the two groups independently (this is the faulty step). It yields $\langle \hat{\mathbf{S}}^2 \rangle_{\text{naive}} = 2(N - N_{\text{singlet}})$, and $N_{\text{singlet}} = \frac{4}{3}\langle \hat{N}_p \rangle$. The reduction of the total spin is proportional to the depletion, which is arguably more intuitive than the Bogoliubov results Eq. (2.45). However, in this wrong calculation, we forget interference terms between the two fictitious groups, arising from the symmetrization of the state. The importance of this term can already be seen in the simple case of a state composed of one singlet state and one atom in the state $m = 0$. If the spins were distinguishable, the state in first quantized form would be

$$|\psi\rangle = \frac{1}{\sqrt{3}}(|0,0,0\rangle - |0,+1,-1\rangle - |0,-1,+1\rangle) \,. \tag{2.47}$$

For indistinguishable spins, the proper symmetrized state is

$$|\psi^S\rangle = \frac{1}{\sqrt{15}}(3|0,0,0\rangle - |0,+,-\rangle - |0,-,+\rangle - |+,0,-\rangle - |-,0,+\rangle - |+,-,0\rangle - |-,+,0\rangle) \,.$$

We can easily compute $\langle \psi | \hat{N}_0 | \psi \rangle = \frac{5}{3}$ whereas $\langle \psi^S | \hat{N}_0 | \psi^S \rangle = \frac{11}{5} > \frac{5}{3}$. We see that the $m = 0$ mode is already amplified by the presence of one atom in addition to the singlet. Of course, this effect is dramatically enhanced when there is a condensate in $m = 0$.

Validity of the Bogoliubov approximation The most stringent condition for the validity of the Bogoliubov approximation comes from the spin given by Eq. (2.42). The treatment clearly fails for $q < \frac{U_s}{2N}$, where it predicts $\langle \hat{\mathbf{S}}^2 \rangle < 0$. On the other hand, for the populations, self-consistency requires $\langle \hat{N}_p \rangle \ll N$, that is to say $q \gg \frac{U_s}{N^2}$ [Eq. (2.39)]. To be more quantitative, in Section 2.4.3, figure 6, we compare these results with an exact diagonalization. We see that the Bogoliubov approximation is indeed more accurate for the population than for the spin (at low q).

2.4.2 Exact treatment at $q = 0$

Total spin eigenstate For $q = 0$, the Hamiltonian Eq. (2.25) can be written as

$$\hat{H}_{\text{SMA}} = \frac{U_s}{2N}\hat{\mathbf{S}}^2 \,. \tag{2.48}$$

This Hamiltonian can be diagonalized analytically (see [41,48,50] and also appendix B). Its eigenstates are the angular momentum states $|N, S, M_z\rangle$, where $S \in [0, N]$ is an integer that has the same parity as N in order to satisfy to the exchange symmetry. M_z is an integer in $[-S, S]$. The eigenvalues are

$$E(N,S) = \frac{U_s}{2N}S(S+1) \,. \tag{2.49}$$

Ground state For simplicity, let us focus on the situation N even. The macroscopic singlet state with vanishing spin $S = 0$ is the ground state at $q = 0$ (clearly satisfying the zero magnetization constraint). It is perfectly invariant upon spin rotation, as a consequence of the rotational symmetry of the Hamiltonian Eq. (2.48). For $N = 2$, the singlet pair state $|2, 0, 0\rangle$ is given in the Zeeman basis by Eq. (2.46). For larger N, the "macroscopic singlet state" is obtained by symmetrization (under particle exchange) of the state $|2, 0, 0\rangle^{\otimes \frac{N}{2}}$. This state is very different from a mean-field state given by Eq. (2.29), since $|2, 0, 0\rangle$ cannot be factorized in a product of single particle states (it is a two-particle entangled state). We introduce the singlet-pair creation operator,

$$\hat{A}^\dagger = \frac{1}{\sqrt{3}} \left(\hat{a}_0^{\dagger 2} - 2\hat{a}_{+1}^\dagger \hat{a}_{-1}^\dagger \right) . \tag{2.50}$$

In the number basis, the singlet state can be written as [40, 41, 43]

$$|N, 0, 0\rangle = \hat{A}^{\dagger \otimes \frac{N}{2}} |\text{vac}\rangle_{\text{nb.basis}} . \tag{2.51}$$

$$\tag{2.52}$$

In the appendix B, we show that for large N, the probability distribution of N_0 in the singlet state is $\mathcal{P}(N_0) \simeq \sqrt{N/N_0}/2$. From this, we compute the mean value and variance of $\hat{N}_0$. We obtain

$$\langle \hat{N}_0 \rangle = \frac{N}{3} , \tag{2.53}$$

$$\Delta \hat{N}_0^2 \simeq \frac{4N^2}{45} \simeq 0.3N^2 . \tag{2.54}$$

We remark that the mean is consistent with the isotropy of the singlet state, and the variance characterizes a distribution with super-Poissonian fluctuations. We will study this remarkable state in detail in Chapter 7.

2.4.3 Numerical results and summary

We diagonalized numerically the SMA Hamiltonian Eq. (2.25) for $N = 100$ atoms, under the constraint of exactly vanishing magnetization. We show the results for $q > 0$ in figure 6. We summarize the results of Sec. 2.4.1 and Sec. 2.4.2 as follows:

- $q > U_s$: The interactions play a negligible role and the mean field treatment works fine. The cloud is condensed in the nematic state $|N : \mathbf{e}_z\rangle = |m = 0\rangle^{\otimes N}$.
- $\frac{U_s}{N} < q < U_s$: The condensate is slightly depleted and well described by a Bogoliubov approximation. The distribution of atoms in the $m = \pm 1$ mode obeys a thermal Bose-Einstein distribution. While the total spin steadily decreases between $q \sim U_s$ and $q \sim U_s/N$, the depletion remains small. This can be understood as a bosonic amplification of the condensed mode $m = 0$.
- $q < \frac{U_s}{N}$: The Bogoliubov approximation breaks down, the condensate has extensive occupation of the three modes, with macroscopic fluctuations (of order $\sim N$). On the other hand, the total spin has microscopic fluctuations (of order ~ 1).
- $q < \frac{U_s}{N^2}$: The ground state is close to the macroscopic singlet state (exact at $q = 0$). The latter shares the rotational symmetry of the Hamiltonian, and thus has equal population in the three modes and a vanishing total spin.

2.5 Entanglement in a spinor BEC

In experiments presented in Chapters 5 to 7, we will pay particular attention to the presence of entanglement in our system. We quantify the entanglement relatively to two partitionings of the system, in terms of group of atoms (or block) or in terms of degree of freedom (modes). In the present section, we introduce the measure of entanglement and the two partitionings. These notions will find a more concrete meaning in the discussion of the experiments, and we will always recall the definition.

Entangled states Deviations from the mean field prediction occur when the ground state cannot be described by the ansatz $|N : \zeta\rangle = |\zeta\rangle^{\otimes N}$. Product states of this form are the only symmetric separable states, and thus, the failure of the mean field description indicates entanglement between the atoms. The two-mode squeezed vacuum state defined in Eq. (2.41) and the singlet state defined in Eq. (2.51) are entangled states.

For completeness, let us briefly introduce a third remarkable entangled state, the so-called "twin-Fock state" (TFS), which has exactly half of the atoms in $m = +1$ and half in $m = -1$. It can be written in the number basis as

$$|N : \text{TFS}\rangle = |\frac{N}{2}, 0, \frac{N}{2}\rangle_{\text{nb.basis}} . \tag{2.55}$$

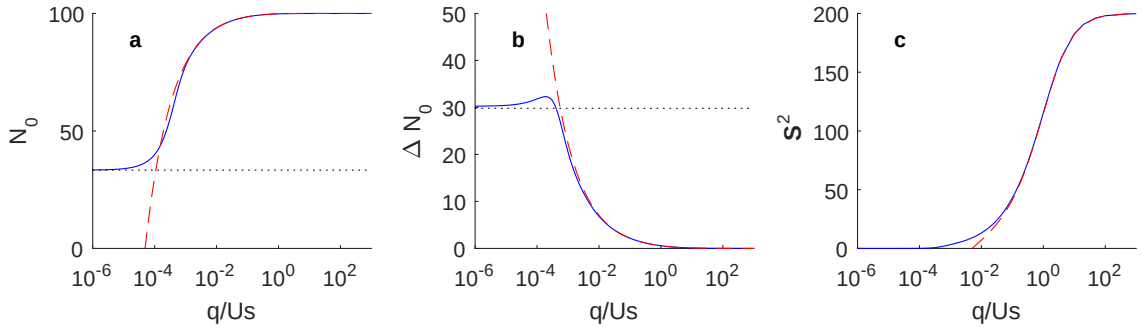

Figure 6: Ground state of an antiferromagnetic spin-1 BEC of $N = 100$ atoms, versus the QZE q. The solid line is the result of a numerical diagonalization. The red dashed lines are the predictions of the Bogoliubov theory. The black dashed line is the singlet state asymptote for $q = 0$. We show the mean population N_0 (a), standard deviation ΔN_0 (b) and total spin $\mathbf{S}^2$ (c).

The TFS is the ground state for large negative QZE ($-q \gg U_s$), under the constraint $s_z = 0$. In that case the mean field ground state is highly degenerate and corresponds to the whole family of nematic states $|N : \mathbf{\Omega}\rangle$, where $\mathbf{\Omega}$ lies in the (xy)-plane. This resembles the situation $q = 0$, although the degeneracy is lesser here, because of the QZE that breaks $SO(3)$ rotational symmetry. Even though the TFS has a very simple form in the number basis, it is a non-classical state that can be used to perform metrology beyond the standard quantum limit [69].

Having identified these interesting states, a natural question that arises is how to classify them. An exhaustive answer goes far beyond the scope of this manuscript [70]. We only introduce a few entanglement criteria and figures-of-merit well suited to the states we have produced. In particular in Chapter 5, we will define squeezing parameters, that can reveal entanglement and sometimes metrological enhancement. In this chapter, we turn to another, more general quantity, the entanglement entropy, to quantify the amount of entanglement in a given state.

Entanglement entropy Let us divide the full system in two complementary partitions, A and B with Hilbert spaces H_A and H_B. We first consider a pure state $|\psi\rangle \in H_A \otimes H_B$. We write $\rho = |\psi\rangle\langle\psi|$ the total density matrix, and $\rho_A = \mathrm{Tr}_B(\rho)$ the reduced density matrix, where Tr_B stands for the partial trace over a basis of H_B. The value of any local (acting separately on A and B) observable is fully determined by ρ_A and ρ_B. The entanglement entropy is the Von-Neuman entropy of state ρ_A,

$$\mathcal{S}(\rho_A) = -\mathrm{Tr}_A(\rho_A \ln \rho_A)\,. \tag{2.56}$$

If the state is separable, *i.e.* $|\psi\rangle = |\psi_A\rangle \otimes |\psi_B\rangle$, ρ_A is a pure state with zero entropy. Otherwise $\mathcal{S}(\rho_A) > 0$ measures the amount of information shared between A and B. The Von-Neumann entropy is conserved under unitary operations. If they are local, the entanglement entropy is also conserved.

For mixed states, the Von-Neumann entropy is larger than zero for the total state, and a non-zero entropy of the reduced state does not necessarily indicate entanglement. Instead, one should measure the mutual information,

$$\mathcal{I}(A, B) = \mathcal{S}(\rho_A) + \mathcal{S}(\rho_B) - \mathcal{S}(\rho)\,. \tag{2.57}$$

$\mathcal{I}(A, B) > 0$ indicates entanglement. In the rest of this Section, we only consider pure states.

Let us point out, that despite its theoretical interest (*e.g.* [71]), the Von-Neumann entropy is in general difficult to access experimentally [72]. Indeed, it is a non-linear function of the density matrix that requires in general the knowledge of the entire quantum state in order to be calculated. We have been able to measure the entanglement entropy of non-classical states using two distinct methods. In Chapter 7, we use a full reconstruction of the state produced in the experiment. In Chapter 5, we create entanglement using reversible dynamics. $\mathcal{S}(\rho_A)$ can be measured on the entangled state and $\mathcal{S}(\rho)$ after further evolution, on a "disentangled" state (relying on the conservation of the entropy under unitary evolution).

Partitioning To go further, we should explicit A and B for our system. In the SMA, the only degree of freedom is the spin. We can think of two simple ways to divide the system (we use the same names as in [70]):

- A is composed of a fixed number of atoms n. B is composed of the remaining $N - n$ atoms. We call such a division *block partitioning*. The term "block" comes from an analogy with spins localized on a lattice. In our case, the spins are "itinerant" and indistinguishable, so this name should not be taken too literally. Yet, the reduced density matrix of A is perfectly well defined, providing one takes the indistinguishably into account [70, 73].

- A is composed of the atoms in a given spin state, $e.g.$ $m = +1$. B is composed of the atoms in the remaining states, $m = 0, -1$. In that case, we talk about *mode partitioning*.

Basically a pure state has block (mode) entropy if it is not separable in first (second) quantization. When dealing with a fixed number of distinguishable particles, the first definition is more natural. When dealing with a fluctuating number of particles, blocks with a fixed number of atoms cannot be define, and the mode partitioning has to be used. In our situation, the two partitionings are well defined and both are often used in the literature for models comparable to ours ($e.g.$ itinerant spin $1/2$, see for instance [70] and the references therein).

Block entropy Single particle operations, such as spin rotations are local. On the other hand, a collision between an atom from block A and an atom from block B is a non-local operation and can thus modify the entanglement. For now, we will focus on the situation where A is composed of a single atom, so that $\rho_A = \rho^{(1)}$ is the single particle density matrix. It can be written in the standard state basis as

$$\rho^{(1)}_{i,j} = \frac{1}{N}\langle \hat{a}^\dagger_i \hat{a}_j \rangle \,. \tag{2.58}$$

The state we considered are $SO(2)$ symmetric, such that $[\rho^{(1)}, \hat{S}_z] = 0$ and $\rho^{(1)}$ is diagonal in the standard basis. Using also $s_z = 0$, we can express the entropy as

$$\mathcal{S}(\rho^{(1)}_{S_z=0}) = -(1-2n_p)\ln(1-2n_p) - 2n_p \ln(n_p)\,, \tag{2.59}$$

with $n_p = \langle \hat{N}_p \rangle / N$ the reduced number of pair. The entropy is maximal for a uniform distribution, $n_p = \frac{1}{3}$ and $\mathcal{S}^{(1)}_{\max} = \ln(3)$.

Let us now examine how $\rho^{(1)}$ and its entropy evolve in the ground sate of the SMA Hamiltonian:

- $q \gg U_s$: Nematic state, $n_p = 0$, and $\mathcal{S}(\rho^{(1)}) = 0$.
- $\frac{U_s}{N} < q$: Two-mode squeezed vacuum. $n_p \simeq \sqrt{\frac{U_s}{8qN^2}}$, and $\mathcal{S}(\rho^{(1)})$ is given by Eq. (2.59).
- $q = 0$: Singlet state, $n_p = \frac{1}{3}$ and $\mathcal{S}(\rho^{(1)}) = \ln(3)$.
- $-q \gg U_s$: Twin-Fock state, $n_p = \frac{1}{2}$ and $\mathcal{S}(\rho^{(1)}) = \ln(2)$.

At $T = 0$, an ensemble of non-interacting bosons forms a perfect BEC and $\rho^{(1)}$ has one non-zero eigenvalue (and no entropy). When $\rho^{(1)}$ has several macroscopic eigenvalues of order ~ 1[2], the condensate is said to be fragmented [74]. This will be the subject of Chapter 7.

Mode entropy When A is defined as the ensemble of atoms in a single mode m, $e.g.$ $m = +1$, mode entropy simply results from having an undetermined number of atoms in m. A mere spin-rotation (that are no longer local operations, since they mix the modes) may thus create mode entanglement. For instance, the nematic state $|N : \mathbf{e}_z\rangle$ has no atom in $m = +1$ and $\mathcal{S}(\rho_A) = 0$. After a $\pi/2$ rotation, $|N : \mathbf{e}_x\rangle$ has a binomial distribution of N_{+1}. Hence $\mathcal{S}(\rho_A) > 0$ and the state has mode entanglement. Note that mode entanglement depends on the modes that are chosen. For instance if we choose x as a quantization axis, $|N : \mathbf{e}_z\rangle$ is entangled and $|N : \mathbf{e}_x\rangle$ is not[3]. The standard basis seems to be a very natural choice. A motivation could come from the facts, that a spin-dependent force, easy to realize in practice, could be used to transform spin-entanglement in the standard basis into spatial entanglement. However, as was pointed out in [75], a superselection rule should be taken into account: it is impossible to couple states with different numbers of atoms. For instance let us consider one atom brought into the superposition $(|m = +1\rangle + |m = -1\rangle)/\sqrt{2}$. In the number basis, this state is expressed as $(|1,0,0\rangle + |0,0,1\rangle)/\sqrt{2}$ and is mode-entangled. Let us assume that using a magnetic force, we map the spin modes $m = \pm 1$ onto two spatial modes A and B (we let aside the $m = 0$ mode). The state then looks like a Bell-state, useful to perform non-classical protocols, $e.g.$ quantum teleportation. However, such protocols would require to couple the state $|1\rangle_A$ to $|0\rangle_A$ (*idem* for B), which is impossible because of atom number conservation. More generally, to estimate the mode-entanglement useful for quantum information protocols, the superselection rules can be taken into account by projecting the quantum state onto states with fixed local atom number [75]. If we consider a single mode, the only degree of freedom is the number of atoms in the mode, and the projection results in a mixed state, with no entanglement[4].

[2] The single-particle density matrix is often normalized to N in the literature. We take it normalized to one, because the entropy $-\mathrm{Tr}\rho \log \rho$ is defined for $\mathrm{Tr}\rho = 1$.

[3] Similarly but in another context, a Mott insulator has no *spatial* mode entanglement whereas a superfluid has [72]. The situation is reversed in momentum space.

[4] More generally, the superselection rules also render useless the entanglement created via two-modes mixing only, such as spin rotation or any single-particle operation.

The direct mapping of the three spin modes available in a spin-1 BEC onto three spatial modes is thus not a good strategy to observe non-local quantum phenomena. Yet, recent experiments have shown that mode entanglement created in a spinor BEC in the single-mode regime could still be spatially distributed [76–78], and used to perform quantum information protocols. In these experiments, entanglement is created through spin-mixing collisions in a tight trap. The confinement is then removed and the cloud expands. The spin entanglement results in quantum correlations between different regions of the clouds. More precisely, for two entangled regions A and B, and a set of non-commuting local observables $\hat{X}_A$ and $\hat{P}_A$ acting in A. For an observer in A, the simultaneous knowledge of $\langle \hat{X}_A \rangle$ and $\langle \hat{P}_A \rangle$ is limited by Heinsenberg uncertainty relation. However, for an entangled state, additional knowledge can come from a measurement performed in B [76,77]. This phenomenon is known as Einstein-Podolsky-Rosen steering.

Interest in mode entanglement can also come from analogies with phenomena involving virtual particles. For instance, in the Unruh effect, virtual particles appear to an accelerating observer as if it were a thermal radiation. In that case, the mode entropy takes the same form as thermal entropy, with the temperature determined by the acceleration. An analogous effect has been observed in a driven BEC [79]. More precisely, modulating the interacting strength using a Feshbach resonance, the production of a pair of atoms with opposite momenta is stimulated. Individual momentum modes have a large entropy. However, by reversing the dynamics, the authors of [79] were able to show that (some) coherence still exists between the opposite modes, and that (part of) the entropy corresponds to entanglement entropy. A similar mechanism occurs in our system, as shown above in Sec. 2.4.1. The TMSV has a thermal occupation of the modes $m = \pm 1$, although it is a pure state. The effective temperature is related to the QZE q and the spin-dependent interaction strength U_s (see App. C).

These considerations motivate the measurement of the mode entropy in Chapter 5. We consider A to be the $m = +1$ mode. Below is the entropy in the ground sate of the SMA Hamiltonian, keeping the constraint $S_z = 0$.

- $q \gg U_s$: Nematic state, $\mathcal{S}(\rho_{+1}) = 0$.
- $\frac{U_s}{N} < q$: Two-mode squeezed vacuum. $n_p \simeq \sqrt{\frac{U_s}{8qN^2}}$, and $\mathcal{S}(\rho_{+1}) = -2n_p \ln(n_p) - (1 - 2n_p)\ln(1 - 2n_p)$.
- $q = 0$: Singlet state, $\mathcal{S}(\rho_{+1}) \simeq \ln(N) - 1$.
- $-q \gg U_s$: Twin-Fock state, $\mathcal{S}(\rho_{+1}) = 0$.

The maximal value of the entropy is $\mathcal{S}_{+1,\max} = \ln(N)$. For large N the entanglement entropy of the singlet states tends to this value. On the other hand, while the TFS has significant block entropy, it has no mode entropy.

Phase diagram For completeness we show in figure 7 the entanglement entropies in the same phase diagram $(s_z, \frac{q}{U_s})$ as in the Sec. 2.3.2. It is important here to specify the magnetization constraint. We take a Dirac distribution centered on $\langle \hat{S}_z \rangle = s_z N$. In other words, we compute the ground state in the eigenspace of $\hat{S}_z$ with eigenvalue $s_z N$. This results in a significant block entropy, because Fock states are entangled under such partitioning. For instance, for $s_z = \frac{1}{2}$ and large q, the ground state is the twin-Fock state $|\frac{N}{2}, \frac{N}{2}, 0\rangle$.

The main message of the diagram is the large increase of the entanglement (either block, or mode) near the transition. It is overall larger in the ordered (BA) phase, for $q > q_c$ and peaked on the singlet state, for $s_z = 0$ and $q = 0$.

2.6 Summary

In this Chapter, we reviewed some key features of trapped ultra-cold gases of spin-1 Sodium atoms. We discussed the many-body Hamiltonian. Single particle contributions include the kinetic energy, trapping potential and Zeeman effect. For the latter we took care to include the second order (in magnetic field) term, arising from the different couplings of the nuclear and electronic spins that compose the hyperfine spin. This so-called quadratic Zeeman shift is relevant due to the rotational symmetry of the Hamiltonian around the magnetic field axis, and the consequent conservation of the longitudinal spin. We then turned to the derivation of the scattering potential and expressed it as a spin-exchange interaction.

Having derived the full Hamiltonian, we introduced the single mode approximation to decouple the spatial and spin degrees of freedom. We treated the spatial degrees of freedom using a mean-field ansatz, and obtain an effective Hamiltonian for the spin only. This Hamiltonian is at the core of all the physics discussed in the rest of this manuscript. We discussed the validity of the SMA, underlying the effective spin Hamiltonian. We explained how the antiferromagnetic interaction acts to spatially separate the spin sate $m = 0$ from $m = \pm 1$. We briefly presented experiments where this phenomenon occurs. However, in tight traps, the quantum pressure prevents the creation of spin domains. This situation is achieved in all experiments discussed from now on.

We computed the energy and discussed the equilibrium state within a mean-field approximation. Under the conservation of magnetization, we showed the phase diagram in the (s_z, q) plane. It exhibits a second order transition. We then provided a quantum treatment, focusing on the situation of a cloud with exactly zero magnetization. At large enough q the cloud forms a perfect BEC, well described by the mean-field states with all atoms in $m = 0$. For lower q, the condensate gets depleted. Small

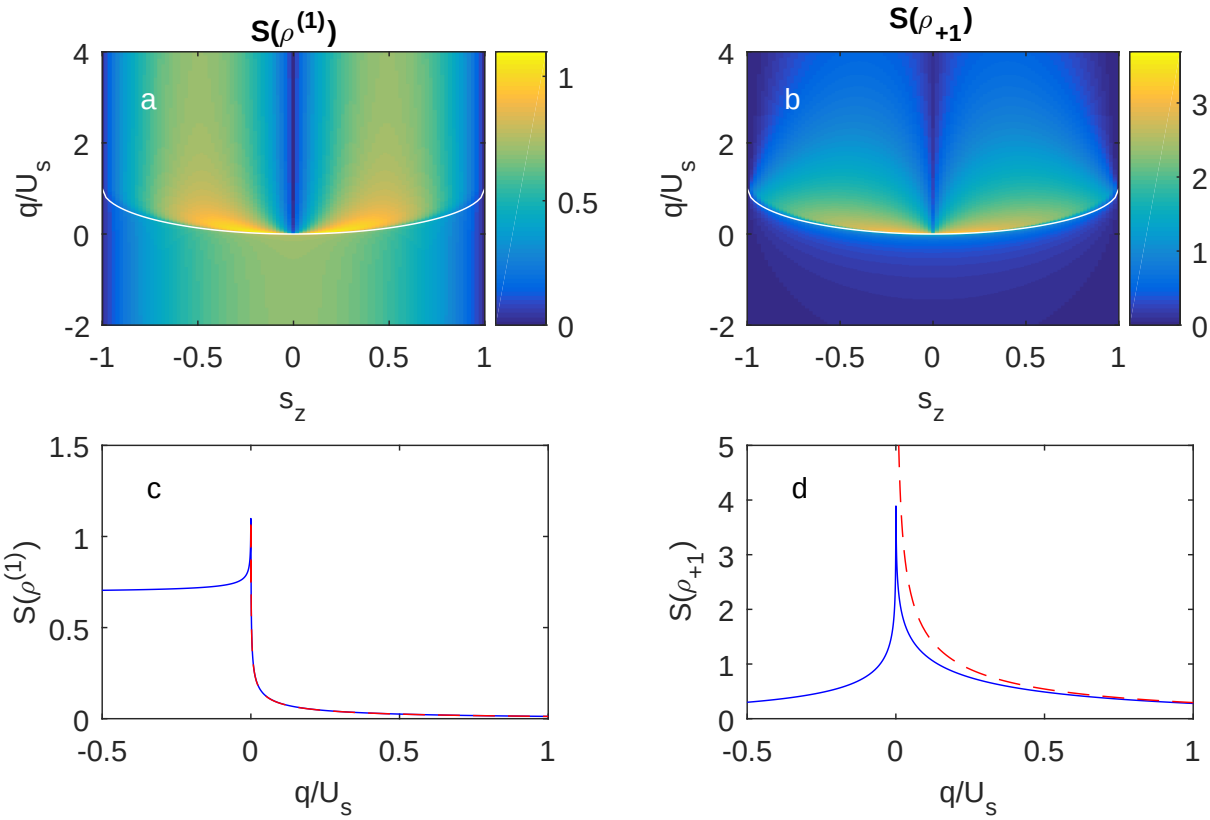

Figure 7: Single-particle entropy (a) and mode entropy (b) in the ground state of a spinor BEC of $N = 100$ atoms, with fixed magnetization s_z, and versus the QZE q. The lower panels c and d are cuts along the $s_z = 0$ line of the diagram a and b, respectively. The red dashed line is the result of the Bogoliubov approximation.

depletions can be studied with a Bogoliubov approach. The ground state is then a two-mode squeezed vacuum. The empty modes $m = \pm 1$ are populated according to a thermal distribution, but are perfectly correlated. At $q = 0$, the Hamiltonian reduces to the interaction term. It is rotationally symmetric (in spin space) and can be diagonalized exactly. For antiferromagnetic interaction, the ground state is the singlet state, characterized by a vanishing collective spin.

Deviations from the mean-field results indicate entanglement between the atoms. This is a property of a quantum state given a partitioning of the system. Two partitionings are often used in the literature, the "block" and "mode" partitionings. Once the system is divided into subsystems, entanglement can be measured as the amount of entropy in a given subsystem. We computed the block and mode entropies of the ground state. The two partitionings give different results, but both show a peak at the phase transition, and both ae maximal at $q = 0$ and $s_z = 0$, for the singlet state.

Chapter 3

Experimental set-up and techniques

Bose-Einstein condensation (BEC) occurs when the thermal de Broglie wavelength λ_T, becomes comparable to the distance between the atoms. The usual figure of merit is the phase space density

$$\mathcal{D} = n\lambda_T^3 \,, \tag{3.1}$$

where n is the density. By cooling down the atoms λ_T is increased ($\lambda_T \propto T^{-1/2}$) but, $\mathcal{D} \sim 1$ requires extremely low temperatures, on the order of a milliKelvin at usual densities, and much below ($\sim$ 100 nK) in dilute gases. Such temperatures are not within the reach of cryogenic methods. Instead, the atoms are confined in wall-free optical or magnetic traps and suspended in ultra-high vacuum. The usual experimental procedure combines direct laser cooling followed by evaporative cooling. It led to the first observation of BEC in 1995 [3, 4], nearly 70 years after Einstein's theoretical prediction. In these early experiments, the BEC was held in a magnetic trap. It has the disadvantage of only trapping a few Zeeman states, the low-field seekers. On the contrary, an optical trap confines almost identically all Zeeman states and a spinor BEC can be produced [80].

In the present chapter, we introduce the set-up and methods we use to produce, manipulate and probe a spinor BEC of ^{23}Na atoms. The chapter is divided into two parts.

First, we focus on the preparation steps. We quickly summarize how light-matter interactions can be used to produce dissipative and conservative forces for cooling and trapping purposes. We then turn to our implementation of these techniques. The set-up has been described thoroughly in previous theses [81, 82], and its most distinctive features are discussed in the publications [83–85]. Moreover, we did not participate in the construction. For these reasons, we only give a brief description, for completeness.

In a second part, we report on our effort to count the Zeeman populations with a resolution close to a single atom. This was an important prerequisite for the experiments described in chapters 5 to 7. We first motivate our choice of using fluorescence instead of absorption imaging. We then describe the experimental set-up, time sequence and image processing. We conclude with an evaluation of the performance of this new method. This work is also described in [86] (mostly in the supplementary material).

3.1 Production and manipulation of spin-1 Bose-Einstein condensates of Sodium atoms

3.1.1 Optical cooling and trapping

We use light to cool the atoms, trap them and image them. In a crude approximation, the microscopic mechanism can be reduced to an exchange of excitation from the light wave to the atoms and from the atoms to the vacuum (spontaneous emission) or back into the wave (stimulated emission). Spontaneous emission is most relevant near resonance, when the atoms are excited with a significant probability. The action of the light can then be expressed as a dissipative force acting on the atoms, the radiation pressure. Off-resonance, stimulated emission dominates and produces a conservative force, the dipolar force. These phenomena are described in many references, for instance [87]. Here, we briefly recall some important results relevant for the remaining of the chapter.

The radiation pressure force We consider here an idealized two-level atom, illuminated by a monochromatic plane wave of frequency ω and intensity I. Let ω_0 be the energy splitting and Γ the lifetime of the excited state. We consider first the near-resonant case where $\delta = \omega - \omega_0 \ll \omega_0$. The flux of spontaneously emitted photons is

$$\Gamma_{\rm sp} = \frac{\Gamma}{2} \frac{\frac{I}{I_{\rm sat}}}{1 + 4\frac{\delta^2}{\Gamma^2} + \frac{I}{I_{\rm sat}}} \,. \tag{3.2}$$

The saturation intensity $I_{\rm sat}$ depends on the transition and on the polarization of the light. In our case, it can be expressed as $I_{\rm sat} = (\hbar\omega^3\Gamma)/(12\pi c^2)$ [88]. Let k be the wave vector of the incoming photons. The average momentum of the spontaneously emitted photons vanishes, so that the mean force, called the radiation pressure, is $\Gamma_{\rm sp}\hbar$k.

For a moving atom, the Doppler effect makes the detuning velocity-dependent. In particular, if the atoms move against a red-detuned wave, the frequency is shifted closer to resonance and the radiation pressure increases. Using three pairs of counter propagating red-detuned beams an effective friction force $\mathbf{F} = -\alpha\mathbf{v}$ (for low enough v) is achieved. This set-up is called an optical molasses.

With an additional magnetic field gradient and carefully chosen circularly-polarized light, the detuning is made position-dependent and a spring force is produced on top of the friction force. This is called a magneto-optical trap (MOT). It constitutes a very powerful tool to bring a hot gas down to very low temperatures. However the coldest temperature that can be achieved is ultimately limited by the stochastic nature of spontaneous emission. To overcome this difficulty, the gas is first laser-cooled in a MOT and then transferred to a conservative trap, where it can be further evaporatively cooled.

The dipolar force We now consider the case of large detunings, where stimulated emission prevails. In that case no energy is taken on average from the light and the force derives from the potential (for large enough detuning)

$$V_{\text{trap}} = \frac{3\pi^2 c^2}{2\hbar\omega_0^3}\frac{\Gamma}{\delta} I(\mathrm{r})\,. \tag{3.3}$$

The different scaling of the dipolar ($\propto 1/\delta$) and radiation pressure ($\propto 1/\delta^2$) forces with the detuning makes it possible to have a dipolar trap with negligible heating coming from spontaneous emission. In such a trap, a gas can be further cooled evaporatively. Briefly, the trap depth is lowered to let the most energetic atoms spill away. This is done at a slow enough rate to let the ensemble thermalize (it thus requires sensible interactions between the atoms). To the price of loosing atoms, the phase space density can be increased by several orders of magnitude.

In practice, we use Gaussian beams. If z is the direction of propagation,

$$I(\mathrm{r}) = I_0 \frac{w_0^2}{w(z)^2} \exp\left(-2\frac{x^2+y^2}{w(z)^2}\right)\,, \tag{3.4}$$

where w_0 is the waist of the beam, $w(z) = w_0\sqrt{1+\frac{z^2}{z_R^2}}$ and $z_R = \frac{\pi w_0^2}{\lambda}$ with λ the wavelength of the light. We are interested in the low energy states, localized at the bottom of the trap. This justifies to expand expression (3.4) for $x, y, z \ll w_0$. Up to a constant, it gives a harmonic potential

$$V_{\text{trap}}(\mathrm{r}) = \frac{1}{2}M(\omega_x^2 x^2 + \omega_y^2 y^2 + \omega_z^2 z^2)\,, \tag{3.5}$$

where M is the atomic mass. The trap frequencies are $\omega_x = \omega_y = \sqrt{\frac{4V_0}{mw_0^2}}$ and $\omega_z = \sqrt{\frac{2V_0}{mz_R^2}}$, and $V_0 \propto I_0$ is the potential depth. Note that the longitudinal confinement along the z axis is only due to the divergence of the beam, and is much weaker than the transverse confinement (typically, $\frac{\omega_{x,y}}{\omega_z} \simeq 100$).

We use such single-beam trap to produce highly elongated ("cigar-shape") clouds [53]. For all experiments discussed in this manuscript, we use a trap formed at the intersection of two orthogonal laser beams. Let the second beam be along the x axis. We typically set the power of the two lasers so that the single-beam potential depths are equal. The trap frequencies are then $\omega_x = \omega_z = \sqrt{\frac{4V_0}{mw_0^2}}$ and $\omega_y = \sqrt{2}\omega_{x,z}$ (neglecting the longitudinal confinement). Thus, a cross dipole trap provides strong confinement in the three directions of space, although it is not perfectly isotropic.

The case of sodium atoms The cooling transition we use is the D_2 line, $3^2S_{1/2}, F = 2 \to 3^2P_{3/2}, F' = 3$ (see figure 8). The associated wavelength is $\simeq 589$ nm, which corresponds to yellow light. Of course, an atom is not a two-level system. In particular, an excited atom can relax via spontaneous emission down to $3^2S_{1/2}, F = 2$, but also $3^2S_{1/2}, F = 1$. In that later case, the atoms are brought back in the cooling cycle thanks to another beam, the "repumper", resonant with the $3^2S_{1/2}, F = 1 \to 3^2P_{3/2}, F' = 2$ transition.

3.1.2 Production of a spinor BEC

For the sake of completeness, we briefly describe how we produce a spinor BEC. However, I did not contribute to the building of the experiment, nor to the optimization of the protocols described in this section.

Magneto-optical trap Our experiment starts with the loading of the magneto-optical trap (MOT). The near-resonant light used for cooling, repumping and imaging is produced by frequency sum of two infrared lasers at 1064 nm and 1319 nm in a non-linear crystal. To achieve high efficiency, the crystal is placed inside a cavity, resonant with both infrared lasers. The frequency is locked on a transition line of iodine molecules, near the cooling transition. The power at the output of the cavity is $\simeq 550$ mW. The set-up is described in details in [83] and in the thesis of Emmanuel Mimoun [81].

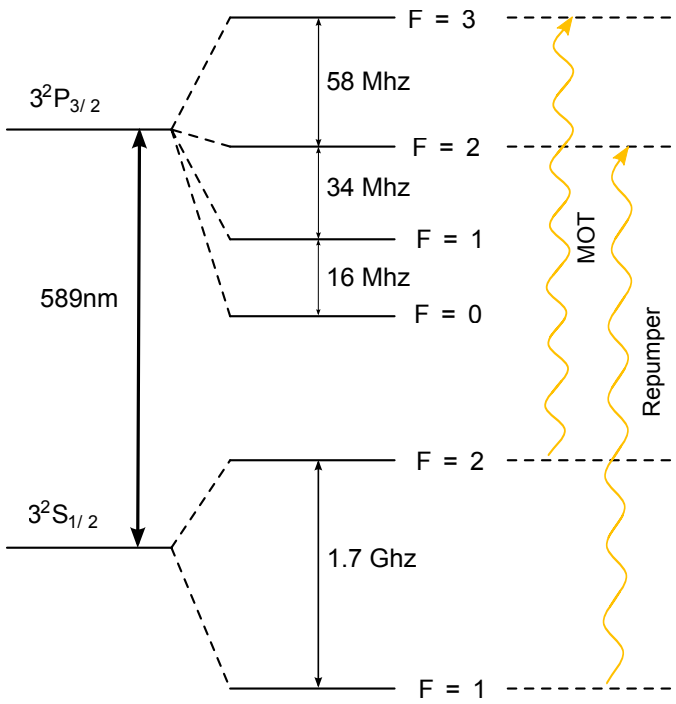

Figure 8: Energy structure of a sodium atom relevant for our experiment.

The other ingredient for the realization of a MOT is of course the atomic source. A typical solution is a beam of atoms leaving an oven and slowed down in a so-called Zeeman slower [89]. In our experiment we use a custom option described in [84]. Sodium dispensers are located inside the chamber. When heated up (in practice, we drive them with a current of 3.5 A) they release Sodium atoms. From this ambient vapor the MOT can be loaded. The downside is the pressure increase inside the chamber. Indeed, collisions between the trapped atoms and the residual gas limit the lifetime of our samples. To circumvent this issue, the dispensers are only fired once a week, overnight. It produces a very thin coating of sodium atoms inside the chamber. At the beginning of each sequence, we shine UV LEDs to release these atoms by a mechanism called light-induced desorption. This increases momentarily the sodium pressure inside the chamber. Roughly a hundred milliseconds after the UV light is switched off, the pressure is almost back to its background level, of $\sim 10^{-11}$ mbar, as low as we can measure. However, a dim residual background persists on a much longer timescale. We observed this effect when we implemented fluorescence imaging. It will be discussed in Sec. 3.2.

After ~ 6 s of loading, the number of atoms in the MOT reaches a value of $\sim 10^7$. The phase space density is about $\mathcal{D} = 10^{-6}$.

Evaporation in the conservative dipole traps The next step is the transfer of the atoms to the conservative trap. It is a red detuned optical crossed dipole trap (CDT), folded onto itself at an angle of $45°$ in the horizontal plane (see figure 9). Its waist is $\simeq 40\,\mu$m, much smaller than the MOT size ($\simeq 1$ mm). The loading of a CDT from a MOT is a non-trivial process involving many physical effects. It has been studied in [90] and the optimization of our experiment is discussed in [85].

The intensity of the CDT is then ramped down in 2 s. As the trap depth decreases, so does the stiffness of the trap ($\omega \propto \frac{\sqrt{P}}{w}$). The collision rate thus decreases and evaporation becomes less and less efficient. For this reason, we use exponential ramp, to extend the duration let for thermalization. Yet, this is not enough, and eventually evaporation stops, before reaching the BEC threshold. To circumvent this issue, the atoms are loaded into a tight "dimple" trap. It is composed of two independent beams, one in the horizontal plane and one along the vertical axis (see figure 9). They have smaller waists ($\simeq 20\,\mu$m) and hence larger stiffness than the CDT at identical potential depth. As evaporation proceeds in the CDT, the coldest atoms start accumulating in the dimple trap. This results in a significant increase of the density, and when the CDT is switched off the phase space density is close to 1. The evaporation can be carried on further (for 5 s) in the dimple trap where we reach Bose-Einstein condensation.

Characterization of the dipole trap It is important to know accurately the trapping frequencies and waists of the dipole trap. These frequencies could be deduced from a measurement on the beams outside the chamber. But it is much more accurate to measure them directly with the atoms (among other sources of uncertainty, absorption on the view port limits our knowledge of the intensity on the atoms). The procedure is the following. We produce a cloud polarized in the $F = 1, m = +1$ state and apply a magnetic force in order to displace the center of the trap. We then remove the force and monitor the subsequent oscillations of the cloud. The frequency is the trap frequency $\omega \propto \frac{\sqrt{P}}{w}$. We can perform this for all three axis (although only two are generally

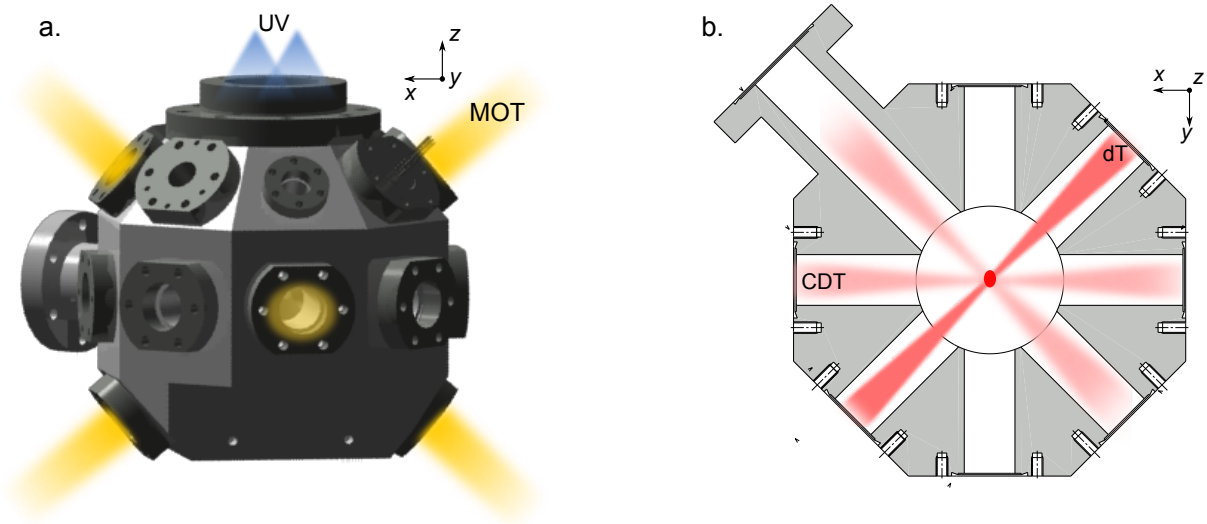

Figure 9: a. Science chamber illuminated by the UV LEDs and the cooling beams during the MOT loading. b. Horizontal cut showing the optical dipole traps.

necessary for revolution-symmetric beams).

3.1.3 Manipulation of the internal state

In the dipole trap, the temperature is much smaller than the hyperfine energy splitting, so that all atoms are in the manifold $F = 1$. The three Zeeman component $m = 0, \pm 1$ are trapped identically. We present in this section how we can use an oscillating field to perform spin rotation, and a gradient to create a spin dependent force. All these procedures were already implemented when I arrived.

Spin rotation We often need to rotate the spin of the atoms in order to trigger dynamics, or to diagnostic the state of the atoms. We do this by applying radio-frequency (RF) magnetic field $\mathrm{B}_{\mathrm{RF}} = B_{\mathrm{RF}} \sin(\omega t)\mathrm{e}_y$. The Hamiltonian is[1]

$$\hat{h}_Z = p\hat{s}_z + \hbar\Omega \sin(\omega t)\hat{s}_y \,, \tag{3.6}$$

where $\Omega = g\mu_B \|\mathrm{B}_{\mathrm{RF}}\|/\hbar$ is the Rabi frequency. In the frame rotating at the frequency ω around z, the Hamiltonian becomes

$$h_Z^{\mathrm{rot}} = (p - \hbar\omega)\hat{s}_z + \hbar\Omega \left(\cos^2(\omega t)\hat{s}_y + \cos(\omega t)\sin(\omega t)\hat{s}_x\right) \,. \tag{3.7}$$

For $\omega \gg \Omega$, we can neglect the time dependent terms (this is known as the rotating wave approximation). On resonance, $p = \hbar\omega$ and the Hamiltonian reduces to $h_Z^{\mathrm{rot}} = \hbar\Omega\hat{s}_y/2$. It achieves spin-space rotation, as shown by the equation of evolution of the spin operator

$$\frac{d\hat{\mathbf{s}}}{dt} = \frac{\Omega}{2}\mathrm{e}_y \times \hat{\mathrm{s}} \,. \tag{3.8}$$

The vectors $\mathrm{n}_{1,2}$ that parametrize the state in the Bloch-Rabi picture verify the same equation. For instance, the nematic state aligned along the z-axis evolves as

$$|\psi(t)\rangle = \cos(\Omega t)|z\rangle + \sin(\Omega t)|x\rangle \,, \tag{3.9}$$

where $|x\rangle = (|-1\rangle - |+1\rangle)/\sqrt{2}$ is the nematic state aligned along the x-axis.

[1] In this paragraph, we neglect the quadratic Zeeman energy (QZE) and the interaction. Indeed, the duration of the pulse used to perform Rabi-oscillation is on the order of tens of microseconds. On this timescale, the QZE and interaction have essentially no effect.

Magnetic force For imaging and purification purposes, we apply a spin selective force. This is achieved in a magnetic field gradient

$$\mathrm{B}_g = b' \begin{pmatrix} -\frac{x}{2} \\ -\frac{y}{2} \\ z \end{pmatrix} , \tag{3.10}$$

on top of the bias field $\mathrm{B}_0 = B_0 \mathrm{e}_z$. For $|\mathrm{B}_g| \ll |B_0|$ the energy in state $m = \pm 1$ is to the first order in b' (here again we neglect the quadratic Zeeman energy)

$$\langle \hat{h}_Z \rangle_m = pm + 2g\mu_B b' z m \,. \tag{3.11}$$

In a semi-classical picture, atoms in the spin state m feel the force $\mathbf{F}_g = -2g\mu_B b' m \mathrm{e}_z$. In practice, we can achieve an acceleration on the order of the gravitational acceleration $g \simeq 10\,\mathrm{m/s^2}$ for $b' \simeq 15\,\mathrm{G/cm}$.

3.1.4 Magnetic field control

Production of magnetic fields We produce the bias magnetic fields using three pairs of coils located around the chamber. They can provide fields up to $\sim 3\,\mathrm{G}$ (0.3 mT) in any direction. We also have a large 1 m×1 m coil around the chamber, in the horizontal plane containing the atoms, for noise compensation (see paragraph below). An additional set of two water-cooled coils produce the magnetic field gradient required for the MOT and in order to apply a spin-selective force. When supplied with 120 A, the gradient at the center of the science chamber amounts to $\simeq 15\,\mathrm{G/cm}$ (0.15 T/m). Finally, a single smaller coil located on top of the chamber is used for producing an RF oscillating field.

Calibration of the magnetic field The amplitude of the field on the atoms is determined using RF-spectroscopy. We produced a polarized BEC (that is to say, with all atoms in the same Zeeman state m), for instance in $m = 0$. We apply a RF field for t_p, with a small amplitude to initiate a Rabi oscillation. In the limit of a weak pulse, the fraction of atoms measured in the $m = \pm 1$ states is $n_\pm \simeq \frac{\Omega^4 t_p^2}{\Omega^2 + \delta^2}$, where Ω is set by the amplitude of the RF field and δ the detuning between the driving frequency and the Larmor frequency (propotional to the magnetic field). This defines a Lorentzian line of width Ω, from which the detuning can be deduced. This formula is valid for $\Omega t < 1$. In order to achieve good accuracy on the measurement of δ, we want to have small Ω. A typical spectroscopy line is presented on figure 10.

In practice, to fully calibrate the field produced by the three pairs of coils, we performed several spectroscopy experiments, for various currents. We also estimated the bandwidth characterizing the dynamical response of the coils (this is important for the experiments described in chapter 4). We fed the coils with a current oscillating at 277 Hz, and then performed a spectroscopy at different times of the oscillation. The amplitude we measured is 20% smaller than for the static calibration. Assuming a first order filter, this corresponds to a bandwidth of ~ 500 Hz. We believe it is not limited by the intrinsic bandwidth of the electric circuit, but most likely by eddy currents induced in the chamber.

Noise compensation We continuously measure the fluctuations of the magnetic field using a probe located outside the chamber. The dominant contribution, on the order of 3.4 mG root-mean-square (rms) and with a time scale of ~ 10 Hz are presumably due to the nearby metro line[2]. Such fluctuations are not acceptable for the experiments described in the Chapter 6 and 7 and we thus implemented a compensation system. Fortunately, the fluctuation of the field are very homogeneous in space and almost perfectly aligned along the vertical axis. For this reason we can use a simple feed-forward set-up to cancel this noise. The "metro" field is measured outside the lab (in order not to be influenced by the sequence running). The signal (after removal of the offset and multiplication by a tunable gain) is then used to control the current in a single 1 m×1 m square coil located in the plane of the atoms. By using a large coil we minimize the error between the field measured by the probe and seen by the atoms (The probe is ∼10 cm away from the center of the vacuum chamber).

After tuning the gain, the probe records fluctuations of 0.4 mG rms (figure 10 b), very similar to what we measure along the other axes. We estimate the magnetic field noise on the atoms by measuring the minimal linewidth we can achieve in RF-spectroscopy. We use this for a fine tuning of the compensation. We measured a minimal linewidth of $\simeq 0.4$ kHz, corresponding to fluctuations of 0.6 mG (figure 10 a), compatible with the direct estimation. The minimal field used in the experiments presented in chapter 6 and 7 is 4 mG. At this level, the residual fluctuations are not a limitation for the physics we want to explore.

3.1.5 Absorption imaging

Let us briefly describe here the procedure we follow to image the cloud. It can be decomposed into two steps: time-of-flight (TOF) and imaging. For imaging, we have used two different schemes, namely absorption and fluorescence. The former was implemented before I arrived, and we briefly describe it here. We have contributed to the realization of fluorescence imaging, and this scheme will be described in detail in section 3.2.

[2] A strong evidence is the correlation between the noise amplitude and the metro schedule

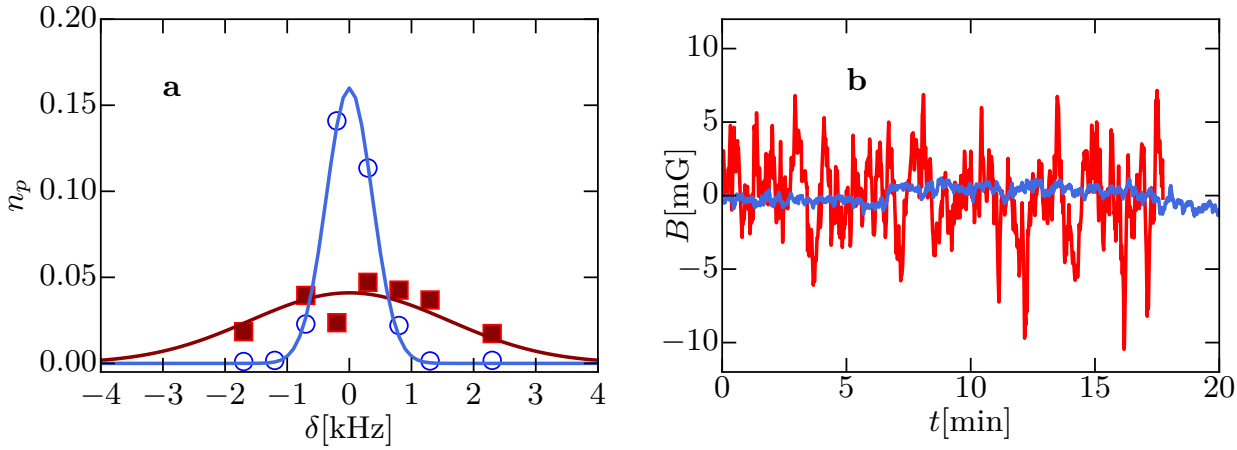

Figure 10: a RF-spectroscopy with (blue empty circle) and without (red full squares) magnetic field compensation. The error bar represents one standard deviation. b Fluctuations of the magnetic field along the z-axis with (blue line) and without compensation (red line).

Time-of-flight and Stern-Gerlach In this step, the trap is turned off. The cloud falls freely and expands due to the quantum pressure and the repulsive interactions. During that time, we apply a magnetic force to spatially separate the three Zeeman states, using the same principle as in the famous Stern-Gerlach experiment. For long enough TOF (in practice, for absorption imaging, we use 3 ms) the three spin states are completely separated as can be seen on figure 11.

Absorption imaging Absorption imaging is a common technique in ultra-cold gas experiments [89]. The procedure we use has been described in detail in previous theses (*e.g.* [91]). Here we briefly recall the principle. We shine a probe beam resonant with the D2 line (the same as for cooling) on the atoms, together with the repumper beam. The pulse typically lasts 10 μs. The probe beam propagates along the vertical axis, and is projected onto a CCD camera after going through the chamber (see figure 13). The atoms absorb part of the incoming light and reemit it in all directions. For dilute clouds, the variation of intensity I is related to the density n through the Beer-Lambert law $\frac{\partial I}{\partial z} = -n\Gamma_{\rm sp}(I)\hbar\omega$, where $\Gamma_{\rm sp}(I)$ is given by eq. (3.2) for a two-level system. After integration, the column density $n_{\rm col}(x,y) = \int \mathrm{r}n(\mathrm{r})$ is related to the intensity before (I_2) and after (I_1) the atoms via [92]

$$n_{\rm col}(x,y) = \frac{1}{\sigma_0}\ln\left(\frac{I_2(x,y)}{I_1(x,y)}\right) + \frac{I_2(x,y) - I_1(x,y)}{\sigma_0 I_{\rm sat}}\,, \tag{3.12}$$

where $\sigma_0 = 3\lambda_0^2/(2\pi)$ is the resonant scattering cross section.

In practice, the image of the background I_2 is constructed from a set of empty images and an algorithm known as "Best Reference Picture". The same analysis is used to remove the background of fluorescence images, and we postpone the description to the next section. We have given the expression of σ_0 and $I_{\rm sat}$ for a two-level system (and circularly polarized light). However, as we have seen, the electronic structure of Na is more complex and these parameters are in fact calibrated experimentally. The same type of calibration is required for fluorescence imaging, and will also be discussed in the next section (see also [52, 91]).

Absorption imaging provides information on the spatial density of the clouds. The integrated signal gives the population in each Zeeman state. However, it comes with significant noise due to the fact that the probe beam is directly impinging on the CCD. Part of the noise is composed of classical intensity fluctuations of the laser. In theory this noise can be removed through image analysis. On the other hand, the shot noise of the incident light constitutes a fundamental limitation on the performance of absorption imaging, which cannot be removed through image analysis. This is a serious issue for experiments that requires a precise counting of the Zeeman population.

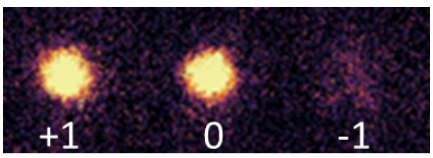

Figure 11: Absorption image of the three clouds after Stern-Gerlach separation.

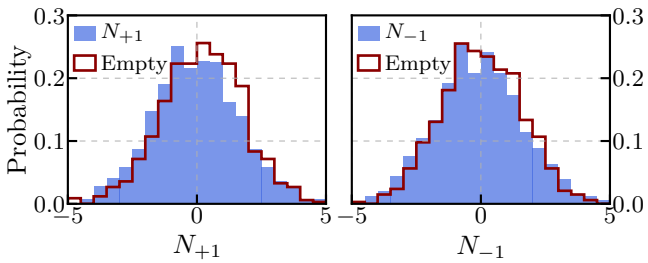

Figure 12: Histogram of the population in $m = \pm 1$ after spin filtering.

3.1.6 Status at the end of the evaporation

Internal state We showed in Chapter 2 that the magnetization $m_z = (N_{+1} - N_{-1})/N$ is a conserved quantity, which constitutes a very important constraint on the state of the BEC at the end of the evaporation.

The "natural" magnetization of the cloud after loading of the CDT is $m_z \simeq -0.7$. This value can be tuned between -0.7 and 0 using a radio-frequency pulse before the evaporation starts. The pulse brings the atoms into a coherent superposition of the three spin states, but the coherence is rapidly lost due to collisions and magnetic field inhomogeneity. We end up with a statistical mixture, with the desired magnetization. The latter is almost conserved over the evaporation, unless we use a distillation procedure.

Spin distillation is used to produced polarized cloud with $m_z \simeq -1$. It relies on a magnetic field gradient applied on top of a bias field along the vertical axis to produce a spin-dependent force. We choose it to compensate the gravity for $m = -1$. It has no effect on $m = 0$ and it adds up to the gravity for $m = +1$. The evaporation rate is then faster for $m = +1$ and $m = 0$, and the clouds is almost fully magnetized at the end of the ramp.

In most experiment we performed, we actually want to start with a BEC with all atoms in $m = 0$. To prepare such a BEC, we set initially $m_z = 0$, and evaporate in a large bias field of ~ 3 G. The quadratic Zeeman shift $q/\hbar \simeq 2.5$ kHz is much larger than the spin-dependent interaction energy and at zero magnetization, all condensed atoms are in the $m = 0$ Zeeman state. On the other hand, the lowest temperature we can measure are on the same order as q/k_B. The thermal atoms are expected to be distributed between the three spin states. In practice, for the most shallow trap, we measured about 0.98% of the atoms in the $m = 0$ state. This indicates a very small thermal fraction.

Yet, the population of $m = \pm 1$ is not strictly zero. To reduce it further, we use the same configuration as for the spin-distillation procedure discussed above. The difference is that we do this in a very shallow trap, just strong enough to hold the atoms against gravity. With an additional magnetic force pulling them down, atoms in $m = +1$ spill away without relying on evaporation. By changing the direction of the bias field, we also remove the $m = -1$ atoms. We call this procedure "spin-filtering".

On a single shot, using fluorescence imaging (see section 3.2), we can count the Zeeman population with an accuracy of ~ 1.6 atoms, which does not allow us to insure that there are no atoms in $m = \pm 1$. On a set of ~ 1000 shots of a spin-filtered BEC of ~ 4000 atoms, we measured $\overline{N_p} = -0.05 \pm 0.04$. We show the histogram of the atom number $N_{\pm 1}$ in the $m = \pm 1$ states after spin filtering in figure 12 and compare them to the distribution on empty images. We see no significant differences between the two distributions.

Atom number We reach after evaporation an atom number on the order of $N \sim 10^3$ to 10^4. For the experiments described in chapters 6 and 7 this number is too large and we aim to work with $N \sim 100$. One way to reduce the atom number is by lowering the trap depth in order to let some atoms spill away. However, below a certain trap depth we lose all the atoms. Close to this threshold, the atom number is very sensitive to minute changes in the trap depth (due to fluctuation of intensity or trap alignment), and thus fluctuates a lot. It makes it difficult to realize small samples reliably by simply lowering the trap depth. Instead, after a first spin-filtering, we use a radio frequency pulse to bring the atoms in the superposition

$$\sqrt{\epsilon}|m = 0\rangle + \sqrt{\frac{1-\epsilon}{2}}(|m = -1\rangle - |m = +1\rangle)\,. \tag{3.13}$$

After another "spin-filtering", we are left with ϵN atoms in the state $|m = 0\rangle$ inside the trap. We can achieve $\epsilon \ll 1$ with reasonable fidelity so that the atom number fluctuations are not dramatically increased (on the order of 10%).

Temperature The temperature and condensed fraction of the gas can in principle be deduced from the densities measured using absorption imaging. We describe the procedure very briefly since it is quite standard (see *e.g.* [89]). Moreover, it only provides us with an upper bound to the temperature in the experiments discussed in this manuscript.
For a thermal cloud, one can neglect interactions in first approximation. In that case, the TOF expansion after released from a harmonic trap can be solved analytically [26]. For time t_{TOF} long compared to the trapping period, the spatial density $n(\mathrm{r}, t_{\mathrm{TOF}})$ is

proportional to the initial distribution in momentum space $n(\mathrm{p}, t = 0)$. The latter is given by a Bose distribution, and more simply, in the large $\mathbf{p}$ limit ($i.e.$ the wings of the distribution), it approaches a Boltzman distribution $n(\mathbf{p}) \propto \exp(-\mathbf{p}^2/(2Mk_bT))$. For a BEC in the Thomas-Fermi regime [26], one can neglect the quantum pressure, and the expansion in TOF is then given by scaling laws [93]. The spatial density keeps the shape of inverted parabola.
Combining these two results, the density profile of a condensed gas at finite temperature is composed of a central peak corresponding to the BEC on a larger pedestal formed by the thermal cloud. From a fit of the wings of the distribution the temperature can be extracted ($e.g.$ using a bimodal fit of the whole profile, or a Gaussian fit of the wings only [89, 91]). This procedure works well for thermal fraction larger than $\sim 20\,\%$. For colder clouds, the signal-to-noise ratio in the wings of the distribution is too small to be fitted reliably. All experiment described in the following are performed in that regime and we can only give an upper bound to the temperature $T \lesssim 100$ nK, and the condensed fraction $f_c \gtrsim 0.8$. Thermometry of our system has been performed extensively in the thesis of Camille Frapolli [91].

3.2 Fluorescence Imaging

3.2.1 Why fluorescence imaging?

Motivation In experiments described in Chapters 5 to 7 of this manuscript, we aim at observing reduced quantum fluctuations of the collective spin of mesoscopic ensembles of atoms (from a few to a few hundred atoms). More precisely, it always boils down to a measurement of the spin component along the quantization axis (the direction of the bias magnetic field), $\hat{S}_z = \hat{N}_{+1} - \hat{N}_{-1}$. The other spin components can be mapped onto that one thanks to a spin-rotation. These experiments are performed in the single-mode regime, and the spatial distribution of the atoms is fixed. We are mostly interested in counting the Zeeman population as accurately as possible. In this section, we report on our implementation of "Stern-Gerlach fluorescence imaging" that leads to a resolution near the single atom limit. The experimental set-up and protocols described in Sec. 3.1 were all (with the exception of the magnetic field compensation) implemented before I arrived. The fluorescence imaging methods constitutes my main contribution to the experimental set-up, and is discussed here in detail (see also [86]). The experiments described in Chapter 4 were performed before this work, using the absorption imaging set-up described in Sec. 3.1.5.

Let us start with a brief overview of our fluorescence scheme. Three counter propagating red-detuned beams are used to form a molasses. The light scattered from the atoms is collected on a camera (see figure 13). Thanks to the friction force at play in a molasses, the expansion of the clouds is relatively slow, and a long exposure time is possible. The signal is the integral over the molasses duration of the fluorescence intensity impinging on the camera. In this scheme, because of the diffusion of the atoms in the molasses, we loose all information on the spatial distribution of the atoms in the trap. For this reason, we kept in the experimental set-up a parallel optical path to perform absorption imaging when spatial resolution is needed ($e.g.$ for alignment of the dipole trap).

Brief overview of the state of the art Single atom resolution is achieved most easily for trapped individual particles, such as ions, or neutral atoms in optical tweezers. Typically the atoms are illuminated with near-resonant light, and fluorescence photons are collected through a large numerical-aperture microscope objective. Using deep traps, it is possible to expose the atoms for hundreds of milliseconds up to a few seconds before they are lost (even longer for trapped ions). The method can be generalized to atoms in 2D optical lattices (this is called a "quantum gas microscope"). Imaging individual sites requires an excellent small spatial resolution (typically below 1 μm). Most importantly for our topic, this technique works only for sites with single occupancy. Indeed, light assisted collisions lead to severe losses in tightly confined ensembles. Another possibility demonstrated in [94], is to hold the atom in a MOT. Because the density is typically much smaller than in a dipole trap, single atom sensitivity has been demonstrated for up to $\sim 10^3$ atoms [94].

The issue when imaging trapped particles is that it is difficult to resolve the internal state. This is why in spinor condensates the atoms are usually imaged after having spatially separated the Zeeman states, using a Stern-Gerlach set-up. To our knowledge, the lowest noise level using absorption imaging is reported in [95], and amounts to 3.7 atoms[3]. On the other hand, using fluorescence imaging, a noise level of 13 atoms was reported in [11]. The combination of Stern-Gerlach separation and optical molasses comes with technical difficulties that will be developed below. This is probably why most spinor BEC uses absorption imaging. However, this technique comes with a strong limitation on the sensitivity that can ultimately be achieved.

The limit of absorption imaging Let us start by pointing out that there are *a-priori* no fundamental limits that forbid the detection of a single atom using absorption imaging. It was experimentally demonstrated for a single ion [96]. Yet, for the vast majority of experiments achieving single atom resolution, fluorescence is being used. Even in [96], after careful optimization of the absorption imaging, fluorescence gives better counting resolution. This can be understood after a simple estimation of the signal-to-noise ratio (SNR) of absorption imaging.

[3] The noise reported in this paragraph is the standard deviation of the atom number on empty images. It is typically larger on atomic images, due $e.g.$ to losses.

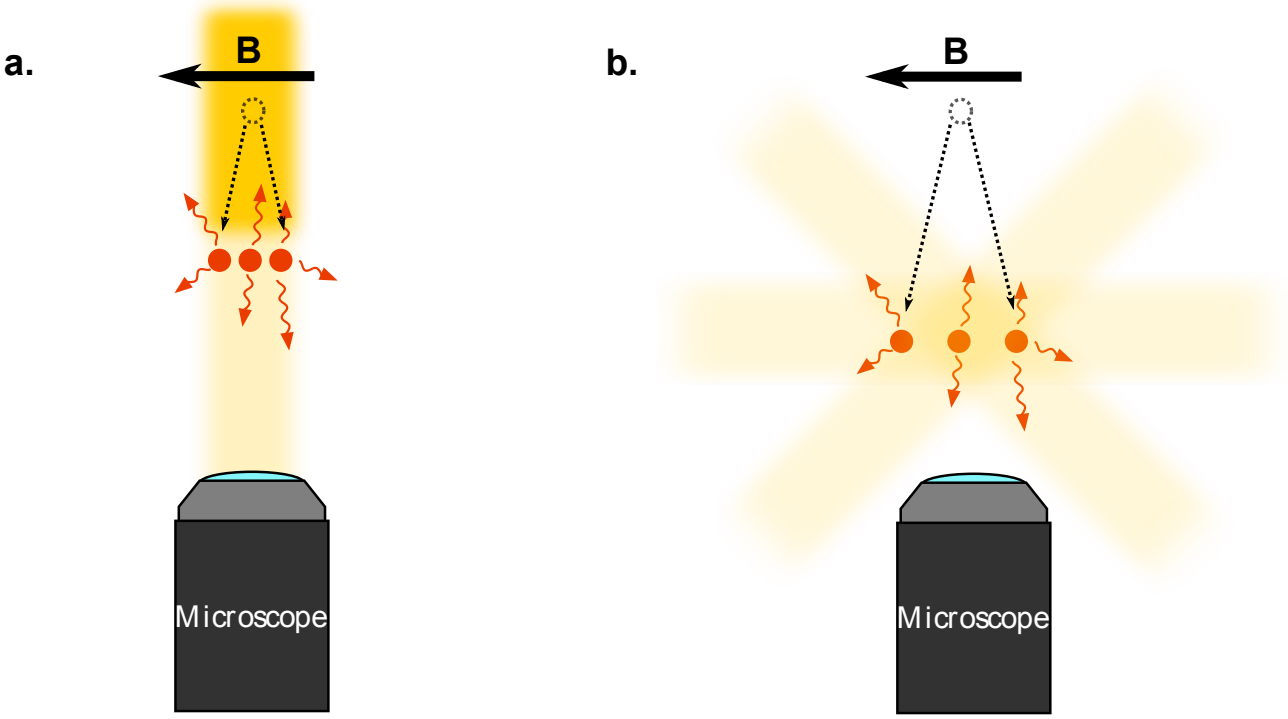

Figure 13: Imaging sequence. The Zeeman states are separated in a magnetic field gradient in time-of-flight. The atoms are then illuminated with a probe beam for absorption imaging (a) or with the molasses beams for fluorescence imaging (b).

We use the 2-level atom picture presented in 3.1.1. We recall the absorption rate on resonance [Eq. (3.2)]

$$\Gamma_{\rm sp} = \frac{\Gamma}{2}\frac{s}{1+s}\,, \tag{3.14}$$

where $s = \frac{I}{I_{\rm sat}}$. The rate of incoming photons on the surface A occupied by the atom(s) is $\phi_{\rm in} = \frac{IA}{\hbar\omega}$. The ratio of the two defines the contrast

$$\mathcal{R} = \frac{\Gamma_{\rm sp}}{\phi_{\rm in}} = \frac{\sigma_0}{A(1+s)}\,, \tag{3.15}$$

where $\sigma_0 = 3\lambda_0^2/(2\pi)$ is the resonant scattering cross-section, and using $I_{\rm sat} = (\hbar\omega^3\Gamma)/(12\pi c^2)$. For a duration of exposure $t_{\rm exp}$, the signal of a single atom is

$$\mathcal{S} = \Gamma_{\rm sp} t_{\rm exp}\,. \tag{3.16}$$

In the best case scenario, the probe beam fluctuations are given by the shot noise fluctuations, and the noise is

$$\mathcal{N} = \sqrt{\phi_{\rm in} t_{\rm exp}}\,. \tag{3.17}$$

Thus, the SNR of a single atom is

$$\text{SNR} = \sqrt{\mathcal{R}\mathcal{S}}\,. \tag{3.18}$$

In [96], the detection of a single ion is achieved with $\mathcal{R} = 0.03$. In this experiment, A is limited by diffraction to $\sim 0.5\,\mu$m, and the ion is strongly confined, so that it can scatter hundreds of photons and still remaining trapped. The situation is much less favorable for an atomic ensemble in free space. First, A is limited by the size of a cloud, for typical experimental conditions, we have $A \sim \pi\times(20\,\mu\text{m})^2$ and $\mathcal{R} \sim 10^{-4}$. In addition, the exposure duration is limited by the effect of the radiation pressure. After a few hundreds of photon are scattered (in practice we use $t_{\rm exp} = 10\,\mu$s), because of the Doppler shift, the atoms are out of resonance with the probe light. These constraints yield in our case to SNR $\simeq 0.1$, quite far from the single-atom resolution. On the one hand, after optimization, $t_{\rm exp}$ may be increased and A decreased. On the other hand, we know the two-level picture overestimates the scattering rate (by a factor ~ 2, see [52, 91]). Last but not least, we neglected important experimental realities. For instance, additional noise *e.g.* due to classical fluctuations of the probe intensity (these are actually on the same order as the shot-noise

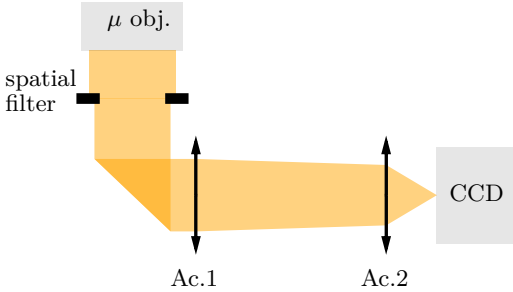

Figure 14: Sketch of the fluorescence imaging set-up. The light is collected in a microscope objective. A spatial filter hides stray light scattered on the chamber view-ports. A first achromatic lens Ac.1 is used to reduced the divergence of the beam. A second achromatic lens project creates an image of the atoms on a CCD camera.

for us [52]). Initially, using absorption imaging we had an accuracy on the total atom number on the order of ~ 60 atoms [52]. Overall, it appears very challenging to reach single atom resolution with absorption imaging in our situation. We thought better results could be obtained thanks to fluorescence imaging. The rest of the chapter is dedicated to our implementation of this method.

3.2.2 Experimental set-up

Molasses beam We use the same beams as for the cooling light and the repumper. The intensity is about $3.1\,\mathrm{mW/cm^2}$/beam at the center of the beams. The saturation intensity is $I_{\mathrm{sat}} = 6.2\,\mathrm{mW/cm^2}$ (assuming perfectly circular polarizations). This set-up is straightforward to implement in the experiment. The drawback is that fluorescence imaging cannot be fully optimized without degrading the MOT performances and *vice versa*. On the one hand, the size of the beam has to be quite large for proper loading of the MOT. On the other hand, the amount of stray light scattered from various surfaces in the beam path (viewport and chamber walls) and collected by the imaging system is larger for larger beam sizes. As a compromise, we found that reducing the sizes of the four oblique beams (see fig.13) from 11 mm to $\sim$ 7 mm suppresses the amount of stray-light by 75 %, while reducing the atom number in the MOT by only $\sim 30\%$.

Optics The first requirement of the optical system is to collect as much fluorescence photons as possible. For this purpose, we use a microscope objective[4] located at the bottom of the science chamber, characterized by a numerical aperture NA$= 0.3$ and a focal length $f = 40\,\mathrm{mm}$. The atoms are near the object plane of the objective. The light coming out from the objective is slightly diverging. We use a $f = 500\,\mathrm{mm}$ achromatic lens located right after the objective to contain the divergence of the beam, and a $f = 75\,\mathrm{mm}$ (NA$= 0.32$) achromatic lens to form an image on the camera (see figure 14). The measured magnification of the whole system is $\simeq 1.5$. A small magnification is favorable since it reduces the size of the image on the CCD, and therefore the amount of electronic noise in the integration area. As mentioned before, the spatial resolution is not a concern, we are only interested in the population. However, a small magnification requires a small focal length (given the focal length of the objective), which is not easily combined with a large numerical aperture without important optical aberrations. The set-up described here is a satisfying compromise. Its NA is mostly limited by the microscope objective (a spatial filter described in the next paragraph slightly reduces it), the electronic noise contributes for a negligible amount of the total noise and we observe no optical aberrations.

Spatial filtering Important sources of stray light are the upper viewports of the chamber through which the molasses beams go. They scatter light, some of which is collected by the microscope objective. Fortunately, most of it can be filtered out, at a reasonable cost on the fluorescence signal. The viewports constitute well located sources, far from the microscope objective (compared to the focal lens). We observe that their image is formed close to the focal point of the objective contrary to the image of the atoms ("near infinity"). The image of the viewports can thus be blocked by a carefully-designed spatial filter placed near the image plane of the objective, as shown in figure 12. The noise is reduced by $\simeq 40\%$ while the signal is reduced by only 6%.

Camera We use a high efficiency, scientific grade CCD camera to record the fluorescence signal. The quantum efficiency η is defined as the number of photons needed (on average) to produced one digital count at the output of the camera read-out register. We measured η using a source of light with Poissonian statistics. In that case, for N_φ incident photons, the mean number of counts is ηN_φ, with a variance $\eta^2 N_\varphi$. The ratio of the two gives η. In practice, we use a laser as a source. By scanning N_φ

[4] Custom made by Melles Griot to be diffraction limited at 589 nm and 1064 nm. It is also used to focus the vertical dimple trap on the atoms.

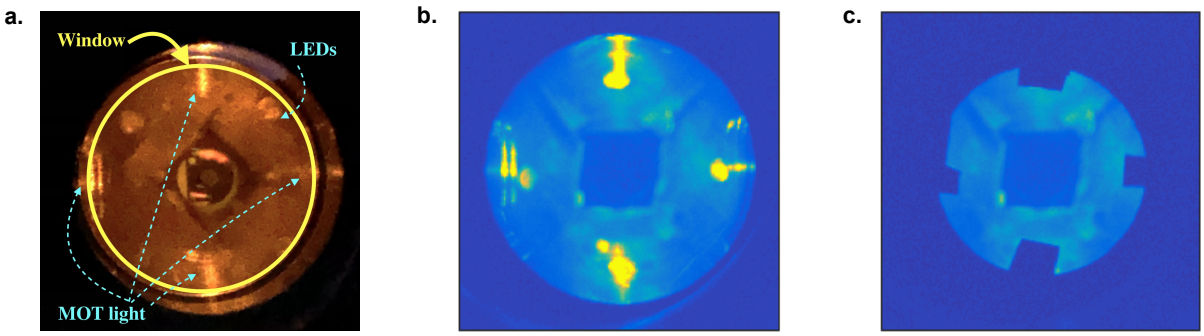

Figure 15: a Picture (taken with a photo camera) of the inside of the chamber view from the bottom (through the microscope objective), with the imaging light on. b,c Same picture taken with the CCD camera with (b) and without (c) the spatial filter. We clearly see four bright spots coming from the viewport (the imaging system is focused on the viewport). They are completely blocked by the spatial filter. The walls of the chamber still scatter some residual light that cannot be filtered out. The darker square in the middle corresponds to the upper vertical viewport.

we verified that it is indeed shot-noise limited for $N_\varphi < 3000$ (for higher N_ϕ, intensity fluctuations dominates). We measured $\eta = 0.73$. Relying on this calibration, we will report the signal and noise of our imaging system in photon units.
The electronic noise of the camera read-out signal comes from two mechanisms. Instead of a photon, thermal excitations can promote an electron from the valence band to the conduction band. This is usually known as dark current. It is importantly reduced by cooling the sensor (to $-70°$C in our case), and by electronically "cleaning it" over the sequence (the pixels are continuously read before the exposition starts). As a result, the dark current is completely negligible. More important is the read-out noise $\Delta\mathcal{N}_R$ coming from the conversion of the charge of a pixel into a voltage and then to a digital count. $\Delta\mathcal{N}_R$ can be significantly decreased by merging the charge of several pixels into one larger unit, called macro-pixel, before reading. This technique is known as "hardware binning". There are two downsides to hardware binning: the loss of spatial resolution and the possible "blooming", coming from the overflow of charge in the macro-pixel. We decided to bin the pixels by 64 (one macro-pixel is a square of 8×8 pixels). The loss of spatial resolution is of no importance to us, and blooming occurs only for large fluorescence signal (when $N \sim 10^4$), which is not the regime we are interested in.

We measured the electronic noise by taking images with the CCD hidden from any light. The noise (standard deviation of the number of counts) of a square macro-pixel of size $B \times B$ pixels, is

$$\Delta\mathcal{N}_R = 3.60 + 0.36 \times B \ \text{ photons}\,. \tag{3.19}$$

The offset of $3.60 + 0.36 = 3.96$ photons is the read-out noise of a single pixel. If the hardware binning was working perfectly, it would also be the noise of a macro-pixel. On the other hand, if we don't use hardware binning, the noise is $3.96 \times B$ (the B^2 individual pixels are uncorrelated). For $B = 8$, $\Delta\mathcal{N}_R \simeq 6.5$ instead of $\Delta\mathcal{N}_R \simeq 32$ without hardware binning. Thanks to that correction, the electronic noise only contributes marginally ($\sim 10\%$) to the total noise, which is dominated by stray light (see section 3.2.5)

3.2.3 Loading and diffusion in the optical molasses

Time-of-flight and Stern-Gerlach The Zeeman states are spatially separated during time-of-flight (TOF) in a magnetic field gradient. The separation d_{SG} that is achieved essentially sets the maximal duration of molasses we can afford (and thus the fluorescence signal), before the three clouds start to overlap. We thus want d_{SG} to be maximal, which requires a long TOF and a strong gradient. However, the latter is detrimental to the molasses. Indeed, if the gradient is significant when we shine the light, we have by definition a MOT (instead of a molasses), and the ± 1 atoms are brought back to the center. In fact, at equivalent gradients, the magneto-optic force produced in a MOT is orders of magnitude larger than the magnetic Stern-Gerlach force. It is therefore a great concern to avoid this situation and to reduce the gradient before the end of the TOF. Extinction of the magnetic field can take significant time (several milliseconds) due to eddy currents in the science chamber. The best compromise between large separation and small residual gradient is found experimentally, with the time spent in the molasses before overlap of the three clouds taken as a figure of merit. There are several parameters to optimize, the duration of the TOF t_{TOF}, and the magnetic field sequence, including the gradient for the Stern-Gerlach separation and the bias field.

First, we found that the longest TOF we can afford is $t_{\mathrm{TOF}} = 18$ ms, limited by the fall of the atoms outside the molasses beams (past this time, the signal decreases). Then, we optimize the duration during which the magnetic field gradient is present. The time sequence is the following. The gradient first increases for ~ 3 ms before being ramped down for 10 ms. The separation is $d_{SG} \simeq 1.3$ mm.

Optimization of the molasses The physics of optical molasses has been the subject of many theoretical and experimental investigations [97–99]. The simple case of a single particle can be described as a Brownian motion, with the absorption of laser photon followed by spontaneous emission leading to a random walk in momentum space. For low enough density, this result can be generalized to an ensemble of atoms, and the size of the cloud R evolves according to a diffusive law $R \propto \sqrt{t}$.
After 18 ms of TOF, and for the mesoscopic clouds that we work with, the distance between atoms in the molasses is $\sim 10\,\mu$m, much larger than the wavelength, and collective effects such as multiple scattering are not expected to play an important role. However, the random walk in the ideal case is significantly biased if residual magnetic fields on the order of $\sim$ 100 mG are present, leading to a net force acting on the atoms. We optimize the current feed into the coils during the molasses in order to compensate the ambient field and minimize the clouds size. We found that the optimum is not exactly the same for the three spatially separated clouds, and that it depends on t_{mol}. This is due to spatial and time dependence of the magnetic field, caused by the slow extinction of the gradient applied for the separation. The optimization is done for a given duration t_{mol}, and a compromise between the size of the three clouds is made (see figure 16).

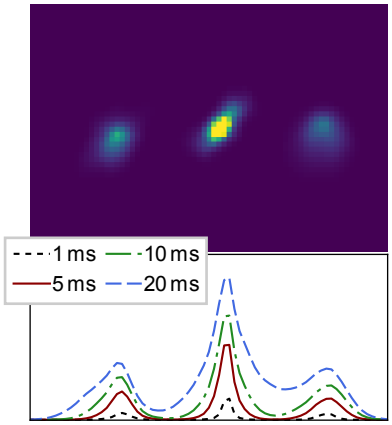

Figure 16: The upper panel is the fluorescence signal after $t_{\mathrm{mol}} = 5$ ms. The lower panel shows the profile along the separation axis for various molasses duration.

We optimize the detuning of the molasses for the "best" magnetic field configuration. The optimum is given by a compromise between larger photon flux (close to resonance) and slower expansion (far from resonance). We found experimentally that the total signal is maximized for $\delta/(2\pi) \simeq -9.9$ MHz ($\simeq -\Gamma$).

Diffusion in the molasses The CCD camera is exposed during the whole molasses phase, and the image we record represents the time integrated fluorescence signal. Let $\overline{\phi}_m$ be the mean photon flux, and $n_{\mathrm{col},m}(\mathrm{r}, t)$ be the column density of the clouds initially corresponding to the state $m = 0, \pm 1$ at time t of the molasses and position $\mathrm{r} = (x, y)$. The fluorescence intensity is

$$I_m(\mathrm{r}, t_{\mathrm{mol}}) = \int_0^{t_{\mathrm{mol}}} dt \overline{\phi}_m n_{\mathrm{col},m}(\mathrm{r}, t)\,. \tag{3.20}$$

For simplicity, we use the same continuous coordinate r for I_m and $n_{\mathrm{col},m}$, although in practice there is a magnification factor and a discretization into pixels. A simple estimate of the size of the cloud is given by the variance of I_m

$$R^2(t_{\mathrm{mol}}) = \frac{1}{N_m \overline{\phi}_m t_{\mathrm{mol}}} \int d^3\mathrm{r} \int_0^{t_{\mathrm{mol}}} dt (\mathrm{r} - \bar{\mathrm{r}}_m)^2 \overline{\phi}_m n_{\mathrm{col},m}(\mathrm{r}, t)\,. \tag{3.21}$$

where $\bar{\mathrm{r}}_m$ is the mean position of the cloud m. This can be reexpressed as a function of the variance $\sigma(t)^2$ of the density $n_{\mathrm{col},m}$:

$$R^2(t_{\mathrm{mol}}) = \frac{1}{t_{\mathrm{mol}}} \int_0^{t_{\mathrm{mol}}} dt \sigma^2(t)\,. \tag{3.22}$$

In the ideal molasses picture, $n_{\mathrm{col},m}$ is a Gaussian of variance $\sigma^2 = \sigma_0^2 + 2Dt$. In order to take into account the experimental imperfections mentioned above, we use a heuristic formula $\sigma(t)^2 = \sigma_0^2 + 2Dt + Ct^2$, so that,

$$R^2(t_{\mathrm{mol}}) = \sigma_0^2 + Dt + \frac{C}{3} t^2\,. \tag{3.23}$$

We show in figure 17 the results of a measurement of $R^2(t_{\mathrm{mol}})$ versus t_{mol} for the three Zeeman states. From a fit we extract the parameters D and C. The behavior is slightly different for the three clouds. For $m = -1$ it is consistent with a purely diffusive expansion, while for $m = 0, +1$, we measure a slight curvature. In any case, the expansion is much faster than the pure Brownian motion prediction. Residual magnetic fields are probably playing a major role.

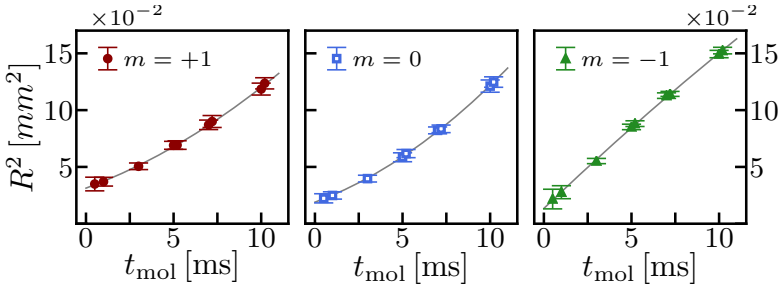

m	σ_0^2[mm^2]	D[mm^2/ms]	C[mm^2/ms^2]
$+1$	15.6×10^{-3}	5.68×10^{-3}	0.95×10^{-3}
0	9.46×10^{-3}	5.68×10^{-3}	1.37×10^{-3}
-1	6.73×10^{-3}	14.7×10^{-3}	-0.32×10^{-3}

Figure 17: Spatial variance $R^2(t_{\mathrm{mol}})$ for the three Zeeman components. The solid lines are quadratic fits $R^2(t_{\mathrm{mol}}) = \sigma_0^2 + Dt + \frac{C}{3}t^2$.

Atom losses in the molasses Let us mention that light-assisted collisions can play a non-negligible role in the molasses, even for small clouds [94]. This is an additional source of uncertainty on atom counting, which increases with t_{mol}. In theory, these losses could be observed as a reduction of the total photon flux over time, for a cloud with fixed initial atom number N. From this we could compute the optimal t_{mol}. However, fluctuations of N in the preparation of our samples make it difficult to evaluate this small effect in this simple way. We use another method based on the use of squeezed state, that will be detailed in 3.2.5.

3.2.4 Image analysis

Removing hot pixels Some images are polluted by "hot" pixels. These are very localized regions (usually one pixel, sometimes a few) of high intensity, often saturated, *e.g.* due to cosmic rays impinging on the detector. They are relatively frequent events (few percent of the shots). They are easily detected by computing the numerical Laplacian of the image. When a hot pixel is detected, it is replaced by the mean over the adjacent pixels.

Removing the background We already mentioned in sec. 3.2.2 the presence of stray-light photons scattered on the walls and viewports of the science chamber. We discuss here another source of stray light. We attribute it to the fluorescence of the residual background gas of Sodium present in the chamber. We recall that the density of Sodium atoms is momentarily increased for the loading of the MOT using UV light (see 3.1.2). Then, the ambient pressure decreases rapidly ($\sim$ 100 ms) to a very low value ($\sim$ 10^{-11} mbar). Yet, the remaining sparse vapor can still fluoresce. We show the profile and total signal recorded without trapped atoms on figure 18, for a various duration after the UV LEDs are turned off. The parasitic signal decreases on a much longer timescale of $\sim$ 50 s. The offset corresponds to the light scattered on the science chamber.

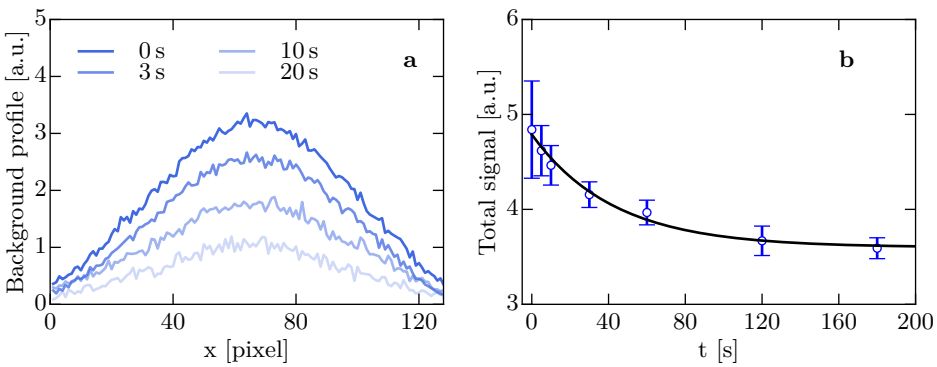

Figure 18: a Profile of the fluorescence signal emitted by the background gas, for various delays after shinning the UV LEDs. b Integrated signal. The solid line is an exponential fit, with a characteristic decay time $\tau \simeq 50$ s. The asymptote corresponds to the stray light scattered off the walls and viewports of the science chamber.

The total number of stray light photons (scattered and background fluorescence) amounts for the signal of roughly a thousand atoms. Fortunately, the contribution to the mean signal can be removed very efficiently with an algorithm know as "Best Reference Picture" (BRP, also called "eigenface method") [100]. From a set of empty reference images, the algorithm computes the linear combination closest to the atomic image in a region of comparison (ROC, see fig. 19). The distance between the two images is taken

	mean		std. dev.		Shot-noise
	No BRP	BRP	No BRP	BRP	-
$m = +1$	4.4×10^5	26	2.4×10^3	772	663
$m = 0$	4.8×10^5	-36	3.7×10^3	785	681
$m = -1$	3.8×10^5	2	2.0×10^3	687	628

Table 3.1: Mean and standard devation of the number of photons on empty images, after $t_{\text{mol}} = 5$ ms of molasses, with and without noise removal analysis (BRP). The last column gives the straight light shot noise (it is the square root of the signal given in the first column). We see the BRP reduces the noise almost to that level.

as the sum over all the ROC pixels of the intensity difference square (using this distance the BRP can be computed very efficiently). The working principle of the algorithm assumes that the background signal in the region of interest (ROI) where the atomic signal is located, is correlated to the background signal in the ROC. This is true for instance in the case of intensity fluctuation of the MOT/repumper light. For the best use of the BRP it is therefore important to make sure that the set of reference and atomic images have the same background. In particular, the reference images have to be taken with the same delay after extinction of the UV light, to have the same amount of background gas fluorescence. The shot noise of the stray light has no spatial correlations. This noise cannot be reduced through image processing, which only reduces the offset and the classical intensity fluctuation. We report on the performance of the BRP algorithm in Table 3.1. It brings the offset to a negligible value and the standard deviation almost at the shot noise level.

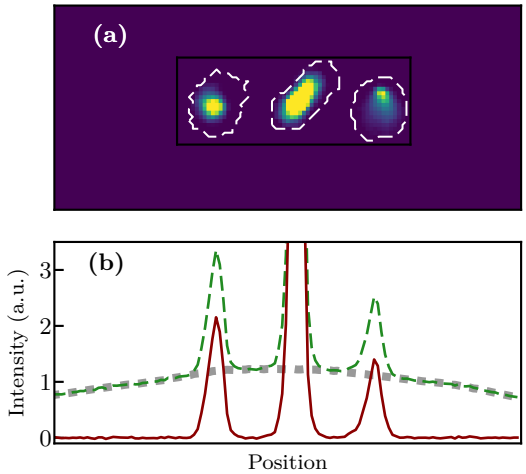

Figure 19: (a) Typical fluorescence image, with optimize ROI (dashed-white line). The hashed region is the ROC used to compute the BRP. (b) Profile before noise removal using the BRP algorithm (green dashed line) and after removal (solid red line). The dotted gray line shows the profile of the BRP.

Choice of the region of interest The final step of the imaging processing is the integration of the signal over some regions of interest (ROI) from which the atom number can be deduced. A ROI for a given Zeeman component m needs to fulfill three conditions:

a) It contains almost all the signal coming from the atoms initially in the state m.

b) It contains a negligible signal coming from atoms initially in $m' \neq m$.

c) It is as small as possible given a) in order to minimize the noise (stray light and electronic).

We start by taking a large square as the initial ROI A_m. We verify that the choice of A_m satisfies a) by making sure that the integrated signal increases linearly over time. To check that b) holds, we produce a cloud polarized in m' and measure the evolution of the signal in A_m. At some point it starts increasing, indicating the "leak" of some m' atoms from $A_{m'}$ into A_m. This sets the maximal duration for the molasses given the ROIs A_m. To fulfill c), we construct optimized ROIs, A'_m in the following way. We repeat several times a typical experiment, and compute the average image. In each raw ROI A_m, we sort the pixels by decreasing signal (see figure 20). A'_m is the reunion of the brightest pixels that contain 99% of the signal. In figure 21 we verify the requirements listed above with a cloud polarized in $m = 0$. We mentioned that we have used optimal ROIs of different sizes (170 and 200 pixels) described in Chapter 7, resulting into slightly different imaging noise.

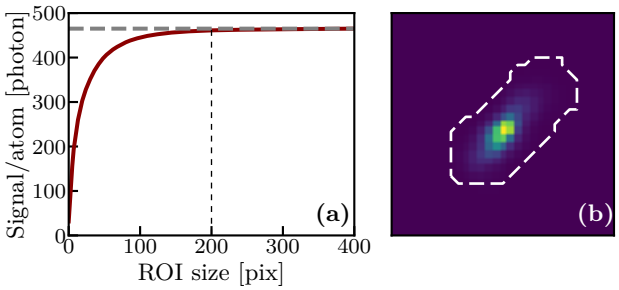

Figure 20: (a) Integrated signal versus the size of the optimized ROI $A'_{m=0}$ (red line) for $t_{\mathrm{mol}} = 5$ ms. The horizontal dashed line is the signal in the raw ROI $A_{m=0}$. The vertical line indicates the cutoff size. The optimized ROI is delimited by the white dashed line in (b).

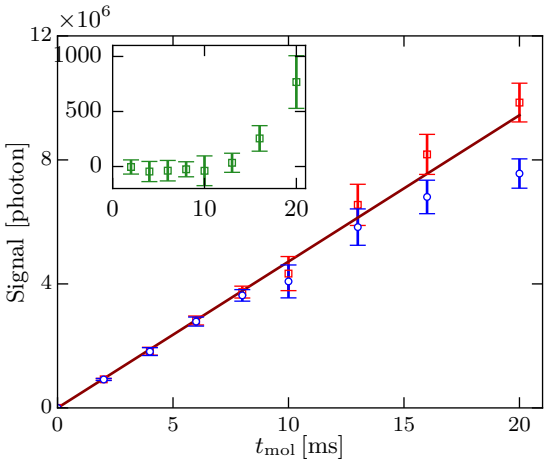

Figure 21: Integrated signal in the raw ROI $A_{m=0}$ (red squares) and optimized $A'_{m=0}$ (blue circles), for a cloud with all atoms in $m = 0$. $A'_{m=0}$ is optimized for $t_{\mathrm{mol}} = 5$ ms, we clearly see that it is too small for t_{mol} above ~ 10 ms. The inset shows the integrated signal in $A'_{m=+1}$. For $t_{\mathrm{mol}} \geqslant 10$ ms, we start to see a "leakage" of the $m = 0$ atoms in $A'_{m=+1}$.

3.2.5 Performance of the atom counting

Fluorescence Signal Let us consider a cloud with N_m atoms in the Zeeman component m. Let $\overline{\phi}_m$ be the average photon flux received per atom, and $\overline{\phi}_{m,\mathrm{bg}}$ the average flux of stray light photons received in A'_m. The mean signal is then

$$\overline{S}_m = N_m \overline{\phi}_m t_{\mathrm{mol}} + \overline{\phi}_{m,\mathrm{bg}} t_{\mathrm{mol}} \,. \tag{3.24}$$

The BRP algorithm described in the previous Section 3.2.4 allows us to subtract the background contribution almost perfectly. Let S_m^{BRP} be the number of counts in A'_m on a given shot after processing. On average, $\overline{S}_m^{\mathrm{BRP}} = N_m \overline{\phi}_m t_{\mathrm{mol}}$. For a given $\overline{\phi}_m$, we obtain an unbiased estimate of the atom number

$$\mathcal{N}_m = \frac{S_m^{\mathrm{BRP}}}{\overline{\phi}_m t_{\mathrm{mol}}} \,. \tag{3.25}$$

Calibration of the absorption imaging system relied on the measurement of the size of the BEC. Indeed, because of the repulsive interaction, the latter is related to the atom number. This method is detailed in previous theses [52, 54, 101]. However, we obtain in this thesis more accurate results using a method that does not rely on absorption imaging. The idea is to look at the statistics of a coherent spin state, known to be Poissonian. It is analogous to the method briefly described in sec. 3.2.2 for the calibration of the camera quantum efficiency. We start from a cloud in the state $|N : \mathbf{e}_z\rangle = |0\rangle^{\otimes N}$, *i.e.* with all atoms in $m = 0$. We use a resonant RF field to rotate this state by a variable angle θ around the y-axis, thus preparing the state

$$|N : \mathbf{\Omega}\rangle = \left(\cos\theta|0\rangle + \sin\theta \frac{1}{\sqrt{2}}\left(|-1\rangle - |+1\rangle\right)\right)^{\otimes N} \,. \tag{3.26}$$

For a cloud in this state, the Zeeman populations are

$$N_0(\theta) = \cos^2\theta N \,, \qquad N_{\pm 1} = \frac{1}{2}\sin^2\theta N \,, \tag{3.27}$$

and the variance of $S_z = N_{+1} - N_{-1}$ is

$$\Delta S_z^2(\theta) = N_{+1} + N_{-1} \,. \tag{3.28}$$

Those four equations are independent and sufficient to determine the three fluxes $\overline{\phi}_m$, $m = 0, \pm 1$ and total atom number N. The results of the calibration are presented in figure 22. The simple two-level atom picture (sec. 3.1.1) predicts a fluorescence flux

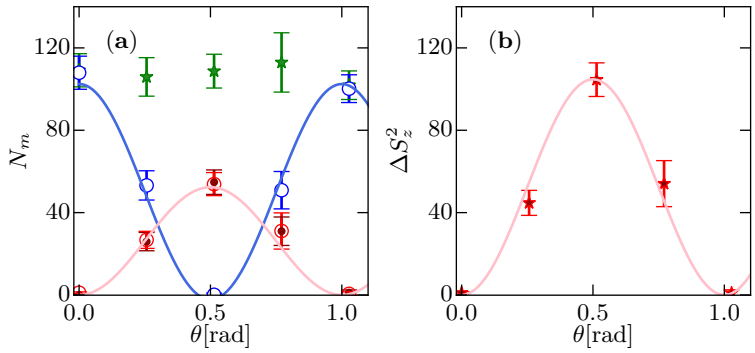

$\overline{\phi}_{+1}$[photon/ms]	$\overline{\phi}_0$[photon/ms]	$\overline{\phi}_{-1}$[photon/ms]
93 ± 3	89 ± 3	86 ± 3

Figure 22: (a) Evolution of the population N_0 (blue circles), N_{+1} (red dots) and N_{-1} (red circles) when rotating $m = 0$. The green stars are the total atom number and the solid lines are a fit. Together with the evolution of the fluctuations $\Delta S_z^2 = N_{+1} + N_{-1}$ (b) the photon fluxes are fully determined. The results are shown in the table.

$$\overline{\phi}^{\text{th}} = \eta \frac{\text{NA}^2}{4} \frac{\Gamma}{2} \frac{\frac{I}{I_{\text{sat}}}}{1 + 4\frac{\delta^2}{\Gamma^2} + \frac{I}{I_{\text{sat}}}} \,. \tag{3.29}$$

Using our experimental parameters, $\eta \simeq 0.73$, NA$\simeq 0.33$, $\Gamma \simeq -\delta \simeq 2\pi \times 10\,\text{MHz}$, $I \simeq 3.1\,\text{mW/cm}^2$ and $I_{\text{sat}} = 6.2\,\text{mW/cm}^2$, we find

$$\overline{\phi}^{\text{th}} \simeq 195\,\text{photon/ms} \,. \tag{3.30}$$

This figure is roughly twice as large as the measured flux. This difference could be expected. Indeed, the multi-level structure of the atoms tend to reduce the scattering cross-section of the atoms. The same effect is observed in absorption imaging (see *e.g.* [52, 101]), by a comparable amount. A more accurate treatment would require a precise knowledge of the polarization of the light at the location of the atoms. The reduction of the NA by the optical filter, the divergence of the beam, and losses over the optical path also contribute to the reduction.

Total Noise We show in Figure 23 the mean signal and variance on empty images. It can be expressed as

$$\Delta S^2_{\text{empty},m} = \overline{\phi}_{m,\text{bg}} t_{\text{mol}} + \alpha t^2_{\text{mol}} + \Delta \mathcal{N}_R^2 \,. \tag{3.31}$$

The first term is the stray light shot noise contribution. The second term is due to shot-to-shot intensity fluctuations. The last term is the read out noise, measured on "dark images" and given by Eq. (3.19). The shot-noise term scales linearly with t because it has no time correlation. Similarly, it scales linearly with the size of the ROI because it has no spatial correlations either. For this reason, it cannot be canceled by image analysis. The shot-to-shot intensity fluctuations are almost perfectly correlated in space and time (on the time scale of the molasses) leading to a quadratic scaling. Fortunately, they are strongly suppressed by the BRP algorithm. We report on Figure 23 the parameters $\overline{\phi}_{m,\text{bg}}$, α and $\Delta\mathcal{N}_R$ of Eq (3.31) extracted from a fit of the $\Delta S^2_{\text{empty},m}(t_{\text{mol}})$. The contribution of the intensity fluctuations dominates over the shot-noise for $t_{\text{mol}} > 15$ ms. For $t_{\text{mol}} = 5$ ms, the shot noise amounts for $\sim 85\,\%$ of the total noise on empty images. From now on, we will neglect the other contributions.

For an image with atoms, there are two additional sources of noise, atom losses in the molasses (see 3.2.3) and fluorescence shot noise. The later is equal to the stray light shot noise when $N_m \overline{\phi}_m = \overline{\phi}_{m,\text{bg}}$, that is for $N_m \sim 10^3$. In the experiments where the atom number resolution was crucial, we typically worked with N_m ranging from a few tens to a few hundreds of atoms so that we can neglect the fluorescence shot noise. The error on the atom number estimate is

$$\Delta \mathcal{N}_m = \sqrt{\frac{\overline{\phi}_{m,\text{bg}}}{\overline{\phi}_m^2 t_{\text{mol}}}} + \Delta N_{m,\text{loss}} \,. \tag{3.32}$$

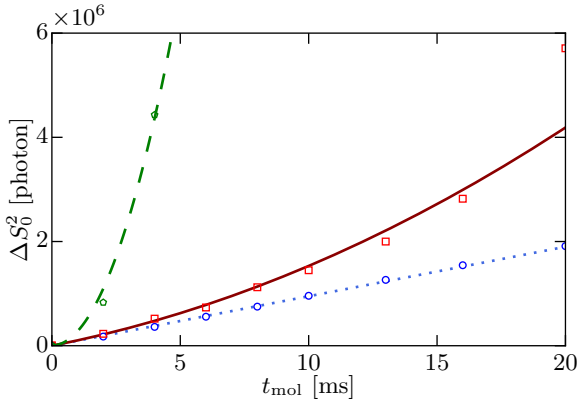

m	$\Delta\mathcal{N}_R^2$ [photon]	$\overline{\phi}_{m,\mathrm{bg}}$[photon/ms]	α[photon/ms^2]
0	7.5×10^3	9.3×10^4	5.8×10^3
+1	5.9×10^3	8.8×10^4	6.1×10^3
−1	6.2×10^3	7.9×10^4	5.4×10^3

Figure 23: Fluctuations of the number of counts (in photon unit) on an empty image, in the ROI A_0', before BRP subtraction (green pentagons) and after (red square). The lines are quadratic fits, the parameters are given in the table below for the processed images. The blue circles show the mean signal $\overline{S}_0$, in photon units ($i.e.$ the shot noise level).

The contribution of the first term is minimized for $t_{\mathrm{mol}} = 10$ ms (the longest we can afford to keep the clouds well separated) and amounts in that case to $\simeq 1.2$ atoms. However, a time dependence is hidden in $\Delta N_{m,\mathrm{loss}}$, which increases with time. This yields an optimal molasses duration $t_{\mathrm{mol}} < 10$ ms. As mentioned before (sec. 3.2.3), the amount of losses is typically very small and blurred out by atom number fluctuations of the initial state in a direct measurement. At the end of the day, we set-up fluorescence imaging in order to measure sub-shot noise fluctuations of the spin components of a squeezed state. Such a state, namely a two-mode squeezed vacuum (TMSV) is used for the final optimization and calibration of the experimental parameters (t_{mol} and a fine tuning of the flux $\overline{\phi}_m$).

Fine tuning of the photon flux using squeezed states We will detail in Chapter 5 how we produced and characterized a TMSV state. For the present purpose of imaging calibration, we are only interested in one of its properties: the numbers of atoms in the $m = +1$ and $m = -1$ state are equal. Therefore $\langle \hat{S}_z \rangle = 0$ and $\Delta\hat{S}_z = 0$. In fact, to reveal the physics discussed in the Chapter 5 to 7 a measurement of S_z (possibly after a spin rotation) with accuracy close to one atom is required, while the knowledge of the absolute population is not as necessary. We assume a small error on the photon flux $\overline{\phi}_m^{\mathrm{meas}}$ calibrated following the method described above. Let the real photon flux be $\overline{\phi}_m^{\mathrm{real}} = (1+\epsilon_m)\overline{\phi}_m^{\mathrm{meas}}$, where $\epsilon_m \ll 1$. To first order in ϵ_m, an estimator of the magnetization is

$$\mathcal{S}_z = \frac{S_{+1}}{\overline{\phi}_{+1}^{\mathrm{meas}}} - \frac{S_{-1}}{\overline{\phi}_{-1}^{\mathrm{meas}}}\,, \tag{3.33}$$

$$\mathcal{S}_z = \left(\frac{S_{+1}}{\overline{\phi}_{+1}^{\mathrm{real}}} - \frac{S_{+1}}{\overline{\phi}_{-1}^{\mathrm{real}}}\right)\left(1 + \frac{\epsilon_{+1}+\epsilon_{-1}}{2}\right) + \left(\frac{S_{+1}}{\overline{\phi}_{+1}^{\mathrm{real}}} + \frac{S_{+1}}{\overline{\phi}_{-1}^{\mathrm{real}}}\right)\frac{\epsilon_{+1}-\epsilon_{-1}}{2}\,. \tag{3.34}$$

For a perfect TMSV state, the mean and variance of the magnetization estimators are

$$\overline{\mathcal{S}}_z = \langle \hat{N}_{+1} + \hat{N}_{-1} \rangle \frac{\epsilon_{+1}-\epsilon_{-1}}{2}\,, \tag{3.35}$$

$$\Delta\mathcal{S}_z^2 = \Delta(\hat{N}_{+1} + \hat{N}_{-1})^2 \left(\frac{\epsilon_{+1}-\epsilon_{-1}}{2}\right)^2 + \Delta\mathcal{S}_{z,\mathrm{imag.}}^2\,, \tag{3.36}$$

When $\epsilon_{+1} = \epsilon_{-1}$, the mean vanishes and variance is minimal (bounded by the imaging noise). This enables a fine tuning of the relative flux between ±1, but not of the fluxes absolute value (we would need to determine $\epsilon_{+1} + \epsilon_{-1}$ as well). However, this is enough for the physics explored in the following.
In practice, we set $\epsilon_{-1} = 0$ and scan ϵ_{+1}. The results are reported on figure 24. The minimum of $\Delta\mathcal{S}_z$ and the zero of $\mathcal{S}_z$ almost coincide, which is a strong indication for a small miscalibration. It is corrected by setting $\epsilon_{+1} \simeq 0.02$. We can expect the same level of error on the total atom number. This has no impact on the results presented in the next chapters.

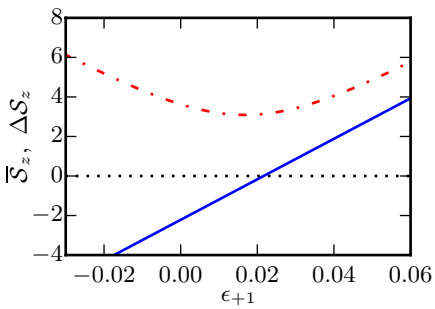

Figure 24: $\Delta\mathcal{S}_z$ (dash-dotted red line) and $\overline{\mathcal{S}}_z$ (blue line) as a function of the correction factor ϵ_{+1} ($\epsilon_{-1} = 0$). The minimum of $\Delta\mathcal{S}_z$ and the zero of $\mathcal{S}_z$ coincide almost perfectly.

m	Signal [photon]	Total noise [photon]	Total noise [atom]
$+1$	447	772	1.7
0	465	785	1.7
-1	428	687	1.6

Table 3.2: Signal and noise of the fluorescence imaging scheme.

Optimization of the molasses duration Finally, we optimize the duration of the molasses using a TMSV. We simply measure $\Delta\mathcal{S}_z$ for different molasses duration. The results are reported in figure 25. The noise is minimal at $t_{\mathrm{mol}} = 5$ ms. We attribute the increase past this time to atom losses in the molasses, as discussed in Sec. 3.2.3.

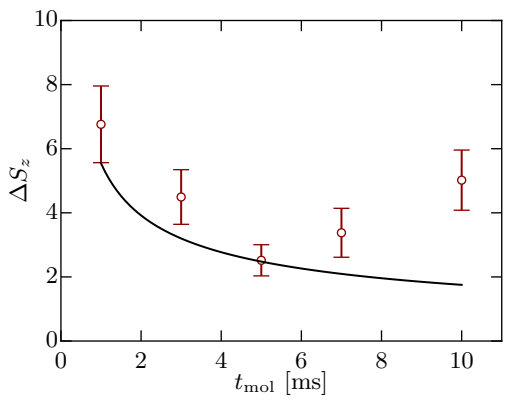

Figure 25: Standard deviation $\Delta\mathcal{S}_z$ measured for a TMSV state of ~ 200 atoms versus the duration of the molasses (red circles). The black line is the shot noise level. The deviation for $t_{\mathrm{mol}} > 5$ ms is interpreted as atom losses.

Summary We report in Table 3.2 the experimental values of the signal and noise for $t_{\mathrm{mol}} = 5$ ms. For the experiment discussed in the last Chapter, we were able to reduce the noise to slightly lower values, partly due to smaller ROIs and better alignment of the molasses beams.

3.2.6 Possible improvements

Our implementation of Stern-Gerlach fluorescence imaging has, to our knowledge, the best counting resolution for mesoscopic spinor BECs (let aside gases in optical lattices). We will see in the next chapters that it allows us to observe and characterize non-classical state of a few hundred atoms. For many experiments, the noise level of 1.6 atoms remains a limiting factor. We discuss here possible improvements on the setup that could allow one to further improve the counting resolution.

First, one could try to increase the signal. It seems difficult to extend the duration of the molasses, because of the losses. The photon flux could be increased using a microscope objective with larger NA, but in our experiment it would have required significant changes of the setup, and it would have come with an increase of stray light. In fact, the most significant and easiest improvement could be obtained by reducing the amount of stray light. It could bring the single atom signal-to-noise ratio above

one. Indeed, with the current signal, the electronic noise amounts to $\simeq 0.2$ atoms and the fluorescence shot noise of a hundred atoms amounts to $\simeq 0.4$ atoms.

A simple way to reduce the noise, consists in reducing the integration region (the ROI). In our case, the distortion of the residual magnetic field gradient is responsible for expansion in the molasses faster than what one could hope. One way to cancel this effect would be to use linearly polarized light. The difficulty for that, comes from the fact that in our scheme, we use the same light as for the MOT. One could use liquid crystal retarders to change the polarization of each beam after the MOT and before the imaging molasses. Stray light could also be decreased by using smaller beams, centered on the atoms after the TOF. In order not to compromise the MOT, one could use motorized irises, that would be partially closed after the MOT and before the imaging. Alternatively, we could also use another set of beams, independent from the MOT ones.

Chapter 4

Spin-mixing dynamics and relaxation of a driven spinor Bose-Einstein condensate

The present and following two chapters are dedicated to the physics of spinor Bose-Einstein condensates brought out-of-equilibrium. We present a series of experiments performed in a strongly confining trap, such that to a good approximation, a single spatial mode is common to the three Zeeman sublevels and the dynamics occur within the spin degree of freedom only. The spin state of an atom can change through collisions, leading to a so-called spin-mixing dynamics. Collisions between atoms in a thermal gas usually result in a rapid thermalization of an out-of-equilibrium system. On the contrary, in ultra-cold gases, collisions are a coherent process, very different behaviors are expected and have been observed [12, 58–63, 65, 102, 103].

In the experiments presented in this Chapter we realize an out-of-equilibrium BEC by preparing the spin-1 atoms in a superposition of the three spin states. Coherent collisions result in oscillations of the spin populations. This dynamic can be seen as an internal version of the Josephson effect. In our work, we build on this analogy and use a parametric excitation to reproduce the "inverse AC-Josephson effect", where an oscillating voltage applied on a Josephson junction leads to a steady current. We observed resonances when the driving frequency is near the single-particle energy splitting, given by the quadratic Zeeman shift. Finite size and non-linearities arising from the interactions distinguish our system from real Josephson junctions.

After a longer evolution time, we observe the relaxation of the system, presumably due to the coupling between the BEC and the thermal cloud. Interestingly, near resonance, we observe the existence of high energy stationary states, stabilized by the drive. Moreover, we found a frequency window where on the contrary, the low-energy states are destabilized. The combination of these two effects results in a hysteretic behavior. A microscopic modeling of the relaxation process is very challenging, and a common, simpler approach to the problem relies on the introduction of phenomenological dissipative terms in the equations of evolution. Following this approach, the exploration of the driven dynamics allows us to discriminate between different dissipative terms.

This work has been published in [45] and this article constitutes the rest of the present chapter, except for the outlook 4.7.

Beginning of the article [45]

4.1 Introduction

The Josephson effect is the hallmark of macroscopic quantum phenomena in quantum fluids, from superconductors [104–107] to superfluid Helium [108–111], polariton systems [112–114] and ultracold atoms in double-well potentials [6, 115–119]. In all variants, the phase of a macroscopic wave function is controlled by an external bias parameter. In Superconducting Josephson Junctions (SCJJs), a voltage bias determines the relative phase between the two superconducting order parameters on each side of the junction and the supercurrent is proportional to the sine of this phase [104–106]. This leads to some remarkable phenomena, such as the AC Josephson effect where a static voltage generates an oscillating current at the characteristic Josephson frequency ω_0. Conversely, in the "inverse AC Josephson effect" schematized in Fig. 26a [105–107], an oscillating voltage $V(t)$ quasi-resonant with ω_0 can carry a DC current across the junction.

In SCJJs, resonances occur when the drive frequency ω fulfills $k\omega = \omega_0$ for integer k [105]. These resonances appear in the form of Shapiro spikes in the voltage-current characteristics of the driven junction at constant bias voltage, or steps at constant bias current [107]. Shapiro steps are at the core of Josephson voltage standards, which are essentially perfect frequency-voltage converters enabled by macroscopic quantum effects [107]. Energy dissipation plays a crucial role in such devices [107]. Indeed without dissipation, the system would not relax towards the exact resonance where the macroscopic phase locks to the drive. Ultracold atoms exhibit two variants of the Josephson effect. In the first variant ("external Josephson effect"), two superfluids are

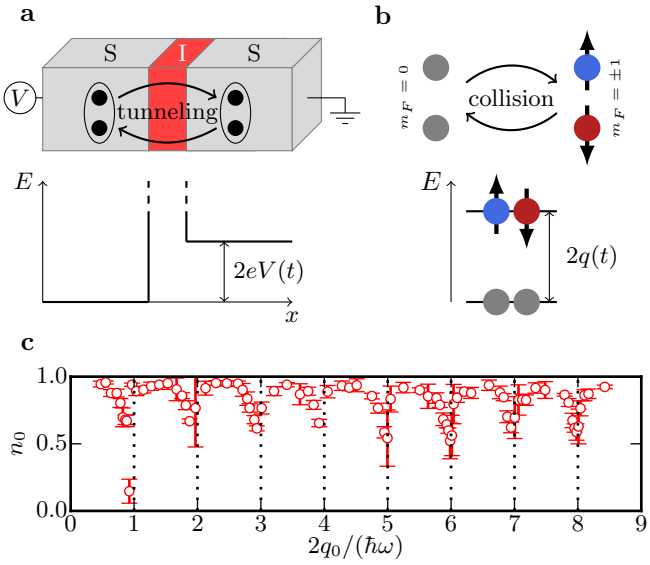

Figure 26: Analogy between two physical systems exhibiting macroscopic quantum coherence: a superconducting Josephson junction (SCJJ–a) and a spin-1 atomic Bose-Einstein condensate (BEC–b). For SCJJs (respectively, BECs), tunneling through the barrier (resp., spin-mixing interactions) generates an electric current (resp., a spin current) controlled by the relative phase across the barrier (resp., between the Zeeman components of the spin-1 wave function). An external energy bias $E(t)$ controls the rate of change of the relative phase: the electrostatic energy $E(t) = 2eV(t)$ for SCJJs, with V the voltage and $2e$ the charge of a Cooper pair, and the quadratic Zeeman energy $E(t) = 2q(t)$ of a pair of $m = \pm 1$ atoms for spin-1 BECs. If the energy bias is modulated around a static value E_0, a Shapiro resonance occurs when the modulation frequency ω fulfills the resonance condition $k_0\hbar\omega = E_0$, with k_0 a positive integer. c: Observation of several ($k_0 = 1 - 8$) Shapiro resonances in a spin-1 atomic condensate after a relaxation time of 30 s. Here, n_0 is the reduced population of the $m = 0$ Zeeman state, and q_0 is the static QZE. The experiment was performed with a sodium Bose-Einstein condensate containing $N \approx 2 \cdot 10^4$ atoms, with a magnetization per atom $m_{||} = 0$. We varied q_0 for a fixed drive frequency $\omega/2\pi = 100$ Hz.

coupled through a weak link [6, 115–119], in direct analogy with the SCJJs. In the second variant ("internal Josephson effect"), coherent dynamics can occur between internal degrees of freedom [35, 44]. Here we focus on the specific case of spin $F = 1$ atoms, with $m = 0, \pm 1$ the magnetic quantum number labeling the Zeeman components, as illustrated in Fig. 26b. An applied magnetic field plays the role of the external bias. The Josephson-like internal dynamics is generated by coherent, spin-changing collisions of the form $2 \times (m = 0) \leftrightarrow (m = +1) + (m = -1)$ instead of single-particle tunneling [48, 102]. Compared to the original SCJJ, cold atom implementations of the Josephson effect have an important asset when one tries to elucidate the microscopic mechanisms at play in the device: the typical time scales are on the order of milliseconds or longer, enabling a time-resolved study of the dynamics which is difficult to access in superconducting systems, where the microscopic time scales are in

the picosecond range.

So far most experimental studies on atomic spinor gases were performed with only a static bias and no modulation [58–67, 102, 103]. The driven case was explored only recently, with experiments demonstrating either the freezing of the evolution by frequent "kicks" in spin space [120], or spin-nematic squeezing near a parametric resonance [121]. In this article, we extend the analogy between SCJJs and atomic spinor gases to the driven regime, where Shapiro resonances occur. Using a spin-1 Bose–Einstein condensate (BEC) of sodium atoms, we observe such resonances (see Fig. 26c) and characterize them in the non-linear regime, where the phase dynamics is not solely controlled by the external static bias. We study the coherent dynamics at short times and the relaxation at long times (tens of seconds, corresponding to tens of thousands of the drive oscillation period). Near resonance, in the strongly driven regime, we find that the driven BEC relaxes to asymptotic states that are not stable without drive (Fig. 26c). In this sense, our system constitutes a many-body version of the celebrated Kapitza pendulum [122,123]. The stationary states correspond to phase-locked solutions of the Josephson equation, generalized to include dissipation and analogous to the stationary states of driven SCJJs [107].

In our experiments, dissipation presumably results from interactions between condensed and noncondensed atoms that lead to damping of coherent macroscopic phenomena and thermalization. Thermalization of driven quantum systems has been studied intensely in the past few years [124–126]. The general expectation is that energy is absorbed from the drive, eventually heating to infinite temperatures [127–129]. However, the heating time scale τ_h can become extremely long. Rigorous proofs are only available for high-frequency modulation and systems with a bounded spectrum: Refs. [130–132] have shown that $\tau_h = e^{\mathcal{O}(\omega/\Delta)}$, with Δ^{-1} the faster intrinsic timescale of the non-driven system and $\omega \gg \Delta$ the modulation frequency. For times $t \ll \tau_h$, the system may attain a pre-thermalized "Floquet-Gibbs" state corresponding to the equilibrium state of an effective, secular Hamiltonian. In this work we use near-resonant modulation and probe a system with an *a priori* unbounded spectrum [1]. We observe a long-time steady state that differs from both the infinite temperature state and a Floquet-Gibbs state associated with the secular Hamiltonian.

We introduce in this article a phenomenological model obtained by adding a suitable dissipative term to the coherent, Josephson-like equations describing the spinor dynamics. We compare its predictions with those of a former model used in the literature to describe relaxation in atomic Josephson-like settings. These two models can be roughly classified as amplitude or phase damping, respectively. Their predictions are barely distinguishable from each other without driving but differ spectacularly in the strongly driven case. More precisely, the "phase-damping model" proposed in [61], is clearly incompatible with the experimental observations, whereas our "amplitude-damping model" agrees quantitatively with them. This suggests that our experimental results can be used as a benchmark for *ab initio* theories of a driven many-body system, as they constrain strongly the form of damping prevailing in experiments.

The paper is organized as follows. In Section 4.2, we review the main features of our experiment and of the theoretical description of spinor condensates. We highlight the analogies and differences with Josephson physics in superconducting junctions. We also discuss for later reference spin-mixing oscillations without driving, highlighting both the coherent features [58–63, 103] and the dissipative aspects [61]. In Section 4.3, we turn to the driven system and characterize experimentally and theoretically the non-linear secular dynamics in the vicinity of the resonance. Measuring both the Zeeman population and the relative phase of the atoms, we identify two regimes, an "oscillating regime" where the atomic phase is locked to the drive, and a "rotating regime" where the atomic phase runs independently from the drive. In Section 4.4, we study the relaxation of the driven spin-1 BEC for long evolution times. In a narrow frequency window around each Shapiro resonance, we observe relaxation to a non-equilibrium steady state that has no analog in the non-driven system. We also show that the system displays hysteresis when the drive frequency is scanned accross a Shapiro resonance. Finally, we conclude and draw some perspectives of this work in Section 4.5.

4.2 Spin-mixing oscillations

This section is devoted to the theoretical modelling of a spinor Bose–Einstein condensate, as well as its experimental implementation and characterization. We first focus on the coherent dynamics of the system in the mean-field and single mode approximations, and we show that it can be viewed as a classical one-dimensional Hamiltonian system. Here the relevant canonically conjugate variables are n_0 and θ, where n_0 is the population of the $m = 0$ Zeeman state, and θ a particular combination of the phase of the three Zeeman states. We emphasize the deep analogies that exist between the equations of motion of the spinor gas and those of a driven SCJJ, with n_0 playing the role of the supercurrent and θ the role of the phase difference across the junction. We then present our experimental setup and explain how we access these two relevant variables n_0 and θ. Finally, we describe two simple models for the relaxation of the dynamics of the spinor BEC. In particular, we show experimental results that indicate that in the non-driven case, it is not possible to discriminate between these two relaxation models.

[1] The single-mode spin Hamiltonian has a bounded spectrum, but only describes the low-energy sector of the full Hilbert space.

4.2.1 Coherent dynamic of spinor condensates

Relevant contributions to the energy

We consider spin $F = 1$ atoms immersed in a spatially uniform magnetic field $\boldsymbol{B} = B\boldsymbol{u}$, where the orientation $\boldsymbol{u}$ is taken as quantization axis. The atoms can occupy all three Zeeman states $|F, m\rangle_{\boldsymbol{u}}$, where $m = 0, \pm 1$ refers to the eigenvalue of $\hat{\boldsymbol{f}} \cdot \boldsymbol{u}$ and where $\hat{f}_{x,y,z}$ are the spin-1 matrices.

As for most magnetic materials, the dynamics and equilibrium properties of spinor condensates are governed by (i) the Zeeman energy $\sim \mu_{\mathrm{B}} B$ in the applied magnetic field, where μ_{B} is the Bohr magneton, and (ii) the spin-dependent interactions. In this work, the direction of the applied magnetic field varies in time, but only on a time scale much longer than the Larmor period $h/\mu_{\mathrm{B}} B$. The single-particle spin states then follow adiabatically the changes of the direction of $\boldsymbol{B}(t)$ (see Appendix 4.6.1 for more details). For relatively low values of B, the Zeeman energy of a single atom is thus given by

$$\hat{h}_{\mathrm{Z}} = p(t)\hat{f}_z + q(t)\left[\hat{f}_z^2 - 1\right] + \mathcal{O}(B^3). \tag{4.1}$$

In this expression, the linear Zeeman term proportional to $p(t) = g_F \mu_{\mathrm{B}} B(t)$ ($g_F = -1/2$ the Landé factor) is essentially the contribution of the spin of the valence electron, and the quadratic Zeeman energy (QZE) proportional to $q(t) = \alpha_q \boldsymbol{B}^2$ (with $\alpha_q \approx h \times 277\,\mathrm{Hz/G^2}$ for sodium atoms) gives the first correction due to the nuclear spin [35].

Interactions between alkali atoms are mainly due to short-range van der Waals interactions. Magnetic dipole-dipole interactions are usually much weaker [133]. Neglecting the latter, the interaction potential between two atoms is invariant under spin rotations. On the other hand, the Zeeman term is invariant only by rotations around the quantization axis $\boldsymbol{u}$, which thus constitutes the symmetry axis of the problem. For a many-atom system, this symmetry implies that the longitudinal magnetization per atom, $m_{||} = \langle \hat{\boldsymbol{F}} \cdot \boldsymbol{u} \rangle / N$, with $\hat{\boldsymbol{F}}$ the total spin operator and N the total atom number, is a conserved quantity [35, 48, 58]. The linear Zeeman energy, proportional to $m_{||}$, can then be eliminated without loss of generality by transforming to a frame rotating around the quantization axis $\boldsymbol{u}$ at the Larmor frequency (see Sec. 4.2.1). The Zeeman energy then reduces to the QZE alone, $\hat{h}_{\mathrm{Z}} = q(t)\left[\hat{f}_z^2 - 1\right] + \mathcal{O}(B^3)$.

Single-mode regime

We focus in this work on the so-called *single-mode regime* of spinor condensates [48, 134, 135]. This regime is realized for a condensate confined in a tight trap, such that spin excitations correspond to energies much lower than the confinement energy associated with the spatial variations of the wave function. In this situation, the lowest energy states correspond to various spin states, but to the same single-mode spatial orbital $\overline{\phi}(\mathbf{r})$. It is convenient to use a second-quantized notation and to introduce the operator $\hat{a}_m$ annihilating a boson in the single-particle state $|F, m\rangle_{\boldsymbol{u}} \otimes |\overline{\phi}\rangle$. The spin physics is then described by an effective low-energy spin Hamiltonian [35, 136],

$$\hat{H}_{\mathrm{s}} = \frac{U_{\mathrm{s}}}{2N}\hat{\boldsymbol{F}}^2 - q\hat{N}_0. \tag{4.2}$$

Here N is the total atom number, U_{s} is a spin-dependent interaction energy determined by the single-mode orbital,

$$U_{\mathrm{s}} = \frac{4\pi\hbar^2 N a_s}{m_{\mathrm{Na}}} \times \int |\overline{\phi}(\boldsymbol{r})|^4 \, \mathrm{d}^3 r\,, \tag{4.3}$$

with $a_s \approx 0.13$ nm the spin-dependent scattering length [137] and m_{Na} the mass of a sodium atom. The QZE is proportional to q and to the operator $\hat{N}_0 = \hat{a}_0^\dagger \hat{a}_0$ counting the population in the Zeeman state $m = 0$. The procedure for calibrating U_{s} is described in Appendix 4.6.2. Note that by construction the Hamiltonian in Eq. (4.2) is valid only at low energies. In particular, it cannot describe the noncondensed modes involving orbital degrees of freedom other than $\overline{\phi}(\mathbf{r})$.

In the single-mode regime, almost all atoms condense at low temperature into the same single-particle state $\boldsymbol{\Psi} = \boldsymbol{\zeta} \otimes \bar{\phi}(\boldsymbol{r})$, with $\boldsymbol{\zeta}$ a complex vector independent of space. The components $\zeta_m = \sqrt{n_m} e^{i\phi_m}$, where n_m is the fractional (normalized to the total atom number) population of the Zeeman state m, are not independent. Accounting for (i) an overall normalization, (ii) an irrelevant global phase, and (iii) the conservation of magnetization leaves only three independent real variables. A convenient choice for these variables are the relative population n_0 of the $m = 0$ state and the two relative phases

$$\theta = \phi_{+1} + \phi_{-1} - 2\phi_0, \quad \eta = \phi_{+1} - \phi_{-1}. \tag{4.4}$$

The rate of change $\hbar\dot{\theta}$ can be interpreted as a chemical potential difference driving the "reaction" $(m = +1) + (m = -1) \leftrightarrow 2 \times (m = 0)$, with a "chemical equilibrium" reached for $\theta = 0$ or π (see Eq. (4.10) below). The phase η would describe the Larmor precession due to the linear Zeeman term in the original Zeeman Hamiltonian. The transformation $\zeta_m \to \zeta_m e^{-i\frac{mpt}{\hbar}}$ to a frame rotating at the Larmor frequency around the quantization axis $\boldsymbol{u}$ removes the contribution $\propto p$ to the Zeeman Hamiltonian, without loss of generality.

In this work, we focus on the case $m_{||} = 0$, so that $n_{+1} = n_{-1}$. The spin energy for a condensate in the state $\mathbf{\Psi}$ is then

$$E_s(n_0, \theta, t) = U_s n_0(1 - n_0)(1 + \cos\theta) - q(t)n_0. \tag{4.5}$$

Note that this energy does not depend on the phase η. For a static QZE $q > 0$ and antiferromagnetic interactions $U_s > 0$, it is minimal for the so-called polar state [138] with $n_0 = 1$ that minimizes separately the Zeeman and interaction terms in Eq. (4.5).

Spin-mixing and Josephson physics

The equations of motion for a spin-1 BEC in the single mode approximation can be derived from the Gross-Pitaevskii energy functional (see [35] and references therein). We start with the dynamical part of the Lagrangian for the Schrödinger equation $i\hbar \int \mathbf{\Psi}^* \cdot \dot{\mathbf{\Psi}}$ and expresses it in terms of the spin variables. Subtracting the Zeeman and interaction energies (4.5), we obtain the Lagrangian for $m_{||} = 0$,

$$\mathcal{L}(n_0, \theta, \dot{\theta}, t) = \frac{\hbar}{2} n_0 \dot{\theta} - E_s(n_0, \theta, t). \tag{4.6}$$

The two Euler–Lagrange equations for n_0 and θ

$$\frac{\mathrm{d}}{\mathrm{dt}} \frac{\partial \mathcal{L}}{\partial \dot{\theta}} = \frac{\partial \mathcal{L}}{\partial \theta}, \qquad \frac{\mathrm{d}}{\mathrm{dt}} \frac{\partial \mathcal{L}}{\partial \dot{n}_0} = \frac{\partial \mathcal{L}}{\partial n_0}, \tag{4.7}$$

read in this particular case

$$\frac{\hbar}{2} \dot{n}_0 = -\frac{\partial E_s}{\partial \theta}, \qquad \frac{\hbar}{2} \dot{\theta} = \frac{\partial E_s}{\partial n_0}. \tag{4.8}$$

The explicit form of these equations of motion is thus [102]

$$\hbar \dot{n}_0 = 2U_s\, n_0(1 - n_0) \sin\theta\,, \tag{4.9}$$

$$\hbar \dot{\theta} = -2q(t) + 2U_s\,(1 - 2n_0)\,(1 + \cos\theta). \tag{4.10}$$

For this choice of the Lagrange function, the conjugate momentum of the phase θ is

$$p_\theta \equiv \frac{\partial \mathcal{L}}{\partial \dot{\theta}} = \frac{\hbar}{2} n_0, \tag{4.11}$$

The Hamilton formulation of the dynamics corresponds therefore to a one-dimensional system, with the classical Hamiltonian $\mathcal{H} = p_\theta \dot{\theta} - \mathcal{L}$ defined as

$$\mathcal{H}(p_\theta, \theta, t) \equiv E_s(n_0 = 2p_\theta/\hbar, \theta, t). \tag{4.12}$$

The corresponding Hamilton–Jacobi equations are identical to Eq. (4.8). Note that in this formulation, E_s represents the *total* energy (kinetic plus potential) of the one-dimensional system.

Eqs. (4.9,4.10) contain the two main ingredients for Josephson physics [44]. Consider first Eq. (4.9): the "spin current" $\dot{n}_0$ is generated by *coherent* spin-mixing interaction processes controlled by the phase θ. This is analogous to the celebrated Josephson relation $I_s \propto \sin\phi$ linking the supercurrent I_s in a SCJJ to the relative phase ϕ between the two superconductors on each side of the junction. The additional factor $n_0(1 - n_0)$ enforces that the population n_0 stays in the interval $[0, 1]$ and thus simply corresponds to a slowing down of the dynamics when the BEC reaches one of the extreme points $n_0 = 0$ or $n_0 = 1$.

Consider now the second equation of motion Eq. (4.10): the external bias $q(t)$ –analogous to the voltage drop $V(t)$ across the junction– controls the rate of change $\dot{\theta}$ of the relative phase. This is analogous to the second Josephson relation $\hbar\dot{\phi} = 2eV$ with $2e$ the charge of a Cooper pair. Here, we also find an additional term [the last term of Eq. (4.10)], which describes how interactions can alter the resonance and the dynamics of the phase.

To summarize, the equations of motion describing the coherent dynamics of a driven spinor condensate present a deep analogy with those of a driven SCJJ, with identical dominant contributions. There exist however differences between Eqs. (4.9,4.10) and the "standard" Josephson relations, which essentially reflect the fact that these gases can be viewed as closed interacting systems; therefore Josephson-like phenomena typically lead, in the present case, to population oscillations of large amplitude (comparable to the total atom number), and not to a steady current as for superconducting circuits connected to charge reservoirs.

4.2.2 Experimental setup and protocol

In this paper, we focus on the situation where the static bias $q_0/h \sim 300$ Hz is much larger than $U_s/h \sim 30$ Hz. We present in this subsection the experimental protocol from which we infer the relevant variables n_0 and θ, and we illustrate it on the static case, *i.e.*, when $q = q_0$ is constant in time. In the regime $q_0 \gg U_s$ (called Zeeman regime in [103]), the QZE determines the phase evolution up to small corrections, $\theta(t) \approx \theta(0) - 2q_0 t/\hbar$. Eq. (4.9) then predicts harmonic oscillations of n_0 at the frequency $\approx 2q_0/\hbar$, with a small amplitude $\propto U_s/q_0$ [58–60, 102, 103]. These oscillations constitute the analogue for spinor gases of the AC-Josephson effect: a constant DC bias induces a periodic AC current.

Condensate preparation

In order to observe experimentally the AC spin oscillations induced by a static bias q_0, we prepare a quasi-pure condensate of spin-1 sodium atoms in a crossed optical dipole trap. The condensate contains $N \approx 10^4$ atoms, with a condensed fraction $\gtrsim 0.9$. The condensate is initially polarized in the $m = +1$ state (except in Section 4.4.4). Our main observables are the relative populations n_m of the Zeeman sublevels $m = 0, \pm 1$. We measure these populations using absorption imaging[2] after a time-of-flight in a magnetic field gradient separating the different Zeeman components ("Stern-Gerlach imaging"). The experimental setup, preparation steps and Stern-Gerlach imaging were described in detail in our previous publications [37, 56].

In the experiments described in the following, we initiate spin-mixing dynamics by rotating the internal state of the spin-polarized BEC. This spin rotation is the only exception to the adiabaticity condition indicated above. Experimentally, we apply a radiofrequency field resonant at the Larmor frequency for a time $t_{\pi/2} \approx 40\,\mu$s, resulting in a rotation by an angle of $\pi/2$ around an axis orthogonal to the quantization axis $\boldsymbol{u}$. With the Zeeman state $|m = +1\rangle$ as starting point, the internal state after rotation is $\frac{1}{2}\left(|m = +1\rangle + |m = -1\rangle\right) + \frac{1}{\sqrt{2}}|m = 0\rangle$. Hence the initial $m = 0$ population and longitudinal magnetization are respectively $n_{0,\mathrm{i}} = 1/2$ and a $m_{||} = 0$.

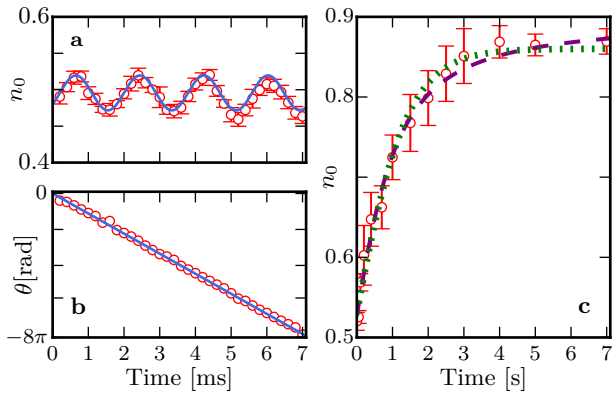

Figure 27: a-b: Spin-mixing oscillations without driving in the Zeeman regime $q_0 \gg U_s$. The time evolution of the population n_0 in (a) and the relative phase θ in (b.). c: Relaxation of n_0 at long times. The red points correspond to the experimental data and the lines show the fit results for the two dissipative models DM 1 (dotted green line) and DM 2 (dashed purple line) introduced in Sec. 4.2.3. The values of the fit parameters are given in Sec.4.2.3.

Measurement of the phase θ

The spin-mixing dynamics is characterized by oscillations of both the population n_0 and the phase θ. The Stern–Gerlach imaging procedure mentioned above readily provides the value of n_0. An example is given in Fig. 27a, which shows the expected sinusoidal evolution of $n_0(t)$ in the non-driven case. We use the method introduced in [37] to measure the phase θ. This method relies on the fact that the orientation of the transverse magnetization per atom $\boldsymbol{m}_\perp$ (controlled by the phase η, see Section 4.2.1) varies randomly for each realization of the experiment. Indeed, the spin energy E_s depends only on the magnitude of $\boldsymbol{m}_\perp$ but not on its orientation. After averaging over many realizations, the distribution of $\boldsymbol{m}_\perp$ has a zero mean but a non-zero variance,

$$\langle m_\perp^2 \rangle = 2n_0(1 - n_0)(1 + \cos\theta), \tag{4.13}$$

that depends explicitely on $\cos\theta$. Here $\langle\cdot\rangle$ denotes a statistical average over the realizations.

In practice, we apply a radio-frequency pulse to induce a spin rotation of $\pi/2$ around the y axis and measure the magnetization $m'_{||}$ after rotation. We repeat the experiment typically $N_{\mathrm{mes}} = 10 - 20$ times and calculate the variance $\langle m'^2_{||} \rangle$ of the experimental results. Using $\langle m'^2_{||} \rangle = \langle m_\perp^2 \rangle / 2 + \mathcal{O}(1/N_{\mathrm{mes}})$, we infer the value of $\cos\theta$. In order to determine unambiguously the phase θ itself, we assume that θ wraps monotonically around the unit circle to obtain the illustrative result shown in Fig. 27b.

4.2.3 Relaxation of spin-mixing oscillations

Experimental observation of a dissipative behavior

In the non-driven case, we observe experimentally that for long evolution times, the spin-mixing oscillations are damped and the population $n_0(t)$ eventually relaxes to the expected equilibrium value $n_0 \approx 1$. An exemple of this dissipative behavior is shown in Fig. 27c. The characteristic time scale is a few seconds, to be contrasted with the millisecond time scale of the coherent oscillations shown in Fig. 27a.

[2] This work was done before the implementation of fluorescence imaging described in Chapter 3.

This relaxation, first observed in [61], corresponds to a *loss of energy* of the spinor BEC. Eqs. (4.9,4.10) describe a Hamiltonian dynamics where the energy $E_s(n_0, \theta)$ is a constant of motion [102]. As a result, a point or an orbit of the classical phase space (n_0, θ) cannot be attractive, and relaxation cannot occur within this framework. However, experimental systems are never perfectly isolated, and their coupling to (many) other degrees of freedom playing the role of an energy reservoir enables energy dissipation and thermalization. In experiments with ultracold atoms, noncondensed particles forming a bath of collective excitations are inevitably present at non-zero temperature and constitute a primary candidate to explain relaxation. We expect that the interaction of the BEC with this bath acts to restore thermodynamic equilibrium, *i.e.* a BEC with all atoms in $m = 0$ for $q_0 > 0$, with a small decrease of the condensed fraction f_c. This is indeed what we observe in Fig. 27c, with a typical relaxation time (~ 1 s) that depends on q_0 [61].

Phenomenological modelling of the dissipation

An *ab initio* theoretical description of the thermalization dynamics in a spinor BEC would require to go beyond the Bogoliubov [136, 139, 140] or classical field [125] descriptions that are only applicable at short times. In this work, we study relaxation over several seconds, *i.e.* several hundred/thousand times the intrinsic time scales $h/U_s \sim 30$ ms and $h/2q_0 \sim 1$ ms set by interactions and QZE, respectively. To the best of our knowledge, no general framework is available to describe strongly out-of-equilibrium dynamics for single-component gases, let alone spin-1 systems.

Therefore, in order to describe the experimental observations and gain some insight on the dynamics, we take in this work a phenomenological approach. Following [61,115,119,141], we add "by hand" a dissipative term to the coherent spin-mixing equations of motions Eqs. (4.9,4.10):

$$\dot{n}_0 = \dot{n}_0|_{\text{coh}} + \dot{n}_0|_{\text{diss}}\,, \tag{4.14}$$

$$\dot{\theta} = \dot{\theta}\Big|_{\text{coh}} + \dot{\theta}\Big|_{\text{diss}}\,. \tag{4.15}$$

The first dissipative model (DM 1) that we consider was originally proposed in Ref. [61],

$$\text{DM 1}: \dot{n}_0|_{\text{diss}} = 0, \qquad \dot{\theta}_0\Big|_{\text{diss}} = \beta_1 \dot{n}_0. \tag{4.16}$$

Liu *et al.* argue that the dissipative term in Eq. (4.16) is the only term linear in $n_0, \theta, \dot{n}_0$ or $\dot{\theta}$ that can explain their measurements [61]. Anticipating on the results in the driven case that will be presented later, we have found that the dissipative model 1 can reproduce our experimental results without driving, but fails to predict the observed steady state in the strongly driven case. This motivated us to explore other dissipative models, not necessarily linear in n_0, θ or their derivatives. We propose in this article the alternative

$$\text{DM 2}: \dot{n}_0|_{\text{diss}} = -\beta_2 n_0(1-n_0)\dot{\theta}, \qquad \dot{\theta}_0\Big|_{\text{diss}} = 0. \tag{4.17}$$

In the context of cold atoms, similar dissipative terms have been proposed [115,119,141], mainly in analogy with those describing Ohmic dissipation in SCJJs. The DM 1 corresponds to a resistor connected in series with the junction, and the DM 2 to a resistor in parallel with the junction ("resistively shunted junction model"). The dimensionless phenomenological constants β_1, β_2 are real numbers, which are chosen positive to ensure that the energy E_s always decreases. Indeed, the dissipated power reads for a time-independent QZE

$$\mathcal{P}_{\text{diss}} = \frac{\mathrm{d}E_s}{\mathrm{d}t} = \dot{n}_0|_{\text{diss}} \frac{\partial E_s}{\partial n_0} + \dot{\theta}\Big|_{\text{diss}} \frac{\partial E_s}{\partial \theta} \tag{4.18}$$

which simplifies into $\mathcal{P}^{(1)}_{\text{diss}} = -\frac{\hbar}{2}\beta_1 \dot{n}_0^2$ for DM 1 and $\mathcal{P}^{(2)}_{\text{diss}} = -\frac{\hbar}{2}\beta_2 n_0(1-n_0)\dot{\theta}^2$ for DM 2. In both cases we find energy dissipation provided that the phenomenological damping coefficients $\beta_{1/2} \geq 0$.

Relaxation in the non-driven case

For long times, the population n_0 displays oscillations on top of a slowly varying envelope $\overline{\overline{n}}_0$, where the double bar denotes a coarse-grained average over a time long compared to the period of the spin-mixing oscillation $h/(2q_0)$, but short compared to the relaxation time $\tau_{1/2}$. In Appendix 4.6.3), we show that the solution of the DM 1 is well approximated at long time by

$$\text{DM 1}: \overline{\overline{n}}_0 \approx 1 - \frac{\tau_1}{t}, \tag{4.19}$$

with $\tau_1 = \hbar q_0/(\beta_1 U_s^2)$. The DM 2 predicts

$$\text{DM 2}: \overline{\overline{n}}_0 = \frac{n_{0,\text{i}}}{n_{0,\text{i}} + (1-n_{0,\text{i}})e^{-t/\tau_2}}, \tag{4.20}$$

with $\tau_2 = 2\hbar/(\beta_2 q_0)$. Here $n_{0,\mathrm{i}}$ is the initial value of n_0.

We have compared the predictions of the two models to the experimental results shown in Fig. 27c. For this comparison, we account for a small but non-zero thermal fraction. The measured population in $m = 0$ can be written

$$n_0 = f_c n_{0,c} + n_0', \tag{4.21}$$

with $n_{0,c} = N_{0,\mathrm{c}}/N_c$ (resp. n_0') the fraction of condensed (resp. noncondensed) atoms in $m = 0$. Here $N_{m,\mathrm{c}}$ denotes the population of condensed atoms in the m state, $N_c = \sum_m N_{m,\mathrm{c}}$ the number of condensed atoms, $f_c = N_c/N$ the condensed fraction and N the total atom number. We assume for simplicity that thermal atoms are distributed equally among all Zeeman sublevels, so that $n_0' = (1 - f_c)/3$.

We use Eq. (4.21) in combination with the dissipative models 1 or 2 for $n_{0,\mathrm{c}}$ to fit the experimental data in Fig. 27c, using f_c and the relaxation times $\tau_{1/2}$ as free parameters. We find comparable best-fit parameters for both models : $f_c \approx 0.85(2)$, $\tau_1 \approx 0.18(2)$ s for DM 1, $f_c \approx 0.80(2)$, $\tau_2 \approx 0.86(10)$ s for DM 2. The corresponding phenomenological damping parameters are $\beta_1 \approx 0.20(2)$ and $\beta_2 \approx 1.30(15) \times 10^{-3}$. The two dissipative models fit well our measurements in Fig. 27c, with a small difference that appears at long times, but which is not statistically significant. We conclude that discriminating between the two models is difficult in the non-driven case. We will see later in the article that this is no longer the case in the driven case, where the differences are spectacular at long times.

4.3 Shapiro Resonances

We now turn to the main topic of this paper, where a sinusoidal modulation of the QZE with frequency ω drives the spinor dynamics. We are interested in the case where $\hbar\omega$ and q_0 are comparable, allowing for a resonant behavior of the system (Sec. 4.3.1). We focus in this section on the short-time dynamics, where the effect of dissipation is negligible. In Sec. 4.3.2, we model the evolution close to a resonance by secular equations of motion, which depend on two time-averaged variables $\overline{n}_0$ and ϕ. The quantity $\overline{n}_0$ is the average of the population n_0 over the time period $2\pi/\omega$. The definition of the secular phase ϕ is more involved and will be made explicit in Sec. 4.3.2. We then explain how to access experimentally the value of ϕ (Sec. 4.3.3). We finally show that our experimental results in this short-time regime are in excellent agreement with the prediction of the secular equations (Sec. 4.3.4).

4.3.1 Observation of Shapiro resonances

In all what follows we use a sinusoidal modulation of the QZE around a bias value q_0 according to

$$q(t) = q_0 + \Delta q \sin(\omega t + \varphi_{\mathrm{mod}})\,\Theta(t), \tag{4.22}$$

with $\Theta(t)$ the Heaviside step function. Experimentally, the x component B_x of the magnetic field is static, and the y component $B_y = \Delta B \cos[(\omega t + \varphi_{\mathrm{mod}})/2 + \pi/4]\,\Theta(t)$ is modulated in a sinusoidal fashion. The QZE is given by Eq. (4.22) with $q_0 = \alpha_q(B_x^2 + \Delta B^2/2)$ and $\Delta q = \alpha_q \Delta B^2/2$.

In a perturbative picture, spin-mixing resonances occur when a pair of atoms in $m = 0$ can be resonantly transferred to a pair $m = \pm 1$ by absorbing an integer number k of modulation quanta, *i.e.* when $k\hbar\omega = 2q_0$. We define the detuning by

$$\hbar\delta = 2q_0 - k_0\hbar\omega, \tag{4.23}$$

with k_0 the closest integer to $2q_0/(\hbar\omega)$.

The left column of Fig. 28 shows how the population n_0 evolves in time for several values of the modulation frequency ω close to the first resonance with $k_0 = 1$, such that $\delta \ll q_0$. The dynamics of n_0 can be described as the combination of (i) a fast (frequency $\omega \simeq 2q_0/\hbar$) micromotion with a small amplitude, visible in the inset of Fig. 28a1, and (ii) a slow oscillation with a large amplitude. The period of the slow oscillation is a hundred milliseconds or more, much longer than the intrinsic timescales set by the drive period, the QZE or the spin-dependent interactions. This slow dynamics is the result of the coherent build-up over hundreds of periods of the micromotion. The slow "Shapiro oscillations" observed near resonance can be viewed as the counterpart for our closed system of the DC current observed near Shapiro resonances in modulated SCJJs.

Fig. 29 shows the generic behavior observed for longer times, where we observe (i) a damping of the contrast of the oscillations on a time scale of several hundred milliseconds, and (ii) a drift of the baseline value of n_0 towards the equilibrium value without driving, $n_0 = 1$. We attribute the damping (i) mainly to fluctuations of the experimental parameters, leading to shot-to-shot fluctuations of the period and amplitude of the oscillations and therefore to their dephasing after averaging over several realizations of the experiment. We believe that the main contribution comes from small ($\Delta N/N \sim 8\,\%$) fluctuations of the atom number. These fluctuations induce fluctuations $\Delta U_{\mathrm{s}}/U_{\mathrm{s}} \sim 6\,\%$ of the $N-$dependent interaction strength U_{s} [see Appendix 4.6.2 for the calibration of the dependence $U_{\mathrm{s}}(N)$].

We show in Fig. 28 and Fig. 29 the theoretical results obtained by solving numerically Eqs.(4.9,4.10) with the dissipative term (4.17) for different interaction strengths U_{s}, and averaging over a Gaussian distribution of U_{s} with mean and variance deduced

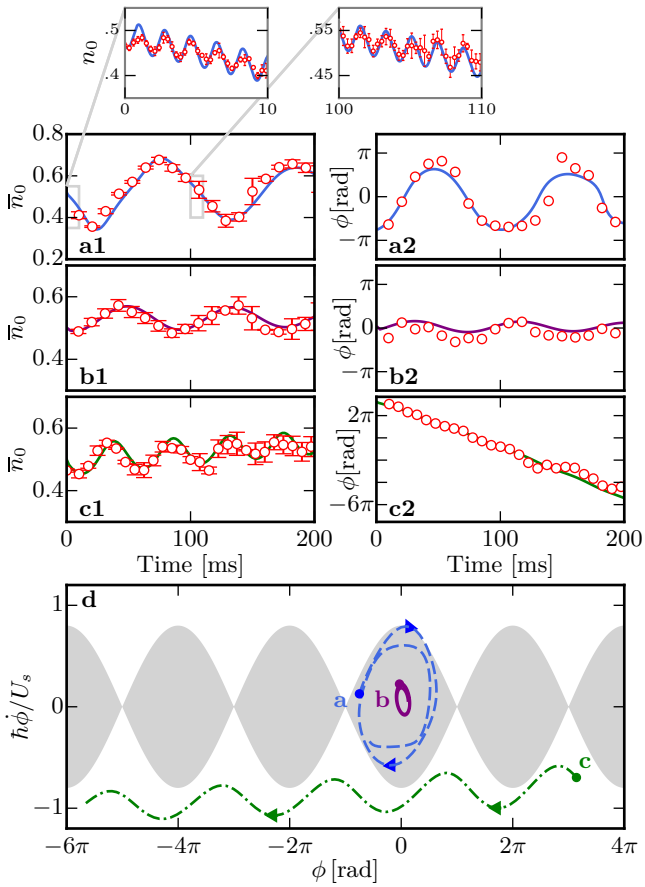

Figure 28: Observation of secular oscillations near the first Shapiro resonance $k_0 = 1$. We show the relative population $\overline{n}_0$ (a-c1) and phase ϕ (a-c2) versus time. The parameters in a1-2,b1-2 correspond to the oscillating regime of the pendulum model, while c1-2 correspond to the clockwise-rotating regime. The lines show the numerical solutions of the dissipative model 2 [Eq. (4.17)] with $\beta_2 = 1.3 \cdot 10^{-3}$. The calculated curves are further averaged to account for experimental fluctuations of U_s (see text). The last panel d shows a phase-space portrait of the trajectories in the $(\phi, \dot{\phi})$ plane, with $\dot{\phi}$ calculated from Eq.(4.25). The dashed blue, solid purple and dashed-dotted green line correspond to a1-2, b1-2 and c1-2, respectively. The shaded area covers the phase-space region explored in the oscillating regime of the pendulum model. In the main panels, the observation times are integer multiple of the modulation period $T = 2\pi/\omega$. The data are thus a stroboscopic observation of the secular dynamics, free of the additional micromotion. The two insets in **a1** (with a smaller time sampling) show the micromotion around the main secular oscillation. The static bias is $q_0/h = 276$ Hz, the modulation amplitude $\Delta q/h = 43.6$ Hz ($\kappa \simeq 0.08$), and $U_s/h \approx 30$ Hz. The detuning is $\delta/2\pi = -5.7$ Hz (a1-2,b1-2) and 18 Hz (c1-2). For curves b1-2, we varied the initial phase (see text) to be in the harmonic regime: $\theta(0) = -0.5(2)$ rad for a1-2,c1-2 and $1.45(2)$ rad for b1-2.

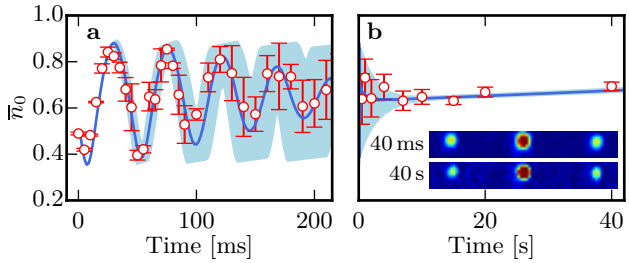

Figure 29: a: Damping of Shapiro oscillations. The solid blue curve is calculated from the dissipative model 2 (DM 2) and averaged over the fluctuations of U_s caused by atom number fluctuations (see text). The shaded area corresponds to the standard deviation of the distribution of n_0 induced by these initial fluctuations. The static bias is $q_0/h = 276$ Hz, the detuning $\delta/2\pi = -18$ Hz, and the modulation amplitude $\Delta q/h = 218$ Hz ($\kappa \simeq 0.36$). The interaction strength is $U_s/h \approx 32$ Hz for $t = 0$ and decays to ≈ 20 Hz for $t = 40$ s due to atom losses during the hold time in the optical trap. b: Long-time relaxation of the secular population $\overline{n}_0$ to a steady state. We attribute the small drift of the steady state population to the decay of U_s.

from the measured atom number statistics. We checked that for relatively short times (say, < 200 ms), the dissipation plays a negligible role and the observed damping of the oscillations is essentially due to the fluctuations of U_s.

In the rest of this Section, we focus on the initial oscillations shown in Fig. 28, neglecting the role of dissipation, and postpone the discussion of relaxation at long times to Sec. 4.4.

4.3.2 Secular equations for near-resonant driving

For our experimental situation with $q_0 \gg U_s$ and for a modulation frequency close to the k_0 Shapiro resonance ($|\delta| \ll q_0$), we derive in Appendix 4.6.4 effective equations of motion for the slowly evolving components by averaging over the fast micromotion. These secular equations of motion read

$$\hbar\dot{\overline{n}}_0 = 2\kappa U_s \overline{n}_0(1-\overline{n}_0)\sin\phi, \tag{4.24}$$

$$\hbar\dot{\phi} = -\hbar\delta + 2U_s(1-2\overline{n}_0)(1+\kappa\cos\phi). \tag{4.25}$$

Here, $\overline{n}_0$ is the time average of n_0 over one modulation period $T = 2\pi/\omega$, and the secular phase ϕ is related to the time-average $\overline{\theta}$ of the phase by

$$\phi = \overline{\theta} + k_0(\omega t + \varphi_{\mathrm{mod}} + \pi/2). \tag{4.26}$$

The interaction terms driving the spin dynamics are renormalized by a factor

$$\kappa = J_{k_0}\left(\frac{2\Delta q}{\hbar\omega}\right), \tag{4.27}$$

with J_k the kth-order Bessel function of the first kind. Note that our modulation scheme is limited to $\Delta q < q_0$. Together with the secular approximation, this implies that $0 < \kappa < 1$.

The secular equations Eqs. (4.24,4.25) have a structure similar to the original spin-mixing equations Eqs. (4.9,4.10) with the replacements $q \to -\hbar\delta/2$ and $e^{i\theta} \to \kappa e^{i\phi}$. Accordingly, Eqs. (4.24,4.25) derive from the classical Hamiltonian of the secular motion with the canonical momentum $p_\phi = \hbar\overline{n}_0/2$,

$$\mathcal{H}_{\mathrm{sec}}(p_\phi, \phi) = E_{\mathrm{sec}}(\overline{n}_0 = 2p_\phi/\hbar, \phi) \tag{4.28}$$

and

$$E_{\mathrm{sec}}(\overline{n}_0, \phi) = -\frac{\hbar\delta}{2}\overline{n}_0 + U_s\overline{n}_0(1-\overline{n}_0)(1+\kappa\cos\phi). \tag{4.29}$$

The different dynamical regimes are best understood in the limit of small driving, $\kappa \ll 1$. We show in Appendix 4.6.4 that the secular equations Eqs. (4.24,4.25) reduce for $\kappa \to 0$ to the ones describing the motion of a one-dimensional rigid pendulum of natural frequency $\Omega = \sqrt{2\kappa}U_s/\hbar$, with the secular phase ϕ representing the angle of the pendulum. The pendulum admits two dynamical regimes, either oscillations around the stable equilibrium point $\phi = 0$, or full-swing rotations with ϕ running from 0 to 2π. The period of the oscillations diverges at the transition between the two regimes.

The same qualitative conclusions hold outside of the weak driving limit. A numerical solution of the equations of motion shows that the positions of the resonance and of the separatrix shift to slightly higher frequencies with increasing driving strength. From Eq. (4.26), we note that the regime of small oscillations ($\phi \approx 0$) corresponds to an atomic phase $\overline{\theta} \approx -k_0(\omega t + \varphi_{\mathrm{mod}} + \pi/2)$ locked to the drive. Conversely, the regime of full-swing rotations ($\phi \approx -\delta t$) corresponds to a free-running atomic phase $\overline{\theta} \approx -2q_0 t/\hbar$, barely affected by the drive.

4.3.3 Measurement of the secular phase ϕ

In order to observe the two dynamical regimes, we now concentrate on the evolution of the phase ϕ, since the population $\overline{n}_0$ oscillates in both cases.

We measure the secular phase using a variant of the method of Section 4.2.2 that allows us to lift the phase ambiguity. We measure $\cos\theta$ as before for stroboscopic times $t_p = pT$ and a quarter of period later $t_p + T/4$, with p a positive integer and $T = 2\pi/\omega$ the period of the modulation. Assuming $\phi(t_p) \approx \phi(t_p + T/4)$ (in accordance with the secular approximation), we obtain, after converting θ to ϕ using the definition of the latter in Eq. (4.26), a simultaneous measurement of $\sin\phi(t_p)$ and $\cos\phi(t_p)$ at stroboscopic times t_p.

Obtaining confidence intervals on the measurement of ϕ is far from obvious. The statistical spread of $\sin\phi(t_p)$ and $\cos\phi(t_p)$ can be quantified using the quantity $S = \langle\cos\phi\rangle^2 + \langle\sin\phi\rangle^2$, equal to 1 if ϕ is perfectly determined and vanishing for ϕ completely random. We find that S decreases with a characteristic time scale ~ 200 ms. Physically, we attribute this decay essentially to the fluctuations of U_s coming from atom number fluctuations translating into a phase spread increasing with time. Mathematically, the probability distribution $\mathcal{P}(\phi)$ of ϕ that derives from our expected distribution of U_s has a complicated shape due to the non-linearities of the spin-mixing equations. We did not pursue a sophisticated statistical analysis accounting for the peculiarities of $\mathcal{P}(\phi)$, and use instead the quantity S introduced above to estimate when the measurement of the phase is reliable. We arbitrarily choose the criterion $S \geq 1/2$ corresponding to measurements times $t \leq 200$ ms.

In an ideal experiment strictly described by Eq. (4.22), the modulation would be turned on instantaneously at $t = 0$. The initial phase $\theta(0) = 0$ would then be determined by the preparation of the initial state. In practice, a small delay of $\Delta t = 100\,\mu$s is present between the preparation and the beginning of the modulation, and the modulation settles to the form in Eq. (4.22) after $1 - 2$ ms, due to the transient response of the coils used to generate the modulation B_y. During this short transient ($\ll \hbar/U_s$), the populations barely evolve but the phase changes because of the QZE. Both effects can be incorporated as an initial phase shift

$$\theta_0 = -\frac{2}{\hbar} \times \left[q_0 \Delta t + \int_0^{+\infty} [\tilde{q}(t) - q(t)] dt \right]. \tag{4.30}$$

Here $\tilde{q}$ denotes the instantaneous QZE actually experienced by the atoms and $q(t)$ the ideal step-like profile. The extra phase shift is $\theta_0 \approx -0.5$ rad for the data in Fig. 28a1-2. We can also insert on purpose a variable delay between the preparation step and the start of the modulation to tune the initial phase θ_0. We used this technique to record the data in Fig. 28b1-2, which are otherwise obtained for identical conditions as in Fig. 28a1-2.

We plot in Fig. 28 (right column) the results for ϕ for the first resonance $k_0 = 1$. For small detuning, the phase oscillates around $\phi = 0$, *i.e.* the dynamics of the BEC phase is phase-locked with the drive (panels a1-2,b1-2.). The excursion of the phase away from $\phi = 0$ depends on the detuning and the initial phase, which we can tune (panels b1-2) to have $\phi(t = 0) \simeq 0$. For a given initial phase, when δ exceeds a critical value corresponding to the transition betweeen the two dynamical regimes, phase locking no longer occurs and the BEC phase runs freely from 0 to 2π, corresponding to the "rotating pendulum"case (panels c1-2).

4.3.4 Period and amplitude of the secular oscillations

We extract the amplitude and period of the secular oscillations by fitting a periodic function

$$n_0(t) = \sum_{j=0}^{3} a_j \cos(jt/T_{\text{sec}} + \phi_0)\,, \tag{4.31}$$

to the data. We restrict the fit to the first two periods of the secular motion, with the amplitude $a_j \in \boldsymbol{R}$ of the harmonics and the initial phase ϕ_0 as free parameters. Fig. 30 shows the period T_{sec} and amplitude for the first resonance $k_0 = 1$ versus detuning. The results agree well with a numerical solution of Eqs. (4.9,4.10) (*i.e.*, without taking dissipation into account), and with the pendulum model. Close to resonance, the measured amplitude is systematically lower than the theoretical prediction. This can be qualitatively explained by the presence of noncondensed atoms that do not participate in the coherent secular dynamics.

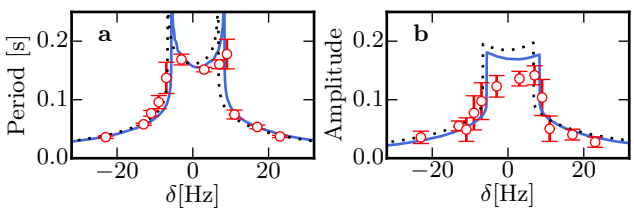

Figure 30: Period (**a**) and amplitude (**b**) of the secular oscillations versus detuning δ for the same parameters as in Fig. 28. The solid blue lines show the numerical solutions of Eqs. (4.9,4.10), and the dotted black lines the analytical solution of the pendulum model.

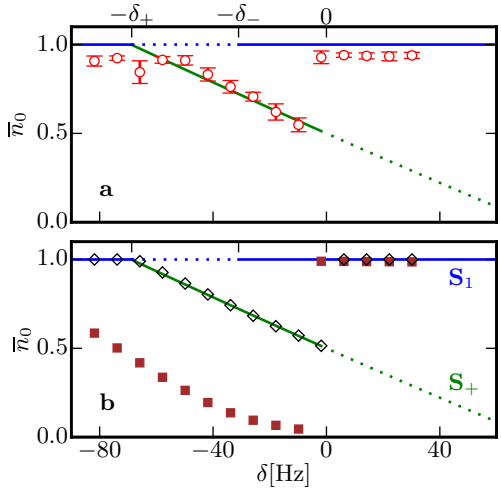

Figure 31: a: Measured population n_0 as a function of detuning δ after a relaxation time of 10 s. The experiment is performed near the first resonance $k_0 = 1$ ($\hbar\omega \approx 2q_0$) with $n_{0,\mathrm{i}} = 0.5$. The static bias is $q_0/h \approx 277$ Hz, the modulation amplitude is $\Delta q/h \approx 227$ Hz ($\kappa \simeq 0.4$), and the interaction strength is $U_\mathrm{s}/h \approx 26$ Hz. b: Numerical solutions of the dissipative models 1 (Eq. 4.16, brown squares) and 2 (Eq. 4.17, black empty diamonds). In both panels, the horizontal blue (respectively oblique green) line corresponds to the stationary state S_1 (resp., S_+). The solid (resp. dotted) segments correspond to the stable (resp. unstable) region according to DM 2 (see Section 4.4.2).

4.4 Long-Time Relaxation

In this Section, we focus on the state reached for long evolution times, after relaxation has taken place. We observe that after the damping of the slow, large amplitude Shapiro oscillations, the population $\bar{n}_0$ reaches a steady state that persists for tens of seconds [3]. We characterize this steady state and show that it can differ from the equilibrium points of either the non-driven Hamiltonian $\mathcal{H}$ or the secular Hamiltonian $\mathcal{H}_\mathrm{sec}$. We then take explicitly into account the dissipation using the two models DM 1 and DM 2 introduced in Sec. 4.2.3. We show that DM 2 leads to predictions in good agreement with our observations, whereas DM 1 is clearly excluded. Then, we study the new fixed points that can appear in the presence of this dissipation, and we discuss their stability. In particular there exist some regions of parameter space where two fixed points can be simultaneously stable or metastable. This leads to the possibility of observing a hysteretic behavior, which we confirm experimentally.

4.4.1 Observation of a Non-Equilibrium Steady State

Fig. 31 shows a typical measurement for strong driving ($\kappa = 0.38$) near the first resonance $k_0 = 1$. We monitor how the steady state value changes as a function of detuning δ. We find that the system relaxes to $\overline{n}_0 \approx 1$, except in a range of negative detunings close to the resonance where the population $\overline{n}_0$ takes values between ≈ 0.5 and 1. The steady state reached in this strongly driven situation does not correspond to the thermodynamic equilibrium point in the absence of modulation, *i.e.* the ground state of $\mathcal{H}$ defined in Eq. (4.12) with $q(t) = q_0$, obtained for $\overline{n}_0 = 1$. It does not correspond either to the minimum of the secular Hamiltonian $\mathcal{H}_\mathrm{sec}$ defined in Eq. (4.28), obtained for $\overline{n}_0 = 1$ for $\delta > 0$ and $\overline{n}_0 = 0$ for $\delta < 0$. This contrasts strongly with the non-driven case where the thermodynamic equilibrium state $n_0 \approx 1$ is always observed at long times.

In the experimental results shown in Fig. 26c, we observe the same behaviour for higher resonances, up to $k_0 = 8$ (limited by the maximal magnetic field we can produce). In order to record this set of data, we set $\omega/2\pi = 100$ Hz and scanned simultaneously the bias value q_0 and driving strength Δq, keeping $\Delta q/q_0$ and therefore the secular renormalization factor κ approximately constant. After a wait time of 30 s, we observed that the system relaxes for all k_0 to the same stationary state as for the first resonance. In the following, we therefore concentrate on the case $k_0 = 1$ as in the previous Section.

We use the same dissipative models introduced in Section 4.2.3 to explain the experimental observations. We show in Fig. 31 b the result of a direct numerical solution (with no secular approximation) of Eqs. (4.14,4.15) for the dissipative models 1 and 2. We observe that the DM 1 fails to reproduce the measured steady state populations, while the DM 2 predicts a long-time behaviour consistent with the experimental results. This contrasts with the non-driven case, where both models lead to similar predictions. In the following, we specialize to the DM 2 and explore its consequences for the long-time steady state.

[3] The steady state population slightly changes over time due to atom losses and/or evaporation of thermal atoms, that change the condensed atom number and thereby U_s (see Fig. 29). The time scale for these changes is very slow (around 10 s) and modifies significantly U_s from its initial value only after very long times (by about 17 % in 10 s), much longer than the typical time-scales for the dynamics. We therefore discard these changes for the discussion in the main text.

4.4.2 The fixed points and their stability

We now look for (possibly metastable) secular solutions of dissipative model 2 where the population $\overline{n}_0$ is stationary. We derive generalized secular equations as in Section 4.3 starting from Eqs. (4.14,4.15,4.17) defining the DM 2. Observing from Eq. (4.26) that $\dot{\overline{\theta}} \approx -\omega + \dot{\phi}$, we find

$$\hbar\dot{\overline{n}}_0 = \overline{n}_0(1-\overline{n}_0)\left(2\kappa U_s \sin\phi + \beta_2\hbar\omega - \beta_2\hbar\dot{\phi}\right). \tag{4.32}$$

The phase dynamics is still determined by Eq. (4.25). From Eq. (4.32), we identify four possible states for which $\dot{\overline{n}}_0 = 0$.

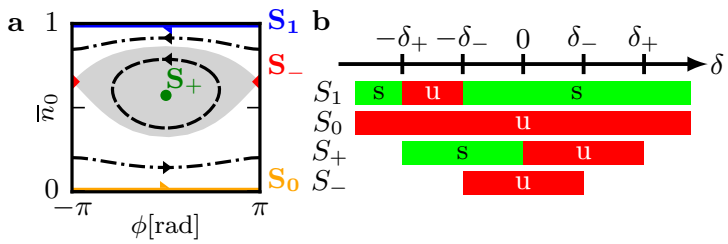

Figure 32: Fixed points of the dissipative spin-mixing model 2. a: Phase space portrait of the stationary solutions of Eqs. (4.24,4.25). The two limit cycles are labeled S_0 ($\overline{n}_0 = 0$, solid orange line) and S_1 ($\overline{n}_0 = 1$, solid blue line) and the two fixed points S_+ (green dot) and S_- (red diamond). The black lines show typical trajectories in the oscillating (dashed line) or rotating (dash-dotted lines) regimes. The shaded area covers the oscillating regime. The plot is shown for $\delta/2\pi = -10$ Hz, $U_s/h = 25$ Hz, $\kappa \simeq 0.38$ ($\delta_-/2\pi \simeq 32$ Hz) and a damping coefficient $\beta_2 \to 0^+$. b: Table summarizing for $\beta_2 \to 0^+$ the ranges of detuning where each stationary solution is stable ('s') or unstable ('u'). The boundaries $\delta_\pm$ are defined after Eq. (4.33).

The first two states correspond to $\overline{n}_0 = 0, 1$. In these two limiting cases, the relative phase θ (and thus ϕ) is physically irrelevant and can take any value. These two solutions, labeled S_0, S_1 in the following, correspond to "limit cycles" in the language of dynamical systems [142]. The other two stationary states, labeled $S_\pm$, correspond to fixed points of the dissipative equations of motion where $\dot{\overline{n}}_0 = \dot{\phi} = 0$. They correspond to the secular phases $\phi_+ = \epsilon, \phi_- = \pi - \epsilon$, where the angle ϵ obeys $\sin\epsilon = -\beta_2\hbar\omega/(2\kappa U_s)$. The populations at the fixed points are

$$\overline{n}_{0,\pm} = \frac{1}{2}\left(1 - \frac{\delta}{\delta_\pm}\right), \tag{4.33}$$

with:

$$\hbar\delta_\pm = 2U_s(1 \pm \kappa\cos\epsilon). \tag{4.34}$$

Fig. 32a shows the location of the stationary solutions in a secular phase-space portrait $(\overline{n}_0, \phi)$. For each sign of the detuning δ, one of the two limit cycles $S_{0,1}$ corresponds to the minimum of the secular energy E_{sec}. The fixed point S_+ is always the maximum of E_{sec} and S_- is a saddle point.

Dissipation must be present, but not too strong, in order to ensure the existence of an attractive fixed point of the dynamics. Indeed, the fixed points $S_\pm$ disappear when $\beta_2 \geq 2\kappa U_s/(\hbar\omega)$. If the dissipation stength β_2 is too large or the driving strength too small, the drive cannot provide enough energy to overcome the dissipation and create a metastable state. This is confirmed by other experiments that we performed with a weaker driving strength $\kappa \sim 0.08$, where we found that the relaxation to the fixed point was less robust than the one shown in Fig. 31.

For the experiments shown in Fig. 31, we find $\phi_+ \approx 0.04$ corresponding to the weak dissipation limit, $\epsilon \propto \beta_2 \to 0^+$. In this situation, the positions of the fixed points are well approximated by $\hbar\delta_\pm \approx 2U_s(1 \pm \kappa)$. They are therefore independent of the precise value of β_2 to first order in the small parameter ϵ.

We study the dynamical stability of the stationary solutions in App. 4.6.6 for a phenomenological damping coefficient $\beta_2 \to 0^+$. We summarize the results in Fig. 32b. The drive destabilizes S_1 in a small region of positive detunings around the resonance, while S_0 is always unstable because of the dissipation. The fixed point S_+ is stable only for $\delta < 0$, while S_- is always unstable.

At first glance, one may expect that energy dissipation always induces relaxation to an energy minimum. In fact, at the fixed point $S_\pm$, the atomic phase locks to the drive with a small phase lag, such that the power absorbed from the drive exactly compensates the power loss due to dissipation. This phase-locking enabled by dissipation stabilizes the system in a highly excited state (App. 4.6.4), reminiscent of the dissipative phenomenon leading to Shapiro steps in SCJJs [107].

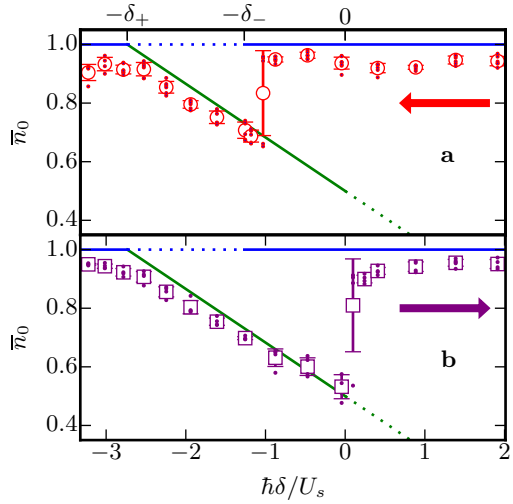

Figure 33: Observation of hysteresis in the relative population n_0 after a detuning ramp. We prepare a spinor BEC with $n_{0,\mathrm{i}} \simeq 1$, and scan the detuning by changing q_0 for fixed $\omega/2\pi = 277$ Hz and $\Delta q/h = 227$ Hz. In a (respectively, b), the ramp decreases (resp., increases) from $\delta_i \approx 2.0\, U_s/\hbar$ (resp., $\delta_i \approx -3.3\, U_s/\hbar$). The horizontal blue (resp., oblique green) line correspond to S_1 (resp., S_+). The solid (resp., dotted) segments corresponds to the stability (resp., instability) regions. The small dots show individual measurements, the squares their average, and the error bars their standard deviation.

4.4.3 Interpretation of experimental results

We can now interpret the experimental findings of Fig. 31. The position of the stable fixed point S_+ in the limit $\beta_2 \to 0$ is shown in Fig. 31, and explains well the observed steady state populations for $\delta \in [-\delta_+, 0]$. Outside this window, the system relaxes to the equilibrium state S_1 with $n_0 \approx 1$. We interpret the observed "trapping" in the state S_+ as follows. A system prepared with $n_{0,\mathrm{i}} \approx 0.5$ tends to relax to the ground state S_1 of $\mathcal{H}$, as observed for $|\delta| > \delta_+$ where there is no fixed point. For $\delta \in [-\delta_+, 0]$, the derivative of the phase $\dot{\phi}$ diminishes in absolute value as $\overline{n}_0$ increases because of the dissipation, and it progressively vanishes. At this point, which corresponds to S_+, $\dot{\overline{n}}_0$ also vanishes and the system remains trapped in this state. On the contrary, for $\delta \in [0, \delta_+]$, S_+ corresponds to $\overline{n}_{0,+} \leq 1/2$ and $|\dot{\phi}|$ increases as $\overline{n}_0$ increases. The trajectory tends to move the system away from S_+. As a result, dissipation acts as in the non-driven case and the system eventually reaches S_1.

The scenario described above explains all observations but one. In Fig. 26c, for very small but negative δ near the first resonance, the system relaxes to $\overline{n}_0 \simeq 0.16$. This observation is consistent with thermalization in the secular Hamiltonian where the lowest energy state is $\overline{n}_0 = 0$ when $\delta < 0$. The residual deviation with respect to $\overline{n}_0 = 0$ observed experimentally may be due to a non-zero thermal fraction or an incomplete thermalization.

4.4.4 Hysteretic Behavior

According to the stability diagram of Fig. 32b, there is no single stationary solution that would be stable for all detunings δ. Furthermore, there are two stable solutions S_+ and S_1 in the interval $[-\delta_-, 0]$. In such a situation, one can expect some hysteretic behaviour, which we searched for using a slightly different procedure than in the rest of the article.

We prepared a BEC in the state $m = 0$, such that $\overline{n}_{0,i} \sim 1$ (up to thermal atoms in $m = \pm 1$). We apply the modulation as before but slowly ramp the static bias q_0 over a ramp time of 3 s, and then hold the driven system at the final q_0 value for 7 s. This amounts to a slow ramp of the detuning δ decreasing (respectively, increasing) from δ_i to δ_f in Fig. 33a (resp., Fig. 33b). For decreasing ramps with $\delta_i > \delta_+$, the system remains in S_1 in the domain $\delta > -\delta_-$ where S_1 is stable. Continuing the ramp further, S_1 becomes unstable and we find that the system relaxes to S_+ as in the previous experiments. Conversely, for an increasing ramp starting from $\delta_i < -\delta_+$, the system follows S_+ while it is stable, *i.e.* for $\delta_f \in [-\delta_+, 0]$ and S_1 otherwise. We therefore observe an hysteresis cycle spanning the interval $\delta \in [-\delta_-, 0]$ where both S_1 and S_+ are stable.

4.5 Conclusion

In conclusion, we have observed the analogue for a driven spin-1 BEC of the Shapiro resonances characteristic of the AC Josephson effect in SCJJs. The population dynamics near each resonance corresponds to a slow and non-linear secular oscillation on top of a rapid micromotion. We have found that the driven spin-1 BEC relaxes at long times to asymptotic states phase-locked to the drive and that are not stable without it. We proposed a phenomenological model of dissipation that describes quantitatively the relaxation process and its outcome. The dynamics in the driven case allows us to discriminate between different phenomenological

models, in contrast to the situation without driving where these different models lead to similar predictions. The microscopic origin of the dissipation remains to be investigated. While dissipation probably comes from interactions between condensed and noncondensed atoms, a quantitative description of these interactions and of the resulting thermalization process is lacking. The procedure we used in this paper led to a set of dissipative equations which are essentially generalized Gross-Pitaevskii equations. While we have found excellent agreement between the experimental results and the predictions of these equations, our procedure is purely phenomenological and whether these generalized Gross-Pitaevskii equations can be derived from first principles or not remains an open question. A detailed microscopic study of dissipation in this setup would also be useful to understand other types of driven quantum gases where an optical lattice potential [143] or the interaction strength [144] are modulated.

Another interesting question is related to the occurence of deterministic chaos in a spinor BEC [145]. Without driving, chaotic behavior can be ruled out for a spin-1 BEC on the basis of the Poincaré-Bendixson theorem [142]: the dynamics is indeed obtained from the one-dimensional Hamiltonian $\mathcal{H}$, with only two variables θ and $p_\theta \sim n_0$. To allow for a chaotic behavior, one needs to consider higher spin BECs [146] or driven spin-1 BECs [145], with time playing the role of a third variable. However when the secular approximation holds, we recover an effective time-independent one-dimensional problem with the Hamiltonian $\mathcal{H}_{\rm sec}(p_\phi \sim n_0, \phi)$, which excludes again a chaotic behavior. One thus expects to find chaos only in situations where the secular approximation breaks down. Using the non-dissipative spin-mixing equations and adapting the methods of [145] to our system, we have found numerically that chaos can be present in the vicinity of Shapiro resonances for strong modulation and small bias, $\Delta q \sim q_0 \sim U_{\rm s}$. For almost all experiments reported in this paper, where $q_0 \gg U_{\rm s}$, we did not find any evidence of chaotic behaviour. The only exception is the situation investigated in Fig. 26**c**., where $q_0 \simeq h \times 100$ Hz is only three times larger than $U_{\rm s}$. The deviation from the fixed point near $\delta = 0$ for the first resonance could be connected to the onset of chaotic behavior, which is an interesting direction to explore in future work[4].

Finally, a promising application of driven spinor gases is the dynamical control of the strength of spin-mixing interactions, viewed as a matter-wave equivalent of parametric amplifiers in quantum optics. Such parametric amplifiers are phase-sensitive, and are also known to generate squeezing (see [65,67,147] for the spinor case). This enables interferometric measurements below the standard quantum limit [64,66,148,149]. A promising direction for the development of devices operating at the Heisenberg-limit are the so-called $SU(1,1)$ interferometers [66,149], which can be viewed as Mach-Zehnder interferometers where the beam splitters are replaced by parametric amplifiers. As shown in Appendix 4.6.5, the quantum version of the secular single-mode Hamiltonian [48] is renormalized by driving as in the mean-field Gross–Pitaevski framework. This implies that spin-mixing collisions can be enabled by moving close to a Shapiro resonance for a controllable duration, and then disabled by detuning the system away from resonance. Such dynamical control over the spin-mixing process could significantly improve the performances of matter-wave $SU(1,1)$ interferometers [66].

4.6 Supplementary materials

4.6.1 Adiabatic following

We consider a gas of spin-1 atoms in a magnetic field $\boldsymbol{B} = B(t)\boldsymbol{u}(t)$ with time-dependent amplitude B and orientation $\boldsymbol{u}$. We take the instantaneous direction $\boldsymbol{u}(t)$ of $\boldsymbol{B}$ as quantization axis. The label $m = 0, \pm 1$ then corresponds to the instantaneous Zeeman state $|m\rangle_{\boldsymbol{u}}$, *i.e.* the eigenstate of $\hat{\boldsymbol{f}} \cdot \boldsymbol{u}$ with eigenvalue m, with $\hat{f}_{x,y,z}$ the spin-1 matrices. The atomic spins precess around $\boldsymbol{u}$ at the characteristic Larmor frequency $\omega_L = \mu_B B/2$. The atom internal state follows adiabatically changes of B and $\boldsymbol{u}$ if the adiabatic condition $\dot{\omega}_L \ll \omega_L^2$ holds at all times. Here the dot denotes a time derivative. In our experiment, this condition can also be written $\omega B_y \ll \omega_L |\boldsymbol{B}|$. In most of this work, the Larmor frequency is around $\omega_L \sim 2\pi \times 0.7$ MHz. Since $B_y \leq |\boldsymbol{B}|$, the sufficient condition $\omega/\omega_L \sim 10^{-3} \ll 1$ is always fulfilled.

4.6.2 Calibration of $U_{\rm s}$

We calibrate the interaction strength $U_{\rm s}$ using the well-established behavior of spin-mixing oscillations without driving [58–60, 102, 103]. For a given total atom number N, we fit the observed population oscillations with the numerical solutions of Eqs. (4.9,4.10) treating $U_{\rm s}$ as a free parameter, all other parameters being kept constant. We show the fitted values of $U_{\rm s}$ versus N in Fig. 34. The dependence on atom number reflects the fact that our experiments are in the crossover between the ideal gas (where $U_{\rm s}$ is independent of N) and the Thomas-Fermi regime (where $U_{\rm s} \propto N^{2/5}$). We use the heuristic function $U_{\rm s}(N)/h = a(1 + (N/N_0)^b)$ to calibrate the dependence, with best fit parameters $a \simeq 20$ Hz, $b \simeq 3.5$ and $N_0 \simeq 19\,000$. Small fluctuations of N induce fluctuations of $U_{\rm s}$ according to $\delta U_{\rm s} = ab(N/N_0)^b \delta N/\langle N\rangle$. In our experiment, we have typically $\langle N\rangle \simeq 13\,000$ and $\delta N \simeq 1\,000$, which correspond to $\langle U_{\rm s}\rangle/\hbar \simeq 25$ Hz and $\delta U_{\rm s}/\hbar \simeq 1.5$ Hz.

[4] See the outlook 4.7

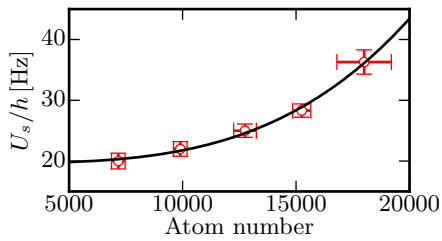

Figure 34: Interaction strength U_s measured for different atom number. The black solid line is an heuristic fit (see main text). The QZE is static and equal to $q_0/h \approx 0.7$ Hz$\ll U_s$ ($B_x \approx 50$ mG).

4.6.3 Relaxation of spin oscillations without driving

The spin dynamics without driving consists of a "fast" evolution of the population and of the relative phase θ superimposed on a slowly-varying envelope $\overline{\overline{n}}_0$. In the limit $q_0 \gg U_s$, the envelope of n_0 relaxes to $n_0 = 1$ over times long compared to the period $\sim \hbar/(2q_0)$ of spin-mixing oscillations. Averaging in a time window long compared to this period, we obtain effective equations for $\overline{\overline{n}}_0$ that can be solved analytically. For the dissipative model 1 with the initial condition $n_0(0) = n_{0,\mathrm{i}}$, we find that $\overline{\overline{n}}_0$ obeys the implicit equation, $f(\overline{\overline{n}}_0) = f(n_{0,\mathrm{i}}) + t/\tau_1$, with $f(x) = 2\ln[x/(1-x)] + (2x-1)/[x(x-1)]$ and $\tau_1 = \hbar q_0/(\beta_1 U_s^2)$. For $t \gg \tau_1$, the solution is well approximated by Eq. (4.19). For the dissipative model 2, we obtain Eq. (4.20) by direct integration.

4.6.4 Secular dynamics

Derivation of the secular equations

In this Section, we derive the secular equations Eqs. (4.24,4.25). Integrating formally Eq. (4.10), we rewrite $\theta = \alpha - 2p$, where

$$p(t) = \frac{1}{\hbar}\int_0^t q(t')dt' = \overline{p} - \frac{\eta}{2}\cos(\omega t + \varphi_{\mathrm{mod}}). \tag{4.35}$$

Here $\overline{p} = \frac{q_0 t}{\hbar} + \frac{\chi}{2}$ and α verifies $\hbar\dot{\alpha} = 2U_s(1-2n_0)(1+\cos\theta)$. We introduced a modulation index $\eta = 2\Delta q/(\hbar\omega)$ and an initial phase $\chi = \eta\cos\varphi_{\mathrm{mod}}$.

We now assume that the driving frequency is close to a parametric resonance, *i.e.* $\omega \sim 2q_0/(\hbar k_0)$ for some integer k_0, and that $q_0 \gg U_s$. All physical variables feature in general a large-amplitude secular motion occurring on time scales much longer than the modulation period, plus rapidly-varying terms oscillating at harmonics of $2q_0/\hbar$ that describe the micromotion. In the regime $q_0 \gg U_s$, the amplitude $\sim U_s/q_0$ of the micromotion of n_0 and α is small. Taking the time average over one period of the modulation, $\overline{\cdot} = \frac{1}{T}\int_0^T dt\cdot$, eliminates the micromotion in Eqs. (4.9,4.10),

$$\hbar\dot{\overline{n_0}} \approx 2U_s\overline{n_0}(1-\overline{n_0})\overline{\sin\theta}, \tag{4.36}$$

$$\hbar\dot{\overline{\alpha}} \approx 2U_s(1-2\overline{n_0})\left(1+\overline{\cos\theta}\right). \tag{4.37}$$

We compute the time average of trigonometric functions of θ using the Jacobi-Anger expansion, $e^{ia\sin(\theta)} = \sum_{k=-\infty}^{+\infty} J_k(a)e^{ik\theta}$, with J_k a Bessel function of the first kind. Neglecting the micromotion of α, we can write $\overline{e^{i\theta}} \approx e^{i\overline{\alpha}}\overline{e^{-2ip}}$, with

$$e^{-2ip} = \sum_{k=-\infty}^{+\infty} J_k(\eta)e^{i\left(-\frac{2q_0}{\hbar}+k\omega\right)t + ik(\phi_{\mathrm{mod}}+\pi/2)-i\chi}. \tag{4.38}$$

The term $k = k_0$ in the expansion gives rise to a slowly varying secular contribution, while all other terms average out over one period of the modulation. Neglecting the non-resonant terms, we obtain $\overline{e^{-2ip}} = \kappa e^{i\zeta(t)}$, with $\hbar\delta = 2q_0 - k_0\hbar\omega$, $\zeta(t) = k_0(\phi_{\mathrm{mod}} + \pi/2) - \chi - \delta t$ and $\kappa = J_{k_0}(\eta)$. This finally leads to

$$\overline{e^{i\theta}} \approx \kappa e^{i\phi} \tag{4.39}$$

where the secular phase $\phi = \zeta + \overline{\alpha}$ is defined as

$$\phi = -\delta t + \overline{\alpha} + k_0(\varphi_{\mathrm{mod}} + \pi/2) - \chi. \tag{4.40}$$

Eqs. (4.24,4.25) follow from Eqs. (4.36 to 4.40).

From Eq.(4.40), we can relate ϕ to the atomic phase, $\overline{\theta} = \phi - k_0(\omega t + \varphi_{\mathrm{mod}} + \pi/2)$. This equality shows that when ϕ is oscillating, θ also oscillates around the phase of the drive $-k_0(\omega t + \varphi_{\mathrm{mod}} + \pi/2)$, up to a constant.

Rigid Pendulum Model

In the weak driving regime, $\kappa \ll 1$, the $\kappa \cos\phi$ term in Eq. (4.25) is negligible. Moreover, the amplitude of variation of $\overline{n}_0$ is small. To prove the last point, we integrate Eqs. (4.24,4.25) and obtain the implicit equation $\left[g(x)\right]_{\overline{n}_{0,i}}^{\overline{n}_0(t)} = -\kappa\left[\cos x\right]_{\phi_i}^{\phi(t)}$, with $g(x) = \left(1 - \frac{\hbar\delta}{2U_s}\right)\ln\left(\frac{x}{1-x}\right) + 2\ln(1-x)$. This implies that the amplitude of variation of $\overline{n}_0$ is indeed small when $\kappa \ll 1$. This allows us to linearize Eq. (4.24).
With the initial condition $n_{0,i} = 1/2$, we obtain $\hbar\dot{\overline{n}}_0 \simeq \frac{\kappa U_s}{2}\sin\phi$. Taking the time derivative of Eq. (4.25), we then find that the phase obeys the pendulum equation

$$\ddot{\phi} + \Omega^2 \sin\phi = 0\,, \tag{4.41}$$

with natural frequency $\Omega = \sqrt{2\kappa}U_s/\hbar$. The angular velocity of the pendulum $\dot{\phi}$ is determined by $\dot{\phi} = -\delta + 2U_s(1 - 2\overline{n}_0)$.

Energy balance

In this Section, we compute the power delivered by the drive in the framework of DM 2. In particular, we show that at the fixed points $S_\pm$, it compensates for the dissipated energy. For simplicity, we focus on the first resonance $k_0 = 1$ and assume $\kappa \ll 1$. The time derivative of the total energy is

$$\frac{dE_{\text{spin}}}{dt} = \mathcal{P}_{\text{drive}} + \mathcal{P}^{(2)}_{\text{diss}}\,, \tag{4.42}$$

with $\mathcal{P}_{\text{drive}} = -\dot{q}n_0$, and $\mathcal{P}^{(2)}_{\text{diss}} = -\frac{\hbar}{2}\beta_2 n_0(1-n_0)\dot{\theta}^2$. We introduce $\tilde{n}_0$, the component of n_0 oscillating at $\sim \omega$. The product $\dot{q}\tilde{n}_0$ does not vanish after taking the time-average in the expression for $\mathcal{P}_{\text{drive}}$.

From Eq. (4.38), the $k = 0$ component of $\sin\theta$ oscillating at $\sim \omega$ is $\widetilde{\sin\theta} = -\cos(\omega t + \varphi_{\text{mod}} - \phi)$. The amplitude of the sidebands near-resonant with the drive [term $k = 2$ in Eq. (4.38)] are negligible in the limit $\kappa \ll 1$. Using $\tilde{n}_0 = \mathcal{O}(U_s/q_0) \ll 1$ to simplify Eq. (4.9), we find

$$\tilde{n}_0 = -\frac{2U_s}{\hbar\omega}\overline{n}_0(1-\overline{n}_0)\sin(\omega t + \varphi_{\text{mod}} - \phi)\,. \tag{4.43}$$

Using $\kappa \simeq \Delta q/(\hbar\omega)$ (true if $\kappa \ll 1$), the average power delivered by the drive is finally

$$\overline{\mathcal{P}}_{\text{drive}} = -\omega\kappa U_s\overline{n}_0(1-\overline{n}_0)\sin\phi\,. \tag{4.44}$$

When there is no dissipation, this expression can be written as $\overline{\mathcal{P}}_{\text{drive}} = -\hbar\omega\dot{\overline{n}}_0/2$. This result has a microscopic interpretation if one treats the driving field as a quantized electromagnetic field. One photon is absorbed to promote a pair of atoms in the $m = 0$ state to a pair with one atom in $m = +1$ and another in $m = -1$. The energy in the field is, up to a constant, $E_{\text{field}} = N\hbar\omega n_0/2$, and $\overline{\mathcal{P}}_{\text{drive}}$ correspond to the energy per unit time transferred back and forth from the field to the atoms. Eq. (4.42) can also be interpreted as a statement that $N\overline{E}_{\text{spin}} + \overline{E}_{\text{field}}$ is constant.

With dissipation, the system relaxes to the fixed point S_+ or to S_0. The second case is trivial, since the drive and dissipated power both vanish. Let us discuss the first case. At the fixed points S_+, the atomic phase is locked to the drive, *i.e.* $\dot{\theta} \approx -\omega$ and $\overline{\mathcal{P}}^{(2)}_{\text{diss}} \approx -\frac{\hbar\omega^2}{2}\beta_2\overline{n}_0(1-\overline{n}_0)$. The energy balance can be rewritten as

$$\left.\frac{dE_{\text{spin}}}{dt}\right|_{S_+} \approx -\omega\overline{n}_0(1-\overline{n}_0)\left[\kappa U_s\sin\phi_+ + \frac{\beta_2\hbar\omega}{2}\right]\,, \tag{4.45}$$

The term in brackets in the right hand side of Eq. (4.45) vanishes exactly, as the secular phase takes the value $\sin\phi_+ = -\beta_2\hbar\omega/(2\kappa U_s)$ at S_+ (see Sec. 4.4.2). At the fixed point, the phase lag between the atomic phase and the drive is therefore such that the power delivered by the drive exactly compensates for the energy dissipation.

4.6.5 Quantum treatment of the modulated SMA Hamiltonian

We start from the SMA Hamiltonian in Eq. (4.2), which we rewrite as

$$\hat{H}_{\text{spin}} = -q(t)\hat{N}_0 + \frac{U_s}{2N}\left(\hat{V} + \hat{W} + \hat{W}^\dagger\right).$$

We defined the operators $\hat{V} = \hat{S}_z^2 + 2\hat{N}_0(N - \hat{N}_0)$ and $\hat{W} = 2(\hat{a}_0^\dagger)^2\hat{a}_{+1}\hat{a}_{-1}$. Applying the unitary transformation

$$\hat{U}_1 = e^{-i\int_0^t \frac{q(t')dt'}{\hbar}\hat{N}_0} = e^{-ip\hat{N}_0}, \tag{4.46}$$

the transformed Hamiltonian is

$$\hat{H}_1 = \hat{U}_1 \hat{H} \hat{U}_1^\dagger + i\hbar \frac{d\hat{U}_1}{dt} \hat{U}_1^\dagger \,, \tag{4.47}$$

$$\hat{H}_1 = \frac{U_\mathrm{s}}{2N} \left[\hat{V} + \hat{U}_1 \left(\hat{W} + \hat{W}^\dagger \right) \hat{U}_1^\dagger \right] . \tag{4.48}$$

We introduce the Fock basis $|N_0, M_z\rangle$ with $N_{\pm 1} = (N - N_0 \pm M_z)/2$. The operators $\hat{W}$ (respectively $\hat{W}^\dagger$) only couples states with $M_z = M_z'$ and $N_0 = N_0' + 2$ (resp. $N_0 = N_0' - 2$). As a result, the matrix elements of $\hat{U}_1 \hat{W} \hat{U}_1^\dagger$ in the Fock basis are the same as the ones of $e^{-2ip}\hat{W}$, implying the equality of both operators.

We now derive an effective Hamiltonian describing the slow secular dynamics. We proceed as in Section 4.6.4, using the Jacobi-Anger expansion to rewrite the phase factors and taking the time average over one period of the modulation assuming small detuning δ. We obtain an effective time-averaged Hamiltonian,

$$\overline{\hat{H}_1} = \frac{U_\mathrm{s}}{2N} \hat{V} + \frac{\kappa U_\mathrm{s}}{2N} \left(e^{i\zeta(t)} \hat{W} + e^{-i\zeta(t)} \hat{W}^\dagger \right) . \tag{4.49}$$

We finish the calculation with a second unitary transformation $\hat{U}_2 = e^{-i\frac{\zeta(t)}{2}\hat{N}_0}$ to obtain an effective time-independent Hamiltonian

$$\hat{H}_\mathrm{eff} = -\frac{\hbar\delta}{2} \hat{N}_0 + \frac{U_\mathrm{s}}{2N} \hat{V} + \frac{\kappa U_\mathrm{s}}{2N} \left(\hat{W} + \hat{W}^\dagger \right) . \tag{4.50}$$

With a mean-field *ansatz* for the many-body spin state, we obtain from this effective Hamiltonian the same secular energy E_sec [Eq. (4.29)] as in the classical treatment, *i.e.* mean-field approximation and time averaging can be done in any order.

4.6.6 Stability of the stationary solutions of dissipative model 2.

Stability of the fixed points $S_\pm$

To discuss the stability of the fixed points $S_\pm$, we linearise Eqs. (4.32,4.25) using $\overline{n_0} = \overline{n}_{0,\pm} + \delta\overline{n}_{0,\pm}$ and $\phi = \phi_\pm + \delta\phi_\pm$. We find

$$\hbar \begin{pmatrix} \delta\dot{\overline{n}}_{0,\pm} \\ \delta\dot{\phi}_\pm \end{pmatrix} = M_\pm \begin{pmatrix} \delta\overline{n}_{0,\pm} \\ \delta\phi_\pm \end{pmatrix} , \tag{4.51}$$

$$M_\pm = \begin{pmatrix} 0 & \pm 2\kappa U_\mathrm{s} n_{0,\pm}(1 - n_{0,\pm}) \cos\epsilon \\ -2\hbar\delta_\pm & -2\kappa U_\mathrm{s} \frac{\delta}{\delta_\pm} \sin\epsilon \end{pmatrix} .$$

The solutions are stable if the eigenvalues of the matrices $M_\pm$ have negative real parts. For simplicity, we consider the situation $|\sin\epsilon| = \beta_2\hbar\omega/(2\kappa U_\mathrm{s}) \ll 1$. One can show that the results below hold as long as $\beta_2\hbar\omega/(2\kappa U_\mathrm{s}) < 1$, the same condition as for the existence of the fixed points.

In the limit $\epsilon \ll 1$, the eigenvalues of M_+ are approximately given by $X_{+,1} \simeq \beta_2\hbar\omega\frac{\delta}{2\delta_+} + i\sqrt{\Delta}$, and $X_{+,2} = X_{+,1}^*$, with $\Delta = 8\overline{n}_{0,+}(1 - \overline{n}_{0,+})\kappa(1+\kappa)U_\mathrm{s}^2$. Therefore, S_+ is stable for $\delta < 0$, and unstable otherwise. Turning to S_-, the eigenvalues are $X_{-,1} \simeq \sqrt{\Delta}$ and $X_{-,2} \simeq -X_{-,1}$ to leading order in β_2, and S_- is therefore always unstable. Note that our conclusions are established for the experimentally relevant case $0 \leq \kappa < 1$. The roles of $S_\pm$ would be reversed for $\kappa < 0$.

Stability of the limit cycles $S_{0,1}$

We focus first on S_1. We consider small deviations, *i.e.* $\overline{n}_0 = 1 - \epsilon$ and linearize Eqs. (4.32,4.25) to the lowest order in ϵ,

$$-\hbar\dot{\epsilon} = 2\kappa U_\mathrm{s} \sin\phi\epsilon + 2\beta_2 q_0 \epsilon \,, \tag{4.52}$$

$$\hbar\dot{\phi} = -\hbar\delta - 2U_\mathrm{s}(1 + \kappa\cos\phi) \,. \tag{4.53}$$

We integrate Eq. (4.52),

$$\left[\ln\epsilon\right]_{\epsilon(0)}^{\epsilon(t)} = -\frac{2\kappa U_\mathrm{s}}{\hbar} \int_0^t \sin\phi(t')dt' - \frac{2\beta_2 q_0 t}{\hbar}.$$

Making the change of variable $t \to \phi$ and using Eq. (4.53), we find

$$\epsilon(t) = \epsilon(0) e^{-4t/\tau_2} \frac{1 + a_1\cos\phi(0)}{1 + a_1\cos\phi(t)}, \tag{4.54}$$

$$\hbar\dot{\phi} = -(2U_s + \hbar\delta)(1 + a_1\cos\phi(t)) \,. \tag{4.55}$$

with $a_1 = 2\kappa U_\mathrm{s}/[2U_\mathrm{s} + \hbar\delta]$ and $\tau_2 = 2\hbar/(\beta_2 q_0)$. If $|a_1| < 1$, ϵ is bound to a vincinity of $\epsilon(0)$. If $|a_1| > 1$, eq. (4.55) shows that ϕ must vanish, which results in a divergency of ϵ. Therefore, $\epsilon(t)$ diverges iif $|a_1| > 1$. This defines the instability region of S_1 as $\delta \in [-2U_\mathrm{s}(1+\kappa), -2U_\mathrm{s}(1-\kappa)]$. This result is independent of the precise value of β_2 as long as it is strictly positive. A similar calculation for S_0 with $\epsilon = \overline{n}_0$ yields

$$\epsilon(t) = \epsilon(0) e^{4t/\tau_2} \frac{1 + a_0 \cos\phi(0)}{1 + a_0 \cos\phi(t)}, \tag{4.56}$$

with $a_0 = 2\kappa U_\mathrm{s}/[2U_\mathrm{s} - \hbar\delta]$. Due to the exponential divergency, we find that S_0 is always unstable.

End of the article [45]

4.7 Outlook: chaotic dynamics

In the mean-field approximation, our system is described by the two variables (n_0,θ). In the static situation, energy is conserved (here we ignore the dissipation), and spin-mixing trajectories correspond to equal-energy contours. Given that the energy is a smooth function of (n_0,θ), two trajectories that are arbitrarily close cannot diverge, and hence chaos cannot occur. To be more general, the Poincaré-Bendixson theorem forbids chaos in two dimensions for an isolated system. When we drive the dynamics, the energy is no longer conserved which opens the possibility for chaotic behaviors. In the secular approximation, we obtained a new conserved quantity, the secular energy given by Eq. (4.29), such that chaos is again excluded. The conditions of validity of the secular approximation reads $2q_0 \gg U_s$. We show in figure 35 Poincaré maps consisting of the series of points $[n_0(t_n), \theta(t_n)]$, where $t_n = n2\pi/\omega$ and n is an integer. We compute numerically several maps corresponding to different ratios q_0/ω. When the secular approximation holds, the map corresponds to smooth lines, whereas for a chaotic behavior one expects a diffuse cloud of points. We have chosen $\omega = 5U_s$, and we have plotted the Poincaré maps for various q_0, keeping $q_0 = \Delta q$. This is close to the situation realized in the experiment of figure 26c. For the largest q_0 we observe smooth maps but for $2q_0/\omega \lesssim 1$ we observe a chaotic behavior. In particular, for the first resonance $2q_0/\omega = 1$, we observe closed trajectories in the middle of the map (oscillating regime), open trajectories on the edges $n_0 \simeq 1$ and $n_0 \simeq 0$ (running phase), and a small chaotic region near the separatrix. This region becomes smaller for higher resonances, as the secular approximation is better verified. The onset of chaos in a very similar system, a driven two-component spinor BEC, has been observed in [150].

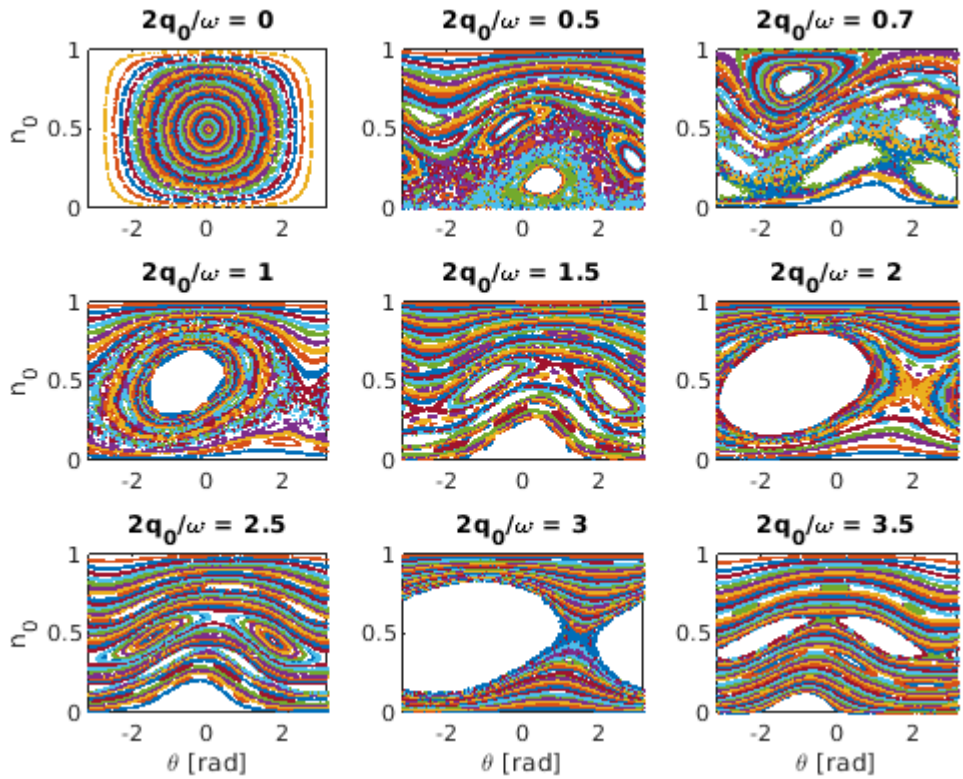

Figure 35: Poincaré maps, for various $q_0 \simeq \Delta q$ (the first panel correspond to $q_0 = \Delta q = 0$). Here $\omega \simeq 5U_s$. A map is obtained by numerically solving the dynamics for different initial conditions (here $n_0(0)$ variable and $\theta(0) = 0$) and reporting with different colors the series $[n_0(t_n), \theta(t_n)]$ that we obtained. White areas in the map are simply regions that are not accessed given the chosen set of initial conditions.

Phase space portraits are only meaningful for classical systems. Indeed, the Heisenberg uncertainty principle implies that a quantum state cannot be represented by a point in phase space. Yet, it is possible to get a qualitative insight from a semi-classical picture, where a "quantum trajectory" is obtained by averaging nearby classical trajectories represented in a phase portrait. In a chaotic regime, two initially close trajectories can diverge, and one expects the generation of highly non-classical states, making this situation particularly worthy of further studies. In a non-chaotic system, the semi-classical picture hints to instabilities as good levers to produce non-classical states. This is the approach we pursue in the next chapter.

Chapter 5

Beyond the mean-field dynamics: spin-squeezing and quantum fluctuations

In Chapter 2, we studied the phase diagram of a spinor Bose-Einstein condensate embedded in a magnetic field, in the single mode regime [28, 29, 55]. For a cloud with vanishing magnetization, a quantum phase transition occurs when the quadratic Zeeman energy (QZE) q goes through zero. For $q > 0$ the mean field ground state has all atoms in $m = 0$, *ie* it is the nematic state $|N : \mathbf{e}_z\rangle$ aligned along the magnetic field axis z. For $q < 0$ all the nematic states lying in the (xy)-plane are degenerate and minimize the mean-field energy. At the critical point $q = 0$, all nematic states are degenerate.

The vicinity of the phase transition, where the antiferromagnetic interaction energy U_s is the dominant energy scale, constitutes an ideal regime to observe deviations to the mean-field picture. Indeed, we have seen in Chapter 2 that the ground state for $q \ll U_s$ is entangled. Qualitatively, the effect of interactions can be understood in terms of quantum fluctuations, which mix the degenerate coherent states. For instance at $q = 0$ the ground state corresponds to a coherent superposition with equal weight of all the degenerate nematic states $|N : \mathbf{\Omega}\rangle$. Quantum fluctuations can also seed spin-mixing dynamics in situations where a mean-field treatment predicts no evolution. For instance, the nematic state $|N : \mathbf{e}_z\rangle$ is a fixed point of the mean-field spin-mixing equations (used in Chapter 4) for all q, and yet, we observe significant dynamics after a quench through ($q < 0$), or near ($0 < q \ll U_s$) the phase transition. These two situations, represented schematically in Fig. 36, and the resulting beyond mean-field spin mixing are the subjects of the present chapter.

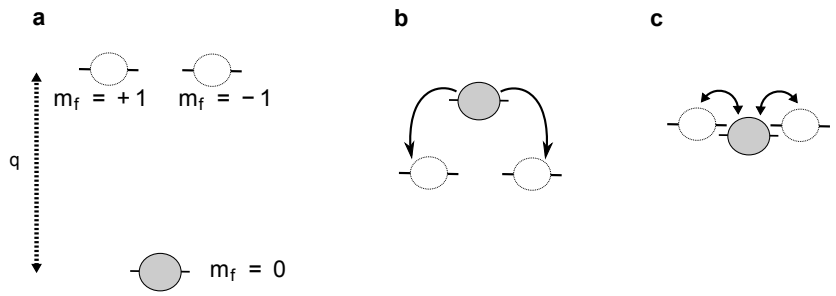

Figure 36: Sketch of the quadratic Zeeman energies. The initial situations correspond to a BEC with all atoms in $m = 0$, in a large magnetic field, so that $q \gg U_s$ and the system is very close to the ground state (a). Modulating near a Shapiro resonance, an effective negative QZE is created and the BEC becomes unstable (b). Correlated pairs are produced in the initially empty $m = \pm 1$ modes. Alternatively, reversible pair production can be realized in the stable regime, when $q \ll U_s$ (c).

We will first study quenches through the phase transition. We make use of the driving technique described in Chapter 4 to realize an effective negative QZE. In that case the nematic state $|N : \mathbf{e}_z\rangle$ becomes unstable. Within a Bogoliubov approximation, our system is analogous to the optical parametric amplifier [32]. More precisely, we realize a situation close to spontaneous parametric down-conversion. In that set-up, a nonlinear crystal is used to generate pairs of correlated photons, in two different, initially empty modes, from photons in a so called pump-mode. This process creates the two-mode squeezed vacuum (TMSV) state, an entangled state that can out-performed classical states in interferometric experiments [69]. Owing to this remarkable property, squeezed states of light [32], such as the TMSV, are the subject of many investigations and an exciting potential application is the improvement on the sensitivity of gravitational wave interferometers [151, 152]. Similarly, there has been recently a lot of efforts to produce squeezed states of atomic ensembles [9–11], which could be used, *e.g.* for clocks or inertial sensors. On that line of thoughts, we will put in the first part the emphasis on squeezing, and on its relation to entanglement. We will also comment on the similarities and differences between the optical and atomic parametric amplifiers.

The study of quenches to the critical region, just above the phase transition ($0 < q \ll U_s$) provides new insights on the nature of the state produced by via spin-mixing. Indeed, in this regime, the dynamics is reversible, which allows us to demonstrate

coherence and entanglement between the modes. We also study the effect of a coherent seed on the dynamics. These last experiments show the role of the quantum fluctuation for seeds that are small enough, and allow for the observation of the cross-over from the Bogoliubov to the mean-field regimes as the size of the seed increases.

5.1 Spin squeezed state

Squeezed states are a class of entangled states that have been extensively studied theoretically and experimentally. They can be produced in several platforms ranging from optics [32] to atomic gases [9], and can outperform classical states in interferometric experiments. In this section, we briefly review different definitions of squeezed states. We start with the case of a single bosonic mode, describing $e.g.$ a mode of the electromagnetic field. The case of several modes, which correspond to our system, is more complex, and various definitions of squeezing are encountered in the literature (see $e.g.$ [9] for a review).

5.1.1 Squeezing of a single bosonic mode

We consider a bosonic mode $\hat{a}$, and the two conjugated observables

$$\hat{X} = \frac{1}{\sqrt{2}}(\hat{a}^\dagger + \hat{a}) \,, \qquad \text{and} \qquad \hat{P} = \frac{i}{\sqrt{2}}(\hat{a}^\dagger - \hat{a}) \,. \tag{5.1}$$

The Heisenberg relation reads

$$\Delta X \Delta P \geq \frac{1}{2} \,. \tag{5.2}$$

A coherent state, defined as an eigenstate of $\hat{a}$, is considered as a semi-classical state of a harmonic oscillator. Indeed, in a coherent state, the expectation values of the position and momentum observables obey to classical equations of motion [51]. Moreover, their variances are equal, and saturate the Heisenberg uncertainty relation, $\Delta X = \Delta P = 1/\sqrt{2}$. This value is refereed to as the shot noise. A state that has ΔX or ΔP below the shot noise is called a squeezed state. The uncertainty relation implies that when an observable is squeezed, its conjugate is "anti-squeezed" and displays fluctuations above the shot noise.

5.1.2 Spin squeezing of two bosonic modes

We now consider two bosonic modes $\hat{a}_{+1}$ and $\hat{a}_{-1}$. We define the collective pseudo-spin operator $\hat{\mathbf{J}}$

$$\hat{J}_x = \frac{1}{2}(\hat{a}^\dagger_{+1}\hat{a}_{-1} + \hat{a}^\dagger_{-1}\hat{a}_{+1}) \,, \quad \hat{J}_y = \frac{1}{2i}(\hat{a}^\dagger_{+1}\hat{a}_{-1} - \hat{a}^\dagger_{-1}\hat{a}_{+1}) \,, \quad \hat{J}_z = \frac{1}{2}(\hat{N}_{+1} - \hat{N}_{-1}) \,. \tag{5.3}$$

These operators fulfill the angular momentum commutation relations and $\hat{\mathbf{J}}$ can be viewed as the total angular momentum of an ensemble of identical bosons carrying a (pseudo) spin-1/2. We have $\hat{\mathbf{J}}^2 = \hat{N}_p(\hat{N}_p + 1)$ where $\hat{N}_p = (\hat{N}_{+1} + \hat{N}_{-1})/2$. One Heisenberg relation reads

$$\Delta J_x \Delta J_y \geq \frac{|\langle \hat{J}_z \rangle|}{2} \,. \tag{5.4}$$

Two other relations are obtained by permutation of the indices. A spin coherent state of N particles is a pure state with no correlation between the particles. For an ensemble of pseudo-spin 1/2 bosons, a coherent state can be seen as a state with all pseudo-spins pointing in the same direction, for instance z. In that case we have

$$|J_z| = \frac{N}{2} \qquad \text{and} \qquad \Delta J_x^2 = \Delta J_y^2 = \frac{N}{4} \,. \tag{5.5}$$

This is analogous to the one-mode case: the Heisenberg bound Eq. (5.4) is saturated and the uncertainty is equally distributed between $\hat{J}_x$ and $\hat{J}_y$. However, this analogy holds only for our arbitrary choice of axis, the other two Heisenberg relations are trivially verified since $\langle \hat{J}_x \rangle = \langle \hat{J}_y \rangle = 0$.

Kitagawa and Ueda proposed in [153] the following definition of spin squeezing: a state is squeezed if and only if the variance of one spin component orthogonal to the mean spin, is below $\frac{N}{4}$. Let z be the direction of the spin, and x the orthogonal direction with minimal spin fluctuations. A squeezing parameter can be defined as

$$\xi_{KU} = \frac{2\Delta J_x}{\sqrt{N}} \,. \tag{5.6}$$

For coherent states, $\xi_{KU} = 1$, and thus spin-squeezing in the sense of [153] indicates correlations between the spins (or entanglement).

5.1.3 Metrological spin squeezing

Alternatively, the question of the squeezing of two or more modes can be addressed from the point of view of quantum metrology. It is a broad field, and we only sum up here some results important for our topic and refer the reader to [9] for a review. The two following results constitute the corner stone of quantum metrology. First, there exists a fundamental bound on the accuracy at which a measurement can be made. Second, this bound is not the same for separable and entangled states. To be more explicit, let us consider a measurement described by a (pseudo) spin rotation of angle θ, corresponding for instance to the phase shift inside a Mach-Zehnder interferrometer. We want to determine θ from the measurement of the observable $\hat{\mathcal{O}}$. In Heisenberg representation, $\hat{\mathcal{O}}$ evolves over a rotation around the y-axis as $|\frac{d\langle\hat{\mathcal{O}}\rangle}{d\theta}| = |[\hat{J}_y, \hat{\mathcal{O}}]|$. The Heisenberg inequality sets an upper bound on the signal

$$|\frac{d\langle\hat{\mathcal{O}}\rangle}{d\theta}| \leq 2\Delta J_y \Delta\mathcal{O}\,. \tag{5.7}$$

Furthermore, using error propagation, the sensitivity is

$$\Delta\theta = \frac{\Delta\hat{\mathcal{O}}}{|\frac{d\langle\hat{\mathcal{O}}\rangle}{d\theta}|}\,, \tag{5.8}$$

$$\Delta\theta \geq \frac{1}{2\Delta J_y}\,. \tag{5.9}$$

For a coherent state, the sensitivity is maximal, when the spin points in the (xz)-plane, in which case, $(\Delta J_y)^2$ is maximal and equal to $\frac{N}{4}$. This sets the "standard quantum limit" (SQL) for separable states. The SQL is not fundamental, an upper bound on $(\Delta J_y)^2$ is $\langle\hat{\mathbf{J}}^2\rangle \simeq N^2/4$, which defines the fundamental Heisenberg limit (HL). It can be reached using the "Schrödinger cat state" defined as the coherent superposition of all spins up and all spins down, with respect to the y axis. In the spin state basis $|j, m_y\rangle_y$ with y as the quantization axis

$$|\psi_{\text{cat}}\rangle = \frac{1}{\sqrt{2}}(|N, N\rangle_y + |N, -N\rangle_y)\,. \tag{5.10}$$

We emphasize that Eq. (5.9) only provides a lower bound to the sensitivity, and states with large ΔJ_y ($e.g.$ statistical mixtures), do not necessarily saturate the bound. However, the Schrödinger cat state does reach the lower limit given by Eq. (5.9), using a parity measurement [9]. The sensitivities at the SQL and HL are given by

$$\Delta\theta_{\text{SQL}} = \frac{1}{\sqrt{N}}\,, \qquad \Delta\theta_{\text{HL}} = \frac{1}{N}\,. \tag{5.11}$$

These two limits can be derived with greater generality [9]. For a given interferometric set-up (including an initial quantum state, a phase imprinting and a measurement), with sensitivity $\Delta\theta$, we can define a metrological squeezing parameter as

$$\xi_m = \frac{\Delta\theta}{\Delta\theta_{\text{SQL}}}\,. \tag{5.12}$$

It quantifies the improvement relatively to the SQL. As such, $\xi_m < 1$ indicates entanglement. The Heisenberg limit reads $\xi_m \geq \frac{1}{\sqrt{N}}$. Note that ξ_m not only depends on the state, but also on the experimental context, and for a given context, there may be states that are not squeezed although they could beat the SQL in another context ($e.g.$, measuring another observable). One paradigmatic set-up is the Ramsey interferometer, used for instance in atomic clocks. It is studied in detail in [154]. In that setting, the squeezing parameter is

$$(\xi_m)_{\text{Ramsey}} = \frac{\sqrt{N}\Delta J_\perp}{J_{\mathbf{u}}}\,, \tag{5.13}$$

where $\mathbf{u}$ indicates the direction of the mean spin and $\Delta J_\perp$ is the minimum of the variance of the spin in an orthogonal direction (and the rotation axis is orthogonal to both).

5.1.4 Entanglement and spin squeezing

Metrological spin squeezing indicates entanglement, but the converse is not true. For instance, the squeezing criterion ξ_{KU} (see Eq. [5.6]) introduced by Kitagawa and Ueda to detect correlations between particles ($i.e.$ entanglement) is not directly linked to metrological improvements [9]. Following this work, various spin squeezing parameters have been introduced to detect entanglement [155, 156], and used in spinor BECs experiments [10, 157, 158]. They are appealing from the point of view of experiments, since they only rely on the measurement of the mean and variance of spin observables. This contrasts with the entanglement entropy defined in chapter 2 which *a-priori* requires the knowledge of the full quantum state. On the other hand, spin squeezing parameters only detect some entangled states and do not constitute a general measure of entanglement, while the entanglement entropy does [71].

Squeezing of an unpolarized state Let us consider the twin-Fock state (TFS), defined as an N particle states, with exactly $N/2$ particles in two orthogonal modes (in our case $m = \pm 1$). In the number basis $|N_{+1}, N_{-1}\rangle_{\rm nb}$, it is defined as

$$|\mathrm{TFS}\rangle = |\frac{N}{2}, \frac{N}{2}\rangle_{\rm nb} \,. \tag{5.14}$$

As seen in Chapter 2, this state is entangled and can be used to perform interferometry below the SQL (and with an Heisenberg scaling, see [69] and App. D). However, the TFS is an unpolarized state, that is to say $\langle \hat{\mathbf{J}}\rangle_{\rm TFS} = 0$, and thus, the squeezing parameters ξ_{KU} and $(\xi_m)_{\rm Ramsey}$ are ill-defined. The same problem occurs for the two-mode squeezed vacuum state (TMSV), defined in the number basis as

$$|\mathrm{TMSV}\rangle = \frac{1}{\sqrt{\mathcal{N}}} \sum_{n=0}^{\infty} \eta^n |n, n\rangle_{\rm nb} \,, \tag{5.15}$$

with $\mathcal{N} = 1 + \langle \hat{N}_p\rangle$ and $|\eta|^2 = \langle \hat{N}_p\rangle/(1 + \langle \hat{N}_p\rangle)$.

A generalized squeezing parameter appropriate to detect the entanglement of unpolarized states, such as the TFS and the TMSV was introduced in [156],

$$\zeta_s^2 = \frac{2\langle \hat{N}_p\rangle \Delta \hat{J}_z^2}{\langle \hat{J}_x^2 + \hat{J}_y^2\rangle - \langle \hat{N}_p\rangle} \,. \tag{5.16}$$

$\zeta_s < 1$ indicates entanglement. For a coherent state $\zeta_s = 1$, while for the TFS or TMSV states, $\zeta_s = 0$. We recall that a metrological squeezing parameter is bounded from below by the Heisenberg limit $\xi_m^2 > 1/N$ and thus ζ_s^{-1} cannot be seen as a metrological gain. However, we show in the appendix D how ζ_s is related to the sensitivity of an interferometric experiment using a TMSV state.

The criterion (5.16) applies to any collective spin. In our situation, the collective spin corresponds to the total pseudo spin of an ensemble of indistinguishable spin-1 atoms in the same spatial mode, and is defined in Eq. (5.3). In that case $\langle \hat{\mathbf{J}}^2\rangle = \langle \hat{N}_p(\hat{N}_p + 1)\rangle \simeq \langle \hat{N}_p^2\rangle$. Furthermore, for the squeezed states we produced experimentally, that are close to a TMSV state, we have $\langle \hat{N}_p^2\rangle \simeq 2\langle \hat{N}_p\rangle^2$, and $\langle \hat{J}_z^2\rangle \ll \langle \hat{J}_x^2 + J_y^2\rangle$, so that

$$\langle \hat{J}_x^2 + \hat{J}_y^2\rangle = \langle \hat{N}_p^2\rangle + \langle \hat{N}_p\rangle =\simeq 2\langle \hat{N}_p\rangle^2 + \langle \hat{N}_p\rangle \,, \tag{5.17}$$

and the squeezing parameter takes the simple form

$$\zeta_s^2 \simeq \frac{\Delta \hat{J}_z^2}{\langle \hat{N}_p\rangle} \,. \tag{5.18}$$

We emphasize that Eq. (5.18) is derived for a state with $\langle \hat{N}_p^2\rangle \simeq 2\langle \hat{N}_p\rangle^2$, and does not hold for a coherent state with $\langle \hat{N}_p^2\rangle \simeq \langle \hat{N}_p\rangle^2$.

5.2 Bogoliubov treatment of the dynamics

5.2.1 Undepleted pump approximation

In this section, we theoretically study the spin-mixing dynamics of a spinor BEC in the single mode regime. We focus first on the situation where the initial state is the nematic coherent state $|N : \mathbf{e}_z\rangle$ with all atoms in the Zeeman sublevel $m = 0$. This state is a fixed point of the mean-field equations of motion (see Chapter 4). However, a more refined treatment based on Bogoliubov theory, shows that quantum fluctuations triggers a significant dynamics when the mean-field energy of the states $m = \pm 1$ is close to the energy of the $m = 0$ state, either slightly above or slightly below. The former situation can be achieved at low magnetic field, such that $q \ll U_s$. The latter requires a negative effective QZE, which can be achieved using an oscillating magnetic field, as demonstrated in Chapter 4. We have realized both situations experimentally, and we consider the generic Hamiltonian

$$\hat{H}_{\rm SMA} = -q'\hat{N}_0 + \frac{U_s}{N}\hat{N}_0(N - \hat{N}_0) + \frac{W}{N}(\hat{a}_0^2\hat{a}_{+1}^\dagger\hat{a}_{-1}^\dagger + \hat{a}_0^{\dagger 2}\hat{a}_{+1}\hat{a}_{-1}) \,. \tag{5.19}$$

In the static situation $q' = q$ is the QZE and $W = U_s$. In the driven case, $q' = \hbar\delta/2$ and $W = \kappa U_s$ where

$$\hbar\delta = 2q_0 - k_0\hbar\omega \qquad \text{and} \qquad \kappa = J_{k_0}\left(\frac{2\Delta q}{\hbar\omega}\right) \,, \tag{5.20}$$

with q_0 the mean QZE, ω and Δq the frequency and amplitude of the modulation, k_0 the index of the Shapiro resonance and J_{k_0} the Bessel function (see Chapter 4, Sec. 4.3.1)

The exchange term $\hat{a}^\dagger_{+1}\hat{a}^\dagger_{-1}\hat{a}^2_0$ reminds one of optical four wave mixing, where it accounts for the conversion in a non-linear crystal, of a pair of photons here in the same "pump" mode, into two photons in different "output" modes. In analogy, we will call the $m = 0$ mode the pump and the $m = \pm 1$ modes the output modes. In this context, the Bogoliubov approximation is often referred to as the "undepleted pump approximation" (UPA). It amounts to take the pump mode as a classical source, using the substitutions (with no loss of generality, we take the phase of the pump to be zero)

$$\hat{a}_0 \to \sqrt{N - \hat{N}_{+1} - \hat{N}_{-1}}\,, \tag{5.21}$$

and conserving only the quadratic terms in $\hat{a}_{\pm 1}$. It yields

$$\hat{H} = V\left(\hat{N}_{+1} + \hat{N}_{-1}\right) + W\left(\hat{a}_{+1}\hat{a}_{-1} + \hat{a}^\dagger_{+1}\hat{a}^\dagger_{-1}\right)\,. \tag{5.22}$$

with $V = q' + U_s$.

5.2.2 Equation of evolution

The calculation of the mean value of few-body operator can be simply done in the Heisenberg picture. The equation of evolution for the operators $\hat{a}_{+1}$ and $\hat{a}^\dagger_{-1}$ form a closed system

$$i\hbar\frac{d}{dt}\begin{pmatrix}\hat{a}_{+1}\\ \hat{a}^\dagger_{-1}\end{pmatrix} = \begin{pmatrix} V & W\\ -W & -V\end{pmatrix}\begin{pmatrix}\hat{a}_{+1}\\ \hat{a}^\dagger_{-1}\end{pmatrix} \tag{5.23}$$

This system has two opposite eigenvalues $\pm\hbar\omega_B$, with

$$\hbar\omega_B = \sqrt{V^2 - W^2}\,. \tag{5.24}$$

When $\hbar\omega_B$ is real, it corresponds to the energy of Bogoliubov excitation (see Chapter 2). However, we emphasize that the calculation holds for all V and W, and in particular, in the window

$$-|W| < V < |W|\,, \tag{5.25}$$

where ω_B is an imaginary number. This corresponds to an unstable regime as will be shown by the calculation of the evolution of $\langle\hat{N}_{\pm 1}\rangle$. Integration of Eq. (5.23) yields

$$\hat{a}_\pm(t) = A^*\hat{a}_{\pm,i} + B^*\hat{a}^\dagger_{\mp,i}\,, \tag{5.26}$$

where

$$A^*(t) = \cos(\omega_B t) + i\frac{V}{\hbar\omega_B}\sin(\omega_B t)\,, \tag{5.27}$$

$$B^*(t) = i\frac{W}{\hbar\omega_B}\sin(\omega_B t),\,. \tag{5.28}$$

Note that when ω_B is imaginary, the sine becomes hyperbolic sine with arguments $|\omega_B|t$.

5.2.3 Evolution of the vacuum

General results From Eq.(5.26), we can compute the mean value and variance of the number of pairs $\hat{N}_{+1}$, starting from the nematic state $|N : \mathbf{e}_z\rangle$, *ie* from the vacuum of $m_F = \pm 1$ atoms. We obtain

$$\langle\hat{N}_{+1}\rangle_{\text{vac}} = \frac{W^2}{\hbar^2\omega_B^2}\sin^2(\omega_B t)\,, \tag{5.29}$$

$$(\Delta\hat{N}_{+1})^2_{\text{vac}} = \langle\hat{N}_{+1}\rangle_{\text{vac}}(1 + \langle\hat{N}_{+1}\rangle_{\text{vac}})\,, \tag{5.30}$$

We recall that the magnetization $\hat{S}_z = \hat{N}_{+1} - \hat{N}_{-1}$ is conserved and remains exactly zero, so does $\hat{J}_z = \hat{S}_z/2$, and the pseudo-spin $\hat{\mathbf{J}}$ is thus perfectly squeezed according to the criterion (5.18). More precisely, the state evolves into a TMSV [33], defined in Eq. (5.15), and which features a thermal distribution of the number of atoms in the output modes $m = \pm 1$.

Unstable regime Let us focus on the driven situation. We have $V = \hbar\delta/2 + U_s$ and $W = \kappa U_s$. The Bogoliubov energy is

$$\hbar\omega_B = \sqrt{\left[\frac{\hbar\delta}{2} + (1-\kappa)U_s\right]\left[\frac{\hbar\delta}{2} + (1+\kappa)U_s\right]}\,. \tag{5.31}$$

The instability window corresponds to

$$-2(1+\kappa)U_s < \hbar\delta < -2(1-\kappa)U_s\,. \tag{5.32}$$

Note that this result was already derived in Chapter 4 using a mean field approximation. The Bogoliubov theory allows us to go one step further. In this unstable regime, ω_B is imaginary and Eq. (5.29) can be rewritten as

$$\langle \hat{N}_p\rangle_{\text{vac}} = \frac{\kappa^2 U_s^2}{\hbar^2|\omega_B|^2}\sinh^2(|\omega_B|t)\,. \tag{5.33}$$

Hence, the number of pairs produced increases exponentially until it is no longer negligible compared to N, leading to the breakdown of the UPA. In Chapter 6, we will explore the regime beyond the UPA. For now, we can make the following qualitative prediction. One expects a peak of the production of pairs when the imaginary part of ω_B is maximal. It occurs on resonance, when the pump and output modes are degenerate. Furthermore, as the pump is consumed, it is reasonable to anticipate a progressive slow down of the dynamics until it eventually stops (or reverse).

This behavior is typically seen in an optical parametric amplifier. However, in our atomic system a difference arises from the spin-conserving collisions, described by the term $\hat{N}_0(N-\hat{N}_0)$ in Eq. (5.19). In the UPA, it boils down to a mean-field shift to the energy, that changes the positions of the resonance from $q' = 0$ to $q' = -U_s$. In Sec. 5.3.3, we will show that beyond the UPA, interesting differences due to interactions occur between the optical and atomic parametric amplifiers.

5.3 Production of a two-mode squeezed vacuum state

We report here on the observation of a two-mode squeezed vacuum state. This work has been published in [86].

5.3.1 Experimental protocol

We produce a BEC of about $N \simeq 2700$ atoms in a magnetic field of $\simeq 3$ G. In this condition, the ground state is very close to the perfect nematic state with all atoms in $m = 0$. We remove thermal atoms in the $m = \pm 1$ states using the spin-filtering technique described in chapter 3. The bias field is then ramped down to 0.46 G, and an oscillating field of amplitude 1.2 G is added on an orthogonal axis. The frequency is chosen near a Shapiro resonance studied in Chapter 4. In practice, we scan the frequency to maximize the number of $m = \pm 1$ atoms. For these experiments we have $\kappa = 0.34$ and $U_s/h = 18$ Hz (the calibration of U_s is discussed in the section 5.4). The spin populations are measured with an accuracy of $\simeq 1.6$ atoms using the "Stern-Gerlach fluorescence imaging" set-up described in Chapter 3.

5.3.2 Experimental results

We found that more pairs are produced near the upper edge of the unstable regime, for $\delta = -24\,\text{Hz} \simeq -2(1-\kappa)U_s/\hbar$. This observation constitutes a first deviation from the UPA prediction, which will be discussed in Sec. 5.3.3. We show in figure 37 the evolution over time of the mean and standard deviation for the observables $\hat{N}_p$ and $\hat{J}_z$. At $t = 0$ the driving starts, and $m = \pm 1$ pairs are produced. However, as the pump gets slightly depleted, the pair production is boosted and quickly deviates from the UPA prediction. Numerical resolution of the Schrödinger equation using the secular Hamiltonian Eq. (5.19) shows a better agreement, up to ~ 200 ms. At that time we observe a saturation of $\langle \hat{N}_p\rangle$ to a value of ~ 200 pairs, while the simulation shows a reduction of $\langle \hat{N}_p\rangle$. Possible effects not included in the simulation are atom losses and interactions with the thermal cloud. As for the measured pseudo magnetization $\langle \hat{J}_z\rangle$, it remains very close to the imaging noise for the whole time. The small increase could be due to atom losses, in the BEC or in the molasses during the detection. In any case, it is much smaller than the shot noise value $\sqrt{\langle \hat{N}_p\rangle/2}$.

At $t = 150$ ms we measure $\langle \hat{N}_p\rangle \simeq 105$, $\Delta\hat{N}_p \simeq 115$, $\Delta J_z \simeq 1.55$ and the spin squeezing parameter ζ_s defined by Eq. (5.16) is $\zeta_s^2 \simeq 0.021 = -16.8$ dB. We show the distribution of N_p and J_z at that time on figure 38. The distribution of N_p is in very good agreement with the prediction of a thermal distribution and verifies $\Delta N_p \simeq \langle \hat{N}_p\rangle$. The distribution of J_z is very narrow, close to that of the imaging noise. For comparison, we show the distribution of J_z for a coherent state with similar mean $\langle \hat{N}_p\rangle$. Our measurement is consistent with the expected normal distribution of variance $\langle \hat{N}_p\rangle/2$, much broader than that of the squeezed state.

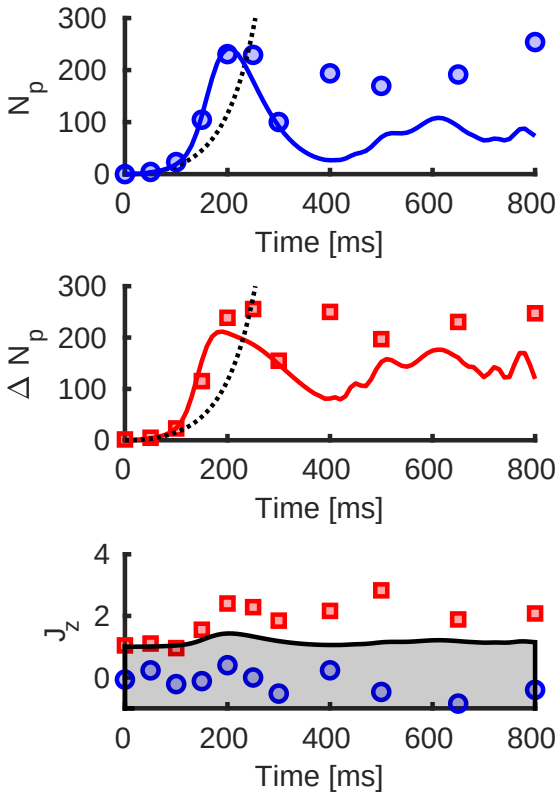

Figure 37: Evolution of the mean number of pairs N_p (upper panel, blue circles) and its standard deviation (middle panel, red squares) versus the duration of the modulation. The dashed black line corresponds to the Bogoliubov approximation, where the mean and standard deviation are almost equal. The numerical solutions of the Schrödinger equation using the secular Hamiltonian Eq. (5.19) are shown as solid lines. The lower panel shows the evolution of the longitudinal pseudo spin J_z, its mean (blue circles) and standard deviation (red squares). The shaded area corresponds to the detection noise.

5.3.3 Interacting parametric amplifier

Here we discuss in more detail the observed discrepancies from the UPA. First, we find that more pairs are produced on the upper edge of the instability region, where the energy of the output mode $m = \pm 1$ is initially larger than that of the pump $m = 0$. In the UPA, the maximum occurs in the middle of the instability region. Second, the dynamics is at intermediate times faster than what the UPA predicts. This contradicts the general expectation that the depletion of the pump should slow down the dynamic. These two deviations from the UPA do not occur in an optical parametric amplifier, and arise here because of the interaction between the pump $m = 0$ and output modes $m = \pm 1$. Qualitatively, it can be understood as follows. In the UPA, the pump-output interaction results in a positive mean-field shift of the output energy. As the pump is depleted, the shift decreases, bringing the system closer to resonance.

As a simple extension to the UPA, we proceed to the following substitution: $\hat{N}_p^2/N \to n_p \hat{N}_p$ and $\hat{a}_0 \to \sqrt{N(1-2n_p)}$ in the exchange term, where $n_p = \langle \hat{N}_p \rangle / N$ is a real number quantifying the normalized number of pairs. With this substitution, the Hamiltonian remains quadratic in the operator $\hat{a}_\pm$ and can be written as in Eq. (5.22), with $V = \delta/2 + U_s(1-2n_p)$ and $W = \kappa U_s(1-2n_p)$. Thus, the Bogoliubov energy given by Eq. (5.24) reads

$$\hbar\omega_B = \sqrt{\left(\frac{\hbar\delta}{2} + U_s(1+\kappa)(1-2n_p)\right)\left(\frac{\hbar\delta}{2} + U_s(1-\kappa)(1-2n_p)\right)}\,. \tag{5.34}$$

We introduce the variable $\delta' = \delta + 2U_s/\hbar$, and $U' = \kappa U_s$. U' corresponds to the spin-changing collisions rate [term $\hat{a}_{+1}^\dagger \hat{a}_{-1}^\dagger \hat{a}_0^2$+h.c. in Eq. (5.19)], and U_s to the rate of spin conserving collisions [term $\hat{N}_p(N - 2\hat{N}_p)$]. The instability window becomes

$$-U'(1-2n_p) \leq \hbar\delta' - 2U_s n_p \leq U'(1-2n_p)\,. \tag{5.35}$$

As n_p increases, the instability window shrinks because of the depletion of the pump, and moves because of the increase of the pump-output interaction. More precisely, the width decreases as $\pm 2U' n_p$, and the center moves by $2U_s n_p$. We can distinguish three situations depending on the relative values of U' and U_s.

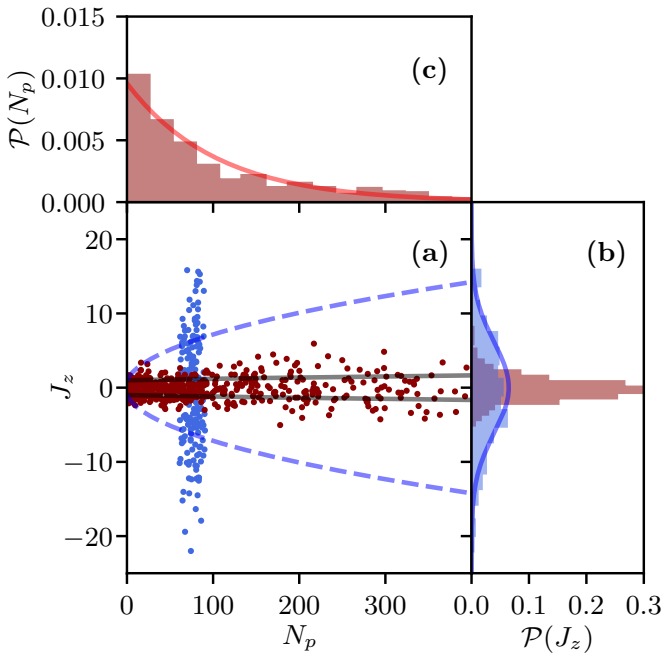

Figure 38: (a) J_z versus N_p for a squeezed state (red dots) and a coherent state (blue dots). The dashed blue line corresponds to the atomic shot-noise level (one standard deviation). The squeezed state is much below that value, almost limited by the detection noise (solid black line). (c) Distribution of the number of pairs N_p. The red line corresponds to the thermal distribution expected for a TMSV. In (b) we show the distribution of J_z for the squeezed state and the coherent state. The latter is much broader due to the shot noise (blue line).

- In the case of the optical parametric amplifier (figure 39 a), $U' = 0$. The instability region does not move. The instability rate is maximal for $\delta' = 0$, and decreases as the pump gets depleted.
- For undriven spin mixing dynamics (figure 39 b), $U' = U_s$. The motions of the center and of the upper edge of the instability window compensate exactly. This leaves the point $\delta' = 2U_s$ always within the instability region. Hence we expect a particularly good agreement with the UPA at that point.
- For driven spin-mixing dynamics (figure 39 c), $U' < U_s$ and the instability window shifts faster than it shrinks. Therefore, starting in the vicinity of the upper bound $\delta' = 2U'$, we expect the evolution to bring the system deeper in the instability region. Here, the effect of the interaction counter-acts the effect of the depletion, and we expect the dynamic to be faster than in the UPA[1].

In figure 40 we present the result of a numerical resolution of the dynamics under the secular Hamiltonian Eq. (5.19) for different κ, keeping U' fixed so that the UPA prediction is fixed. We plot the maximal number of pairs produced over a time $t = 5\hbar/U'$ versus δ' and the time evolution of N_p for $\hbar\delta' = 2U'$. The competition between the depletion of the pump and the pump-output interactions explains qualitatively all the features we see.

5.4 Reversible dynamics: coherence and entanglement

We gave the expression of the TMSV in the number basis in Eq. (5.15). The TMSV can be seen as a broad and coherent superposition of TFS with equal numbers of atoms in $m = \pm 1$. The significant squeezing that we have measured reflects the high correlation between the modes $m = \pm 1$ and is a signature of entanglement between the particles. An interesting question is whether the states we produced experimentally are also entangled in the sense of the modes. We observed a broad distribution of the number of pairs, but so far our measurements are not sufficient to prove the coherence between all the states with well-defined numbers of pairs. Indeed, our findings are *a priori* compatible with a statistical mixture of TFS, such as

$$\rho = \frac{1}{\sqrt{\mathcal{N}}} \sum_{n=0}^{\infty} \eta^{2n} |n,n\rangle\langle n,n| \,. \tag{5.36}$$

[1]The system may even "fall" in the unstable regime if $\delta' \gtrsim 2U'$. It is visible in figure 40 a, where we see the spread of the instability region to slightly larger detuning in the driven situation. However this is a finite size effect. Indeed, according to the UPA, the amplitude of the oscillation in the stable regime (studied in the next section) does not depend on the total number of atoms, and hence in that regime, $n_p \to 0$ as $N \to \infty$.

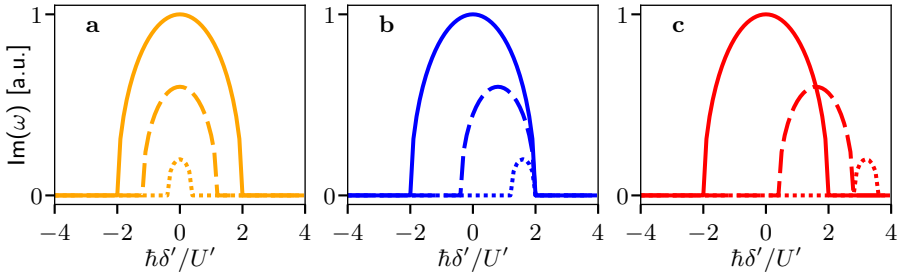

Figure 39: Instability rate versus δ' for various depletions: $n_p = 0$ (solid line), $n_p = 0.2$ (dashed line) and $n_p = 0.4$ (dotted line). We plot it for $\kappa \to \infty$ (a), $\kappa = 1$ (b) and $\kappa = 0.5$ (c), keeping $U' = \kappa U_s$ fixed. The depletion results in an overall decrease of the rate. For the atomic case (b and c), it can be compensated (b) and even overcompensated (c) near $\hbar\delta' \simeq 2U'$ due to the displacement of the instability region.

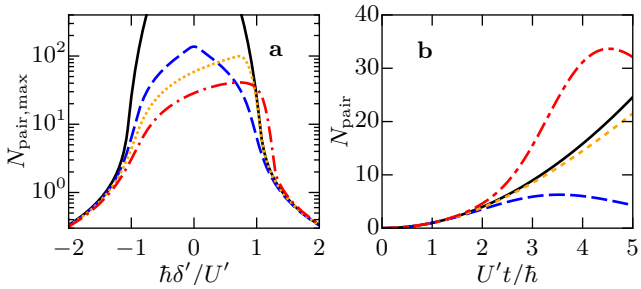

Figure 40: a Maximal number of pairs produced over an evolution time $t = 5/\hbar U'$, versus $\hbar\delta'/U'$. b Evolution of N_p for $\hbar\delta' = 2U'$. The solid black line represents the result of the UPA. The blue dashed line corresponds to $\kappa \to \infty$ ($U' = \kappa U_s$ fixed). It is always below the UPA. The yellow dotted line corresponds to static spin-mixing ($\kappa = 1$). Because of the pump-output interactions the resonance is shifted to the right. On the boundary $\hbar\delta' = 2U'$, pump-output interactions counteract the depletion and the agreement with the UPA is particularly good. The dashed-dotted line corresponds to driven spin-mixing, for which we observe a boost of the dynamics compared to the UPA prediction near $\hbar\delta' = 2U'$. We used $N = 300$ for the numerical calculation.

Part of the "non-classicality" is lost in that mixed state compared to the TMSV given by Eq. (5.15). This is of no consequence for the interferometric experiment we present in Appendix D following [69], but is damageable for other schemes, such as the $SU(1,1)$ interferometer [159].

In this section, we prove the persistence of the coherence, and thus mode entanglement thanks to a study of the dynamics in the stable regime.

5.4.1 Experimental protocol

The preparation of the initial state is the same as in the previous experiment. We produce a BEC of ~ 3000 atoms in a large magnetic field. After spin-filtering, all the atoms are in $m = 0$. The dynamics is however triggered differently. The unstable regime occurs for negative QZE q, which is not possible in the static situation, hence the use of a Shapiro resonance in the previous section. In the stable regime, $q > 0$ and driving the system is not necessary. Instead, we quench the magnetic field to a low value such that $q \ll U_s$. This brings the system close to the phase transition identified in chapter 2, where quantum fluctuations play a major role.

5.4.2 Results

Theoretical expectation For $q > 0$, the system undergoes many-body oscillations. More precisely, it evolves back and forth into a TMSV, with an oscillating number of pairs given by Eq. (5.29). In the limit $q \ll U_s$, the frequency of the oscillations is $\omega_B \simeq \sqrt{2qU_s}/\hbar$ and the amplitude is $\simeq U_s/(2q)$. Self consistency of the UPA requires $q \gg U_s/N$. In this Chapter we focus on that situation. We will explore the regime $q < U_s/N$ in Chapter 6.

Experimental results We show in figure 41 the evolution of the number of pairs after a quench to $q/h \simeq 0.3$ Hz. The mean and standard deviation superimpose almost perfectly according to Eq. (5.30). They are well fitted by the UPA prediction, with

U_s as the only free parameter which determines both the amplitude and frequency of the oscillations according to Eq. (5.29). We find $U_s/h = 18$ Hz, which is consistent with previous calibrations. The pseudo spin $\hat{J}_z = (\hat{N}_{+1} - \hat{N}_{-1})/2$ is almost perfectly conserved with fluctuations mainly limited by detection noise. For long evolution times we observe a progressive damping of the oscillation of the number of pairs. It could be due to shot-to-shot fluctuations of U_s induced by atom number fluctuations. The small increase of $\Delta\hat{J}_z$ indicates atom losses, which may also alter the dynamics. In any case, we found overall a good agreement with the theoretical expectations.

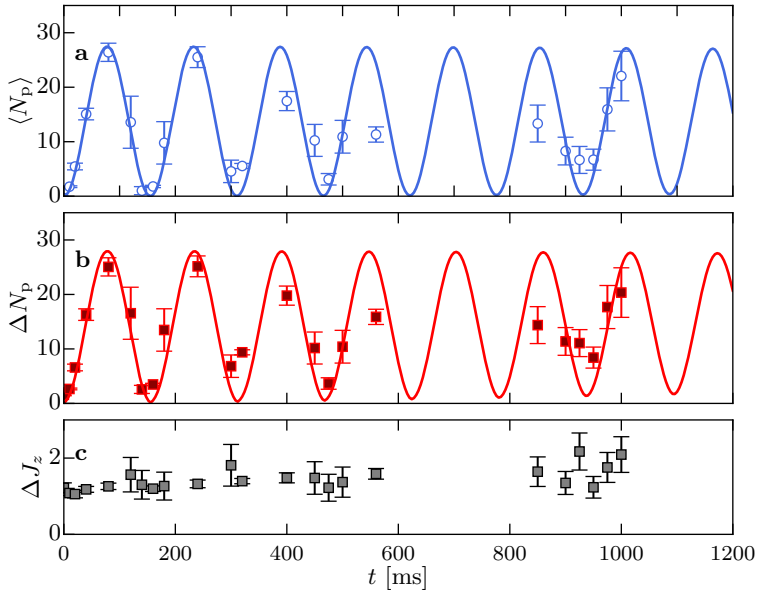

Figure 41: Evolution of the mean number of pairs (a), its standard deviation (b) and the (pseudo) magnetization standard deviation (c). The solid lines are the results of a numerical simulation. Here $q/h \simeq 0.3$ Hz and $U_s/h \simeq 18$ Hz. The error bars correspond to one standard error.

We repeated this experiment at various magnetic fields ($i.e.$ various q). We fit the oscillations and extract a period and amplitude that we report on figure 42. Keeping the same value $U_s/h = 18$ Hz, we found an excellent agreement with the theory, over almost two orders of magnitude for q.

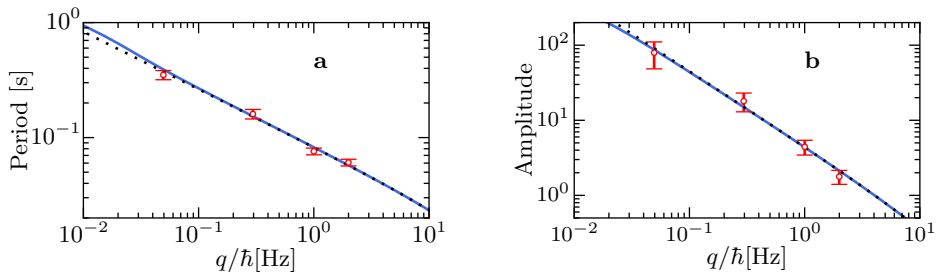

Figure 42: (a) Period and (b) amplitude of the oscillations of N_p versus the QZE q. The solid blue lines are the results of numerical simulation and the black dotted lines are the predictions of the UPA.

Mode entanglement In the UPA, the state produced by the dynamic is the TMSV, and is squeezed in the sense of Eq. (5.16). Here, we focus on the entanglement of the modes. We gave the expression of the TMSV in Eq. (5.15). The reduced density matrix for the mode $m = +1$ (it is clearly the same for $m = -1$) is

$$\rho_{+1} = \frac{1}{1 + \langle \hat{N}_{+1} \rangle} \sum_{n=0}^{\infty} \left(\frac{\langle \hat{N}_{+1} \rangle}{1 + \langle \hat{N}_{+1} \rangle} \right)^n |n\rangle\langle n| \,. \tag{5.37}$$

This is a thermal Bose-Einstein distribution [32], with entropy

$$\mathcal{S}(\rho_{+1}) = -2n_{+1}\ln(n_{+1}) - (1-2n_{+1})\ln(1-2n_{+1})\,. \tag{5.38}$$

where $n_{+1} = \langle \hat{N}_{+1}\rangle/N$ is, using Eq. (5.29),

$$n_{+1} = \frac{U_s}{2qN}\sin^2(\omega_B t)\,. \tag{5.39}$$

We can also define an effective temperature T_{eff} in analogy with the distribution of an ideal thermal gas (see appendix C)

$$k_B T_{\text{eff}} \simeq \langle \hat{N}_{+1}\rangle q \simeq \frac{U_s}{2}\sin^2(\omega_B t)\,. \tag{5.40}$$

This definition of T_{eff} is somewhat arbitrary. The important point is not the precise value of the temperature, but rather its variations, in particular the fact that it is non-monotonic, as the entropy. We emphasize, that in this calculation the total quantum state is pure. The entropy of ρ_{+1} corresponds to entanglement entropy (see Chapter 2, [71]).

We show in figure 43 the evolutions of the entropy and the temperature, for the data set of figure 41. The Von-Neumann entropy $\mathcal{S}(\rho_{+1})$ is simply the Shanon entropy associated with the measurement of N_{+1} [we measure $\mathcal{S}(\rho_{-1}) \simeq \mathcal{S}(\rho_{+1})$]. For N_{meas} measurements of N_{+1}, finite sampling leads to a systematic error (an underestimation) of order N_{+1}/N_{meas} on the Shannon entropy (see *e.g.* [160]). We do not try to correct for this bias. Instead, we only show the points for which we have $N_{\text{meas}} > 10N_{+1}$, to insure the systematic errors are below ten percent. The error bars correspond to $\text{mean}(N_{+1})/N_{\text{meas}}$. The temperature is obtained after an exponential fit of the distribution of N_{+1}.

At short times, the creation of pairs results in an increase of entropy and temperature. The entropy is initially non-zero because of the detection noise. After a full period, we measure $N_p \simeq 0$ and the entropy and temperature are almost back to their initial values. This observation tells us that the total entropy is conserved as far as detection noise allows us to tell, as expected for a unitary evolution. Therefore, the initial increase of $\mathcal{S}(\rho_{+1})$ is due to entanglement between the $m = +1$ mode and the other two modes.

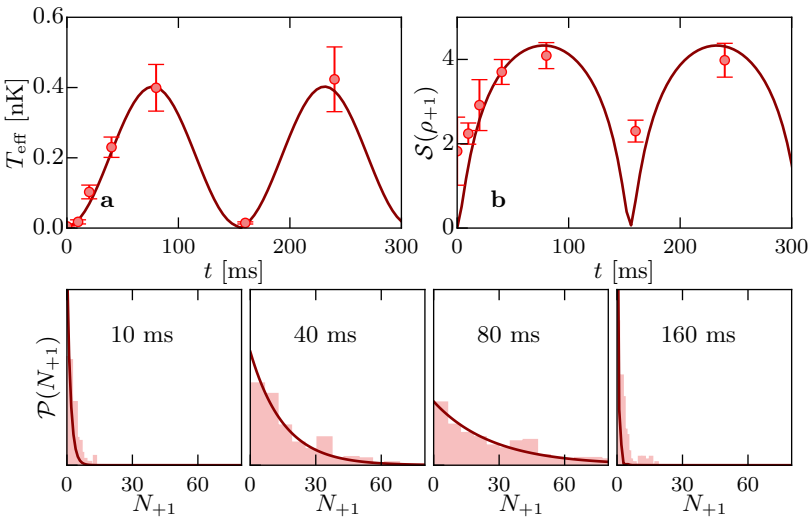

Figure 43: Evolution of the effective temperature (a) and entropy (b) over time, for ρ_{+1} (same data set as for figure 41). The four lower panels show the distributions of the number of atoms in $+1$, from which the entropy and temperature can be calculated. The solid lines are the results of the numerical resolution of the Schrödinger equation.

An analogy can be drawn between the (apparently) thermal distribution of particles generated by a parametric amplifier in initially empty modes, and the radiation seen by an accelerating observer, according to the Unruh effect [161]. In both cases, the Hamiltonian of the system features a non-linear term of the form $\propto \hat{a}_i^\dagger \hat{a}_j^\dagger$+h.c. (coming from the change of frame in the Unruh effect), which can create pairs of particles in modes i and j from the vacuum state. This analogy is developed further in [79], where the interaction strength of condensed atoms was modulated using a Feshbach resonance. In that case, the drive effectively produces the conversion term $\hat{a}_0^2 \hat{a}_{\mathbf{k}}^\dagger \hat{a}_{-\mathbf{k}}^\dagger$+h.c., where $\hat{a}_0$ annihilates an atom of the condensate (the pump mode) and is replaced by $\sqrt{N}$ in the UPA. This exchange term creates pairs of atoms in opposite momentum states $\pm\mathbf{k}$. In that experiment, coherence and entanglement between the external modes has also been demonstrated, using an "entangling-disentangling" scheme as well.

However, the BEC was unstable, and the evolution was reversed by applying a phase shift of π to the pump mode. In the UPA, $\hat{a}_0^2$ becomes $-N$, and if the Hamiltonian reduces to the exchange term, the evolution is perfectly reversed.

In fact, the phase shift that needs to be applied to reverse the parametric amplification dynamics can be measured with a sensitivity below the standard quantum limit. This is the working principle of the so-called SU(1,1) interferometer [159]. It has been demonstrated experimentally with spinor BECs in [13, 14].

5.5 Seeded dynamics

To highlight the role of quantum fluctuations, we also studied the effect of a controlled seed on the dynamics. This allows for the observation of the Bogoliubov to mean-field regime crossover.

5.5.1 Experimental protocol

Up to now, the dynamics started from the vacuum of the $m = \pm 1$ mode. Although our detection noise does not allow us to distinguish reliably the vacuum from a state with one or two atoms on a single shot, averaging over one thousand repetitions, we measure $N_p = -0.050 \pm 0.040$ (see chapter 3) and can safely say that at least for most of the shots, we prepare the vacuum state. We now investigate the effect of a seed on the dynamics. The preparation of the initial state is the same as previously, including spin filtering. At that point there is no seed. We then apply a weak radio frequency pulse to slightly rotate the initial state. The population in the $m = \pm 1$ modes after rotation is $n_{\text{seed}} N$. Before the quench of magnetic field, we also add a tunable delay. During that time, $q \gg U_s$ and spin-changing collisions are completely inhibited by energy conservation. However, a phase $\vartheta \simeq -2qt$ is accumulated between the $m = 0$ and $m = \pm 1$ mode[2]. The initial state can be written as

$$|\text{seed}\rangle = (\sqrt{n_{\text{seed}}} e^{i\frac{\vartheta}{2}} \hat{a}_{+1}^\dagger + \sqrt{1 - 2n_{\text{seed}}} \hat{a}_0 + \sqrt{n_{\text{seed}}} e^{i\frac{\vartheta}{2}} \hat{a}_{-1}^\dagger)^N |\text{vac}\rangle \,. \tag{5.41}$$

We then quench the magnetic field to achieve $q \ll U_s$, and let the system evolve.

5.5.2 Results

Theoretical expectation Using Eqs. (5.26,5.41), we find (for $q \ll U_s$)

$$\langle \hat{N}_{\pm 1} \rangle_{\text{seed}} = \frac{U_s^2}{\hbar^2 \omega_B^2} \sin^2(\omega_B t) \left[1 + 4 N_{\text{seed}} \cos^2(\frac{\vartheta}{2}) \right] + N_{\text{seed}} \,. \tag{5.42}$$

Even a microscopic seed of a few atoms can have a dramatic effect on the population growth. Only a very "pure" system is mostly driven by vacuum fluctuations. The effect of the seed depends importantly on the phase ϑ. In particular, for $\vartheta = \pi$, the seed has no effect.

For a large seed, the number of pairs produced may become significant compared to the total number of atoms, leading to the break-down of the UPA. However, when $N_{\text{seed}} \gg 1$ we expect the mean-field approximation to take over the UPA and give accurate results.

Experimental results We show in figure 44 the number of pairs produced after 80 ms of evolution. We scanned both the phase and the size of the initial seed. For $N_{\text{seed}} \leq 1$, the value of N_{seed} is not measured (it is below our detection noise), but inferred from the power of the RF pulse. The value of U_s is extracted from a fit to the oscillations observed without a seed. Except for the largest seed, our results are in excellent agreement with the UPA. We see a linear amplification of the production of $m = \pm 1$ pairs when we add a seed, and a dependence on the phase. Importantly, when $N_{\text{seed}} \to 0$, we observe a saturation of N_p to a finite value, contrary to the mean-field prediction. This is a clear signature of the role of the vacuum fluctuations. For a large enough seed, the mean-field approximation becomes accurate. It takes over the UPA, which fails when the seed is too large. For $q < U_s$, the mean-field equations of motion are highly non-linear and the frequency of the oscillation depends on the size of the seed. The number of pairs at a given time $t = 80$ ms is therefore a complicated, non-monotonic function of N_{seed}. We show the results of numerical simulation of the mean field dynamics in figure 44. For the largest seed, in phase with the pump, we observe this effect.

5.6 Outlook

In the first part of this chapter, we have reported on the generation of a spin squeezed state. A direct application of such non-classical states is interferometry. In particular, in appendix D we show how the TMSV can be used to measure the rotation of the pseudo-spin with a sensitivity below the standard quantum limit. Pseudo-spin rotations can be achieved using micro-wave coupling to the $F = 2$ hyperfine manifold and interferometric experiments with squeezed states of spinor BEC have been reported

[2] The Larmor precession results in a phase $\eta = pt$ between $m = \pm 1$ of no importance in the following.

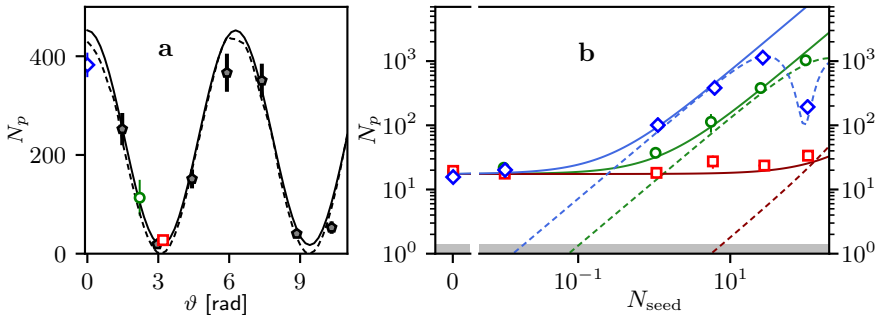

Figure 44: Number of pairs produced after 80 ms of evolution versus the phase of the seed ϑ for $N_{\text{seed}} \simeq 6$ atoms (a), and versus N_{seed} for $\vartheta \simeq 0$ rad (blue diamonds), $\vartheta = 2.2$ rad (green circles) and $\vartheta \simeq 3.2$ rad (red squares) (b). The solid and dashed lines are the results of the Bogoliubov and mean-field approximations, respectively. The gray area corresponds to the detection noise level.

in [11,12]. In these experiments, the detection noise was limiting the performance of the interferometer. Fluorescence imaging may help to make one more step away from the SQL and closer to the Heisenberg limit.

These experiments are relying on measurements of the first or second moment of a collective (pseudo) spin component. However, enhanced sensitivity can sometimes be obtained thanks to the measurement of a microscopic observable. For a TMSV state fed in a Mach-Zehnder interferometer (which effectively achieves a pseudo-spin rotation), greater sensitivity is achieved by measuring the parity of the number of pairs at the output, rather than the collective spin [162].

In a recent experiment [163], parity detection of the spin state of a Dysprosium atom was implemented to perform measurements near the Heisenberg limit. In that experiment, it is the internal state of a single atom that is squeezed, not the collective spin of an atomic ensemble. The large spin $J = 8$ of the Dysprosium atoms can be viewed as the collective spin of a mesoscopic ensemble of sixteen fictitious spin $1/2$, but this number is not scalable. One great challenge in implementing such an experiment in atomic ensembles comes from the fact that a parity measurement requires in general single atom resolution. We are now close to this limit and with further improvement we believe that "Stern-Gerlach fluoresence imaging" could be used to reveal the microscopic details of the distribution of the number of pairs, in particular the parity, thereby enabling new interferometric schemes.

Chapter 6

Relaxation of an isolated quantum system

In Chapter 5, we studied spin-mixing dynamic after a quench of the (effective) quadratic Zeeman energy (QZE) q. For positive and large enough q, the low energy states are weakly perturbed, and the system remains at all time close to its initial state, allowing for the linearization of the Hamiltonian. Up to a Bogoliubov transformation, the system is then analog to a set of two independent harmonic oscillators, and the evolution is fully reversible. We now turn to the study of larger quenches, bringing the system in the critical region, $q \ll \frac{U_s}{N}$ identified in Chapter 2. In that case, the energy eigenstates post-quench are very different from those prior to the quench, and the evolution appears to be irreversible.
We can draw a comparison with a classical system, a gas in an isolated container. Small density fluctuations, induced $e.g.$ by the gentle motion of a speaker, result in sound waves. Ideally this is an isentropic process, described by a wave equation, symmetric upon time reversal. On the other hand, the sudden removal of the piston creates a Joule-Gay-Lussac expansion of the gas, an irreversible process characterized by the creation of entropy. In that case, the irreversibility results from the exponential increase of the phase space accessible to the system. Among all the possible configurations, constituting the microcanonical ensemble, the initial one, where all particles occupy a fraction of the container, is extremely atypical. The vast majority of configurations are typical, $i.e.$ essentially identical with respect to the physical observables such as the coarse grained density. For macroscopic systems, the likelihood of atypical configurations is strongly suppressed, and as time evolves physical observables relax to an equilibrium value. The latter can be computed using an appropriate statistical ensemble, which does not depend on the details of the initial state.
Far from equilibrium isolated quantum systems may also exhibit "irreversible" evolution (irreversible for all practical purposes). This has been the subject of intense theoretical and more recently, experimental investigations. Once again, we are not going to cover this whole field of research, but focus on some important results relevant for the understanding of our experiments (see $e.g.$ [164] for a review).
We start by introducing important definitions and general results regarding the relaxation of isolated quantum systems. We briefly review some experimental work related to this subject. We then focus on the theoretical study of our system, and in particular on the relaxation of a nematic state in a vanishing magnetic field. Finally, we present experimental results, and connect the findings of the present Chapter with those of Chapter 5.

6.1 Relaxation and thermalization of isolated quantum systems

6.1.1 Definitions

We consider the evolution of a pure state $|\psi\rangle = \sum c_n |n\rangle$ under the Hamiltonian $\hat{H} = \sum_n \hbar\omega_n |n\rangle\langle n|$. In practice, the diagonalization of a many-body Hamiltonian is often too challenging for any analytical or numerical approach. Much like in classical statistical mechanics, great simplifications occur if one focuses on physical observables instead of the whole quantum state. We consider one such observable, $\hat{O}$. Without loss of generality, we take $\hat{\mathcal{O}}$ dimensionless and of order one ($e.g.$ $\hat{N}_0/N$). Its mean evolves as

$$\langle \hat{O}(t) \rangle = \sum_n |c_n|^2 O_{nn} + \sum_{n \neq m} c_m^* c_n e^{-i(\omega_n - \omega_m)t} O_{nm} \,. \tag{6.1}$$

Let us write the first term $\langle \hat{O} \rangle_\infty$ and the second $C(t)$. We use overlines for time averages. We start by specifying the meaning of relaxation and thermalization of an observable [164].

1. Relaxation: The observable $\hat{\mathcal{O}}$ is said to relax if

$$\overline{C(t)} \to 0 \qquad \text{and} \qquad \sqrt{\overline{C^2(t)}} \ll 1 \,. \tag{6.2}$$

   In that case, $\langle \hat{\mathcal{O}}(t) \rangle$ reaches the steady value $\langle \hat{O} \rangle_\infty$, and remains close to it at most time. The steady value of any observable that has relaxed is given by $\langle \hat{O} \rangle_\infty = \mathrm{Tr}(\hat{\rho}_{\mathrm{DE}} \hat{O})$, where $\hat{\rho}_{\mathrm{DE}}$ is the so-called diagonal ensemble, defined by the density

matrix

$$\hat{\rho}_{\mathrm{DE}} = \sum_n |c_n|^2 |n\rangle\langle n| \,. \tag{6.3}$$

Note that contrary to statistical ensembles, the diagonal ensemble depends on the details of the initial state (the $|c_n|^2$), often unknown. It is a convenient theoretical object, but with little practical use.

2. Thermalization: The observable thermalizes if its steady value corresponds to the microcanonical prediction

$$\langle \hat{O} \rangle_\infty = \mathrm{Tr}\left(\hat{\rho}_{\mathrm{ME}}(E)\hat{O}\right) \,, \tag{6.4}$$

where $\hat{\rho}_{\mathrm{ME}}$ is the microcanonical density matrix defined by

$$\hat{\rho}_{\mathrm{ME}} = \frac{1}{Z_{\mathrm{MC}}} \sum_{n\in\Omega} |n\rangle\langle n| \tag{6.5}$$

where $Z_{\mathrm{MC}} = \mathrm{Tr}(\hat{\rho}_{\mathrm{ME}})$ and Ω is the set of energy eigenstates with energy $E_m \in [E-\delta E, E+\delta E]$, with $E = \langle \hat{H} \rangle$ and δE a small energy, whose precise value is unimportant (providing it is sufficiently small). The microcanonical ensemble thus only depends on a macroscopic quantity, the energy of the initial state.

6.1.2 Relaxation

We first examine the conditions under which an observable relaxes. The first requirement $\overline{C(t)} \to 0$ occurs naturally thanks to dephasing. More precisely, for a generic interacting Hamiltonian with incommensurate frequencies ω_n, such that after some time t_R long compared to the inverse of the mean gap, it is reasonable to treat the factors $e^{i(\omega_n-\omega_m)t}$ as independent random variables[1]. They do not depend on the state nor on the observable. Moreover, for most far-from-equilibrium states, unless some fine tuning of the initial state has been made, many c_n have comparable values, so that the sum $C(t)$ samples the distribution of $e^{i(\omega_n-\omega_m)t}$ (with $m \neq n$), and thus takes negligible values after a short evolution time.

The second condition for relaxation is the absence of large temporal fluctuations of the expectation value $\langle \hat{O} \rangle$. The occurrence of dephasing is not sufficient to insure that this is the case and further assumptions on the matrix elements O_{nm} are required. Indeed, after dephasing, the fluctuations are

$$\sqrt{\overline{C(t)^2}} \sim \left(\sum_{n\neq m} |c_n c_m O_{mn}|^2 \right)^{\frac{1}{2}} \,. \tag{6.6}$$

If the off-diagonal elements O_{mn} are of order one, this double sum is of order one as well. Relaxation thus requires the off-diagonal elements to be on average much smaller than the diagonal ones.

6.1.3 Thermalization

Eigenstate Thermalization Hypothesis The occurrence of thermalization, expressed as $\mathrm{Tr}(\hat{\rho}_{\mathrm{DE}}\hat{O}) \simeq \mathrm{Tr}(\hat{\rho}_{\mathrm{ME}}\hat{O})$, is arguably more surprising, and demands stronger assumptions. Several scenarios can *a-priori* lead to thermalization (see *e.g.* [165]). A first scenario seems to have a wide range of applicability (we will discuss exceptions later), the eigenstate thermalization hypothesis (ETH) [166, 167]. The ETH states

$$O_{nn} \simeq \mathrm{Tr}(\hat{\rho}_{\mathrm{ME}}(E_n)\hat{O}) \,. \tag{6.7}$$

The ETH is a very strong statement, it means that thermalization occurs at the level of individual eigenstates $|n\rangle$, and does not require any averaging over n. Thus, different distributions of c_n have similar expectation values of physical observables, and the thermalized state is relatively insensitive to the initial one. From Eq. (6.7), Eq.(6.4) follows immediately for any state narrow in energy[2] (c_m significant in a small energy window $E_m \in [E-\delta E, E+\delta E]$). The ETH has only been demonstrated to hold for specific models ([164–166] and references therein) for few-body observables.

Let us consider the thermalization of an initially pure state. As far as the measurements of physical observables are concerned, it becomes indistinguishable from the mixed state $\hat{\rho}_{\mathrm{ME}}$, leading to a loss of information. This is of course just apparent, since the entropy is conserved over a unitary evolution. It follows from the fact that physical observables (the ones most accessible to experiments) are all blind to certain correlations (for instance, correlations between spatially separated particles). Therefore their measurement may not give the entire information on the state.

[1] For commensurate or for a finite number of frequencies one expects "rephasings" at some particular times yielding to revival of the dynamics. Those appear in short time windows separated by long periods with no evolution, and do not forbid relaxation as defined above, provided the time averages are taken over a sufficiently long window.

[2] The ETH alone is not sufficient to guarantee thermalization, but the narrowness of the initial state in energy is a weaker assumption, common in statistical mechanics (required for the equivalence of the statistical ensembles). For instance, it is demonstrated in [165], for quenches of a local Hamiltonian.

Integrable systems An apparent loss of information on the initial is inherent to thermalization. However, some memory of the initial state may be preserved if the Hamiltonian possesses symmetries and thereby if there are conserved quantities. More precisely, a model with an extensive number of conserved quantities is said to be integrable. Such systems do not verify the ETH, and in fact observables do not thermalize in the sense defined above. Yet, the dynamics is *a-priori* not frozen, and may still be very complicated. Indeed, the state contains in general a number of parameters exponential in system size, and hence much larger than the number of constraints[3]. For the same reasons as above, relaxation can occur, at least partially.
The ETH can be extended to integrable systems by replacing the microcanonical ensemble with a generalized Gibbs ensemble (GGE) [164]. The associated density matrix is obtained by maximizing the Von-Neumann entropy under the constraints imposed by the conservation laws. Let $\hat{I}_k$ be the conserved quantities. The GGE can then be written as[4]

$$\hat{\rho}_{\mathrm{GGE}} = \frac{1}{Z} \exp\left(-\beta \hat{H} + \sum_k \lambda_k \hat{I}_k\right) , \tag{6.8}$$

where $Z = \mathrm{Tr} \exp\left(-\beta \hat{H} + \sum_k \lambda_k \hat{I}_k\right)$ is the partition function and the λ_k are Lagrange multipliers introduced to enforce the constraints. They are determined by solving the equations $\langle \hat{I}_k \rangle = \mathrm{Tr}(\hat{I}_k \hat{\rho}_{\mathrm{GGE}})$. These Lagrange multiplier keep some memory of the initial state.

6.1.4 Brief overview of experimental studies with atomic gases

Spinor Bose-Einstein condensates There have been numerous experimental studies of the out-of-equilibrium dynamics of quantum atomic gases. Let us first mention a few works, that explored the evolution of a spinor BEC after a quench of the QZE q. These experiments used Rubidium atoms which has ferromagnetic properties. In [30], the formation of ferromagnetic domains in an elongated geometry was studied. Locally, the spin has a well-defined direction, breaking the SO(2) symmetry. However, the direction is not homogeneous over the whole cloud, and instead forms a complex, apparently random spin pattern. With a similar set-up, the dynamic of the spin-spin correlation function was studied in [168]. In particular, the authors demonstrated the universality of the dynamics in an intermediate regime, between an initial state-specific dynamics and the relaxed state, called "non-thermal fixed point". During that time, the evolution of the spin structure factor is self-similar, *i.e.* after proper rescaling, it can be written as a function of a single variable instead of two (momentum and time). Closer to our experiment, in the single mode regime, the creation of the excitations by a ramp through the nematic to ferromagnetic phase transition was studied in [169]. In all these works, the focus is put on the transient dynamics, rather than on the state after relaxation.
The relaxation of spin-mixing dynamics was studied in chapter 4 and in [170], but in those experiments, the long-time relaxation resulted from a coupling to the thermal cloud, which played the role of a heat bath. In that sense the system (the condensate) was not isolated.

Thermalization of a microscopic Bose-Hubbard system The thermalization of an isolated system consisting of six bosonic atoms on a six site lattice, realizing the Bose-Hubbard model, was demonstrated in [171]. The system is initiated in the Mott insulating regime, with one atom per site and essentially no tunneling. The latter is suddenly switched on to trigger the dynamics. The authors show the thermalization of a local observable, the number of atoms per site (despite the small system size, all statistical ensembles give similar results). Moreover, by measuring the so-called Rényi entropy (similar to the Von-Neumann entropy) locally and globally, they demonstrate the role of entanglement in thermalization: while the state of less than six sites is mixed, the state of the whole six sites system remained almost pure.

Lack of thermalization in 1D gases The absence of thermalization for an almost integrable system was observed in [172]. In that experiment, ultra-cold bosonic atoms in a 1D trap are prepared in a superposition of opposite momentum states using an optical Bragg pulse. At early times, two "blobs" of atoms are bouncing off each other due to the motion in a harmonic trap. After some dephasing time, the spatial distribution settles to a particular stationary shape, incompatible with a thermal distribution. This experiment can be captured by the Lieb-Liniger model, describing a uniform system of bosons in one dimension, with contact interactions. It is an integrable model, with an extensive number of conserved quantities. The Lieb-Liniger model was further studied experimentally in [173]. The authors of this latter work measured higher order correlation functions. They also observed the absence of thermalization and demonstrated relaxation to a GGE. More precisely, they measured correlation functions up to the tenth order and found that about ten "effective temperatures" (*i.e.* Lagrange multipliers) are necessary to account for their observations.

[3] For indistinguishable particles with $\alpha > 1$ degrees of freedom, the restriction to symmetric states yields a scaling of the Hilbert space as N^α, and the conclusion still holds

[4] To simplify the notations, we use a generalized canonical ensemble, instead of generalized microcanonical ensemble. In the thermodynamic limit the two ensembles are equivalent.

6.2 Relaxation of a spinor BEC in the SMA: theoretical results

The relaxation in models involving a few bosonic modes has recently been the subject of theoretical investigations. The case of two modes (effective spin 1/2) is explored in [174, 175], the case of three spatial modes in [176] and finally the case of three spin modes (spin-1) in [177]. However, the latter mostly focuses on the ferromagnetic case, in the regime $q \sim U_s$ and therefore is not directly relevant for our experiments. Here, we present our theoretical investigation of the relaxation for $q = 0$ in the antiferromagnetic case.

Hamiltonian at $q = 0$ We recall that the Hamiltonian in the absence of applied magnetic field reduces to

$$\hat{H}_{\text{SMA}} = \frac{U_s}{2N}\hat{\mathbf{S}}^2 \,. \tag{6.9}$$

The eigenstates are the angular momentum states $|S, M_z\rangle$, where $S \in \{0, 1, .., N\}$ is an integer that has the same parity as N in order to satisfy to the exchange symmetry. M_z is an integer in $\{-S, -S+1, ..S\}$. The eigenvalues are

$$E(S, M_z) = \frac{U_s}{2N}S(S+1) \,. \tag{6.10}$$

Spinor BECs are integrable systems due to the $SO(2)$ ($SO(3)$ at $q = 0$) symmetry which results in the conservation of all projectors onto the manifolds of fixed magnetization (alternatively, all moments $\hat{S}_z^k$ are conserved).

6.2.1 Relaxation of the nematic state at q=0

Let us consider first the evolution of the nematic state $|N : \mathbf{e}_z\rangle$ under the SMA Hamiltonian Eq. (6.9). We solved it numerically and show the results in figure 45. The short time dynamics can be captured by a Bogoliubov approximation as in Chapter 5, but eventually the depletion becomes too important and the approximation fails. The subsequent dynamics appears to be quite complicated. In the spirit of the previous discussion, we focus on the evolution of simple physical observables instead of the whole state, for instance the mean population N_p of the number of $m = \pm 1$ pairs. We can compute $N_p(t)$ analytically for $N \gg 1$. We find (see the appendix E)

$$N_p(t) \simeq \frac{N}{2}\tau F(\tau) \,, \tag{6.11}$$

where $\tau = \sqrt{\frac{2}{N}}\frac{U_s t}{\hbar}$ and $F(\tau) = \int_0^{+\infty} dx e^{-x^2} \sin(2x\tau)$ is the so-called Dawson function. At early times, $F(\tau) \sim \tau$ and we recover the prediction of the result of the Bogoliubov approximation (Chapter 5),

$$N_p(t) \sim \frac{U_s^2 t^2}{\hbar} \,. \tag{6.12}$$

At long times, $F(\tau) \sim 1/(2\tau) + 1/(4\tau^3)$ and N_p relaxes to $N/4$ with the asymptotic behavior

$$N_p(t) \sim \frac{N}{4}\left(1 + \frac{N\hbar^2}{4U_s^2 t^2}\right) \,. \tag{6.13}$$

We now recover the same result by looking at the structure of the eigenstates $|N, S, M_z\rangle$ and using the general arguments introduced in the preceding section.

6.2.2 Relaxation to a Generalized Gibbs Ensemble

Relaxation of physical observables The spectrum Eq.(6.10) is non-linear, allowing for dephasing, and for sufficiently long time, $\overline{\mathcal{O}(t)} \to \text{cte}$. However, this does not guarantee the relaxation of an observable, since large temporal fluctuations are not excluded, as a result of Eq. (6.6). We can show that relaxation occurs if we restrict $\hat{\mathcal{O}}$ to few-body observables, such as the Zeeman populations, the spin components, their first few moments... Indeed, the operator $\hat{a}_m$ only couples states with S and M_z varying by at most one unit. Therefore, in the collective spin state basis $|S, M_z\rangle$, most off-diagonal matrix elements of few-body observables vanish. The double sum in Eq. (6.6) is thus of order $\sim N^{-\frac{1}{2}}$, so that time fluctuations after dephasing can be neglected in comparison to the equilibrium value.

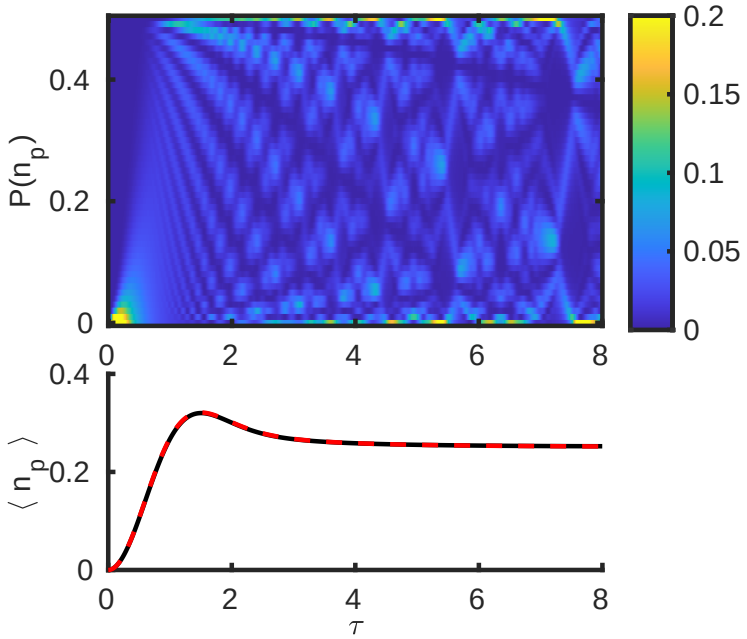

Figure 45: Numerical resolution of the relaxation of the nematic state $|0\rangle^{\otimes N}$, with $N = 100$ atoms, at $q = 0$. We plot the distribution of the reduced number of pairs versus the dimensionless time τ in the upper panel. For $\tau \ll 1$ the distribution is smooth and corresponds to the thermal distribution calculated in the Bogoliubov approximation. At longer times the distribution becomes rather complex. Remarkably, the mean number of pairs (lower panel, solid black line) relaxes to a steady value and shows essentially no evolution when $\tau \gg 1$. It is almost (up to finite size effect) perfectly described by Eq. (6.11) (red dashed line).

Generalized ETH for single-mode spinor BECs The projectors on a manifold of fixed M_z constitute an extensive set of conserved quantities in our integrable system. This prevents the thermalization of physical observables such as $\hat{S}_z$, and less trivially $\hat{N}_0$. Indeed we have (for $S \gg 1$)

$$\langle S, M_z|\hat{N}_0|S, M_z\rangle \simeq \frac{N}{2}\frac{S^2 - M_z^2}{S^2} \,. \tag{6.14}$$

The microcanonical ensemble is composed by all $|S, M_z\rangle$ state such that

$$\frac{U_s}{2N}S(S+1) \simeq E_i \tag{6.15}$$

where E_i is the initial state energy. Let S_i be the closest integer to $\sqrt{2NE_i/U_s} \gg 1$. The expectation value of $\hat{N}_0$ in the microcanonical ensemble is

$$\langle \hat{N}_0\rangle_{\rm MC} \simeq \sum_{M_z=-S_i}^{S_i} \frac{N}{2}\frac{S_i^2 - M_z^2}{S_i^2} \,, \tag{6.16}$$

$$\langle \hat{N}_0\rangle_{\rm MC} \simeq \frac{N}{3} \,. \tag{6.17}$$

This result is a consequence of the $SO(3)$ symmetry, the three Zeeman state are equally populated. Let us now consider an initial nematic state with all atoms in the $m = 0$ state. This state can be expressed as a superposition of $|S, M_z\rangle$ states where $M_z = 0$. By virtue of Eq. (6.14) we have

$$\langle \hat{N}_0\rangle_{\rm GGE} = \frac{N}{2} \,. \tag{6.18}$$

We also remark that provided $S \gg 1$, Eq. (6.14) implies that the expectation value of $\hat{N}_0$ in a spin state $|S, 0\rangle$ is independent on S. This ensures the equivalence between the diagonal ensemble (for the nematic state) and the GGE, according to the generalized

ETH[5]. We can even make a stronger statement, the eigenstates $|S,0\rangle$ that intervene significantly in the initial state ($i.e.$ in the diagonal ensemble) are essentially identical not only for the average $\langle \hat{N}_0 \rangle$, but also regarding the full coarse-grained distribution of n_0 (derived in the appendix B)

$$\tilde{\mathcal{P}}_{\mathrm{GGE}}(n_0) \simeq \frac{1}{\pi\sqrt{n_0(1-n_0)}} \,. \tag{6.19}$$

The tilde indicates coarse-graining over an interval $\Delta n_0 \gg 1/S$. This formula holds for $1 \ll S \ll N$, which is the case for the eigenstates we are interested in (the nematic state is peaked on $S = \sqrt{N}$). We compare in figure 46 $\tilde{\mathcal{P}}_{\mathrm{GGE}}(n_0)$ with the distributions of a few $|S,0\rangle$ states in the number basis. The latter show fast oscillations around $\tilde{\mathcal{P}}_{\mathrm{GGE}}(n_0)$, that average out after coarse-graining. The coarse-grained distribution of n_0 can also be calculated without the magnetization constraint (in the microcanonical ensemble). One then finds $\tilde{\mathcal{P}}_{\mathrm{MC}}(n_0) = 1/(2\sqrt{n_0})$, significantly different from the GGE prediction.

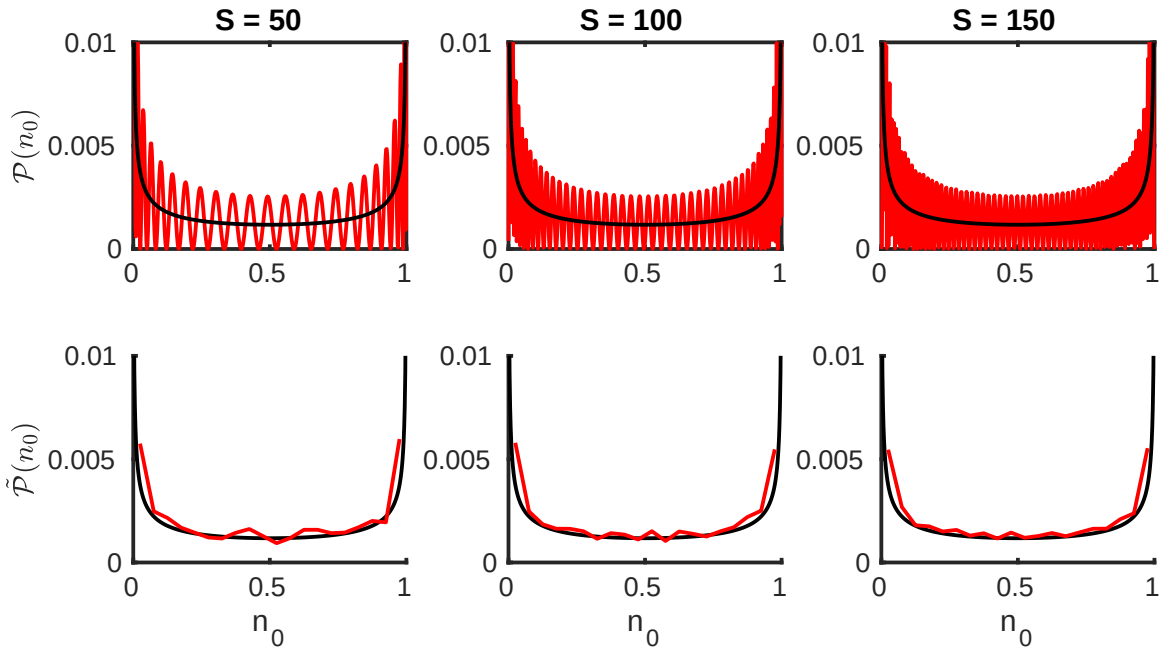

Figure 46: Distribution of the reduced population n_0 in the $|N,S,M_z\rangle$ states, for $N = 1000$, $S = 50, 100, 150$ and $M_z = 0$. The upper panels show the exact distributions and the lower panels the coarse-grained distributions. The black line corresponds to the analytical result given by Eq. (6.19).

The distribution given by Eq. (6.19) can also be obtained after an average over a couple of S states, instead of coarse graining (see App. B). Since the initial state has significant weight onto several spin states (the spin shot noise is $\sqrt{2N}$), we expect the distribution of n_0 to be close to Eq. (6.19), even without coarse graining. As a direct consequence the mode entropy [$i.e.$ the Shannon entropy of the distribution of $\mathcal{P}(n_0)$] is also expected to relax toward the GGE predictions.

Comparison with numerical simulation We now compare the predictions of the microcanonical and GGE with the results of numerical simulations. We report our findings in the table 6.1. They clearly show relaxation to the GGE.

Revivals The analytical formula given in Eq. (6.11) is derived by taking a continuum approximation for the spin, which is only valid in the thermodynamic limit $N \to \infty$. At $q = 0$, the frequencies are multiples of $U_s/(hN)$, and the evolution is periodic for N finite. More generally, for a finite size system, the Poincaré recurrence theorem states that for sufficiently long times, the system comes back arbitrary close to its initial state. However, revivals of the dynamics are very rare for $N \gg 1$, and thus we may still talk about relaxation, understood as the absence of evolution at most times.

[5] The equivalence of $\hat{\rho}_{\mathrm{DE}}$ and $\hat{\rho}_{\mathrm{ME}}$ also holds for other coherent states, that have narrow distribution (determined by the shot noise) in the spin state basis.

	$\overline{n_p}$	$\overline{\Delta n_p}$	$\overline{\mathcal{S}}(\rho_{+1})$
MC	$\frac{1}{3}$	$\sqrt{\frac{1}{45}} \simeq 0.15$	$\ln(N) - 1$
GGE	$\frac{1}{4}$	$\sqrt{\frac{1}{32}} \simeq 0.18$	$\ln(\frac{\pi}{8}N) \simeq \ln(N) - 0.93$
Simu.	$0.249(6)$	$0.177(5)$	$0.96(1)\ln(N) - 1.0(1)$

Table 6.1: Comparison between numerical simulations and the prediction of the microcanonical (MC) and generalized Gibbs ensemble (GGE). The initial state is the nematic state $|0\rangle^{\otimes N}$, and we let it evolve until $\tau = 10$, at which point we consider that it has relaxed and we calculate the observable of interest. We scan N from 100 to 4000 and report the values of a fit of $\mathcal{O}(N)$ versus N. The mean value of the number of pairs clearly excludes the MC and is in very good agreement with the GGE predictions. The standard deviation also pleads in favor of a relaxation in the GGE. The prediction for the entropy is very close for both ensembles, and in good agreement with the numerical simulation.

6.3 Observation of the relaxation of a spinor BEC

6.3.1 Experimental protocols

The procedure is essentially the same as the one described in Sec. 5.4 of the previous chapter. We prepare a BEC with all atoms in $m = 0$ in a large magnetic field. In order to observe relaxation on a short time scale, we use smaller BECs of $N \simeq 100$ atoms (the relaxation time scales as $\sqrt{N}h/U_s$). To keep a substantial interaction strength U_s with such small samples, we recompress the trapping potential after evaporation in 500 ms. The density increases and leads to U_s of the same order as in the previous experiments, $U_s/h \simeq 20$ Hz. After recompression, we quench the magnetic field to a final value as low as 5 mG[6]. In that case, we have $q/h \simeq 7$ mHz, and the condition $q \ll U_s/N$ is well fulfilled. We can thus neglect the QZE term in the Hamiltonian, and we achieve the situation described in the previous section.

6.3.2 Experimental results

Observation of the relaxation to a generalized Gibbs ensemble Our measurements are summarized on figure 47. We observe the relaxation of the number of pair to a steady value. We also show in figure 47 standard deviation and entropy. All observables reach a steady value. In fact the whole (coarse grained) distribution relaxes. However, the magnetization stays almost constant, and due to the conservation of this quantity, the microcanonical ensemble fails to describe the steady state and thermalization does not occur. The generalized Gibbs ensemble predictions are on the other hand in very good agreement with our measurements.

Universal dynamics In principle, at $q = 0$, $n_p(t)$ depends on two dimensionless parameters, N and $U_s t/\hbar$. One remarkable aspect of the evolution predicted by Eq. (6.11), is the dependence of n_p on only one parameter, $\tau = \sqrt{\frac{2}{N}}\frac{U_s t}{\hbar}$. In order to verify this prediction, we prepare clouds with different atom numbers N and different U_s. For each N, we determine U_s by measuring the frequencies of oscillations for $q > U_s/N$ (in the UPA regime), as explained in Chapter 5. After this calibration, all measurements collapse on a universal curve $n_p(\tau)$, shown in figure 48.

Effect of a seed In Chapter 5, Sec. 5.5, we have seen that a coherent seed strongly modifies the dynamics. In the Bogoliubov approximation, the amplitude of the oscillations is essentially multiplied by the amplitude of the seeds. We now study how a seed impacts the relaxation. The situation is more difficult to simulate numerically, because we can no longer restrict the Hilbert space to the kernel of $\hat{S}_z$, and hence the dimension of the Hilbert space is $\propto N^2$. However, for seeds that are small enough, the magnetization and energy of the initial states are barely changed, so that we may expect the predictions of the GGE to still approximately hold. Our measurements are plotted in figure 49. The initial relaxation dynamic is much faster than without a seed, but the steady state value is independent on the seed size (here, for seeds $< 5\%$ of the total atom number). Relaxation erases the nature of the fluctuation (classical or quantum) that initiated the dynamics.

6.3.3 Steady state versus q

We have presented in Chapter 5, Sec. 5.4 the evolution of the state in the reversible regime, where the Bogoliubov approximation holds. This regime corresponds to $q > U_s/N$. In the present chapter, we studied the relaxation when $q < U_s/N$ (we show more data sets on figure 53). We can sum up all results on a single universal curve $\overline{n}_p$ versus Nq/U_s shown in figure 50. For $q > U_s/N$ (oscillating regime) we compute the mean value $\overline{n}_p$ from a fit to $n_p(t)$. This is motivated from the fact that in the Bogoliubov approximation, the GGE expectation for the mean number of pair equals the amplitude of the oscillation. Numerical simulations show that in this regime, after a very long dephasing time, the system relaxes to the GGE. For $q < U_s/N$ we directly

[6] This required compensation of the subway field, as explained in chapter 3.

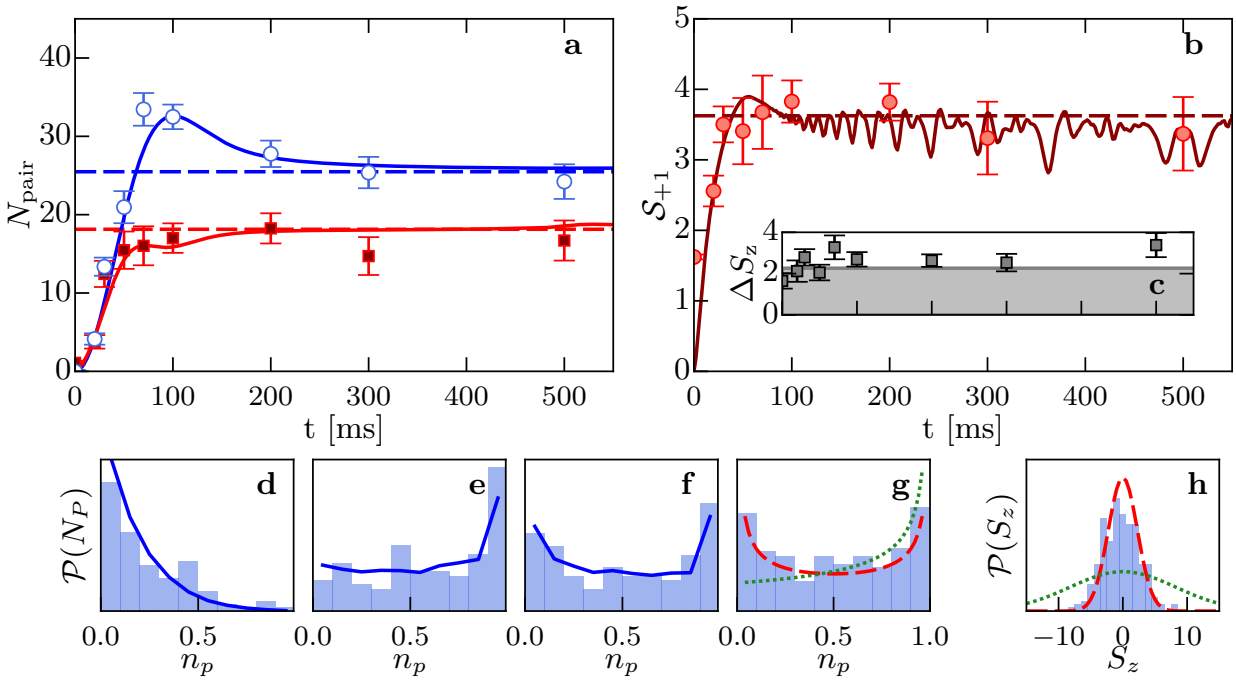

Figure 47: Observation of the relaxation of a nematic state of $N \simeq 100$ atoms in a negligible magnetic field. We show in (a) the evolution of the mean (blue dots) and standard deviation (red squares) of the number of pairs. The solid lines are the results of a numerical simulation and the dashed lines are the predictions of the GGE. In (b) we plot the entropy of the mode $m = +1$. The inset (c) shows the standard deviation of the magnetization, which remains essentially limited by the detection noise (gray area). Despite the large entropy in the mode $m = +1$, it is almost perfectly correlated to the mode $m = -1$. The second row shows the distribution of the number of pairs at different times. At short times (d, 30 ms), it resembles a thermal distribution. As the depletion increases, n_p goes through a maximum, at which point (e, 100 ms) the distribution is peaked on $n_p = 1$. The number of pairs and its coarse grained distribution then settles to a stationary "U" shape (f and g, 200 ms and 500 ms). The solid blue lines are the results of a numerical simulation. In (g) the dashed red and dotted green lines are the predictions of the GGE and MC, respectively. In (h) we plot the histogram of S_z at 500 ms. In that case the dashed red line corresponds to the detection noise (the GGE prediction is a Dirac distribution). Here again, the absence of thermalization is clear.

extract the stationary value of $n_p(t)$ from our data. We compare the results to the diagonal and GGE. Both ensembles have almost identical predictions, except near $q \simeq U_s/N$ where they slightly differ. The steady state obtained after a numerical resolution of the dynamics is not plotted, but indistinguishable from the diagonal ensemble predictions.

Equivalence of the Gibbs ensembles In figure 50, we plot with a red dashed line the expectation of the generalized canonical ensemble (GCE), where the energy is fixed on average, and the magnetization is exactly vanishing. The corresponding density matrix is

$$\rho_{\rm GCE} = \frac{1}{Z}\hat{P}_0 \exp(-\beta \hat{H})\hat{P}_0 \,, \tag{6.20}$$

where $\hat{P}_0$ is the projector onto the kernel of $\hat{S}_z$. Alternatively, we could have used the generalized microcanonical ensemble (GME) defined as

$$\rho_{\rm GME} = \frac{1}{Z}\sum_n \hat{P}_0 |n\rangle\langle n| \hat{P}_0 \,, \tag{6.21}$$

where the sum runs over the energy eigenstates such that $E_n \in [E_i - \delta E, E_i + \delta E]$.

In figure 51, we compare the GME, GCE and diagonal ensembles. When $q \sim U_s$ and $n_p \sim 1/N$, the GME prediction becomes sensitive to the precise value of δE (we take the standard deviation of the initial state energy as δE). For sufficiently large N, the three ensembles essentially overlap. Small differences, which seem to persist as N increases, can be observed near the point $q \sim U_s/N$. Interestingly, at that point, the GCE is also slightly deviating from the diagonal ensemble (although it is closer to it than the GME is). This deviation can be understood by looking at the curve $n_p(E_n)$ shown in figure 52. For $q = U_s/N$, $n_p(E_n)$ is extremely sensitive on the precise value of E_n near the energy of the initial state. However, the region of discrepancy, given by $q \sim U_s/N$, shrinks as N increases and disappears in the thermodynamic limit.

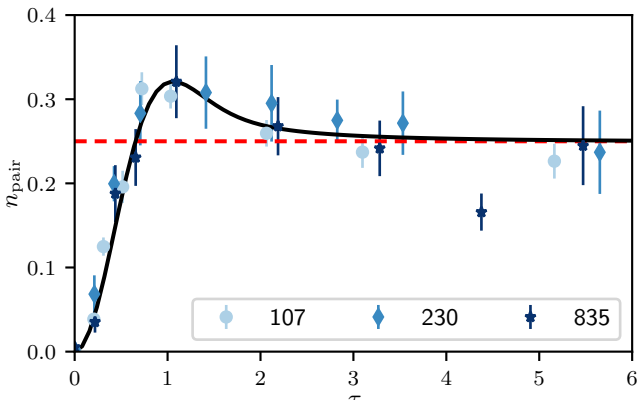

Figure 48: Universality of the relaxation dynamics. We plot the reduced number of pairs, versus the dimensionless time $\tau = \sqrt{\frac{2}{N}}\frac{U_s t}{\hbar}$. We vary the mean atom number from ~ 107 to 835. U_s is calibrated independently each time. The solid black line is the universal function defined in Eq. (6.11). The dotted red line is the GGE prediction.

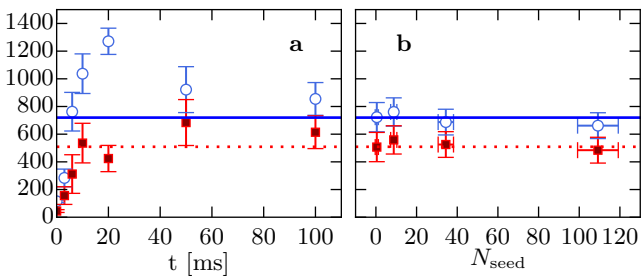

Figure 49: a Relaxation of the observables $\hat{N}_p$ (open circles) and $\Delta\hat{N}_p$ (filled squares). Here $N \simeq 2800$ atoms. A small nematic state with $N_{\text{seed}} \simeq 110$ atoms in the $m = \pm 1$ states is produced on purpose, prior to the quench, to seed the dynamics. The solid blue line (resp. dotted red) is the GGE expectation $\langle \hat{N}_p \rangle = N/4$ (resp. $\Delta\hat{N}_p = N/(4\sqrt{2})$). In b we show the mean value $\langle \hat{N}_p \rangle$ (open circles) and $\Delta\hat{N}_p$ after 500ms of evolution versus the size of the initial seed. The data are in very good agreement with the GGE prediction for all N_{seed}.

6.4 Outlooks

Dynamics of mesoscopic ensembles In this chapter, we investigated the evolution of an initial nematic state in the critical regime $q \ll U_s/N$. We observed the relaxation of the state to a steady value. However, we pointed out that relaxation only occurs for physical observables, not for the quantum state itself. It would be interesting to observe the evolution of the state after these observables have relaxed. Dynamics can be observed in the detailed (not coarse grained) distribution of pairs as shown in figure 45. Alternatively, revivals of the dynamics would also attest of the continuing evolution of the state. Both experiments are technically challenging, but may be successful with small sample of few tens of atoms or so.

Thermalization in a chaotic regime For $q \ll U_s/N$, we observed the relaxation of the state to a generalized Gibbs ensemble, and the absence of thermalization. The underlying reason is the integrability of the effective spin Hamiltonian due to its $SO(2)$ symmetry. In [176], a chaotic regime was shown to exist in a three-mode model. The author of [176] also shows the occurrence of thermalization by the ETH mechanism. In that study, the three modes are supposed to correspond to the three first energy levels of a trap, and the Hamiltonian is quite different from ours and in particular is not integrable. Yet, in our case, magnetic field gradient or microwave dressing to the $F = 2$ level, could be used to break the symmetry of the Hamiltonian. It would be interesting to see if chaotic behavior could arise from the applied perturbation, and observe the cross-over from the integrable to the chaotic regime.

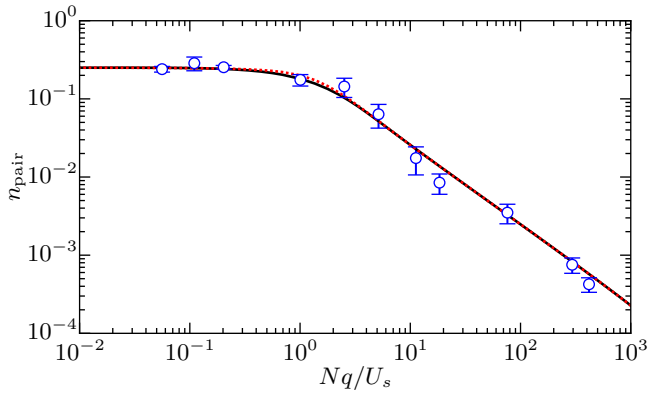

Figure 50: Relaxed (or time averaged) number of pair versus Nq/U_s. The solid black (red dashed) line is the diagonal ensemble (GGE) predictions.

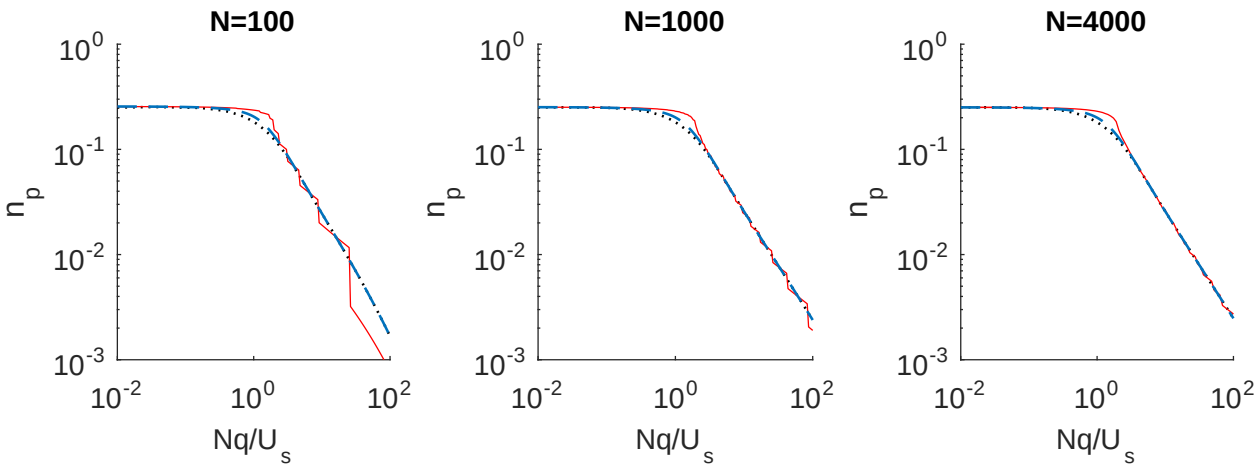

Figure 51: Comparison between the GME (solid red line), the GCE (dashed blue line) and the diagonal ensemble (dotted black line) for increasing atom number N. For $n_p \lesssim 1/N$, the GME contain few (~ 1) states within the energy window $\delta E = \Delta H$, and its prediction are not accurate. For $q \sim U_s/N$, a deviation occurs for the GME (and to a lesser extent to the GCE), which does not seem to disappear as N increases (see main text and figure 52).

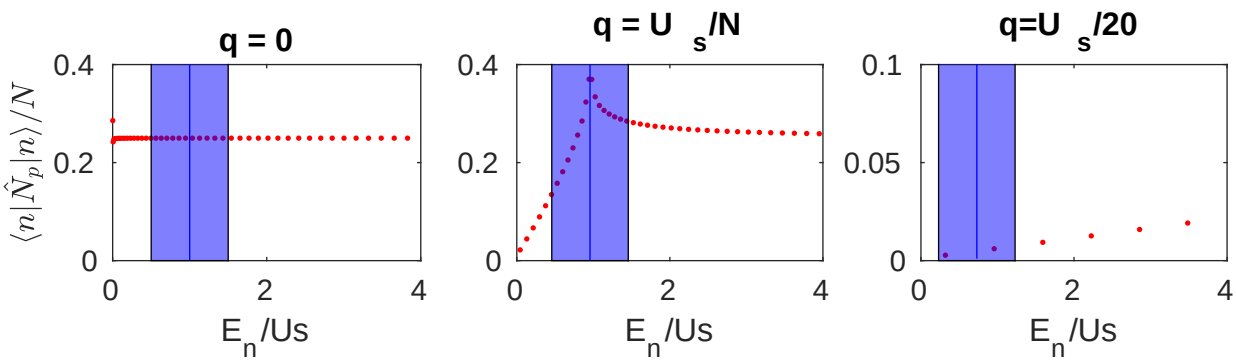

Figure 52: Mean reduced number of pairs $\langle n|\hat{N}_p|n\rangle/N$ in the eigenstate n, versus its energy E_n, for increasing q. The blue shaded area corresponds to the interval of width δE, used to compute the GME average. For $q = 0$, the curve is very smooth and essentially constant, in accordance with the generalized ETH. For $q = U_s/N$, the curve is, on the contrary, very peaked, and the predictions of the GME are sensitive to δE. For $q = U_s/20$, the curve is smooth again, but there are few eigenstates within the interval δE. Hence, the MCE is constituted of few states, and becomes very dependent on the precise value of δE, leading to an "unstability" of the MCE predictions in that interval. This issue disappears in the thermodynamic limit.

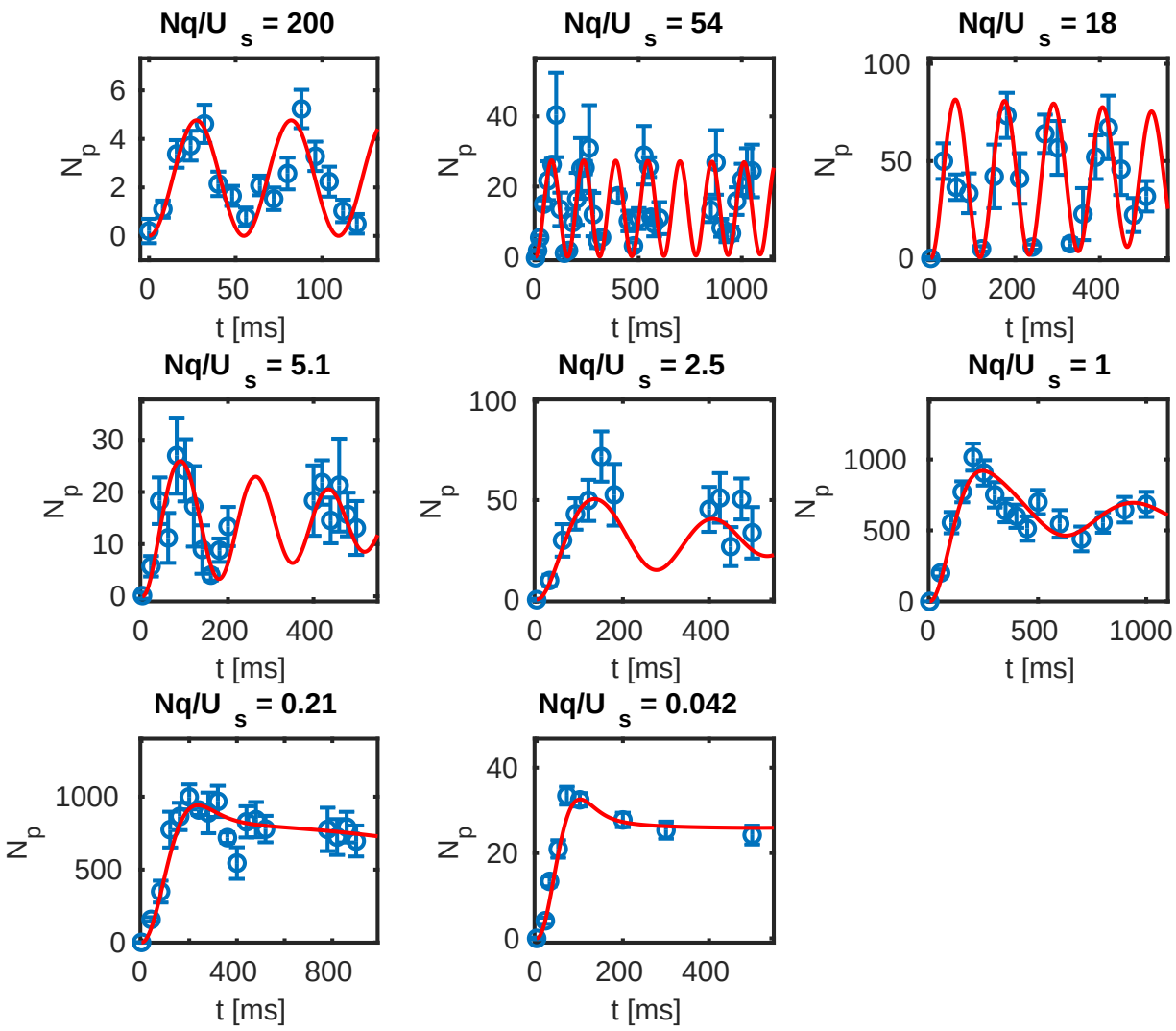

Figure 53: Crossover from reversible oscillations to relaxation of the number of pairs after a quench of the magnetic field. The solid lines are numerical resolutions of the dynamics under the SMA Hamiltonian. For all plots, the error bars correspond to the standard error.

Chapter 7

Fragmentation of a spinor Bose-Einstein condensate

Bose-Einstein condensation (BEC) was originally introduced as a phenomenon occurring in an ideal gas, that is to say, for non-interacting particles. As such, it is merely a statistical effect, fragile and easily jeopardized when several one-body states are near degenerate and compete for condensation. In practice, interactions play a decisive role, and when repulsive, they typically confer to spinless condensates a great robustness [44, 178]. On the other hand, attractive interactions often lead to instability and collapse [44]. It has long been noted that spinor condensates can host an alternative remarkable scenario, called condensate fragmentation, characterized by the absence of a unique one-body state macroscopically occupied [39, 42, 178]. For spin-1 atoms with antiferromagnetic interactions, the underlying microscopic mechanism is the associations of the atoms in singlet pairs.

In a classical system, one qualitatively expects interactions to favor an ordered phase, with low entropy. For instance in a ferromagnet, a stronger coupling between the spins facilitates their spontaneous alignment in a given direction and the appearance of a macroscopic magnetization. Interactions have precisely the opposite effect when they drive the fragmentation of a condensate. Indeed, in that latter case the order parameter (the number of atoms in the condensate) reduces, and may even become microscopic. Furthermore, in many instances, interactions act to restore a symmetry spontaneously broken by the condensate [42, 43]. For instance, we will see that in the case of an antiferromagentic spin-1 BEC, interaction favors a $SO(3)$ symmetric singlet state. The role of the interactions in the fragmentation of a condensate thus resemble that of thermal fluctuations in a classical system, and is often thought in terms of quantum fluctuations. In our context, the similarity between quantum and thermal fluctuations holds quantitatively to a large extent. Indeed, we will see how a fragmented spinor BEC (at zero temperature), can be well described with respect to few-body observables by a thermal state, with a temperature proportional to the interaction strength. However, thermal fluctuations results in a statistical mixture of coherent states, a separable state, while quantum fluctuations produce a coherent superposition of coherent states, with a high degree of entanglement.

An extreme form of fragmentation can occur when the number of degeneracies becomes macroscopic. This is achieved for instance for a charged particle moving in a magnetic field. For each eigenvalue of the Hamiltonian, there exists a macroscopic number of degenerate states forming so-called Landau levels. For neutral atoms the same structure can be obtained by rotating a BEC in a harmonic trap [179]. Classically, in the rotating frame, the atoms experience a centrifugal force, which counter-acts the harmonic confinement, and a Coriolis force, analogous to the Lorentz force produced by a magnetic field. The analogy holds also in the quantum treatment [180]. The large degeneracy occurs when the rotation is fast enough to compensate the trapping potential. In that case, interactions lead to the fragmentation of the condensate and the formation of highly correlated many body states. A macroscopic number of single particle states are occupied, and all signs of condensation are gone. The case of repulsive interaction is particularly interesting, as the system is expected to be in a fractional quantum Hall state [42, 181]. However, such states yet remain to be seen experimentally with ultracold atoms. Let us mention that similarly, the transition from superfluid to Mott insulator observed in [21] can also be seen as an extreme form of fragmentation.

In this Chapter, we report on our realization of a fragmented condensate of singlet pairs. We will start in Sec. 7.1 with a brief discussion of the role of interactions in Bose-Einstein condensation, before focusing in Sec. 7.2 on the case of the fragmentation of an antiferromagnetic spin-1 BEC. We will discuss in more detail the similarities and differences between thermal and quantum fragmentation, and the role played by entanglement in the latter case. This study highlights the peculiar nature, but also the fragility of quantum fragmentation. We will detail in Sec. 7.3 the methods that we have used to produce a fragmented state and report our observation in Sec. 7.4. We performed the full tomography of the state of the system, presented in Sec. 7.5. The reconstruction provides new insight on the nature of the many-body state and demonstrates the role played by entanglement in the condensate fragmentation.

7.1 Fragmentation and the role of the interactions

Definitions A first extension of the definition of BEC to the case of interacting particles was proposed in [74], based on the eigenvalues of the single-particle density matrix $\rho^{(1)}$. We will use the following definitions[1] [182]

- The ensemble forms a *condensate* if $\rho^{(1)}$ has at least one eigenvalue of order one.
- The ensemble forms a *single condensate* if $\rho^{(1)}$ has a single eigenvalue of order one.
- The ensemble forms a *fragmented condensate* if $\rho^{(1)}$ has several eigenvalues of order one.

7.1.1 Protection of a scalar BEC

Ideal gas Let us first consider an ensemble of non-interacting bosons in a box-potential. The single-particle eigenstates are the plane waves with momentum $\mathbf{k}$ and energies $\epsilon_{\mathbf{k}} = (\hbar\mathbf{k})^2/(2M)$. The many-body Hamiltonian is

$$\hat{H}_0 = \sum_{\mathbf{k}} \epsilon_{\mathbf{k}} \hat{a}^\dagger_{\mathbf{k}} \hat{a}_{\mathbf{k}} \,, \tag{7.1}$$

where $\hat{a}^\dagger_{\mathbf{k}}$ creates an atom in state $|\mathbf{k}\rangle$. The equilibrium state is most conveniently described within the grand canonical ensemble. Let T be the temperature ($\beta = 1/k_B T$) and μ the chemical potential. The mean occupation of state $|\mathbf{k}\rangle$ is [26]

$$n_{\mathbf{k}} = \frac{1}{e^{\beta(\epsilon_{\mathbf{k}}-\mu)} - 1} \,, \tag{7.2}$$

where μ is obtained from $N = \sum_{\mathbf{k}} n_{\mathbf{k}}$. As $\mu \to 0$, n_0 diverges, and this term is let aside from the sum. The rest of the sum is then replaced by an integral. In three dimensions it saturates at a critical temperature T_c such that

$$\int d\epsilon \rho(\epsilon) \frac{1}{e^{\beta_c \epsilon} - 1} = N \,, \tag{7.3}$$

where $\rho(\epsilon)$ is the density of state at energy ϵ (in three dimension, $\rho(\epsilon) \propto \sqrt{\epsilon}$). Below T_c, the chemical potential μ equals the ground state energy, atoms accumulate in the ground state and the ensemble forms a single condensate [26].

This scenario of condensation is particularly simple, because the ground state is non-degenerate. However, in the thermodynamic limit, the gap between the ground state and the first excited state vanishes. In such situations, interactions play an important role in determining the structure of the many body state.

Interacting scalar BEC in a box We first briefly study the situation of atoms with contact interactions in a box potential. The Hamiltonian is $\hat{H} = \hat{H}_0 + \hat{H}_{\text{int}}$, with

$$\hat{H}_{\text{int}} = \frac{U}{2} \sum_{\mathbf{k},\mathbf{k}',\mathbf{q}} \hat{a}^\dagger_{\mathbf{k}-\mathbf{q}} \hat{a}^\dagger_{\mathbf{k}'+\mathbf{q}} \hat{a}_{\mathbf{k}} \hat{a}_{\mathbf{k}'} \,. \tag{7.4}$$

We focus on repulsive interactions, *ie* $U > 0$. Let us consider a trial state of the form $\propto \prod_{\mathbf{k}} \hat{a}^{\dagger n_{\mathbf{k}}}_{\mathbf{k}} |\text{vac}\rangle$. In the expression of the energy, we have two types of terms, the "Hartree" terms for $\mathbf{q} = 0$ and if $\mathbf{k} \neq \mathbf{k}'$ the "Fock" or exchange terms $\mathbf{q} = \mathbf{k} - \mathbf{k}'$. This yields

$$\langle \hat{H}_{\text{int}} \rangle = \frac{U}{2} \sum_{\mathbf{k},\mathbf{k}'} n_{\mathbf{k}} n_{\mathbf{k}'} (2 - \delta_{\mathbf{k},\mathbf{k}'}) \,. \tag{7.5}$$

Thus, the interaction energy is twice as larger for atoms in different momentum states. For repulsive interactions the energy is minimized by having all atoms in the same momentum state (within our ansatz), *i.e.* for a single BEC. The energy cost for taking n_1 atoms out of the BEC is at least $n_1 U$ (neglecting the kinetic energy). It thus costs a macroscopic amount of energy to fragment the condensate, and here, repulsive interactions strongly favor single condensation [178, 182].

In the above calculation, we have used trial states which are not eigenstates of the interaction Hamiltonian Eq.(7.4). For weak interactions, a more refine treatment would rely on Bogoliubov theory [26]. This is standard and close to what we have presented in Chapter 2. The result is a small depletion of the condensate, function of the adimensionate parameter $\sqrt{na_s^3}$, where n is the density of the gas and a_s the scattering length characterizing the interaction strength. The depletion is a function of the density, which is an intensive quantity, and hence the condensate is not fragmented as long as the Bogoliubov treatment is valid. This is usually the case in dilute gases, where $na_s^3 \ll 1$, and the quantum depletion is typically very small.

With this brief discussion, we wanted to emphasize that condensate fragmentation is not a typical phenomena occurring as soon as there are interactions. We will now explore situation where fragmentation does occur.

[1] Often in the literature, $\rho^{(1)}$ is normalized to N. We take it normalized to 1, because we will investigate higher order reduced density matrix and it is more convenient to have them all normalized to one.

7.1.2 Fragmentation of a two-modes BEC

Given the previous discussion, one expects attractive interactions to favor fragmentation. It is indeed the case, but the theoretical treatment is more involved (see *e.g.* [43]). From an experimental point of view, attractive BECs suffer from three body recombinations (resulting in losses), which strongly reduces the lifetime, and make it challenging to observe the equilibrium state. For simplicity we turn to the situation where two degenerate modes are competing for Bose-Einstein condensation. A generic Hamiltonian for the interaction is

$$\hat{H}_{\text{int}} = \frac{U}{N}\hat{n}_1\hat{n}_2 \,, \tag{7.6}$$

where $\hat{n}_i$ is the number operator for the mode $i = 1, 2$. This model may be used for instance to describe an ensemble of atoms carrying a pseudo-spin 1/2 [178], or "scalar" interacting atoms, confined in the double well trap [42].
For $U > 0$, we recover the situation described above: a single condensate where all atoms are in one mode is strongly favored. On the other hand, for $U < 0$ the ground state is the "twin-Fock state" (TFS) with $N/2$ atoms in each mode (we assume N even for simplicity). The single particle density $\rho^{(1)}_{i,j} = \langle \hat{a}^\dagger_i \hat{a}_j \rangle / N$ is

$$\rho^{(1)} = \frac{1}{2}\begin{pmatrix} 1 & 0 \\ 0 & 1 \end{pmatrix} \,, \tag{7.7}$$

and the condensate is fragmented. The energy of the TFS is $E_{\text{TFS}} = UN/4$. The non-fragmented BEC which minimizes the energy Eq. (7.6) corresponds to the coherent state

$$|\phi\rangle = \frac{1}{\sqrt{N!2^N}}\left(\hat{a}^\dagger_1 + \hat{a}^\dagger_2\right)^{\otimes N} |\text{vac}\rangle \,. \tag{7.8}$$

It has an energy $E_\phi = U(N-1)/4$. Thus the energy difference with the actual fragmented ground state is only of order $\sim U$. This contrasts with the case $U > 0$, where the cost for fragmentation is of order $\sim NU$. The origin of this difference is easily understood by looking at the spectrum of the Hamiltonian (7.6) plotted in figure 54.

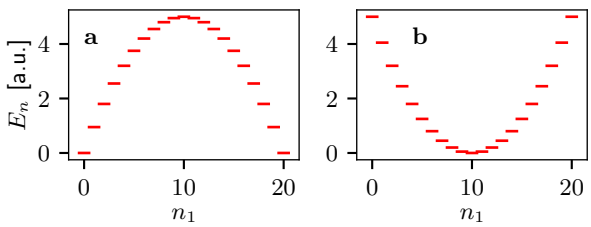

Figure 54: Spectrum of the Hamiltonian (7.6) for $N = 20$. For $U > 0$ (a), the ground state corresponds to a single condensate with $n_1 = 0$ or $n_1 = N$. A large gap separates it from the first excited state. For $U < 0$ (b), the ground state corresponds to the twin-Fock state with $n_1 = N/2$. The condensate is fragmented but this state is fragile, it is separated from the first exited states by a very small gap.

This model is discussed further in [42], where the effect of a small coupling between the two modes is investigated. As our calculation of the energy scales suggests, fragmentation is found to be very fragile against such perturbation. We will now focus on the fragmentation of a spin-1 BEC which shows a very similar behavior.

7.2 Fragmentation of a spin-1 BEC

7.2.1 Hamiltonian and ground state

We recall here some important results of chapter 2. In the single-mode approximation (SMA), all atoms occupy the same spatial mode. The Hamiltonian for the spin, is the sum of the quadratic Zeeman energy (QZE) energy and the antiferromagnetic interaction energy

$$\hat{H}_{\text{SMA}} = -q\hat{N}_0 + \frac{U_s}{2N}\hat{\mathbf{S}}^2 \,. \tag{7.9}$$

- For $q/U_s \to +\infty$, the ground state is the nematic state $|N : \mathbf{e}_z\rangle = |m = 0\rangle^{\otimes N}$, which constitutes a single condensate.
- For $U_s/N^2 \ll q$, the condensate is slightly depleted and well described by a Bogoliubov approximation, which yields $N_p \simeq \sqrt{U_s/(8q)}$. The depletion is thus independent on N and we still have a single condensate.

- For $q \lesssim U_s/N^2$, the Bogoliubov approximation breaks down and the condensate is fragmented.

Let us focus for simplicity on the situation $q = 0$. The family of coherent nematic states $|N : \mathbf{\Omega}\rangle$, obtained by rotation of $|N : \mathbf{e}_z\rangle$, is degenerate and minimizes the mean-field energy. This large degeneracy arises from the fact that the single particle states break the $SO(3)$ symmetry of the Hamiltonian. This symmetry drives the fragmentation of the BEC. Indeed, the requirement that $\rho^{(1)}$ commutes with all rotation matrices implies that $\rho^{(1)}$ is proportional to the identity (Schur's lemma)

$$\rho^{(1)} = \frac{1}{3}\begin{pmatrix} 1 & 0 & 0 \\ 0 & 1 & 0 \\ 0 & 0 & 1 \end{pmatrix} , \tag{7.10}$$

and the condensate is fragmented [40–42].
More generally, the eigenstates of the Hamiltonian Eq.(7.9) at $q = 0$ are the angular momentum states $|N, S, M_z\rangle$, where $S \in [0, N]$ is an integer that has the same parity as N in order to satisfy the exchange symmetry and M_z is an integer in $[-S, S]$. The spectrum is

$$E(N, S) = \frac{U_s}{2N} S(S+1) . \tag{7.11}$$

For simplicity, let us focus on the situation N even. The so-called singlet state with vanishing spin $S = 0$ is the ground state.

We point out that fragmentation occurs for very small QZE, $q \lesssim U_s/N^2$. As the previous section, we observe that fragmentation is a very fragile effect, which does not exist in the thermodynamic limit. We will see in the following Sections how the atom losses and thermal fluctuations may also spontaneously break the $SO(3)$ symmetry and modify the nature of the fragmented state.

7.2.2 Symmetry breaking description

The singlet state can be conveniently written as a superposition of nematic coherent states. We first review some important properties of the latter. The nematic state aligned along the quantization axis z is the state with all atoms in $m = 0$, $|N : \mathbf{e}_z\rangle = |0\rangle^{\otimes}$. By rotation in spin space, we obtain the state aligned along $\mathbf{\Omega} = (\sin\theta\cos\phi, \sin\theta\sin\phi, \cos\theta)$, expressed as

$$|N : \mathbf{\Omega}\rangle = \frac{1}{\sqrt{N!}}\left(-\frac{1}{\sqrt{2}}\sin\theta e^{-i\phi}\hat{a}^\dagger_{+1} + \cos\theta\hat{a}^\dagger_0 + \frac{1}{\sqrt{2}}\sin\theta e^{i\phi}\hat{a}^\dagger_{-1}\right)^N |\text{vac}\rangle . \tag{7.12}$$

Let us write $\Omega_{\pm 1} = \mp\frac{1}{\sqrt{2}}\sin\theta e^{\mp i\phi}$ and $\Omega_0 = \cos\theta$. The action of the annihilation operators on the nematic coherent state takes a simple form:

$$\hat{a}_m|N : \mathbf{\Omega}\rangle = \sqrt{N}\Omega_m|N-1 : \mathbf{\Omega}\rangle . \tag{7.13}$$

The nematic states form an overcomplete basis of the Hilbert space of symmetric states of N spin-1 particles [50,183]. The overlap between two nematic states is (see appendix B)

$$\langle N : \mathbf{\Omega}'|N : \mathbf{\Omega}\rangle = (\mathbf{\Omega}' \cdot \mathbf{\Omega})^N . \tag{7.14}$$

In the large N limit, it is sharply peaked on $\mathbf{\Omega}' = \mathbf{\Omega}$. This quasi-orthogonality of the nematic states makes them very convenient to compute the expectation value of few-body operators. Let us consider a k-body operator in normal order

$$\hat{\mathcal{O}}^{(k)} = \hat{a}^{\dagger k'_+}_{+1}\hat{a}^{\dagger k'_-}_{-1}\hat{a}^{\dagger k'_0}_0\hat{a}^{k_+}_{+1}\hat{a}^{k_-}_{-1}\hat{a}^{k_0}_0 , \tag{7.15}$$

with $\sum k'_m = \sum k_m = k$ and $k \ll N$. Using Eq. (7.13) the matrix elements of $\hat{\mathcal{O}}^{(k)}$ in the nematic state basis are

$$\langle N : \mathbf{\Omega}'|\hat{\mathcal{O}}^{(k)}|N : \mathbf{\Omega}\rangle = \mathcal{O}^{(k)}(\mathbf{\Omega}', \mathbf{\Omega})(\mathbf{\Omega}' \cdot \mathbf{\Omega})^{N-k} . \tag{7.16}$$

with

$$\mathcal{O}^{(k)}(\mathbf{\Omega}', \mathbf{\Omega}) = \frac{N!}{(N-k-1)!}\Omega'^{*k'_+}_{+1}\Omega'^{*k'_0}_0\Omega'^{*k'_-}_{-1}\Omega^{k_+}_{+1}\Omega^{k_0}_0\Omega^{k_-}_{-1} . \tag{7.17}$$

We now come back to the singlet state $|N, 0, 0\rangle$. Due to its rotational invariance, it has the same overlap with all nematic states and can be written as [183]

$$|N, 0, 0\rangle = \frac{\sqrt{N}}{4\pi}\int d^2\mathbf{\Omega}|N : \mathbf{\Omega}\rangle . \tag{7.18}$$

The expectation value of $\hat{\mathcal{O}}^{(k)}$ in the singlet state is

$$\langle\hat{\mathcal{O}}^{(k)}\rangle_{\text{sing}} = \frac{N}{(4\pi)^2}\iint d^2\mathbf{\Omega}d^2\mathbf{\Omega}'\mathcal{O}^{(k)}\left(\mathbf{\Omega}',\mathbf{\Omega}\right)\left(\mathbf{\Omega}'\cdot\mathbf{\Omega}\right)^{N-k}. \tag{7.19}$$

The term $\mathcal{O}^{(k)}\left(\mathbf{\Omega}',\mathbf{\Omega}\right)$ varies significantly when θ or ϕ run through $\sim \pi/k$. On the other hand, the scalar product $\left(\mathbf{\Omega}'\cdot\mathbf{\Omega}\right)^{N-k}$ varies on a scale of $\sim \pi/(N-k)$. For $k \ll N$, we can use the stationary phase approximation, and replace $\left(\mathbf{\Omega}'\cdot\mathbf{\Omega}\right)^{N-k}$ by a Dirac distribution centered on its maxima $\mathbf{\Omega}' = \pm\mathbf{\Omega}$ [183]

$$\left(\mathbf{\Omega}'\cdot\mathbf{\Omega}\right)^{N-k} \simeq \frac{2\pi}{(N-k)\sin\theta}\left(\delta(\theta-\theta',\phi-\phi') + \delta(\theta+\theta'-\pi,\phi-\phi'\pm\pi)\right) \tag{7.20}$$

This approximation entails an error of order $1/N$. It yields

$$\langle\hat{\mathcal{O}}^{(k)}\rangle_{\text{sing}} \simeq \frac{1}{4\pi}\int d^2\mathbf{\Omega}\mathcal{O}^{(k)}\left(\mathbf{\Omega},\mathbf{\Omega}\right), \tag{7.21}$$

up to terms of order N^{k-1} or smaller. This expression can be rewritten as

$$\langle\hat{\mathcal{O}}^{(k)}\rangle_{\text{sing}} \simeq \text{Tr}(\rho_{\text{sb}}\hat{\mathcal{O}}^{(k)}) \tag{7.22}$$

where

$$\rho_{\text{sb}} = \frac{1}{4\pi}\int d^2\mathbf{\Omega}|N:\mathbf{\Omega}\rangle\langle N:\mathbf{\Omega}|, \tag{7.23}$$

corresponds to a (approximate) symmetry breaking description [43]. Indeed, although ρ_{sb} is clearly invariant upon rotations, a possible interpretation is that in each realization of the experiment, the system is in a symmetry-breaking state $|N:\mathbf{\Omega}\rangle$, but with a direction $\mathbf{\Omega}$ picked randomly. Note that such an interpretation would apply to any (overcomplete) basis in which ρ_{sb} is diagonal (for instance the $|N,S,M_z\rangle$ basis) but with a very different meaning, and thus it should not be taken literally.

Deviation to the symmetry breaking description In table 7.1, we compare the expectation values of a few observables, in the singlet state given by Eq. (7.18) and the approximate symmetry breaking description (SBD) given by Eq. (7.23).

- For the mean population and spin, the SBD gives the exact value.
- For the second moment of the population (or for the variance), the SBD gives the correct leading term of order N^2, but misses a term order N.
- For the mean spin square, the SBD gives the leading term of order N^2, which is vanishing. The next term, of order N is non-vanishing for the SBD and corresponds to the shot-noise of the nematic state, equals to $2N$ (see Chapter 2).
- We also look at the mean value of the projector $\hat{\Pi}_0 = |N:\mathbf{e}_z\rangle\langle N:\mathbf{e}_z|$ onto the state with all atoms in 0. The SBD is wrong by a factor of two. This is due to the fact that $\hat{\Pi}_0 = \hat{a}_0^{\dagger N}\hat{a}_0^N/N!$ is a N-body observable, and thus, in the integral of Eq. (7.19), the term $\left(\mathbf{\Omega}'\cdot\mathbf{\Omega}\right)^{N-k} = 1$ can certainly not be replaced by a Dirac distribution[2].

	$\hat{N}_0$	$\hat{\mathbf{S}}$	$\Delta\hat{N}_0^2$	$\hat{\mathbf{S}}^2$	$\hat{\Pi}_0$
Singlet	$\frac{N}{3}$	0	$\frac{4N^2}{45}+\frac{12N}{45}$	0	$\simeq\frac{1}{N}$
SBD	$\frac{N}{3}$	0	$\frac{4N^2}{45}$	$2N$	$\simeq\frac{1}{2N}$

Table 7.1: Comparison between the expectation values of a few observables in the singlet state and in the approximate symmetry-breaking description. For the projector onto the nematic state $|N:\mathbf{e}_z\rangle$, we only give the leading term in the limit $N \gg 1$, since this is enough to distinguish the two states.

We want to be experimentally able to clearly distinguish the singlet state from the SBD. By the definition of the latter, this cannot be achieved through a "rough" measurement of our typical observables ($i.e.$ population or spin). A precise measurement of the spin appears as clear-cut, but requires a high counting resolution, below the shot-noise to exclude the SBD, and at the single atom level to identify unambiguously the singlet state.

[2] The factor of two difference comes from the well defined parity of the singlet state, which only has overlap with states with even atom number in $m = 0$ populated because of the vanishing magnetization. See the appendix B for the expression of the singlet in the number basis.

Measurement of the singlet state The value of $\langle \Pi_0 \rangle \simeq 1/N$ may appear odd at first sight. Indeed, given the single particle density matrix Eq. (7.10), an atom has *a-priori* a probability $1/3$ to be in the state $m = 0$ (cf first column of table 7.1), and thus, one could expect the probability to measure all the atoms in that state to be $1/3^N$, much smaller than $1/N$. The discrepancy comes from the indistinguishability of the particles, which considerably reduces the number of configuration for typical situation, such as $N_0 = N/3$, and thus favors "extreme" situations, such as $N_0 = N$.

Further insight comes from the study of the evolution of the singlet state over a measurement discussed in [183]. This problem is closely related to the measurement of the relative phase of two independent BECs [184]. The authors of [183] conceived a thought experiment, where the spin state of k individual atoms ($k \gg 1$) leaking from a BEC, is measured along different axes. First, they consider a single BEC in the nematic state $|N : \mathbf{\Omega}\rangle$, they show that this protocol allows to determine the alignment $\mathbf{\Omega}$ of the state, with an accuracy $\propto 1/\sqrt{k}$. As for a singlet state, the measurement effectively projects the singlet onto a nematic state with a well defined alignment, picked at random. If the measurement is not read ($e.g.$ due to losses), a singlet state is thus projected onto the SBD (with $N - k$ atoms). At the beginning of the present section, we have emphasized the fragility of the singlet state to very small ($q > U_s/N^2$) QZE. Atom losses appear as another symmetry-breaking mechanism, but here the preferred direction is chosen by the measurement process, completely randomly. The overlap with the SBD increases with the number k of lost atoms, independently on the total number of atoms N[3]. On the other hand, the loss rate is typically $\propto N$ (or larger) and thus, the "bigger" the singlet, the more fragile it is.

7.2.3 Thermal fragmentation

Symmetry breaking description and thermal fluctuations Let us express the SBD in the spin state basis. Because of its $SO(3)$ symmetry, it is proportional to the identity within each S subspace. Thus we only need to compute the matrix elements (that must be independent on M_z)

$$\langle N, S, M_z | \rho_{\rm sb} | N, S, M_z \rangle = \frac{1}{4\pi} \int d^2\mathbf{\Omega} |\langle N, S, M_z | N : \mathbf{\Omega} \rangle|^2 \,. \tag{7.24}$$

In the appendix B we show (see also [185])

$$\langle N : \mathbf{\Omega} | N, S, M_z \rangle \simeq \sqrt{\frac{4\pi}{N}} e^{-\frac{S^2}{4N}} Y_{S,M_z}(\mathbf{\Omega}) \,, \tag{7.25}$$

where Y_{S,M_z} are the spherical harmonic. This expression is valid for $N \gg 1$ and $S \gg 1$. Using it in Eq. (7.24), we obtain

$$\langle N, S, M_z | \rho_{\rm sb} | N, S, M_z \rangle = \frac{1}{N} e^{-\frac{S^2}{2N}} \,. \tag{7.26}$$

at $q = 0$, the Hamiltonian (7.9) can be written as

$$\hat{H}_{\rm SMA} = \frac{U_s^2}{2N} \sum_{S,M} S(S+1) |N, S, M_z\rangle\langle N, S, M_z| \,. \tag{7.27}$$

Up to the approximation $S \gg 1$ (validated *a-posteriori*), the SBD can be seen as a thermal state

$$\rho_{\rm sb} \simeq \frac{1}{N} \exp\left(-\frac{\hat{H}_{\rm SMA}}{k_B T_{\rm sb}} \right) \,, \tag{7.28}$$

with an effective temperature $T_{\rm sb} = U_s/k_B \sim 1$ nK. This results shows the apparent similarity between quantum and thermal fluctuations.

Canonical ensemble Let us consider a general thermal state, within the SMA, so that the spatial degree of freedom is effectively at zero temperature, while the spin is at an effective temperature $T_{\rm spin}$. Such a situation is an idealized picture, but is not completely unrealistic. It describes a cloud out of equilibrium, for which the spin and spatial degrees of freedom have different effective temperatures, and are weakly coupled so that equilibration takes a very long time. The state of the system, given the Hamiltonian (7.9) is (in the canonical ensemble)

$$\rho_{\rm CE} = \frac{1}{Z_{\rm CE}} \exp\left(-\frac{\hat{H}_{\rm SMA}}{k_B T_{\rm spin}} \right) \,, \tag{7.29}$$

[3] This is another way to understand how "extreme configuration" such as $N_0 = N$ are more frequent than expected: once $k \gg 1$ atoms have been measured in say $m = 0$, the state is almost perfectly projected onto $|0\rangle^{\otimes N}$ and the $N - k \gg k$ remaining atoms are in $m = 0$.

Using a continuum approximation (valid for $k_B T_{\rm spin} \gg U_s/N$), the partition function can be calculated

$$Z_{\rm CE} \simeq \frac{1}{2\beta'}(1 - e^{-\beta' N^2}) \,, \tag{7.30}$$

where $\beta' = U_s/(2Nk_B T_{\rm spin})$. From this we can compute the total spin

$$\langle \hat{\mathbf{S}}^2 \rangle \simeq \frac{1}{\beta'} - \frac{N^2}{e^{\beta' N^2} - 1} \,. \tag{7.31}$$

The condition for having mostly the singlet populated reads $T_{\rm spin} \ll U_s/(Nk_B) \sim 10$ pK, while below shot noise fluctuations of the spin require $T_{\rm spin} < T_{\rm sb} \sim 1$nK. This is much colder than the (global) temperatures typically achieve in ultra-cold gases (~ 100 nK). However, using a protocol detailed in Sec. 7.4, we are able to prepare a sample with very low $T_{\rm spin}$. We do not know *a-priori* the precise value of $T_{\rm spin}$ at the end of the experiment, and cannot use Eq. (7.29) to make a quantitative prediction (we will extract $T_{\rm spin} \simeq 30.7 \pm 4.6$ pK from a fit to our data in Sec. 7.5).

7.2.4 Singlet state and entanglement

An essential difference between thermal and quantum fragmentation comes from the fact, that in the latter case, the BEC is in a highly correlated state. In this section we present how to reveal the entanglement.

Squeezing parameter As we have seen is Chapter 2, Sec. 2.4.1, for a separable state of N indistinguishable spins 1, $\langle \hat{\mathbf{S}}^2 \rangle \geq 2N$. Thus, we can introduce the following squeezing parameter[4]

$$\xi_s^2 = \frac{\langle \hat{\mathbf{S}}^2 \rangle}{2N} \,, \tag{7.32}$$

which reveals entanglement when $\xi_s < 1$. For the singlet state $\xi_s = 0$.

Block entanglement The squeezing parameter Eq.(7.32) has the advantage of being straightforward to extract from our measurements. It is well suited to detect entanglement of low spin states, but it does not constitute a general measure of entanglement (for instance it does not detect entanglement for the twin-Fock state or TMSV). We have introduced in Chapter 2 a generic measure of entanglement, based on the partitioning of the ensemble into two "blocks" containing n and $N-n$ atoms. The term "block" comes from models with localized spins [70] ($e.g$ a block can be n adjacent spins) but the situation is less intuitive in the case of itinerant spins. Yet, the reduced density matrix is perfectly well defined, see $e.g.$ [73]. In the appendix F, we propose a derivation of $\rho^{(n)}$ which gives a simple physical picture. We imagine that the atoms are initially confined in a single spatial mode A, are subsequently allowed to tunnel into another spatial mode B. For instance, A and B can be the two wells of a trap. They constitute the two blocks, and the partial trace is taken over the mode B. After selecting a given partition n, we obtain the following normalized reduced density matrix (expressed in the number basis)

$$\rho^{(n) j_+, j_-}_{i_+, i_-} = \binom{N}{n}^{-1} \langle \hat{P}^{(n)\dagger}_{i_+, i_-} \hat{P}^{(n)}_{j_+, j_-} \rangle \,, \tag{7.33}$$

where

$$\hat{P}^{(n)}_{i_+, i_-} = \frac{\hat{a}_{+1}^{i_+} \hat{a}_{-1}^{i_-} \hat{a}_0^{n-i_+-i_-}}{\sqrt{i_+! i_-! (n - i_+ - i_-)!}} \,. \tag{7.34}$$

The reduced density matrix has a clear physical meaning, it fully determines the probability distribution of any measurement performed within a block. For a pure state, a measure of entanglement is given by the Von-Neumann entropy of the reduced density matrix

$$\mathcal{S}_n = -{\rm Tr}_n(\rho^{(n)} \ln \rho^{(n)}) \,. \tag{7.35}$$

A single BEC is not entangled. Let us consider $n = 1$. A "quantum fragmented" BEC (ie at $T = 0$) is by definition entangled, and for this partitioning, the singlet state has maximal entanglement.

[4] This belongs to the family of squeezing parameters used to detect correlations between the spins (see [153] and Chapter 5). It is not directly linked to the metrological gain of an interferometric experiment.

In practice, we reconstruct the full state ρ (see Sec. 7.5) and compute $\rho^{(n)}$ numerically from Eq. (7.33). For a perfect singlet state, $\rho^{(n)}$ can be computed analytically. We start from an expression of the full density matrix in the nematic state overcomplete basis

$$\rho = \frac{N}{(4\pi)^2} \int d^2\mathbf{\Omega} d^2\mathbf{\Omega}' |N:\mathbf{\Omega}\rangle\langle N:\mathbf{\Omega}'| \tag{7.36}$$

We then assume that the atoms are distributed between two modes A and B so that the state becomes[5]

$$\rho = \frac{N}{(4\pi)^2} \int d^2\mathbf{\Omega} d^2\mathbf{\Omega}' |n:\mathbf{\Omega}\rangle_A |N-n:\mathbf{\Omega}\rangle_{BA}\langle n:\mathbf{\Omega}'|_B \langle N-n:\mathbf{\Omega}'| \tag{7.37}$$

We obtain the reduced density matrix by tracing over the mode B. It is convenient to use the spin state basis, the overlap between these states and the nematic states is given in Eq.(7.25) (see App.B and [50]). We obtain

$$\rho^{(n)} = \frac{N}{(4\pi)^2} \sum_{S,M} f_S^{N-n} \int d^2\mathbf{\Omega} d^2\mathbf{\Omega}' Y^*_{S,M}(\mathbf{\Omega}) Y_{S,M}(\mathbf{\Omega}') |n:\mathbf{\Omega}\rangle\langle n:\mathbf{\Omega}'| \tag{7.38}$$

where $f_S^k \simeq [4\pi/k \exp(-S^2/(2k))$. Furthermore, using

$$|nSM\rangle = \frac{1}{\sqrt{f_S^n}} \int d\mathbf{\Omega} Y_{SM}(\mathbf{\Omega}) |n:\mathbf{\Omega}\rangle\,, \tag{7.39}$$

we arrive to

$$\rho_{\mathrm{s}}^{(n)} \simeq \frac{N}{(4\pi)^2} \sum_{SM} f_S^n f_S^{N-n} |nSM\rangle\langle nSM|\,, \tag{7.40}$$

$$\simeq \frac{N}{n(N-n)} \exp\left(-\frac{N}{n(N-n)}\frac{S^2}{2}\right) \tag{7.41}$$

We recognize the expression of a thermal state

$$\rho^{(n)} \simeq \frac{1}{Z_n} \exp\left(-\frac{\hat{H}_{\mathrm{SMA}}}{k_B T_n}\right)\,, \tag{7.42}$$

where $\hat{H}_{\mathrm{SMA}}$ is given by Eq. (7.9) with $q = 0$ and

$$T_n = \frac{U_s}{k_B}\frac{n}{N}\left(1-\frac{n}{N}\right)\,. \tag{7.43}$$

The partition function is $Z_n = N k_B T_n / U_s$. Then entanglement entropy is

$$\mathcal{S}_n = -\mathrm{Tr}(\rho^{(n)} \ln \rho^{(n)})\,, \tag{7.44}$$

$$\simeq \ln Z_n + \frac{1}{k_b T_n}\langle \hat{H}_{\mathrm{SMA}}\rangle\,, \tag{7.45}$$

$$\simeq \ln Z_n - \frac{1}{Z_n T_n}\frac{dZ_n}{d(1/T_n)}\,, \tag{7.46}$$

$$\simeq \ln\left(n\left(1-\frac{n}{N}\right)\right) + 1\,. \tag{7.47}$$

The function $\mathcal{S}_n$ is non monotonic (see figure 55). This result strongly contrasts with the extensivity of the entropy of classical systems ($i.e.$ at large temperature). Note that an isotropic state is fully represented by the spin distribution,

$$\mathcal{P}_n(S) = \frac{1}{Z_n} S(S+1) \exp\left(-\frac{U_s S(S+1)}{2N k_B T_n}\right)\,. \tag{7.48}$$

We compare these analytical results with a numerical calculation using Eq. (7.33) on figure 55 and we observe an almost perfect agreement.

[5] A linear coupling between A and B would result in a binomial distribution of the atom number in these two modes which does not correspond to the state written in Eq.(7.37). The state obtained from Eq.(7.37) after partial tracing over B corresponds to the thermal state of Eq. (7.42) described within the canonical ensemble. The state obtained by coupling linearly A and B without selecting a well defined atom number corresponds to the grand canonical description of the same (in the thermodynamic limit) state.

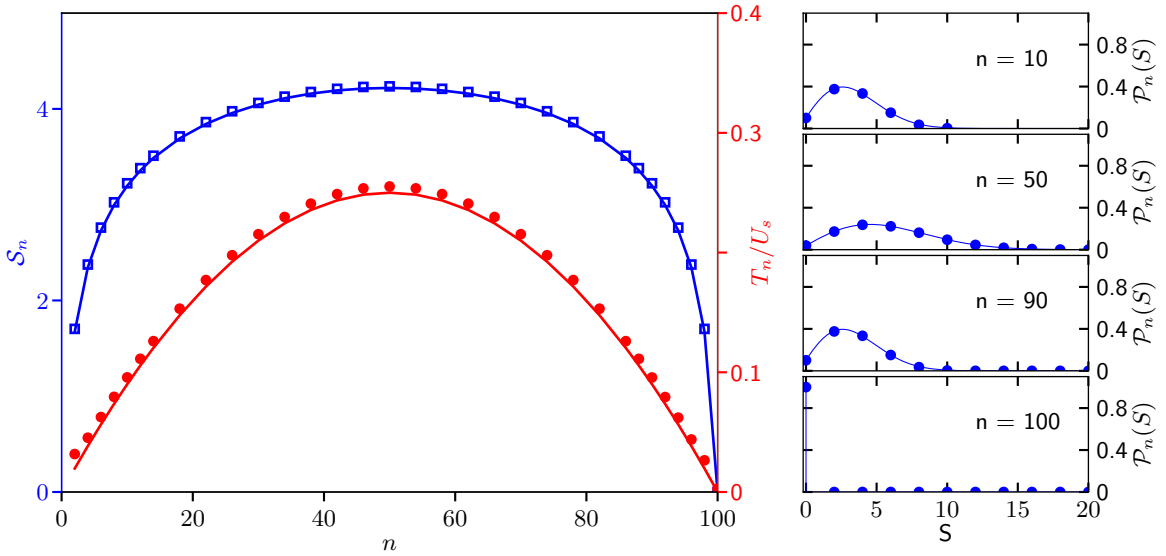

Figure 55: The main panel shows the entanglement entropy (open blue squares) and fitted temperature (filled red circles) of the reduced density matrix $\rho^{(n)}$ of a singlet state with $N = 100$ atoms, computed numerically using Eq. (7.33). The solid lines are the analytical results, corresponding to the thermal distribution Eq. (7.42). The panels on the right show the exact distribution $\mathcal{P}_n(S)$ (dots), and the thermal distribution (solid line) for various n.

7.3 Experimental protocol

Fragmented BECs have been the subject of many theoretical investigations (see *e.g.* [42] for a brief review). In terms of experiments, we should distinguish two types of approaches. A BEC can be fragmented dynamically, for instance after a quench into a regime of instability. This includes the type of experiments discussed in Chapters 5 and 6. Here we focus on situations where quantum fragmentation is observed at equilibrium. This is arguably more challenging and there are few experimental demonstrations reported in the literature. For spinor BECs, we are only aware of the work published in [158]. In this experiment, using an adiabatic following of the ground state of a spinor BEC from $q \sim 2U_s$ (the GS is near the nematic state) to $q \sim -2U_s$ (the GS is near the TFS[6]) a fragmented BEC with a high degree of entanglement is produced. More precisely, they measure a squeezing parameter $\zeta_s^2 = -11$ dB and an entanglement depth of 910^{+9900}_{-450} atoms (one standard deviation) out of 12000 atoms. However, the adiabaticity is not perfectly fulfilled, and they estimate that the first ~ 500 energy eigenstates have comparable overlaps with the final state.

When one tries to produce a fragmented state such as the TFS or the singlet state, an inherent difficulty comes from the near degeneracy of the low-lying eigenstates, the consequent extreme sensitivity of the system to technical fluctuations, and the long preparation time required to insure adiabaticity. More precisely, in the case of our experiment, after the discussion of Sec. 7.2, we arrive at the following specifications (for $N \sim 100$ and $U_s/h \sim 20$ Hz)

- A small QZE $q \lesssim U_s/N^2$ requires a magnetic field at the milliGauss level.
- The spin temperature $T_{\text{spin}} \lesssim U_s/(Nk_B)$ has to be on the order of a few tens of picoKelvin or below.
- The number of atoms lost between the preparation and observation of the state has to be kept of order one or below. For a loss rate τ (assuming one-body losses), the duration of the experiment must be $t \lesssim \tau/N$, on the order of a second.
- Finally, in order to distinguish the low spin states, the spin has to be measured with an accuracy near the single atom level.

The atom number is a strong limiting factor, which can be understood from the fact that fragmentation takes place near a phase transition, in a critical region that shrinks and disappears at the thermodynamic limit. Compared to the work reported in [158], we decided to work with much smaller condensates, with $N \sim 100$ atoms, in order to prevent the production of energy excitations[7]. In the rest of this section, we detail the methods we use to produce and observe a fragmented state.

[6] The atom used in [158] is Rubidium, which has ferromagnetic interactions. Thus the TFS is the ground state only because the constraint of vanishing magnetization. The absolute ground state is doubly degenerate and corresponds to the polarized states with all atoms in $m = \pm 1$ [28].

[7] We are also aided by the fact that sodium atoms have spin-dependent interactions significantly larger than Rubidium.

7.3.1 State preparation

Direct evaporative cooling at $q \sim U_s/N^2$ would not lead to the target state, since it relies on atom losses (which are a source of decoherence) and saturates at low densities at temperature orders of magnitude too large for our purposes. Instead, we prepare a single BEC in a large magnetic field, with all atoms in $m = 0$. We are able to create this state with very low spin entropy, and it thus constitutes a good starting point for an adiabatic ramp towards the phase transition, as sketched in figure 56. More precisely, the sequence we use is the following:

1. After evaporative cooling in a large bias magnetic field of $B_i = 1\,\mathrm{G}$ ($q/\hbar \simeq 300\,\mathrm{Hz}$), we have a BEC with about 2000 atoms in the state $m = 0$. Residual thermal atoms in the $m = \pm 1$ states are removed using spin-filtering.
2. To reduce the atom number, we perform an almost $\pi/2$ rotation which transfers most of the atoms in $m = \pm 1$, and then we "spin-filter" again. We are left with about 104 ± 15 (one standard deviation) atoms in $m = 0$.
3. In order to increase the density and therefore U_s, we recompress the trap. The trap frequencies at the end of the compression are about $(2, 2.8, 2)$ kHz and $U_s/\hbar \simeq 20\,\mathrm{Hz}$.
4. Finally, we ramp the magnetic field down to $B_f \simeq 4\,\mathrm{mG}$ ($q \simeq 4\,\mathrm{mHz}$) in $t_f = 1\,\mathrm{s}$.

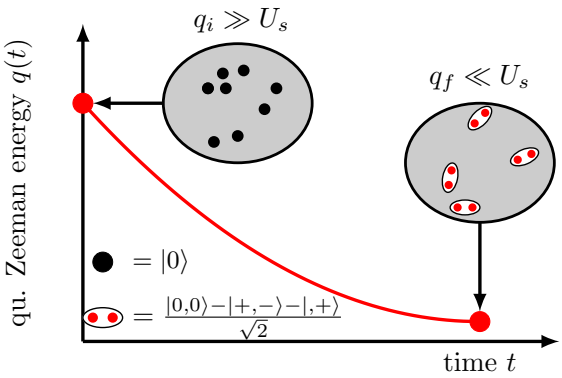

Figure 56: The experiment reported in this chapter consists in an adiabatic following of the ground state of a spinor BEC. The ramp starts with $q_i \gg U_s$, so that the ground state is essentially the nematic state with all atoms in $m = 0$, and stops at $q_f \ll U_s$ where the ground state constitutes a fragmented BEC. The latter is a highly entangled state, which can be viewed as a condensate of singlet pairs.

Adiabatic ramp The magnetic field ramp is designed to fulfill the best the adiabaticity criterion, which is achieved when the energy gap ΔE between the ground state and the first excited state verifies

$$\left|\frac{d\Delta E}{dt}\right| = \epsilon \frac{\Delta E^2}{\hbar}\,, \tag{7.49}$$

where ϵ is a number that characterizes the deviation to adiabaticity, and in that respect should be as small as possible. For almost the whole ramp we have $U_s/N^2 \ll q \ll U_s$, such that the Bogoliubov approximation applies and gives $\Delta E \simeq 2\hbar\omega_B \propto B$. The factor 2 comes from the conservation of $\hat{S}_z$, which imposes to create excitations by pairs (one in each Bogoliubov mode, see App. C). Integration of Eq.(7.49) yields (for $B_i \gg B_f$)

$$\frac{1}{B(t)} - \frac{1}{B_i} \propto \epsilon t \tag{7.50}$$

and thus

$$B(t) = \frac{B_i}{1 + \frac{B_i t}{B_f t_f}}\,, \tag{7.51}$$

and $\epsilon \simeq 1/(2\omega_f t_f)$. In practice, we use $B_i \simeq 1\,\mathrm{G}$ ($q/h \simeq 277\,\mathrm{Hz}$) so that $q \gg U_s$ and the initial state (all atoms in $m = 0$) is very close to the ground state. The ramp duration t_f is given by a compromise between the adiabaticity requirement and decoherence (*e.g.* due to atom losses). For a given t_f there is an optimal B_f, which results from a compromise between the adiabaticity requirement and the distance to $q = 0$. Experimentally we find that $B_f = 4\,\mathrm{mG}$ and $t_f = 1\,\mathrm{s}$ are optimal (in order

to minimize the total spin). With these parameters, $\omega_f = 2\pi \times 0.4\,\text{Hz}$ and $\epsilon = 0.2$. We simulated numerically the evolution of the state over the ramp. We show the results in figure 57 and compare them to the ground state expectation. We see little deviations, indicating that the adiabaticity criterion is well verified. The simulation shows that the state of the system at the end of the ramp is close to the singlet state (the fidelity is $> 80\,\%$). However, we expect deviations due to atom losses and to heat coming from the spatial degrees of freedom. The lifetime of the cloud is limited by one-body losses with a time scale of $\tau \simeq 100\,\text{s}$, thus, approximately one atom is lost on average during the ramp. The coupling to the spatial mode is more difficult to estimate *a-priori*. In Sec. 7.4.2 we will comment on an observation of the decoherence in our sample.

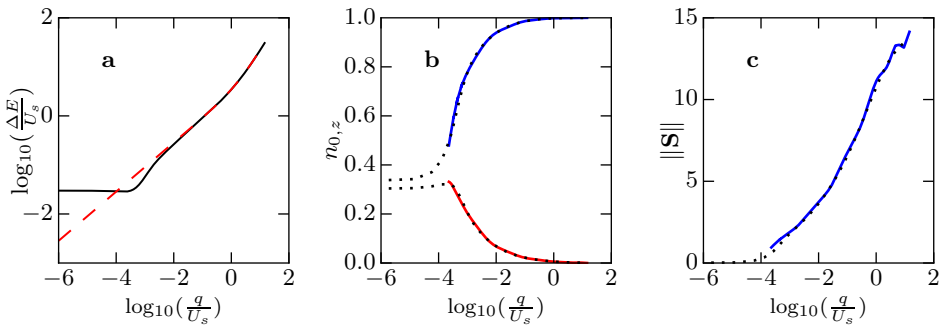

Figure 57: a Energy gap between the ground state and the first excited state of the SMA Hamiltonian Eq. (7.9) versus the QZE q. The solid line is the result of a numerical diagonalization, the dashed line corresponds to the Bogoliubov approximation. b Simulated evolution of n_0 (blue line) and Δn_0 (red line) over the ramp, versus $q(t)$. The dotted line corresponds to the expectation for the instantaneous ground state. c Evolution of the total spin over the ramp (solid line) and in the ground state (dotted line).

7.3.2 Diagnostic of the final state

We use fluorescence imaging (see Chapter 3) to count the population in each Zeeman state. After optimization of the integration region and of the MOT beam alignement, we measure a noise given in table 7.2. The imaging sequence requires a large magnetic

ΔN_+	ΔN_0	ΔN_-
1.2	1.4	1.1

Table 7.2: Detection noise on empty images in number of atoms.

field for the Stern-Gerlach separation. At the end of the adiabatic ramp, we quench the magnetic field to a value of ~ 2.5 G. The QZE $q \sim 1.7\,\text{kHz}$ is much larger than U_s so that spin-mixing dynamics is frozen, and the populations are conserved. We have verified this experimentally by scanning the duration of the ramp of the magnetic field. For short enough ramp, we did not observe any evolution of the populations.

The measurement of the population $N_{0,\pm1}$ gives us access to the value of the spin along the quantization axis, $S_z = N_{+1} - N_{-1}$. In order to measure the other spin components, we use a resonant radio-frequency oscillating field to couple the Zeeman sublevels. However, at the final field of 4 mG, for which $f_L = 2.8\,\text{kHz}$, we are not able to realize Rabi oscillations with a good contrast. This is due to fluctuations of the ambient magnetic field on the order of ~ 1 mG (see Chapter 3) which are not negligible compared to the bias field. To overcome this issue, we quickly (in 6 ms) ramp the magnetic field up to 50 mG. Then $f_L = 35\,\text{kHz}$ and $q/\hbar = 0.7\,\text{Hz}$. Keeping a small QZE is important in order to conserve the spin until the rotation is performed ($i\hbar\hat{S}_\nu = -q[\hat{S}_\nu, \hat{N}_0]$). We verified numerically and experimentally (scanning the intermediate field and the duration of the ramp) that it is indeed the case. Once the rotation is performed, we proceed as described above with Stern-Gerlach imaging.
The axis of rotation is determined by the phase of the RF-field. Let it be the y axis. A $\pi/2$ rotation maps the component $\hat{S}_x$ onto $\hat{S}_z$. In order to measure the $\hat{S}_y$, we insert a rotation around the z-axis before the rotation around the y-axis. This is achieved by simply adding a delay before the RF pulse. Indeed, the bias field is along z by definition, and therefore, the spin is naturally precessing around that axis.

7.4 Observation of a fragmented BEC

7.4.1 Evolution over the ramp

We report in figure 58 **a** our measurement of the mean value and standard deviation of the reduced population $n_0 = N_0/N$ over the ramp. As we decrease the QZE q, the condensate gets depleted, n_0 decreases and displays super-poissonian fluctuations. At the end of the ramp, the population in the three spin states are comparable, $n_0 \simeq 0.4$, $n_{+1} \simeq n_{-1} \simeq 0.3$. Concerning the spin observables (Fig.58 **b**), the measured mean value is compatible with zero all over the ramp and we focus on the standard deviation ΔS_z. It is initially limited by the imaging noise and barely increases over the ramp. On the other hand, ΔS_x steadily decreases and eventually reaches a value of 2.6 atoms, significantly below the initial shot noise level. We observe good qualitative agreement

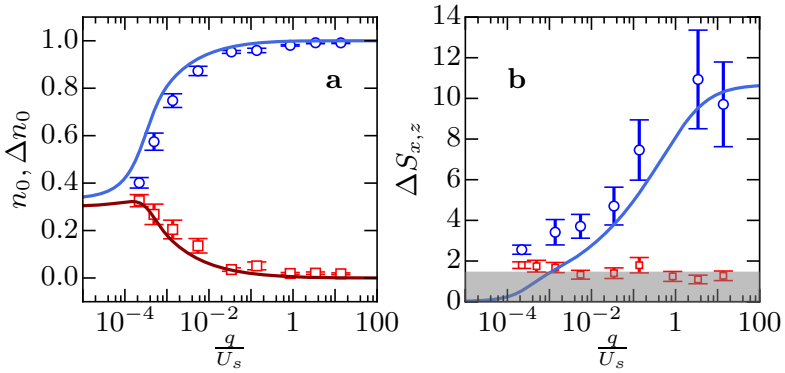

Figure 58: **a** Evolution of the mean reduced population n_0 (blue dots) and its standard deviation (red squares) showing super-Poissonian fluctuations. This contrasts with b the standard deviation of the transverse spin S_x (blue dots) that decreases below the shot noise while the longitudinal spin S_z (red squares) remains close to the imaging noise level (gray area). The solid lines are the value of the observable in the ground state of the Hamilitonian Eq. (7.9). Error bars represent two standard errors.

with the theory, but we notice a systematic deviation for n_0 and ΔS_x, especially towards the end of the ramp. Two effects could explain for this discrepancy: atom losses and heating. We now estimate the role of these effects by looking at the evolution after a hold time.

7.4.2 Lifetime and decoherence

We present in figure 59 the long-time evolution of the fragmented state, while the magnetic field is held at its final value of 4 mG. On a timescale of ~ 20 s, the super-Poissonian fluctuations of the population shrink, and saturate at a value compatible with shot-noise $1/\sqrt{N} \simeq 0.1$. Simultaneously, the standard deviations of both spin-components increase and reaches the shot-noise level at ~ 20 s. Our lifetime $\tau \sim 100$ s is mostly limited by one-body losses due to collisions with atoms of the ambient vapor inside the science chamber. Such losses are isotropic, and for $1 \ll N_{\text{loss}} \ll N$, we expect the total spin to evolve as $\Delta\hat{\mathbf{S}}^2 \simeq 2N_{\text{loss}}$ (the shot-noise) and each spin component as $\Delta S_\nu^2 \simeq 2N_{\text{loss}}/3$. As shown in figure 59, this simple model of decoherence underestimates the growth of the spin. Moreover, it cannot account for the decrease of Δn_0. Indeed, as explained in Sec. 7.2 (see also [183]), as long as the spatial degree of freedom remains condensed, atom losses are expected to lead to a statistical mixture of spin coherent states, which exhibits super-Poissonian fluctuations. The decrease of Δn_0 may be due to heating and a melting of the BEC (possibly driven by intensity fluctuations of the dipole trap).

7.4.3 Characterization of the state at the end of the ramp

Sensitivity to rotations We now focus on the state of the cloud at the end of the ramp. We show in figure 60 the evolution of $n_0(\phi)$ and $\Delta S_z(\phi)$ over a rotation of the spin by an angle ϕ around the y-axis. We compare the fragmented state obtained after the ramp to a nematic state. The latter shows large amplitude oscillations for both observables. In contrast, the fragmented state is fairly insensitive to rotations. This can be understood as a consequence of the $SO(3)$ symmetry of the Hamiltonian Eq. (7.9) at $q = 0$. Yet, due to imperfection in the state preparation, we see small residual oscillations. In particular, $\Delta S_z(\pi/2) = \Delta S_x(0)$ is maximal as expected. Indeed, before the ramp, ΔS_x is shot noise limited, while ΔS_z is vanishing. We have checked the isotropy of the spin in the (xy)-plane by performing a rotation around the quantization axis z prior to a $\pi/2$ rotation around the y-axis.

Using the parameter defined by Eq. (7.32), we measure at the end of the ramp $S_z^2 \simeq 3.55 \pm 0.36$, $S_x^2 \simeq 6.36 \pm 0.70$, thus (assuming $S_y^2 = S_x^2$), $\langle\hat{\mathbf{S}}^2\rangle \simeq 16.27 \pm 1.05$ and $\xi^2 \simeq 0.078 \simeq -11.1$ dB, with no removal of the imaging noise. From a reconstruction of the state (described in Sec. 7.5), which includes the detection noise, we extract $\langle\hat{\mathbf{S}}^2\rangle \simeq 9.91 \pm 0.88$, yielding $\xi^2 \simeq 0.048 \simeq -13.2$ dB.

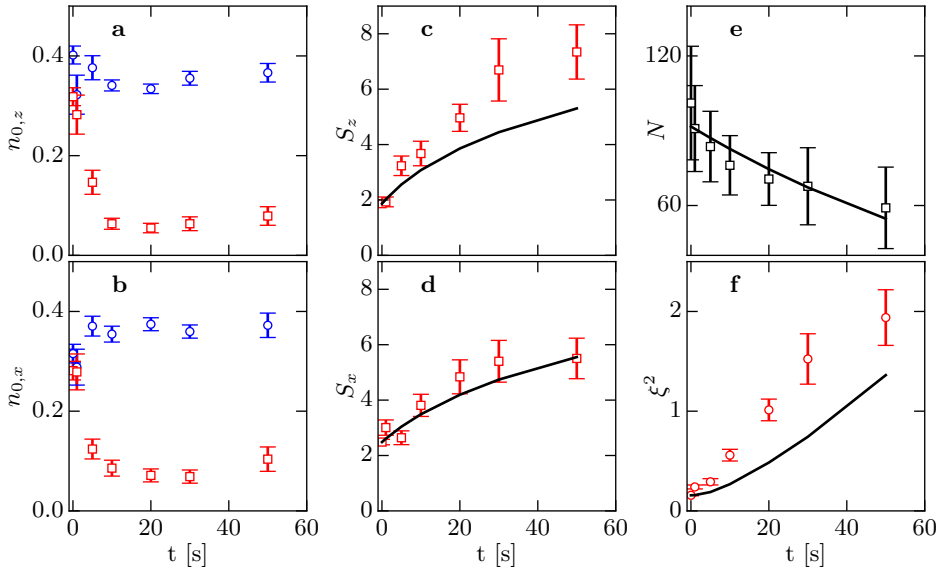

Figure 59: Long time evolution of the fragmented condensate. (a,b) Evolution of the mean reduced population n_0 (blue circles) and its standard deviation (red squares) before (a) and after (b) rotation. (c,d) Evolution of the standard deviation of the spin component S_z (c) and S_x (d). The solid black lines are the predicted evolutions given our atom losses and assuming isotropic losses. (e) Evolution of the atom number. The solid black line is an exponential fit. (f) Evolution of the squeezing parameter given by Eq. (7.32).

Population and spin distributions We present in figure 61, the distribution of the observables n_0 and S_z, for the state before rotation ($n_{0,z}$,S_z) and after a $\pi/2$ rotation ($n_{0,x}$,S_x). For comparison we show the same distributions for the nematic state $|N:\mathbf{e}_z\rangle$. The latter has before rotation $n_0 \simeq 1$ and ΔS_z limited by imaging noise. After a $\pi/2$ rotation, each atom is in the $(|+1\rangle+|-1\rangle)/\sqrt{2}$ state (up to experimental fluctuations). The distribution of S_z is Poissonian, with a width equal to $\sqrt{N}$. Our measurements are in excellent agreement with this prediction. For the fragmented state, the distribution of n_0 is very broad and overall similar before and after rotation. The distribution of S_z is almost identical to that of the imaging noise. The distribution of S_x is only slightly larger and much narrower than for the nematic state.

Single particle-density matrix The single particle density matrix can be fully determined from the evolution of the state under a composition of two rotations. We first rotate the state around the z-axis by a variable angle ϕ. We then rotate the state around the y-axis by an angle $\pi/4$. We measure $N_0^R(\phi)$ and $S_z^R(\phi)$. Neglecting the effects of the interaction and the QZE (the duration of the rotation is $\sim 10\,\mu$s, much faster than $\hbar/q$ and $\hbar/U_s$), we obtain

$$N_0^R(\phi) = \frac{N+N_0}{4} + \frac{1}{\sqrt{2}}\left(\cos\phi(J_x^{+1,0} - J_x^{-1,0}) - \sin\phi(J_y^{+1,0} + J_y^{-1,0})\right) - \frac{1}{2}\left(\cos 2\phi J_x^{+1,-1} - \sin 2\phi J_y^{+1,-1}\right), \tag{7.52}$$

$$S_z^R(\phi) = \frac{1}{\sqrt{2}}S_z - \cos\phi\left(J_x^{+1,0} + J_x^{-1,0}\right) + \sin\phi\left(J_y^{+1,0} - J_y^{-1,0}\right), \tag{7.53}$$

where $J_x^{m,m'} = (a_m^\dagger a_{m'} + a_m a_{m'}^\dagger)/2$ and $J_y^{m,m'} = (a_m^\dagger a_{m'} - a_m a_{m'}^\dagger)/(2i)$ are pseudo-spin operators. They are linked to the single-particle density matrix elements via

$$\rho^{(1)}_{m,m'} = \frac{1}{N}\langle \hat{a}_m^\dagger \hat{a}_{m'}\rangle = \frac{1}{N}\langle \hat{J}_x^{m,m'} + i\hat{J}_y^{m,m'}\rangle\,. \tag{7.54}$$

From a fit to the reduced population $n_0^R(\phi)$ and reduced spin $s_z^R(\phi)$ (fig. 62) we fully reconstruct $\rho^{(1)}$ (fig. 63).

As a control experiment, we reconstructed $\rho^{(1)}$ for a nematic state having comparable populations in the three Zeeman states. We found that $\rho^{(1)}$ has three similar diagonal elements and significant off-diagonal elements (coherences). The spectrum has one dominant eigenvalue $= 0.94 \pm 0.04$, characterizing a single condensate.

For the state produced at the end of the adiabatic ramp, within the measurement accuracy, $\rho^{(1)}$ is diagonal in the number basis, it has three comparable eigenvalues and the state is close to being maximally fragmented. However the measurement of $\rho^{(1)}$ alone does not reveal whether the fragmentation is driven by quantum or classical (*e.g.* thermal) fluctuations. Two-body observables

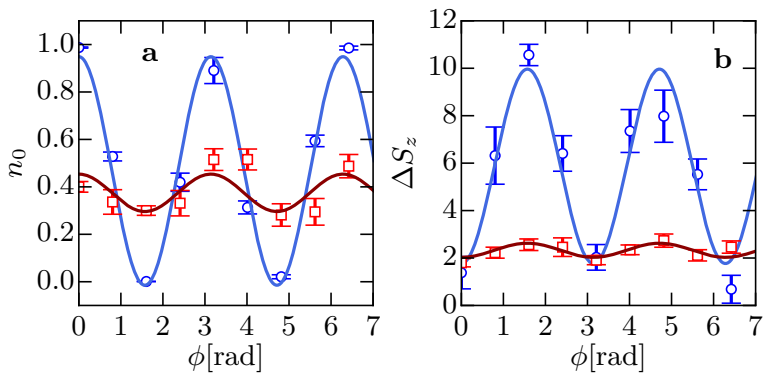

Figure 60: **a** Evolution of the reduced population n_0 over a rotation of the spin for a polar state (blue dots) and a fragmented state (red squares). **b** Evolution of the standard deviation of the longitudinal spin ΔS_z. For both observables, the fragmented state shows a weak sensitivity to rotation compared to the polar state. The solid lines are sinusoidal fits.

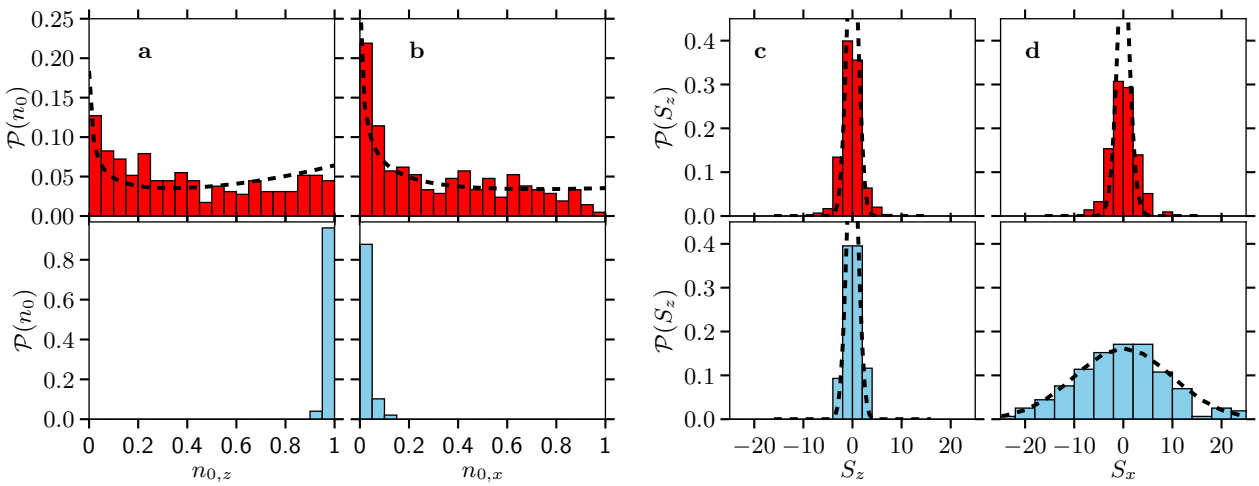

Figure 61: Upper panels: fragmented state, lower panel: polar state. a,b Distribution of n_0 before rotation ($n_{0,z}$,a) and after ($n_{0,x}$,b). For the fragmented state, both distributions are broad and fairly similar, in sharp contrast with the narrow distributions of n_0 in the nematic states. The dashed lines are the results of numerical simulation for $N = 100$. c Distribution of S_z. It is limited by the detection noise (dashed line) for the nematic state, and only slightly larger for the fragmented state. d Distribution of S_x. It limited by the projection noise for the nematic state, and much below that level for the fragmented state.

provide more information, in particular the squeezing of the spin $\hat{\mathbf{S}}^2$ hints towards entanglement as the main mechanism behind the fragmentation. This hypothesis finds a decisive support with a reconstruction of the many-body state.

7.5 Many-body state reconstruction

7.5.1 Introduction

A quantum state fully determines the probability distribution of any observable, and conversely, the probability distributions of a sufficient set of observables, constituting a so-called quorum, fully determine a quantum state. The procedure used to deduce the quantum state from a set of measurements is called a tomography. It can be a formidable task, even for mesoscopic samples. To a large extent, this is due to the exponential increase of the Hilbert space dimension with the number of particles, and thereby of the number of measurements *a-priori* required to fully characterize the state. In the case of indistinguishable particles distributed in a few modes, the restriction to the symmetric subspace alleviates significantly the problem, and various reconstruction techniques have been developed, initially in the context of quantum optics (see *e.g.* [186, 187] for reviews).

One can distinguish two types of approach, those relying on an inverse transformation and those based on statistical inferences. The former have been initially used to reconstruct the state of the electromagnetic field in a single mode, which can be viewed as a harmonic oscillator. Contrary to the classical case, measuring the "position" and "momentum" is not enough to fully determine a generic quantum state. However, the continuous set of "quadratures" obtained by linear combinations of position and momentum, forms a quorum, and can be measured using homodyne detection. The resulting probability distributions are

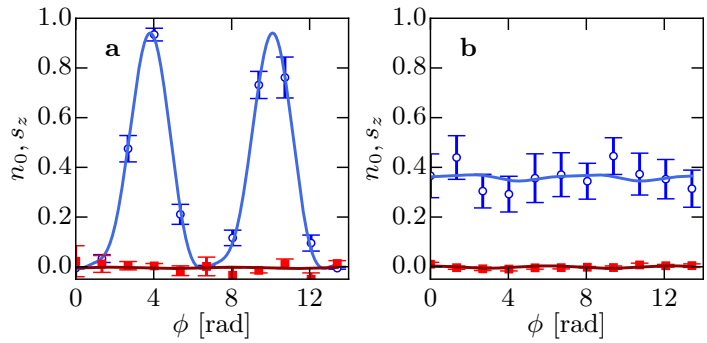

Figure 62: Evolution of the reduced population n_0 (blue dots) and spin s_z (red squares) under the rotations $\mathcal{R}_y(\frac{\pi}{4})\mathcal{R}_z(\phi)$, for a polar (a) and fragmented state (b). The solid lines are the fits from which we extract $\rho^{(1)}$.

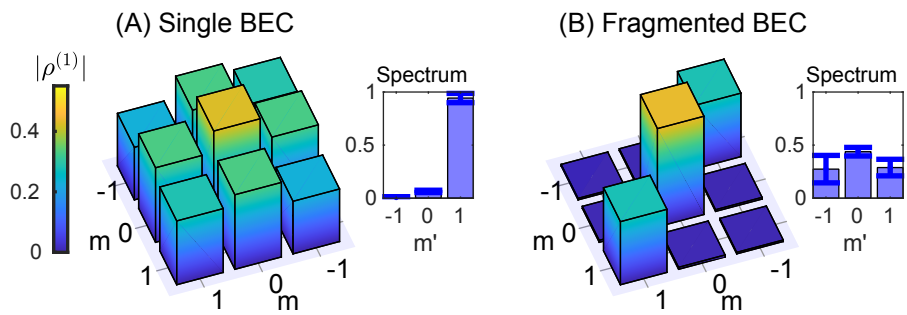

Figure 63: Reconstructed single particle density matrix $\rho^{(1)}$ (we only show the modulus of the matrix elements) for a coherent state (A) and for a fragmented state (B). The former has one eigenvalue of order one, while the latter has three comparable eigenvalues.

linked to the Wigner distribution (characterizing the whole quantum state) via the Radon transform. Using the inverse transform, the quantum state can be deduced from the measurement of the quadratures amplitude. This technique has been used, *e.g.* in the early experiment [188], to reconstruct a squeezed-vacuum state with on average three photons. Tomography based on an inverse transformation has the advantage of being mathematically transparent and easy to implement, but it suffers from important practical draw backs. First, the inverse transformation complexity increases rapidly with the number of modes [187]. Second, it is difficult to take into account experimental imperfections, for instance noisy measurements and finite data sets, which can lead to unphysical reconstructed states (*e.g.* not positive).

Methods based on statistical inferences have been developed, which allow for a better consideration of the experimental realities [186, 187]. Two popular ones are the maximum-likelihood (MaxLik) and maximum-entropy (MaxEnt) methods. In the MaxLik approach, one looks for the state which maximizes the probability to obtain a given data set. The MaxEnt method reconstructs the state that has maximal entropy under some constraints, carefully chosen to reflect the measurements (typically one imposes the mean value of some measured observables). In these approaches, tomography is no longer an inversion problem, but a maximization problem. The solution can be found analytically (MaxEnt) or using an iterative algorithm (MaxLik).

The MaxLik method has been used in two recent spinor BEC (with two internal components and in the SMA) experiments, for the reconstruction of the many-body spin state of a few [189] and a few hundred atoms [15]. The knowledge of the full quantum state allows to extract quantities such as the negativity or the quantum Fisher information [189], which are not observables (they are non-linear functionals of the quantum state) and usually hard to estimate. Similarly, the results of the present section will be used in Sec. 7.5.5 to extract the entanglement entropy. Let us mention that techniques have been developed to extract Fisher information and Rényi entropy without requiring a full tomography [15, 72].

In this section, we report on our implementation of these two techniques to reconstruct the density matrix of the collective state of the atoms at the end of the ramp. Our analysis makes use of about 500 shots of the state at the end of the ramp without rotation and with a $\pi/2$ rotation around y, and about 600 shots for intermediate rotations around the $y-$axis and around the $z-$axis.

Basis for the reconstructed state In the SMA, the state of the system can be written as $\rho = \bigoplus_N \rho^{(N)}$, where $\rho^{(N)}$, the restriction to the subspace with N atoms, can be decomposed in the basis of the collective spin state $|N, S, M_z\rangle$, where $S \leq N$ has the same parity as N due to the exchange symmetry. Let us first consider that N is fixed. The size of the Hilbert space is about $N^2/2 \sim 5000$, larger than the number of measurements that we have performed... Fortunately, we know that in the $|N, S, M_z\rangle$ basis, the state is very localized allowing to truncate the Hilbert space to the states with $S < S_{\max}$. Indeed, we have measured

$\langle \hat{\mathbf{S}}^2 \rangle \simeq 16$ and therefore, the total weight of the states with a spin larger than $S_{\max}$ is less than $16/[S_{\max}(S_{\max}+1)]$. This is a very rough bound, saturated for a very unlikely state which has non-zero weights only in the $S = 0$ and $S = S_{\max}+1$ subspaces. In practice, we reconstructed the state of the system with $S_{\max} = 20$ (we have increased $S_{\max}$ to 40 and verified that the reconstructed state was essentially identical).
We now address the issue of the atom number fluctuations. After projection on the $S \leq S_{\max}$ subspace, the state of the system can be written as $\rho = \bigoplus_N \rho^{(N,S\leq S_{\max})}$. To progress, we make the assumption that all of the matrices $\rho^{(N,S<S_{\max})}$ where S has a given parity are identical. As we have mentioned in Sec. 7.3, lower N are more favorable to reach the very low S state, and thus the approximation is valid only for small fluctuations of N. In practice, N fluctuates by 15 % (one standard deviation), and we found no clear correlations between N and S in the data, which justifies the approximation. Therefore, we write the state of the spin as:

$$\rho = \rho_{\text{even}}^{\overline{N}} \oplus \rho_{\text{odd}}^{\overline{N}+1} , \tag{7.55}$$

where $\overline{N} = 104$. We also perform the reconstructions for $\overline{N}$ between 89 and 119 to evaluate the uncertainty on the reconstructed states (see Sec. 7.5.2).

Imaging noise It is important to carefully take into account the imaging noise that can add systematic errors in the reconstruction of the state. We will see how we take it into account in the two reconstructions protocols. The imaging noise is dominated by stray light shot noise and is thus normally distributed (see Chapter 3)

$$\mathcal{P}_{\text{noise}}(x) = \frac{1}{\sqrt{2\pi\sigma_{\text{noise}}^2}} e^{-x^2/2\sigma_{\text{noise}}^2} , \tag{7.56}$$

with a standard deviation slightly dependent on the Zeeman state and given in the table 7.2.

7.5.2 Maximum likelihood reconstruction

Principle Let $\mathcal{P}(\rho|\{x_j\})$ be the probability for our system to be in the state ρ given our set of measurement outcomes $\{x_j\}$. The only *a-priori* information that we assume on the state of the system is that it can be written as in Eq. (7.55). Bayes theorem yields

$$\mathcal{P}(\rho|\{x_j\}) = \frac{\mathcal{P}(\{x_j\}|\rho)\,\mathcal{P}(\rho)}{\sum_{\rho'} \mathcal{P}(\{x_j\}|\rho')\,\mathcal{P}(\rho')} , \tag{7.57}$$

where $\mathcal{P}(\rho)$ contains the *a-priori* information that we have on the state. In our case, we only assume that ρ can be written as in Eq. (7.55). If so, $\mathcal{P}(\rho) \propto 1$, otherwise $\mathcal{P}(\rho) = 0$. Thus, Eq. (7.57) can be rewritten as

$$\mathcal{P}(\rho|\{x_j\}) = \frac{\mathcal{P}(\{x_j\}|\rho)}{\sum_{\rho} \mathcal{P}(\{x_j\}|\rho)} , \tag{7.58}$$

where the sum is taken over all states of the form given by Eq. (7.55). The MaxLik state ρ_{ML} is defined as the argument maximum of the functional $\mathcal{P}(\rho|\{x_j\})$. We will present the algorithm that we use to compute ρ_{ML}, but before, let us explicit the probability in the right hand side of Eq. (7.58). On a given shot j, we extract three quantities, N_j, $n_{0,j}^R$ and $S_{z,j}^R$ where the superscript R indicates a possible rotation of the state. For the total atom number, according to the Eq.(7.55), only the parity matter, not the absolute value. However, our imaging noise forbids a reliable estimation of the parity of N. For this reason, we reduce $\{x_j\}$ to the measurement of $n_{0,j}^R$ and $S_{z,j}^R$. In the case of the spin measurement, we take into account the imaging noise. It is uncorrelated with the state of the system so that

$$\mathcal{P}(S_{z,j}^R|\rho) = \sum_{|M|\leq S_{\max}} \mathcal{P}_{\text{noise}}(S_{z,j}^R - M)\text{Tr}(\hat{P}_M \hat{\mathcal{R}}_j^\dagger \rho \hat{\mathcal{R}}_j) , \tag{7.59}$$

where $\hat{P}_M = \sum_{S\geq|M|} |S, M_z\rangle\langle S, M_z|$ and $\hat{\mathcal{R}}_j$ the operator describing the rotation applied for the shot j.

Algorithm The algorithm is described in [190]. We present it briefly, using identical notations. The measurement of each observable is binned. We write f_k the frequency of occurrence of a measurement in the bin k. We define $\text{pr}_\text{k} = \text{Tr}(\hat{\Pi}_\text{k}\rho)$ the probability for the outcome to fall in the bin k given the state ρ. Finally, we introduce the operators:

$$\hat{R}(\rho) = \sum_k \frac{f_k}{\text{pr}_\text{k}} \hat{\Pi}_k . \tag{7.60}$$

If ρ describes correctly our data, $\mathrm{pr_k} \simeq \mathrm{f_k}$ and $\hat{R}(\rho) \simeq \mathrm{Id}$. The idea is to compute iteratively the elements of the sequence defined by the recurrence relation

$$\rho_{n+1} = \mathcal{N}_n \hat{R}(\rho_n)\rho_n \hat{R}(\rho_n)\,, \tag{7.61}$$

where $\mathcal{N}_n$ is a normalization factor. In the limit of infinitly small bins, this sequence converge to ρ_{ML} [190]. The population and spin observables do not couple state of different parity, neither do the operator $\hat{R}$, and thus the separability of the parity sectors required by Eq. (7.55) is conserved by the algorithm. Similarly, the matrix ρ_n remains Hermitian, positive and of trace one at every step of the algorithm. We make a few practical remarks:

- We initiate the recurrence with the maximally mixed state $\rho_0 = \mathrm{Id}/(\mathrm{S_{max}}+1)^2$.
- We stop the iteration when the fidelity between ρ_{n+1} and ρ_n is larger than 99.9%. It occurs after ~ 15 iterations.
- We use our whole set of measurements, including all rotations of the state. For each observable that we have measured, the width of the bin is chosen inversely proportional to the number of shots. When we have less shots, the bins are wider and therefore the operators $\hat{\Pi}_k$ are projectors onto larger subspace. This effectively reduces the impact of the measurements that have less shots. If the bins we use are too small for the data set, the algorithm becomes unstable.

Uncertainty To evaluate the uncertainty on the reconstructed density matrix ρ_{ML}, we follow the protocol described in [190]. From ρ_{ML}, we generate random sets of possible outcomes for our measurements (in practice, we simulate our experiment 100 times). For each simulated set of measurements, we perform the reconstruction algorithm and get the maximum likelihood density matrix of the simulated sets $\rho_{\mathrm{ML,sim}}$. The average fidelity between $\rho_{\mathrm{ML,sim}}$ and ρ_{ML} is 96%, indicating a faithful reconstruction. From the reconstructed density matrix, we compute the confidence intervals for the matrix elements of ρ_{ML}, and for the other quantities (temperature, entropy) extracted in Sec.7.5.5. The latter also include the dispersion due to atom number fluctuations, taken into account by performing the reconstruction with different atom numbers $\overline{N}$.

7.5.3 Maximum entropy reconstruction

Principle We report here on an alternative reconstruction scheme. Following the Jaynes principle of maximal entropy, the MaxEnt state ρ_{ME}, is defined as the state of maximal entropy, given a set of constraints imposed to represent our measurements [191]. This prescription can be interpreted in two equivalent ways: (i) The MaxEnt state does not carry any information except that brought by the constraint, *i.e.* by the measurement. (ii) In analogy with statistical mechanics, one can also imagine a statistical ensemble which contains all the states that satisfy to the imposed constraints. We are sure to find the actual state within this ensemble [8]. The associated density matrix is ρ_{ME}.

The constraints are of the form $\mathrm{Tr}(\hat{\mathrm{O}}_\mathrm{i}\rho_{\mathrm{ME}}) = \overline{\mathrm{O}}_\mathrm{i}$, where the $\hat{O}_i$ are some observables that we have measured, and $\overline{O}_i$ the mean values of the outcomes. The MaxEnt state ρ_{ME} is the argument maximum of the functional

$$\mathcal{L}(\rho) = -\mathrm{Tr}(\rho\log\rho) - \sum_\mathrm{i} \lambda_\mathrm{i}\mathrm{Tr}\left(\hat{\mathrm{O}}_\mathrm{i}\rho\right)\,, \tag{7.62}$$

restricted to the exchange-symmetric states. The solution is

$$\rho_{\mathrm{ME}} = \frac{1}{Z}\exp\left(-\sum_i \lambda_i \hat{O}_i\right)\,. \tag{7.63}$$

where $Z = \mathrm{Tr}\left(\exp\left(-\sum_\mathrm{i}\lambda_\mathrm{i}\hat{\mathrm{O}}_\mathrm{i}\right)\right)$, and the Lagrange multipliers λ_i are given by

$$\overline{O}_i = \mathrm{Tr}\left(\hat{\mathrm{O}}_\mathrm{i}\rho_{\mathrm{ME}}\right)\,. \tag{7.64}$$

In practice:

- We have chosen the set of observables $\{S_z^2, S_\perp^2, N_{0z}, N_{0x}\}$.
- We assume $S_x = S_y = S_\perp/2$, which was well verified by performing rotations of the states.
- We do not use the data at intermediate rotations, because we do not have enough measurements for each angle to reliably extract a constraint.

[8] This interpretation assumes that the constraints are indeed verified by the state. In practice this is never exactly the case and an error in the estimation of the constraints results in an error on the MaxEnt state.

- We solve the equations (7.64) numerically.
- The constraint on the measurement of N_0 is much weaker than the ones on the spins, since the distribution of N_0 is close to have maximal entropy.
- We do not impose any constraint on the mean value of $S_{z,\perp}$. Indeed the maximum of entropy is reached for isotropic mixture, for which the mean spin vanishes, which corresponds to our measurement.
- We found that constraining higher moments was not changing significantly the results. Moreover it is important to have a small uncertainty on the constraint we are applying.

Detection noise The detection noise adds a systematic error on the constraint $\langle S_\nu^2 \rangle$ if it is not taken into account. From Eq. (7.59), we extract $\mathcal{P}(M_\nu) = \mathrm{Tr}(\hat{P}_{M_\nu}\rho)$, where $\nu = \{z, \perp\}$, using a fit with $2S_{\max}+1$ parameters. This operation is a discrete deconvolution; the continuous analog, assuming two normal distributions, can be performed analytically, and yields a normal distribution with $\langle S_\nu^2 \rangle_{\mathrm{real}} = \langle S_\nu^2 \rangle_{\mathrm{meas}} - \sigma^2_{\mathrm{noise}}$ (here $\sigma^2_{\mathrm{noise}} \simeq 2.3$). The results of the fit are reported in Table 7.3 and are consistent with this prediction.

	$\langle \hat{S}_z^2 \rangle$	$\langle \hat{S}_x^2 \rangle$
Measured	3.55 ± 0.36	6.36 ± 0.70
Inferred	1.17 ± 0.36	4.37 ± 0.64

Table 7.3: Results of the noise removal on the spin distribution before and after rotation.

Uncertainty We use the same methods as for the MaxLik reconstruction. Once we have determined ρ_{ME}, we simulate our measurements a hundred times (including the addition of imaging noise). For each simulated outcome we construct $\rho_{\mathrm{ME,sim}}$, using the same procedure as for the real data sets (starting from the noise removal). The mean fidelity with ρ_{ME} is 99%.

7.5.4 Results

Comparison of the two reconstructed states Given a data set that allows for an unambiguous characterization of the quantum state, both methods should work and yield essentially the same result. They differ however in the case of an incomplete data set. To illustrate this, we consider two extreme situations:

- The data set consists in many measurements of a few observables. For instance, let us assume that we have only measured $\hat{S}_z$, and find it to be exactly vanishing. All the $|S, M_z = 0\rangle$ state can explain that result. The MaxEnt state is the statistical mixture of all those states with equal weights. The MaxLik state is on the other hand ill defined, since all $|S, M_z = 0\rangle$ states (plus linear combinations and statistical mixtures) maximize the functional Eq. (7.58).
- The data set consists of a few measurements of many observables. In that case, it can be difficult to recast all measurements in a few constraints (with little uncertainty), needed to construct ρ_{ME}. The MaxLik avoids this issue and may work.

In our situation we have many measurements of the observables $\hat{S}_\nu$ and $\hat{N}_{0,\nu}$ for $\nu = z, x$. We have used those to build ρ_{ME}. We have additional measurements at intermediate rotations, but with less data and thus we only used them for the MaxLik reconstruction.

The two reconstruction methods give a similar outcome. The fidelity between the two reconstructed states is $\mathrm{Tr}\left(\sqrt{\sqrt{\rho_{\mathrm{ME}}}\rho_{\mathrm{ML}}\sqrt{\rho_{\mathrm{ME}}}}\right)^2 \simeq 0.94$. We compare both reconstructions on figure 64. They are almost diagonal in the $|S, M_z\rangle$ basis and we thus only show the diagonal elements. The MaxEnt state has a larger entropy, which is by construction expected, but part of the difference may also be due to the smaller data set used for this reconstruction. The MaxLik state has slightly larger error bars, due to the fact that in the MaxLik reconstruction, the lack of information ($i.e.$ lack of measurement) on the state results in uncertainty on ρ_{ML}. For the MaxEnt reconstruction, the lack of information simply results in a larger entropy and the uncertainty on ρ_{ME} only comes from the uncertainty on the constraint ($i.e.$ on the measurement of $\overline{O}_i$). In the following, we will focus on the MaxLik state, which makes use of the whole data set.

7.5.5 Entanglement Entropy

From the reconstructed state, we can compute the successive reduced density matrices $\rho^{(n)}$ given by Eq. (7.33). For this analysis we focus on the MaxLik reconstructed state, projected on the S even subspace. We show the total spin distributions of the density matrix for $n = 53, 93$ and $n = \overline{N} = 104$ in figure 65. For $n < \overline{N}$, they are very well fitted by a thermal distribution, as expected from the results of Sec. 7.2.4. For $n = \overline{N}$, we observe a small deviation from the thermal distribution due to the residual

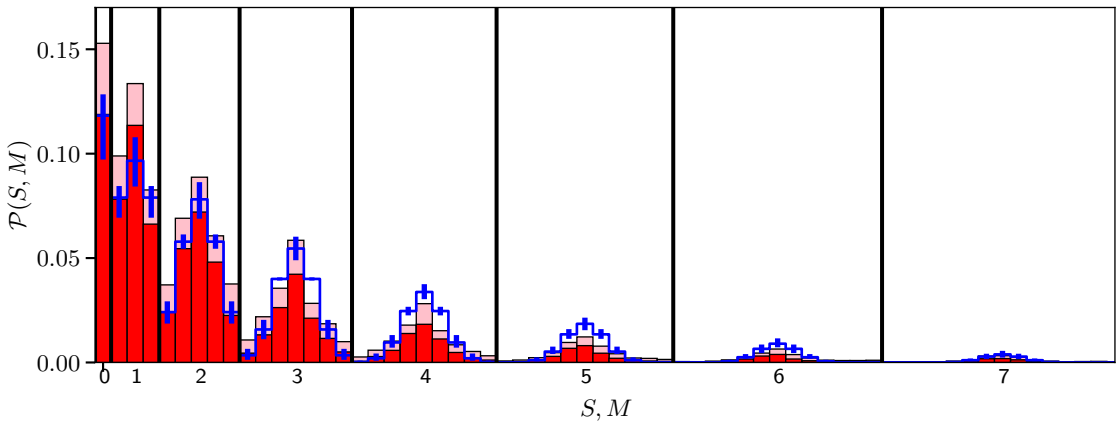

Figure 64: Reconstructed MaxLik (red) and MaxEnt (blue) states in the $|S, M_z\rangle$ basis. We only show the diagonal elements. The solid lines delimits the S subspace, and within a subspace the states are ordered by increasing M_z from $-S$ to $+S$ (the labels refers to the value of S). The error bars (pink area for the MaxLik state) correspond to the 66% confidence interval.

anisotropy of the state; indeed the spin is smaller along the z axis than along the other two axes. We plot the fitted temperatures T_n and entropy $\mathcal{S}_n$ of the state $\rho_{\mathrm{ML}}^{(n)}$ as a function of n/N. The shaded area corresponds to the 66% confidence intervals, which include the uncertainty on the reconstruction (determined from the reconstruction based on simulated data sets), and the atom number fluctuations (performing the reconstruction for different atom numbers).

We observe qualitatively the same behavior as for an ideal singlet state. However, the reconstructed state has a non-zero thermal entropy. As n increases, for $n < N/2$, both the entanglement and thermal entropy increases. For $n > N/2$, the thermal entropy keeps increasing while the entanglement entropy decreases. This competition results in a less pronounced bending of the entropy for $n > N/2$ compared to the theory. Yet, we see a clear reduction of the entropy that cannot be realized with classical states. This effect appears clearly if one looks at the temperature, or the spin distributions.

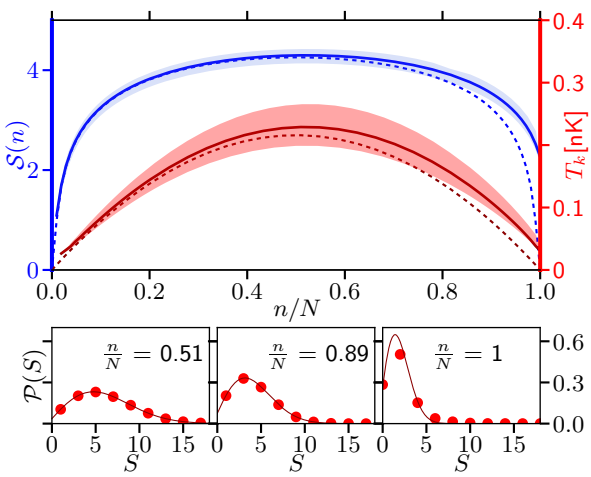

Figure 65: The main panel shows the entropy (blue line) and temperature (red line) of the reduced density matrix $\rho_{\mathrm{ML}}^{(n)}$ for the reconstructed MaxLik state in the N even subspace (solid lines) and the singlet state (dashed lines). The small panel on the right show the spin distribution in the state $\rho_{\mathrm{ML}}^{(n)}$, for $n = 53, 93, 104$ ($N = 104$). The solid lines are thermal fit from which we extract the spin temperature.

Simulated reconstruction of the singlet state The overlap between the MaxLik state and the singlet state is $\simeq 0.28^{+0.03}_{-0.09}$ (restricting to the state to the even parity sector). In theory, it should be $\sim 80\%$ (from a simulation of the evolution over the ramp). Part of the discrepancy is due to imperfection in the state preparation, as discussed in Sec. 7.4.2, but the state reconstruction is also expected to reduce the overlap with the singlet state. Indeed, our counting resolution does not allow us to distinguish two states with consecutive S. In order to estimate the effect of the imperfection in the diagnostic and the reconstruction, we simulated the outcome of the measurement, given a pure singlet state. We then apply the MaxLik reconstruction to this simulated data set. We found that the resulting state has a $\simeq 73\%$ overlap with the singlet state.

7.6 Outlooks: shortcut to adiabaticity

The strategy that we have used to prepare an entangled many-body state consists in an adiabatic ramp, from a product state which can be produced with high fidelity, to the target state. This is a common method, used for instance in [158]. It is straightforward to implement, and robust against small fluctuations of the experimental parameters, such as N and U_s, but the adiabaticity criterion limits the speed, especially near a phase transition where the energy gap becomes very small. In our implementation, the ramp lasts for 1 s, during which we expect the loss of ~ 1 atom. For atom numbers larger than a hundred, satisfying the adiabaticity criterion requires longer duration. It is thus of great interest to be able to design faster, non-adiabatic ramps. This problem belongs to the large field of optimal control. One type of approach, known in the literature as shortcut-to-adiabaticity (although this name could apply to other optimal control approaches) relies on the reverse engineering of a desired evolution [192]. More precisely, one designs the time evolution of one or several relevant observables; for instance let us assume that we want the total spin expectation value $\langle \hat{\mathbf{S}}^2 \rangle$ to decrease linearly[9]. Provided a closed set of equation(s) of evolution of the system, one can compute the evolution of the control parameter(s) (here q) leading to the desired dynamic (here the linear decrease of $\langle \hat{\mathbf{S}}^2 \rangle$). The requirement of a closed set of equations of evolution is a strong limitation to the use of shortcut to adiabaticity, in particular to produce entangled states. For spin-mixing dynamics, a mean-field approximation (see Chapter 4) leads to a system of two equations of evolution, but this approach is not adapted to our case, where the target state is not a mean field state. A more refined treatment could rely on the Bogoliubov theory, or on a continuum approximation (the spin is taken as a continuous variable), introduced in [193]. The latter is used in [194] to investigate theoretically the production of a fragmented spinor condensate. For $N = 100$ atoms, a numerical simulation demonstrates the production of a squeezed state with a spin $S \simeq 4$, in a duration $t \simeq h/U_s$ (corresponding to $\simeq 50$ ms in our case), using a shortcut to adiabaticity. This would constitute a significant improvement (in term of duration) compared to our implementation of adiabatic following. However, in practice we expect the dynamical production to be more sensitive to experimental fluctuations; in our case, fluctuations of U_s would probably constitute a limit to the use of very fast ramps.

[9] In practice, higher degree polynomials are used, in order to have a smooth beginning and end of the ramp.

Chapter 8

Conclusion

8.1 Summary

Chapter 1 We started with a brief presentation of some important aspects of the physics of spinor BECs. We introduced the single-mode approximation, which assumes that the spatial and spin degrees of freedom are decoupled, and which is well verified in all experiments presented in this manuscript. The state of the system is then described by a single spatial wave function, and a many-body spin state. We derived an effective Hamiltonian for the spin and studied its ground state versus the magnetic field. A quantum phase transition occurs at small fields, when antiferromagnetic interactions start to play an important role. In this region the ground state can no longer be described as single (ie non-fragmented) condensate as entanglement emerges.

Chapter 2 We continued with a presentation of the experimental set-up. We focused on our contribution, the implementation of a novel technique to achieve high-counting resolution, which combines a Stern-Gerlach separation followed by fluorescence imaging in an optical molasses. The requirement of a spatial separation of the Zeeman states prevented us from performing fluorescence in a trap, which puts a stringent upper bound on the exposure time. Furthermore, a diffusive behavior in the molasses requires a vanishing magnetic field, which is not easily combined with the Stern-Gerlach separation. In the end, we managed to collect about 450 photons per atom. For a cloud of a few hundred atoms or less, the dominant source of noise comes from stray light shot noise, and amounts to the signal of ~ 1.5 atoms.

Chapter 3 The first experiments we described consist in the parametric excitation of a spinor BEC. Spin-mixing dynamics can be seen as an "internal" analog of the Josephson effect. The Zeeman states $m = 0$ on the one hand and $m = \pm 1$ on the other hand replace the superconductors, and spin-changing collisions insure the coherent coupling in place of the weak-link in a Josephson junction. The quadratic Zeeman energy q plays the role of the voltage, and we modulate q to reproduce the so-called "inverse AC-Josephson effect". In real Josephson junctions, energy dissipation plays a major role and is responsible for the so-called "Shapiro steps" appearing in the intensity-tension curve. Energy is also dissipated in our system, presumably via a coupling between the BEC and the thermal cloud. In the driven situation, a locking of the atomic phase to the modulation enables a transfer of energy to the atoms, which can counter-act the dissipation and lead to new stationary states and hysteresis.

The spin-mixing dynamics discussed in Chapter 4 was triggered by preparing the atoms in a coherent superposition of the three Zeeman-states. The subsequent evolution is well captured by a mean-field approximation. To explore the role of quantum effects, such as quantum fluctuations and entanglement, we preferred to start with all atoms in $m = 0$, which can be realized thanks to magnetic forces pulling $m = \pm 1$ atoms out of the trap. This state is the ground state when the interaction energy is negligible compared to the quadratic Zeeman energy q. From this starting point, entanglement can be generated by ramping down the magnetic field, to reach the vicinity of the phase transition occurring at $q = 0$. We performed two types of experiments, quenches near (or through) the phase transition to study the dynamics, and an adiabatic following to probe the ground state.

Chapter 4 We first reported on our generation of a so-called two-mode squeezed vacuum state. By driving the magnetic field near the Shapiro resonance identified in Chapter 4, the BEC is destabilized, and quantum fluctuations trigger the creation of pairs of atoms in the $m = \pm 1$ states. Thanks to our fluorescence imaging method, we were able to observe a large degree of squeezing, potentially useful for metrology. We then presented another set of experiments, where we perform quenches to a magnetic field above the phase transition and observed periodic dynamics. The reversibility indicates the conservation of phase coherence between the spin modes. We also studied the effect of a small coherent seed on the dynamics, to provide further evidence of the role of quantum fluctuations in initiating the dynamics, and we observed a cross-over from the Bogoliubov to the mean-field regime.

Chapter 5 We carried on with similar experiments, but with lower magnetic fields and smaller atom numbers in order to bring the system deeper in the critical region. Under this condition the Zeeman effect plays a negligible role and the dynamics is fully dictated by the interactions. We observe the relaxation of the system to a steady state. This somehow counter-intuitive behavior results from the structure of the eigenstates of the interaction Hamiltonian. Indeed, we found that the mean value of few-body observables is fairly independent on the eigenstate with vanishing magnetization, in a broad energy window. The magnetization constraint is crucial, and prevents the thermalization of the system defined as the relaxation to the usual statistical ensembles. Instead, we found that a generalized Gibbs ensemble, which includes the magnetization constraint in addition to the usual conservation of energy and total atom number well described our results.

Chapter 6 In the experiment presented in this last Chapter, we slowly bring the system to the critical region, in order to only populate the lowest energy states. We reach a magnetic field such that antiferromagnetic interactions favor a ground state very close to a singlet state with vanishing spin. The macroscopic singlet state is rotationally invariant, and can be seen as the coherent superposition of all nematic states with equal weight. However, the coherence is very fragile, and atom losses or thermal fluctuations can easily lead to the spontaneous breaking of the symmetry. To circumvent this problem we used mesoscopic clouds of typically one hundred atoms. At the end of the adiabatic ramp, we observe the fragmentation of the condensate. Furthermore, we measured a strong squeezing of the spin in all directions, indicating that most atoms have formed singlet pairs. We reconstructed the many-body state and observe a significant occupation of the few lowest energy states only. We extracted the reduced entropy, defined as the entropy of a subsystem of n atoms, ignoring the $N-n$ remaining atoms. In doing so, singlet pairs are virtually broken and the entropy increases. The latter is a non-monotonic function of n and has a maximum near $n \sim N/2$. This non-classical feature indicates entanglement between the two virtual subsystems.

8.2 Main results and outlooks

High sensitivity imaging The implementation of fluorescence imaging was a technical but crucial development made during this thesis. Reaching a detection noise near the single atom level was paramount for the experiments presented in Chapters 5 to 7. In particular, this improvement enabled us to set a new record of spin squeezing for spinor BECs [86]. Yet, imaging noise remained an important limitation for our experiments. Further improvements are possible (see the outlooks of Chapter 3), which may help to reach the Heisenberg limit in an interferometric experiment (Chapter 5) [9, 162].

Spin-1 BEC out of equilibrium The principal novelties in our work on spin-mixing dynamics are the studies related to relaxation. In Chapter 4, we identified energy dissipation to be responsible for the relaxation. We find a phenomenological model which explains non-trivial phenomena (such as bistability and hysteresis), but a microscopic theory is still lacking. In Chapter 6 we observed the condensate reaching a steady state under its own dynamics. This phenomenon can be well understood using general arguments coming from the theory of the relaxation of isolated quantum systems [164]. In this field, a long-standing question regards the range of validity of the eigenstate thermalization hypothesis (ETH). Remarkably, we found that a generalized ETH applies to our relatively simple system. In the situation we have studied, the integrability due to the $SO(2)$ symmetry of the Hamiltonian prevents thermalization. In the continuity of this work it would be very interesting to study the relaxation (and thermalization?) in a chaotic regime. We have seen in the outlook of Chapter 4 that chaos can emerge even in the single-mode regime, under a parametric excitation. It would be interesting to explore theoretically other means to break the integrability.

Spin-1 BEC at equilibrium The realization of a fragmented BEC, fairly close to the singlet state, can be seen as the most significant achievement of this thesis. Pair condensation driven by antiferromagnetic interaction was predicted more than thirty years ago [39], and since then has been the subject of many theoretical studies. The observation of this phenomenon was one of the long term goals of our group, and earlier experiments paved the way to the one presented in this manuscript [52]. This work together with previous studies on the phase diagram [36] and on nematic ordering [37], provides a comprehensive experimental investigation of antiferromagnetic spin-1 BECs in the single mode regime at equilibrium. We now present a long-term project, in the continuity of these works.

Long-term prospective: singlet dimers on an optical lattice The study of correlated states beyond the single-mode regime constitutes a promising direction for future investigations. A particularly interesting set-up, relevant to the simulation of condensed matter system, would make use of an optical lattice to trap the atoms in a periodic potential. In this configuration, the interplay between spatial and spin degrees of freedom yields a very rich phase diagram, studied theoretically using variational approaches in [19, 195–197]. Let us consider the interesting situation where the quadratic Zeeman energy is negligible. The relevant energy scales are the tunneling energy t, the spin-independent interaction strength $\overline{U}$, the spin-dependent one U_s and the chemical potential μ. In practice, $\overline{U} \gg U_s$, and the spatial ordering is dictated by $\overline{U}/t$. Let us consider $\overline{U}/t \gg 1$, and μ such that the system forms a Mott insulator. The magnetic ordering then depends on the ratio U_s/t and the filling (the number of atoms per site). The case of an even filling is the simplest, the atoms on a given site form a singlet state. This is not possible however for odd fillings due to the exchange symmetry, and one needs to consider interactions between atoms of different sites, which can be done

perturbatively in the limit $t \ll \overline{U}$. For two sites, and a filling of one, the energy is minimized when the two atoms form a spin singlet dimer. Given this result, the following ansatz was proposed for a one dimensional lattice (similar dimerized state are also expected in larger dimension) [196, 197]

$$\Psi_{\text{dimer}} = ..\psi_{1,2}\psi_{3,4}.. \tag{8.1}$$

where $\psi_{i,i+1}$ designate a spin-singlet between the atoms of sites i and $i+1$ (this ansatz breaks the translational invariance of the lattice). The wave function (8.1) describes a so-called "dimerized valence bound state" [19]. Such states can also be found in frustrated magnets, and are believed to be at the origin of the high-temperature superconductivity of cuprates [17].

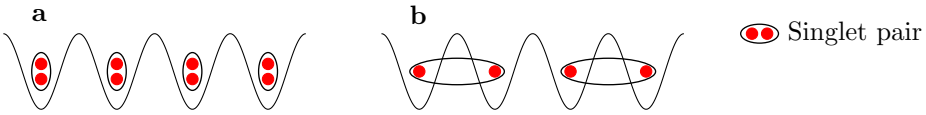

Figure 66: Sketch of singlet insulators. For a filling of two (a), the singlet pairs are localized within one site, while for unity filling (b) they form dimers.

This experiment represents a great technical challenge. The simplest geometry would probably be a one dimensional chain, realized for instance by combining a standing wave for the lattice and a Laguerre-Gauss blue-detuned beam for the radial confinement. The chemical potential can be tuned by changing the atom number. Alternatively, if on top of the lattice potential, there is a harmonic confinement, the chemical potential increases from the center to the edge of the trap.
For the detection, one would ideally combine an excellent spatial resolution to distinguish the lattice sites, with a spin state sensitivity. This has been achieved for spin-1/2 fermionic atoms in two dimensional lattices [198, 199]. The techniques used in these two papers could be applied to bosonic atoms when the site occupation is at most two atoms. For larger fillings, further developments would be required.
Regarding state preparation, we can build on the experience we have acquired with our realization of a condensate of singlet pairs to evaluate the feasibility of an adiabatic ramp to a singlet insulator. We pointed out in Chapter 7 a series of difficulties that appear given the very low energy scale that we want to probe (adiabaticity versus decoherence, magnetic field noise, thermal fluctuations). For two atoms on the same lattice site, the spin interaction energy per atom U_s/N ($N = 2$) could be significantly larger than in the harmonic trap used in our experiment. This phase thus appears within reach of an adiabatic ramp similar to the one we implemented. For the dimerized phase, atoms on different lattice sites interact weakly, the relevant energy scale is $(t/\overline{U})^2 U_s$ [197] with $t/\overline{U} \ll 1$ for an insulator. A more precise estimation of the parameters is needed to compare this situation with our experiment. In particular, the role of thermal fluctuations should be considered with care. In our experiment, we relied on (i) spin-filtering to achieve very small "spin temperature" and (ii) a weak coupling to the spatial mode to avoid thermalization. It is not guaranteed that the same method would work in the experiment envisioned here, where spatial and spin degrees of freedom are intertwined.

Appendix A

Spin and pseudo-spin operators

In this appendix, we recall the definition of the spin-1 spin operator and collective spin operator. We also recall the definition of the collective pseudo-spin, which is the spin that is squeezed in the experiment reported in Chapter 5. Finally, we compute the evolution of the spin and population over a rotation, which are performed via a radio-frequency coupling of the spin states.

A.0.1 Definition

We recall some useful formula.

Spin-1 Matrices

$$s_x = \frac{1}{\sqrt{2}}\begin{pmatrix} 0 & 1 & 0 \\ 1 & 0 & 1 \\ 0 & 1 & 0 \end{pmatrix}, \qquad s_y = \frac{i}{\sqrt{2}}\begin{pmatrix} 0 & -1 & 0 \\ 1 & 0 & -1 \\ 0 & 1 & 0 \end{pmatrix}, \qquad s_z = \begin{pmatrix} 1 & 0 & 0 \\ 0 & 0 & 0 \\ 0 & 0 & 1 \end{pmatrix}. \tag{A.1}$$

Collective spin It is define (in the SMA for simplicity) as $\hat{\mathbf{S}} = \hat{\mathbf{a}}^\dagger \mathbf{s} \hat{\mathbf{a}}$. Explicitly:

$$\hat{S}_x = \frac{1}{\sqrt{2}}\left(\hat{a}_{+1}^\dagger \hat{a}_0 + \hat{a}_0^\dagger(\hat{a}_{+1} + \hat{a}_{-1}) + \hat{a}_{-1}^\dagger \hat{a}_0\right), \tag{A.2}$$

$$\hat{S}_y = \frac{i}{\sqrt{2}}\left(-\hat{a}_{+1}^\dagger \hat{a}_0 + \hat{a}_0^\dagger(\hat{a}_{+1} - \hat{a}_{-1}) + \hat{a}_{-1}^\dagger \hat{a}_0\right), \tag{A.3}$$

$$\hat{S}_z = \hat{N}_{+1} - \hat{N}_{-1}, \tag{A.4}$$

$$\hat{\mathbf{S}}^2 = N + \hat{N}_0 + 2\hat{N}_0(N - \hat{N}_0) + 2(\hat{a}_{+1}^\dagger \hat{a}_{-1}^\dagger \hat{a}_0^2 + \hat{a}_0^{\dagger 2}\hat{a}_{+1}\hat{a}_{-1}) + \hat{S}_z^2. \tag{A.5}$$

Pseudo-spin We focus on the ensemble of $m_F = \pm 1$ atoms. In analogy with an ensemble of spin-1/2 particle, we define a pseudo-spin $\hat{\mathbf{J}}$ as:

$$\hat{J}_x = \frac{1}{2}(\hat{a}_{+1}^\dagger \hat{a}_{-1} + \hat{a}_{-1}^\dagger \hat{a}_{+1}), \tag{A.6}$$

$$\hat{J}_y = \frac{1}{2i}(\hat{a}_{+1}^\dagger \hat{a}_{-1} - \hat{a}_{-1}^\dagger \hat{a}_{+1}), \tag{A.7}$$

$$\hat{J}_z = \frac{1}{2}(\hat{N}_{+1} - \hat{N}_{-1}), \tag{A.8}$$

$$\hat{\mathbf{J}}^2 = \frac{\hat{N}_{+1} + \hat{N}_{-1}}{2}\left(\frac{\hat{N}_{+1} + \hat{N}_{-1}}{2} + 1\right). \tag{A.9}$$

This is the spin that is squeezed in the quench experiments of chapter 5.

In the next paragraph, we also introduce a pseudo spin for the pair of modes $(0, +1)$, $(0, -1)$. We write the pseudo spin constructed from the mode m and m' as $\hat{\mathbf{J}}^{m,m'}$. In the main text we don't precise m and m' since we only use the pair $m = +1$, $m' = -1$.

A.0.2 Spin rotation

Rotation around y We consider the rotation of a spin-1 by and angle θ around the y-axis. The evolution operator is

$$e^{-i\theta s_y} = \begin{pmatrix} \frac{\cos\theta+1}{2} & -\frac{\sin\theta}{\sqrt{2}} & \frac{1-\cos\theta}{2} \\ \frac{\sin\theta}{\sqrt{2}} & \cos\theta & -\frac{\sin\theta}{\sqrt{2}} \\ \frac{1-\cos\theta}{2} & -\frac{\sin\theta}{\sqrt{2}} & \frac{1+\cos\theta}{2} \end{pmatrix} . \tag{A.10}$$

The spin observable transform like vector, for the number observable, $\hat{N}_0$ is given by

$$\hat{N}_0^R(\theta) = \frac{1-\cos 2\theta}{4} N + \frac{1+3\cos 2\theta}{4} \hat{N}_0 - \frac{\sin 2\theta}{\sqrt{2}} (\hat{J}_x^{+1,0} - \hat{J}_x^{-1,0}) - \frac{1-\cos 2\theta}{2} \hat{J}_x^{+1,-1} . \tag{A.11}$$

Rotation around z The evolution operator for a rotation around the quantization axis z is

$$e^{-i\theta s_z} = \begin{pmatrix} e^{-i\theta} & 0 & 0 \\ 0 & 0 & 0 \\ 0 & 0 & e^{i\theta} \end{pmatrix} . \tag{A.12}$$

The single particle state only acquire a phase, and the population do not evolve.

Combine rotation around z and y The phase shift aquired during a rotation around z is revealed by a adding a rotation around y. We consider a first rotation around the z-axis by a variable angle ϕ followed by a rotation around the y-axis by an angle $\pi/4$. Combining the results given above, after some straight forward algebra one finds that the population evolve as

$$\begin{aligned} N_0^R(\phi) = & \frac{N+N_0}{4} + \frac{1}{\sqrt{2}} \left(\cos\phi (J_x^{+1,0} - J_x^{-1,0}) - \sin\phi (J_y^{+1,0} + J_y^{-1,0}) \right) \\ & - \frac{1}{2} \left(\cos 2\phi J_x^{+1,-1} - \sin 2\phi J_y^{+1,-1} \right) . \end{aligned} \tag{A.13}$$

The spin evolves as a vector

$$S_z^R(\phi) = \frac{1}{\sqrt{2}} S_z - \cos\phi \left(J_x^{+1,0} + J_x^{-1,0} \right) + \sin\phi \left(J_y^{+1,0} - J_y^{-1,0} \right) . \tag{A.14}$$

Note that all the pseudo-spin operator intervene in these two equations, thus enabling the full reconstruction of the single particle density matrix as shown in Chapter 7.

Appendix B

Collective spin states

We can write the many-body state of the spin of the condensate spin in many basis. The number basis $|N_{+1}, N_0, N_{-1}\rangle_{nb}$ is composed of the Fock states with a given number of atoms N_m in the spin-1 state $m = 0, \pm 1$. This basis is the most natural one since our diagnostic consist in measuring the various population N_m. The $SO(3)$ symmetry of the interaction Hamiltonian, makes the collective spin state basis $|N, S, M_z\rangle$ composed of the states with a well define spin S and a magnetization M_z more relevant at low make field. Finally we also used the overcomplete basis $|N : \mathbf{\Omega}\rangle$ composed of the coherent nematic state align on the axis $\mathbf{\Omega} = (\theta, \phi)$, which can be convenient in many calculation thanks to the simple action of the annihilation operator on the coherent state. These states are obtain by rotation of the nematic state $|N : \mathbf{e}_z\rangle = |m = 0\rangle^{\otimes N}$.
We provide in this appendix various formula which allow to "navigate" between the different basis. We first explore the relation between spin state and number basis, then coherent state and number basis, then spin state and coherente state basis.

B.1 Spin eigenstate and the number basis

B.1.1 General spin eigenstate in the number basis

The $|N, S, M_z\rangle$ states can be expressed in the number basis [41, 48, 50, 193] as

$$|N, S, M_z\rangle = \frac{1}{\sqrt{\mathcal{N}}}(\hat{S}_-)^P(\hat{A}^\dagger)^Q(\hat{a}^\dagger_{+1})^S|\text{vac}\rangle_{\text{nb}}\,, \tag{B.1}$$

where $P = S - M_z$ and $2Q = N - S$. $\hat{S}_- = \sqrt{2}(\hat{a}^\dagger_{-1}\hat{a}_0 + \hat{a}^\dagger_0\hat{a}_{+1})$ is the spin lowering operator and $\hat{A}^\dagger = \hat{a}^{\dagger 2}_0 - 2\hat{a}^\dagger_{-1}\hat{a}^\dagger_{+1}$ is the singlet creation operator. Finally,

$$\mathcal{N} = \frac{S!(N-S)!!(N+S+1)!!(S-M_z)!(2S)!}{(2S+1)!!(S+M_z)!}\,, \tag{B.2}$$

where !! indicates a double factorial.

B.1.2 Population in a general spin eigenstate

The action of $\hat{a}_0$ on the $|N, S, M_z\rangle$ states is [193]

$$\hat{a}_0|N, S, M_z\rangle = \sqrt{A_-(N, S, M_z)}|N-1, S-1, M_z\rangle + \sqrt{A_+(N, S, M_z)}|N-1, S+1, M_z\rangle \tag{B.3}$$

where the coefficients $A_\pm$ are given by

$$A_-(N, S, M_z) = \frac{(S^2 - M^2)(N+S+1)}{(2S+1)(2S-1)}\,, \tag{B.4}$$

$$A_+(N, S, M_z) = \frac{((S+1)^2 - M^2)(N-S)}{(2S+1)(2S+3)}\,. \tag{B.5}$$

The non-vanishing matrix elements of $\hat{N}_0$ are

$$\langle N, S, M_z|\hat{N}_0|N, S, M_z\rangle = (A_+(N, S, M_z) + A_-(N, S, M_z)\,, \tag{B.6}$$

$$\langle N, S+2, M_z|\hat{N}_0|N, S, M_z\rangle = \sqrt{A_+(N, S+2, M_z)A_-(N, S, M_z)}\,, \tag{B.7}$$

$$\langle N, S-2, M_z|\hat{N}_0|N, S, M_z\rangle = \sqrt{A_+(N, S-2, M_z)A_-(N, S, M_z)}\,. \tag{B.8}$$

In particular, for the singlet state, we can compute

$$\langle \hat{N}_0 \rangle = \frac{N}{3}\,, \tag{B.9}$$

$$\Delta \hat{N}_0^2 = \frac{4N^2 + 12N}{45}\,. \tag{B.10}$$

B.1.3 Singlet state in the number basis

The singlet state is given by (N is necessary even for the singlet)

$$|N,0,0\rangle = \hat{A}^{\dagger\,\frac{N}{2}}|\mathrm{vac}\rangle_{\mathrm{nb}}\,, \tag{B.11}$$

$$|N,0,0\rangle = \sum_{k=0}^{\frac{N}{2}} \frac{\frac{N}{2}!\sqrt{(N-2k)!}}{(\frac{N}{2}-k)!\sqrt{N!}}(-2)^k|k,N-2k,k\rangle_{\mathrm{nb}}\,. \tag{B.12}$$

We replace the factorials by their equivalent in the limit of large arguments. This will result in a small error for the coefficient $k \sim 1$ and $k \sim N$. However, because of the isotropy of the singlet, we know that these states do not contribute significantly (we must have $\langle \hat{N}_0 \rangle = 1/3$). The Stirling formula yield to the simple expression

$$|N,0,0\rangle \simeq \frac{1}{\sqrt{N}} \sum_{k=0}^{\frac{N}{2}} (-1)^k \left(\frac{N}{N+1-2k}\right)^{\frac{1}{4}} |k,N-2k,k\rangle_{\mathrm{nb}}\,. \tag{B.13}$$

The distribution is indeed fairly broad. This motivates a continuum approximation for the relative population n_0. It verifies the statistics

$$\mathcal{P}(n_0) \simeq \frac{1}{2\sqrt{n_0}}\,. \tag{B.14}$$

From this we can compute the mean and variance of n_0.

B.1.4 Nematic state $|0\rangle^{\otimes N}$ in the spin basis

We compute the elements of the nematic state align along z, $|N:\mathbf{e}_z\rangle = |m=0\rangle^{\otimes N}$ in the spin state basis. Clearly, it has non-vanishing elements only on the $M_z = 0$ states. Using eq. (B.1), we compute

$$\langle N:\mathbf{e}_z|N,S,0\rangle = \frac{1}{\sqrt{\mathcal{N}}} 2^{\frac{S}{2}} \sqrt{N!}S!\,. \tag{B.15}$$

After some rearrangements, and using $2p! = 2^p p!$, $(2p+1)!! = (2p+1)!/(2p!!)$, we get

$$\langle N:\mathbf{e}_z|N,S,0\rangle = \left[2^S(2S+1)\frac{N!}{(N+S+1)!}\frac{\frac{N+S}{2}!}{\frac{N-S}{2}!}\right]^{\frac{1}{2}}\,, \tag{B.16}$$

$$= \sqrt{\frac{2S+1}{4\pi} f_S^N}\,. \tag{B.17}$$

where we have introduced [50]

$$f_S^N = 4\pi 2^S \frac{N!}{(N+S+1)!}\frac{\frac{N+S}{2}!}{\frac{N-S}{2}!}\,, \tag{B.18}$$

which will play an important role in the following.
We know that the mean value of the total spin of a nematic state is $2N$. Therefore, we expect the spin states with $S \sim \sqrt{2N}$ to contribute the most. This motivates an expansion with $1 \ll S \ll N$. It leads to the simple formula

$$f_S^N \simeq \frac{4\pi}{N}\exp\left(-\frac{S^2}{2N}\right)\,, \tag{B.19}$$

$$\langle N:\mathbf{e}_z|N,S,0\rangle \simeq \sqrt{\frac{2S}{N}}\exp\left(-\frac{S^2}{4N}\right)\,. \tag{B.20}$$

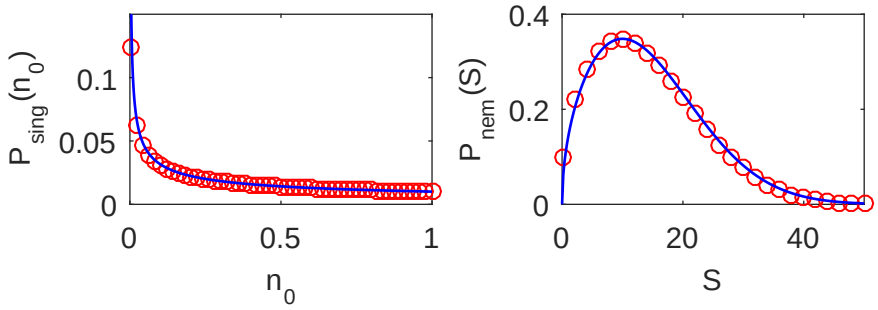

Figure 67: Left panel: singlet state in the number basis (characterized by n_0 only, $S_z = 0$). Right panel: nematic state in the spin state basis (characterized by S only, $S_z = 0$). The red circles are the exact results, the blue line are the approximate formula derive in this appendix. Here $N = 100$, and the approximation are well verified.

B.2 Nematic coherent state in the number basis

The nematic state align along $\mathbf{\Omega} = (\sin\theta\cos\phi, \sin\theta\sin\phi, \cos\theta)$ can be expressed as

$$|N:\mathbf{\Omega}\rangle = \frac{1}{\sqrt{N!}}\left(-\frac{1}{\sqrt{2}}\sin\theta e^{-i\phi}\hat{a}^\dagger_{+1} + \cos\theta\hat{a}^\dagger_0 + \frac{1}{\sqrt{2}}\sin\theta e^{i\phi}\hat{a}^\dagger_{-1}\right)^N |\text{vac}\rangle\,. \tag{B.21}$$

The are obtain by rotation of $|N:\mathbf{e}_z\rangle = |m=0\rangle^{\otimes N}$

$$|N:\mathbf{\Omega}\rangle = e^{-i\phi\hat{S}_z}e^{-i\theta\hat{S}_y}|N:\mathbf{e}_z\rangle\,. \tag{B.22}$$

Let us write $\Omega_{\pm1} = \mp\frac{1}{\sqrt{2}}\sin\theta e^{\mp i\phi}$ and $\Omega_0 = \cos\theta$,

$$|N:\mathbf{\Omega}\rangle = \sum_{j,k}\sqrt{\frac{N!}{j!k!(N-j-k)!}}\Omega^j_{+1}\Omega^{N-j-k}_0\Omega^k_{-1}|j,N-j-k,k\rangle_{\text{nb}}\,, \tag{B.23}$$

and the action of the annihilation operators on the nematic coherent state takes a simple form:

$$\hat{a}_m|N:\mathbf{\Omega}\rangle = \sqrt{N}\Omega_m|N-1:\mathbf{\Omega}\rangle\,. \tag{B.24}$$

The nematic states form an over-complete basis [183], which we will proved by expressing the spin state $|N,S,M_z\rangle$ as a function of the nematic state.

For $N \gg 1$, the following approximation can be useful

$$|N:\mathbf{\Omega}\rangle \simeq \frac{1}{\sqrt{2\pi}}\sum_{jk}\left(\frac{N}{jk(N-j-k)}\right)^{\frac{1}{4}} e^{-\frac{(j-k)^2}{2(j+k)}}e^{-N(\theta-\theta_{jk})^2}e^{i\phi(k-j)}|j,N-j-k,k\rangle_{\text{nb}}\,, \tag{B.25}$$

where $\tan\theta_{jk} = \sqrt{\frac{j+k}{N-j-k}}$.

B.3 Spin eigenstate and the coherent state overcomplete basis

B.3.1 Spin state in the nematic state basis

Let us consider the (unnormalized)e state

$$|\psi\rangle = \int d^3\mathbf{\Omega}Y_{S,M_z}(\mathbf{\Omega})|N:\mathbf{\Omega}\rangle\,, \tag{B.26}$$

where Y_{S,M_z} is a spherical Harmonic. Using Eqs.[B.17,B.22] we can rewrite $|\psi\rangle$ as

$$|\psi\rangle = \int d^3\mathbf{\Omega}Y_{S,M_z}(\mathbf{\Omega})e^{-i\phi\hat{S}_z}e^{-i\theta\hat{S}_y}\sum_T\sqrt{\frac{2T+1}{4\pi}}f^N_T|N,T,0\rangle\,. \tag{B.27}$$

Furthermore, using

$$\langle S', M'|e^{-i\phi\hat{S}_z}e^{-i\theta\hat{S}_y}|T,0\rangle = \delta_{S',T}D^{S'}_{M',0}(\phi,\theta)\,, \tag{B.28}$$

$$\langle S', M'|e^{-i\phi\hat{S}_z}e^{-i\theta\hat{S}_y}|T,0\rangle = \delta_{S',T}\sqrt{\frac{4\pi}{2S'+1}}Y^*_{S',M'}(\mathbf{\Omega})\,, \tag{B.29}$$

where D is the Wigner D-matrix, we obtain [50]

$$\langle N, S', M'|\psi\rangle = \int d^3\mathbf{\Omega}Y_{S,M_z}(\mathbf{\Omega})\sqrt{\frac{2S'+1}{4\pi}f^N_{S'}}\sqrt{\frac{4\pi}{2S'+1}}Y^*_{S',M'}(\mathbf{\Omega})\,, \tag{B.30}$$

$$\langle N, S', M'|\psi\rangle = \sqrt{f^N_S}\delta_{S,S'}\delta_{M_z,M'}\,. \tag{B.31}$$

Thus, $|\psi\rangle = \sqrt{f^N_S}|N,S,M_z\rangle$, and the spin state can be expressed in the nematic state basis as

$$|N,S,M_z\rangle = \frac{1}{\sqrt{f^N_S}}\int d^3\mathbf{\Omega}Y_{S,M_z}(\mathbf{\Omega})|N:\mathbf{\Omega}\rangle\,, \tag{B.32}$$

and for $S \gg 1$, we have

$$f^N_S \simeq \frac{4\pi}{N}e^{-\frac{S^2}{2N}}\,. \tag{B.33}$$

Similarly, we can show that

$$\langle N:\mathbf{\Omega}|N,S,M_z\rangle = \sqrt{f^N_S}Y_{S,M_z}(\mathbf{\Omega})\,. \tag{B.34}$$

B.3.2 Coarse grained distribution of pairs of the spin state

In chapter 6, we are interested in the coarse-grained distribution of N_p for spin state with zeros magnetization and $1 \ll S \ll \sqrt{N}$. We derive it here. For shortness, we write $|k, N-2k, k\rangle_{\rm nb} = |k\rangle_{\rm nb}$, and $|N,S,0\rangle = |S\rangle$. Using Eqs.(B.32,B.25), we obtain

$${}_{\rm nb}\langle k|S\rangle = \frac{1}{Z^N_S\sqrt{2\pi}}\left(\frac{N}{k^2(N-2k)}\right)^{\frac{1}{4}}\int d^2\mathbf{\Omega}Y_{S,0}(\mathbf{\Omega})e^{-N(\theta-\theta_{kk})^2}\,. \tag{B.35}$$

For $S \gg 1$,

$$Y_{S,0}(\Omega) \simeq \frac{(-1)^S}{\pi}\frac{\sin(S\theta-\frac{\pi}{4})}{\sqrt{\sin\theta}}\,. \tag{B.36}$$

Thus, for $S \ll \sqrt{N}$, in the integral above, the term $\sin\theta Y_{S,0}(\theta)$ does not vary much in the region where the exponential is significant (they are two θ_k), and can thus be taken to be constant. We obtain

$${}_{\rm nb}\langle k|S\rangle = \frac{1}{f^N_S\sqrt{2\pi}}\left(\frac{N}{k^2(N-2k)}\right)^{\frac{1}{4}}4\sin(S\theta_k-\frac{\pi}{4})\sqrt{\sin\theta_k}\sqrt{\frac{\pi}{N}}\,, \tag{B.37}$$

with $\sin\theta_k = \sqrt{k/N}$. Further more, using $f^N_S \simeq \sqrt{4\pi/N}$ we obtain

$$|{}_{\rm nb}\langle k|S\rangle|^2 \simeq \frac{2}{\pi}\frac{1}{\sqrt{k(N-2k)}}\sin^2(S\theta_k-\frac{\pi}{4}) \tag{B.38}$$

After coarse graining, $\sin^2(S\theta_k-\frac{\pi}{4}) \simeq 1/2$ and we obtain the result announced in the main text.

Appendix C

Bogoliubov approximation

We study here the ground state of the SMA Hamiltonian in the Bogoliubov regime (see chapter 2), that is to say for small depletion of the BEC, as well as the dynamics.

C.1 Ground state

Bogoliubov Hamiltonian We recall the Bogoliubov Hamiltonian

$$\hat{H}_B = (q + U_s)\left(\hat{N}_{+1} + \hat{N}_{-1}\right) + U_s\left(\hat{a}_{+1}\hat{a}_{-1} + \hat{a}^\dagger_{+1}\hat{a}^\dagger_{-1}\right) . \tag{C.1}$$

It can be diagonalized by using the following transformation [68]

$$\begin{aligned} \hat{\alpha} &= \cosh(\theta)\hat{a}_{+1} - \sinh(\theta)\hat{a}^\dagger_{-1} , \\ \hat{\beta} &= \sinh(\theta)\hat{a}^\dagger_{+1} - \cosh(\theta)\hat{a}_{-1} , \end{aligned} \tag{C.2}$$

with $\tanh(2\theta) = -\frac{U_s}{q+U_s}$. We obtain

$$\hat{H}_B = \hbar\omega_B(\hat{\alpha}^\dagger\hat{\alpha} + \hat{\beta}^\dagger\hat{\beta} + 1) - (q + U_s) , \tag{C.3}$$

with the Bogoliubov energy $\hbar\omega_B = \sqrt{q(q + 2U_s)}$. The longitudinal spin is $\hat{S}_z = \hat{N}_{+1} - \hat{N}_{-1} = \hat{\alpha}^\dagger\hat{\alpha} - \hat{\beta}^\dagger\hat{\beta}$.

Ground state The ground state is the vacuum of Bogoliubov excitation. Clearly, it has vanishing magnetization. We write it in the number basis $|N_{+1}, N_{-1}\rangle_{nb}$

$$|\text{vac}\rangle_B = \sum_{n=0}^{\infty} c_n |n, n\rangle_{nb} . \tag{C.4}$$

The action of α yield

$$0 = \sum_{n=0}^{\infty} c_n \cosh\theta\sqrt{n}|n-1, n\rangle - c_n \sinh\theta\sqrt{n+1}|n, n+1\rangle , \tag{C.5}$$

from which we get the recurrence relation $c_n = \tanh\theta c_{n-1}$. Hence, $c_n = (\tanh\theta)^n c_0$. Without loss of generality, c_0 can be chosen real and positive. Using the normalization condition we obtain

$$c_n = (\tanh\theta)^n \sqrt{1 - \tanh^2\theta} . \tag{C.6}$$

Moreover, the mean value of the number of $m = \pm 1$ pair in the ground state is $\langle\hat{N}_p\rangle = \sinh^2\theta$. With this we finally recover the expression of the ground state announce in the main text:

$$|\text{vac}\rangle_B = |\text{TSVM}\rangle = \frac{1}{\sqrt{1 + \langle\hat{N}_p\rangle}} \sum_{n=0}^{\infty} \left(\frac{\langle\hat{N}_p\rangle}{1 + \langle\hat{N}_p\rangle}\right)^{\frac{n}{2}} |n, n\rangle . \tag{C.7}$$

Thermal statistic The reduced density matrix for the mode $+1$ (it is clearly the same for $m = -1$) is

$$\rho_{+1} = \frac{1}{1 + \langle \hat{N}_{+1} \rangle} \sum_{n=0}^{\infty} \left(\frac{\langle \hat{N}_{+1} \rangle}{1 + \langle \hat{N}_{+1} \rangle} \right)^n |n\rangle\langle n| \,, \tag{C.8}$$

which can be rewritten as

$$\rho_{+1} = \frac{1}{Z} e^{-K\hat{N}_{+1}} \,, \tag{C.9}$$

where $Z = \mathrm{Tr}\left(e^{-K\hat{N}_{+1}}\right)$ and $K = \log(1 + 1/\langle \hat{N}_{+1} \rangle) \simeq 1/\langle \hat{N}_{+1} \rangle$. In analogy with the distribution of a thermal gas of non-interacting Bosons, we can define an effective temperature T_{eff} such that $K = \frac{q}{k_B T_{\text{eff}}}$. It yields to (for substantial depletion)

$$k_B T_{\text{eff}} \simeq \langle \hat{N}_{+1} \rangle q \simeq \sqrt{\frac{qU_s}{8}}. \tag{C.10}$$

C.2 Dynamical production of the TMSV

C.2.1 Operators evolutions

The TSVM is also naturally produced over the evolution of the nematic state $|0\rangle^{\otimes N}$ after a quench. Since we have some experiments using a drive to engineer negative QZE, we will use the more general Hamiltonian:

$$\hat{H} = \alpha \left(\hat{N}_{+1} + \hat{N}_{-1} \right) + U \left(\hat{a}_{+1}\hat{a}_{-1} + \hat{a}^\dagger_{+1}\hat{a}^\dagger_{-1} \right) \,. \tag{C.11}$$

with $\alpha = q + U_s$ and $U = U_s$ in the static case, $\alpha = \frac{\delta}{2} + U_s$ and $U = \kappa U_s$ in the driven case.

The calculation of the mean value of few-body operator can be simply done in the Einsenberg picture (we don't use the Bogoliubov Hamiltonian, in order to treat the stable and unstable cases simultaneously). The equation of evolution for the operators $\hat{a}_{+1}$,$\hat{a}^\dagger_{-1}$ are:

$$i\hbar \frac{d}{dt} \begin{pmatrix} \hat{a}_{+1} \\ \hat{a}^\dagger_{-1} \end{pmatrix} = \begin{pmatrix} \alpha & U \\ -U & -\alpha \end{pmatrix} \begin{pmatrix} \hat{a}_{+1} \\ \hat{a}^\dagger_{-1} \end{pmatrix} \tag{C.12}$$

The Bogolibuov energy is with this Hamiltonian $\hbar\omega_B = \sqrt{\alpha^2 - U^2}$. We emphasize that the calculation holds for $\alpha < 0$. In particular, for $-U_s < \alpha < 0$, in which case, the Bogoliubov energy is actually complex. This corresponds to an unstable regime as will be shown by the calculation.

$$P = \frac{\sqrt{2\alpha}}{2\omega_B} \begin{pmatrix} -\sqrt{\alpha + \omega_B} & -\sqrt{\alpha - \omega_B} \\ \sqrt{\alpha - \omega_B} & \sqrt{\alpha + \omega_B} \end{pmatrix} \,, \tag{C.13}$$

$$P^{-1} = \frac{1}{\sqrt{2\alpha}} \begin{pmatrix} -\sqrt{\alpha + \omega_B} & -\sqrt{\alpha - \omega_B} \\ U_s/\sqrt{\alpha + \omega_B} & U_s/\sqrt{\alpha - \omega_B} \end{pmatrix} \,. \tag{C.14}$$

Then:

$$i\frac{d}{dt} P \begin{pmatrix} \hat{a}_{+1} \\ \hat{a}^\dagger_{-1} \end{pmatrix} = \begin{pmatrix} \omega_B & 0 \\ 0 & -\omega_B \end{pmatrix} P \begin{pmatrix} \hat{a}_{+1} \\ \hat{a}^\dagger_{-1} \end{pmatrix} \,, \tag{C.15}$$

which we can integrate to find:

$$\hat{a}_{\pm}(t) = A^* \hat{a}_{\pm,i} + B^* \hat{a}^\dagger_{\mp,i} \,, \tag{C.16}$$

where:

$$A = \cos(\omega_B t) + i\frac{\alpha}{\hbar\omega_B} \sin(\omega_B t) \,, \tag{C.17}$$

$$B = i\frac{U}{\hbar\omega_B} \sin(\omega_B t) \tag{C.18}$$

We can compute of some observables of interest:

$$\hat{N}_{\pm}(t) = |B|^2 + (|A|^2 + |B|^2)\hat{N}_{\pm} + AB^*\hat{a}^{\dagger}_{+1}\hat{a}^{\dagger}_{-1} + A^*B\hat{a}_{+1}\hat{a}_{-1}\,, \tag{C.19}$$

$$\hat{J}_x(t) = (|A|^2 + |B|^2)\hat{J}_x + AB^*\frac{\hat{a}^{\dagger 2}_{+1} + \hat{a}^{\dagger 2}_{-1}}{2} + A^*B\frac{\hat{a}^2_{+1} + \hat{a}^2_{-1}}{2}\,, \tag{C.20}$$

$$\hat{J}_y(t) = (|A|^2 + |B|^2)\hat{J}_y + AB^*\frac{\hat{a}^{\dagger 2}_{+1} - \hat{a}^{\dagger 2}_{-1}}{2i} + A^*B\frac{\hat{a}^2_{+1} - \hat{a}^2_{-1}}{2i}\,, \tag{C.21}$$

$$\hat{J}_z(t) = \hat{J}_z\,. \tag{C.22}$$

$$\tag{C.23}$$

C.2.2 Full distribution

The calculation of the full state is more involved. It is on the other hand, well known and derive in many references, given the importance of the Bogoliubov Hamiltonian eq.,(C.1) in many fields. We will admit that the vacuum of $m = \pm 1$ pairs evolve into the TSVM define above and refer the reader to [33] for the derivation.

Appendix D

Interferometric sensitivity

We consider here only the two modes $m = \pm 1$, and the associated pseudo-spin define in appendix A. We derive the sensitivity of the twin-fock state (TFS) and two-mode squeezed vacuum (TMSV) to a (pseudo) spin rotation of angle θ around the Y-axis. This is a generic set-up that can describe the Mach-Zehnder or Ramsey interferometer, very common in atomic physics or optics. In such set-ups the mean value of $\hat{J}_z$ is typically measured. For coherent states, this leads to Rabi-oscillation. For the unpolarized state under consideration, $\langle \mathbf{J} \rangle = 0$, and this strategy does not apply. An alternative consists in measuring $\langle \hat{J}_z^2 \rangle$. The sensitivity is then given by

$$\Delta\theta = \frac{\sqrt{\langle J_z^4 \rangle - \langle J_z^2 \rangle^2}}{\mathrm{d}\langle J_z^2 \rangle / \mathrm{d}\theta} \,. \tag{D.1}$$

We first derive $\Delta\theta$ for the TFS, before turning to the TMSV.

D.1 Interferometry with a twin-Fock state

The case of the TFS is studied in [69, 200, 201]. At the output of the interferometer we have $\hat{J}_z' = \cos\theta \hat{J}_z + \sin\theta \hat{J}_x$. The TFS, is written in the number basis as

$$|\mathrm{TFS}\rangle = |N_p, N_p\rangle_{nb} \,. \tag{D.2}$$

and in the pseudo spin basis

$$|\mathrm{TFS}\rangle = |N_p, 0\rangle \,. \tag{D.3}$$

It is in the kernel of $\hat{J}_z$, which greatly simplifies the calculation. The signal is

$$\langle \hat{J}_z'^2 \rangle = \sin^2\theta \langle J_x^2 \rangle \tag{D.4}$$

and the quantum noise is

$$(\Delta J_z'^2)^2 = \langle \hat{J}_z'^4 \rangle - \langle \hat{J}_z'^2 \rangle^2 \,, \tag{D.5}$$

$$(\Delta J_z'^2)^2 = \sin^4\theta \left(\langle \hat{J}_x^4 \rangle - \langle \hat{J}_x^2 \rangle^2 \right) + \sin^2\theta \cos^2\theta \langle \hat{J}_x \hat{J}_z^2 \hat{J}_x \rangle \,. \tag{D.6}$$

Using $\hat{J}_x = \frac{\hat{J}_+ + \hat{J}_-}{2}$ and $\hat{J}_\pm |N_p, m\rangle = \sqrt{N_p(N_p+1) - m(m\pm 1)} |N_p, m \pm 1\rangle$, we get

$$\langle \hat{J}_x^2 \rangle = \frac{N_p(N_p+1)}{2} \,, \tag{D.7}$$

$$\langle \hat{J}_x^4 \rangle = \frac{3N_p^2(N_p+1)^2}{8} - \frac{N_p(N_p+1)}{4} \,, \tag{D.8}$$

$$\langle \hat{J}_x \hat{J}_z^2 J_x \rangle = \frac{N_p(N_p+1)}{2} \,. \tag{D.9}$$

Gathering all pieces, the signal is (for $N_p \gg 1$)

$$\langle \hat{J}_z' \rangle = \frac{N_p^2}{2} \sin^2\theta \,, \tag{D.10}$$

and the noise is

$$(\Delta J_z'^2)^2 = \sin^4\theta \frac{N_p^4}{8} + \sin^2\theta\cos^2\theta\frac{N_p^2}{2}\,. \tag{D.11}$$

The sensitivity is thus

$$\Delta\theta^2 = \frac{\frac{N_p^2}{4}\tan^2\theta + 1}{2N_p^2}\,. \tag{D.12}$$

It is minimal when $\theta^* = 0$, and it then reaches the Heinsenberg scaling $\Delta\theta^* = \frac{\sqrt{2}}{N}$, and is a factor $\sqrt{2}$ above the Heinsenberg limit.

D.2 Interferometry with a two-mode squeezed vacuum

The TMSV can be written as a coherent superposition of TFS with different numbers of atoms

$$|\mathrm{TMSV}\rangle = \sum_{N_p=0}^{\infty} c_{N_p}|N_p, N_p\rangle\,. \tag{D.13}$$

We just need to replace in the expression of the signal and noise, the term in N_p^k by the moment $\langle N_p^k\rangle_{\mathrm{TMSV}}$. In the limit $\langle N_p\rangle \gg 1$, these are (we recall that the statistic is thermal, and use a continuous approximation)

$$\langle \hat{N}_p^k\rangle_{\mathrm{TMSV}} \simeq k!\overline{N_p}^k\,, \tag{D.14}$$

with $\overline{N_p} = \langle \hat{N}_p\rangle$. This leads to

$$\langle \hat{J}_x^2\rangle = \overline{N_p}^2\,, \tag{D.15}$$
$$\langle \hat{J}_x^4\rangle = 9\overline{N_p}^4\,, \tag{D.16}$$
$$\langle \hat{J}_x\hat{J}_z^2 J_x\rangle = \overline{N_p}^2\,. \tag{D.17}$$

And finally

$$\langle \hat{J}_z'\rangle = \overline{N_p}^2\sin^2\theta\,, \tag{D.18}$$
$$(\Delta J_z'^2)^2 = 8\sin^4\theta\overline{N_p}^4 + \sin^2\theta\cos^2\theta\overline{N_p}^2\,. \tag{D.19}$$

The sensitivity is thus

$$\Delta\theta^2 = \frac{8\tan^2\theta\overline{N_p}^2 + 1}{4\overline{N_p}^2}\,. \tag{D.20}$$

It is minimal when $\theta^* = 0$, and is slightly better than a TFS with the same mean number of atom.

D.3 Interferometry with detection noise

We assume that the main limitation comes from the detection noise . We consider that we have produced a perfect TMSV. The result of a measurement is now given by

$$J_z'' = \hat{J}_z' + \mathcal{N}\,. \tag{D.21}$$

We take $\mathcal{N}$ to be a centered and normally distributed. The signal and noise are

$$\langle \hat{J}_z''\rangle = \overline{N_p}^2\sin^2\theta + \Delta\mathcal{N}^2\,, \tag{D.22}$$
$$(\Delta J_z''^2)^2 = 8\sin^4\theta\overline{N_p}^4 + \sin^2\theta\cos^2\theta\overline{N_p}^2 + 4\overline{N_p}^2\Delta\mathcal{N}^2 + (\Delta\mathcal{N})_4\,. \tag{D.23}$$

where $(\Delta\mathcal{N})_4 = \langle\mathcal{N}^4\rangle - \langle\mathcal{N}^2\rangle^2$. The sensivity is finally given by

$$\Delta\theta^2 \simeq 2\tan^2\theta + \frac{1}{4\overline{N_p}^2} + \frac{\Delta\mathcal{N}^2}{\overline{N_p}^2\cos^2\theta} + \frac{(\Delta\mathcal{N})_4}{4\overline{N_p}^4\sin^2\theta\cos^2\theta}. \tag{D.24}$$

In our situation, we have $\Delta\mathcal{N}^2$, $(\Delta\mathcal{N})_4$ order one, much smaller than $\overline{N_p} \sim 100$. In that limit, the optimal working point is slightly shifted from $\theta = 0$ to $\theta^{*4} \simeq \frac{(\Delta\mathcal{N})_4}{8\overline{N}_\mathrm{p}^4}$. The best sensitivity is then

$$\Delta\theta^* \simeq \frac{\sqrt{1 + 4(1+\sqrt{6})\Delta\mathcal{N}^2}}{2\overline{N_p}}, \tag{D.25}$$

where we have used $\langle\mathcal{N}^4\rangle = 3(\Delta\mathcal{N}^2)^2$. The sensitivity is related to the squeezing factor defined in the main text,

$$\Delta\theta^* \simeq \sqrt{\frac{1}{(2\overline{N_p})^2} + (1+\sqrt{6})\frac{\zeta^2}{\overline{N_p}}}. \tag{D.26}$$

Appendix E

Thermalization of the Nematic state $|N : e_z\rangle$

In this appendix, we compute the evolution of the nematic state $|N : \mathbf{e}_z\rangle$ at $q = 0$. We derived in the appendix B in the expression of this state in the spin state basis. To alleviate the notation, since we are only dealing with state of N atoms and zero magnetization, we write $|N, S, 0\rangle = |S\rangle$. We have,

$$|N : \mathbf{e}_z\rangle \simeq \sum_{S=0:2:N} \sqrt{\frac{2S}{N}} e^{-\frac{S^2}{4N}} |S\rangle. \tag{E.1}$$

This is an approximation valid for $N \gg 1$. In that case, the most relevant term of the sum above verify $1 \ll S \ll N$. This will greatly simplify the calculation.
At $q = 0$, the Hamiltonian is $\frac{U_s}{2N}\hat{\mathbf{S}}^2$, so that the state evolves as

$$|\psi(t)\rangle \simeq \sum_{S=0:2:N} \sqrt{\frac{2S}{N}} \exp\left(\frac{S^2}{4N} - i\frac{U_s t S}{2\hbar N}\right) |S\rangle. \tag{E.2}$$

We have used $S(S+1) \simeq S^2$, which is valid for most of the term of the sum. We want to compute the mean value of $\hat{N}_0$ in that state. For $S \ll N$, We have

$$\langle S'|\hat{N}_0|S\rangle = \frac{N}{2}\delta_{S',S} + \frac{N}{4}(\delta_{S',S+2} + \delta_{S',S-2}) \,. \tag{E.3}$$

From this we compute

$$N_0(t) = \frac{N}{2} + N \sum_{S=0:2:N} \frac{S}{N} \exp\left(-\frac{S^2}{2N}\right) \cos\left(\frac{2SU_s t}{N\hbar}\right) \tag{E.4}$$

We introduce the variables $\tau = \sqrt{\frac{2}{N}}\frac{U_s t}{\hbar}$ and $x = \frac{S}{\sqrt{2N}}$. x varies from 0 to $\sqrt{N} \gg 1$ by increment of $dx = \sqrt{\frac{2}{N}}$. The sum can be replaced by an integral for 0 to $+\infty$

$$N_0(t) \simeq \frac{N}{2} + N \int_0^{+\infty} dx x e^{-x^2} \cos(2x\tau) \,, \tag{E.5}$$

$$N_0(t) \simeq N - N\tau \int_0^{+\infty} dx e^{-x^2} \sin(2x\tau) \,, \tag{E.6}$$

where we have used an integration by part. Let us right the integral $F(\tau)$. It verifies $F'(\tau) + 2\tau F(\tau) = 1$, which defines the Dawson function.

When $\tau \to 0$, $F(\tau) \sim \tau$, so that at short time, we recover the results of the Bogoliubov approximation (in the limit $\omega \to 0$),

$$N_0(t) \sim N - \frac{2U_s^2 t^2}{\hbar} \tag{E.7}$$

When $\tau \to \infty$, $F(\tau) \sim \frac{1}{2\tau} + \frac{1}{4\tau^3}$, and

$$N_0(t) \sim \frac{N}{2} - \frac{N^2\hbar}{8U_s^2 t^2} \,. \tag{E.8}$$

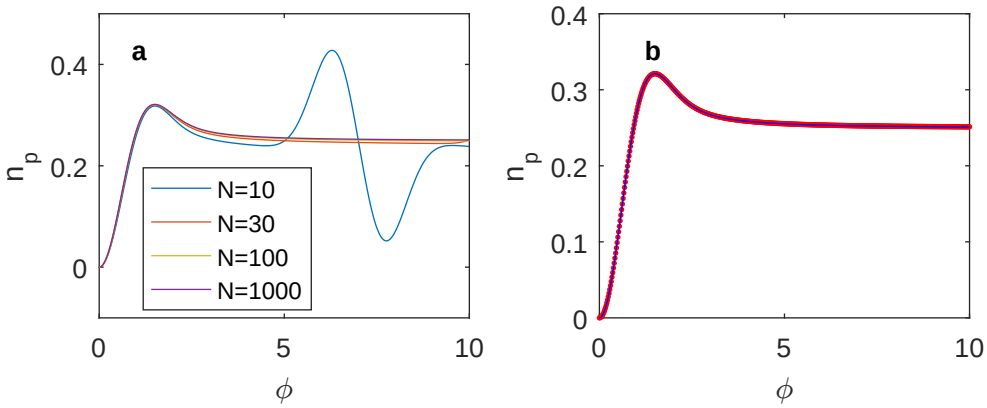

Figure 68: Numerical resolution of the thermalization dynamic of a nematic state at $q = 0$. a n_p vs τ (defined above) for various atom numbers. For small $N = 10$ we see an early revival of the dynamic. For larger N, we observe thermalization, and we verify the universality of the curve $n_p(\tau)$. b The blue line is the exact result for $N = 1000$ atoms, the red dots are the approximate formula derived in this appendix. The error of order $1/N$ is not visible.

Appendix F

Reduced density matrix

F.0.1 Expression of the reduced density matrix

Let us consider a general state of N spin-1, in a single spatial mode, written in the number basis $|N_{+1}\rangle|N_0\rangle|N_{-1}\rangle$ as

$$\rho^{(N)} = \sum_{i_\pm, j_\pm} \rho^{i_+,j_-}_{i_+,i_-} \bigotimes_{m=0,\pm1} |i_m\rangle\langle j_m| \,. \tag{F.1}$$

Where the sums goes over $i_+ = 0 : N, i_- = 0 : (N - i_+)$ and idem for $j_\pm$. Now, let us assume a new spatial mode is accessible to the atoms. We label the two spatial modes A and B, and we use the basis $\bigotimes_m |N_{Am}, N_{Bm}\rangle$, where each ket corresponds to a spin state m, and the two numbers within the kets indicate the number of atoms of spin m in the spatial mode A and B. We now imagine to add a linear coupling between the two spatial modes ($e.g.$ tunneling). If all atoms are initially in A, after some time, the state evolves as

$$\rho^{(N)} \propto \sum_{i_\pm, j_\pm} \rho^{j_+,j_-}_{i_+,i_-} \bigotimes_{m=0,\pm1} \sum_{k_m, l_m} \left[\binom{i_m}{k_m} \binom{j_m}{l_m} \right]^{\frac{1}{2}} \kappa^{k_m + l_m} |k_m, i_m - k_m\rangle\langle l_m, j_m - l_m| \,. \tag{F.2}$$

where κ is a number characterizing the strength and duration of the coupling (it won't play any role in the following). We then project $\rho^{(N)}$ onto states with n atoms in A and $N - n$ atoms in B, and trace over the spatial mode B to obtain $\rho^{(n)}$[1]. In the sum of Eq. (F.2), we have $\sum k_m = \sum l_m = n$, and $i_m - k_m = j_m - l_m$. The factor κ is then taken to the power n, and is simply a constant. Furthermore, noticing that (we are back to the spin basis, $|N_+, N_-\rangle = |N_+, N_0 = N - N_+ - N_-, N_-\rangle$)

$$\rho^{j_+,j_-}_{i_+,i_-} = \langle i_+, i_-|\rho^{(N)} \left[\prod_{m=0,\pm1} \left(\frac{(j_m - l_m)!}{j_m!} \frac{(i_m - k_m)!}{i_m!} \right)^{\frac{1}{2}} \hat{a}_m^{\dagger l_m} \hat{a}_m^{k_m} \right] |i_+, i_-\rangle, \tag{F.3}$$

we can rewrite the sum as

$$\rho^{(n)} = \frac{1}{\mathcal{N}} \sum_{k_\pm, l_\pm} \mathrm{Tr}\left(\rho^{(N)} \hat{P}^{(n)\dagger}_{l_+,l_-} \hat{P}^{(n)}_{k_+,k_-} \right) |k_+, n - k_+ - k_-, k_-\rangle\langle l_+, n - l_+ - l_-, l_-| \,. \tag{F.4}$$

where

$$\hat{P}^{(n)}_{k_+,k_-} = \frac{\hat{a}_{+1}^{k_+} \hat{a}_{-1}^{k_-} \hat{a}_0^{n-k_+-k_-}}{\sqrt{k_+! k_-! (n - k_+ - k_-)!}} \,, \tag{F.5}$$

and $\mathcal{N}$ is a normalization constant. We take $\rho^{(n)}$ to be normalized to one, thus

$$\mathcal{N} = \sum_{i,j,k_+,k_-} \rho^{i,j}_{i,j} \binom{i}{k_+} \binom{j}{k_-} \binom{N - i - j}{n - k_+ - k_-} \,, \tag{F.6}$$

using twice the identity $\sum_q \binom{p}{q}\binom{r}{s-q} = \binom{p+r}{s}$ we obtain

$$\mathcal{N} = \binom{N}{n} \,. \tag{F.7}$$

[1] For instance, one could imagine that the atoms in B are lost, or equivalently that an observer has only access to the mode A. The projection is necessary to have blocks with well-defined atom numbers, otherwise, the state of mode A, will be a mixture of the $\rho^{(n)}$, with n within $\sim \overline{n} \pm \sqrt{\overline{n}}$ (shot-noise), and $\overline{n}$ given by κ.

F.0.2 Iterative calculation in the spin-state basis

It is cumbersome to use the above formula to compute the state we are interested in which has non-zero weights only on a few states in the spin state basis. Here we show the formula we use for an efficient calculation of $\rho^{(n)}$. We use an iterative method and hence we only need to know Tr_1, which we apply on $\rho^{(n)}$ to get $\rho^{(n-1)}$. We start with

$$\rho^{(n)} = \sum c_{SM}^{TP} |nSM\rangle\langle nTP| \,, \tag{F.8}$$

We then use the expression of the spin state in the coherent nematic state basis [50]

$$|nSM\rangle = \frac{1}{\sqrt{f_S^n}} \int d\mathbf{\Omega} Y_{SM}(\mathbf{\Omega}) |n:\mathbf{\Omega}\rangle \,, \tag{F.9}$$

where

$$f_S^n = \frac{4\pi n! 2^S (\frac{n+S}{2})!}{(\frac{n-S}{2})!(n+S+1)!} \,. \tag{F.10}$$

We arrive at

$$\rho^{(n)} = \sum c_{SM}^{TP} \frac{1}{\sqrt{f_S^n f_T^n}} \int\int d\mathbf{\Omega} d\mathbf{\Omega}' Y_{SM}(\mathbf{\Omega}) Y_{TP}^*(\mathbf{\Omega}') |n:\mathbf{\Omega}\rangle\langle n:\mathbf{\Omega}'| \,. \tag{F.11}$$

This form is convenient to trace over the state of k particles, it simply amounts to splitting the coherent state $|n:\mathbf{\Omega}\rangle = |k:\mathbf{\Omega}\rangle|n-k:\mathbf{\Omega}\rangle$. We take $k=1$, and we use [50]

$$\langle n:\mathbf{\Omega}|nSM\rangle \sqrt{f_S^n} Y_{SM}(\mathbf{\Omega}) \,, \tag{F.12}$$

to obtain

$$\rho^{(n-1)} = \sum c_{SM}^{TP} \frac{f_1^1}{\sqrt{f_S^n f_T^n}} \int\int d\mathbf{\Omega} d\mathbf{\Omega}' Y_{SM}(\mathbf{\Omega}) Y_{TP}^*(\mathbf{\Omega}') Y_{1m}^*(\mathbf{\Omega}) Y_{1m}(\mathbf{\Omega}') |n-1:\mathbf{\Omega}\rangle\langle n-1:\mathbf{\Omega}'| \,.$$

where the sum is now taken over S, M, T, P and $m = \pm 0, 1$. The matrix element in the spin state basis are

$$d_{S_1M_1}^{T_1P_1} = \langle n-1 S_1 M_1 | \rho^{(n-1)} | n-1 T_1 P_1 \rangle \,,$$
$$d_{S_1M_1}^{T_1P_1} = \sum c_{SM}^{TP} \frac{f_1^1 \sqrt{f_{S_1}^{n-1} f_{T_1}^{n-1}}}{\sqrt{f_S^n f_T^n}} \int\int d\mathbf{\Omega} d\mathbf{\Omega}' Y_{SM}(\mathbf{\Omega}) Y_{TP}^*(\mathbf{\Omega}') Y_{1m}^*(\mathbf{\Omega}) Y_{1m}(\mathbf{\Omega}') Y_{S_1M_1}^*(\mathbf{\Omega}) Y_{T_1P_1}(\mathbf{\Omega}') \,,$$

We then express the integral in function of Clebsch-Gordan coefficient

$$\int d\mathbf{\Omega} Y_{S_1M_1}^*(\mathbf{\Omega}) Y_{S_2M_2}^*(\mathbf{\Omega}) Y_{SM}(\mathbf{\Omega}') = \sqrt{\frac{(2S_1+1)(2S_2+1)}{4\pi(2S+1)}} \langle S_1 0 S_2 0 | S0\rangle \langle S_1 M_1 S_2 M_2 | SM\rangle \,,$$

and using also $f_1^1 = 4\pi/3$ to obtain

$$d_{S_1M_1}^{T_1P_1} = \sum c_{SM}^{TP} \sqrt{\frac{f_{S_1}^{n-1} f_{T_1}^{n-1} (2S_1+1)(2T_1+1)}{f_S^n f_T^n (2S+1)(2T+1)}} \langle S_1 010 | S0\rangle \langle T_1 010 | T0\rangle \langle S_1 M_1 1m | SM\rangle \langle T_1 P_1 1m | TP\rangle \,.$$

The sum is taken over S, M, T, P and $m = 0, \pm 1$, but the selection rules of the Clebsh-Gordan coefficient implies that only the term with $T = S \pm 1$ and $M = M_1 + m$ are non-zero. This makes the above expression useful for the calculation of the reduced density matrix.

Bibliography

[1] C. N. Cohen-Tannoudji, "Nobel lecture: Manipulating atoms with photons," *Reviews of Modern Physics*, vol. 70, no. 3, p. 707, 1998.

[2] A. D. Ludlow, M. M. Boyd, J. Ye, E. Peik, and P. O. Schmidt, "Optical atomic clocks," *Reviews of Modern Physics*, vol. 87, no. 2, p. 637, 2015.

[3] M. H. Anderson, J. R. Ensher, M. R. Matthews, C. E. Wieman, and E. A. Cornell, "Observation of Bose-Einstein condensation in a dilute atomic vapor," *Science*, vol. 269, no. 5221, pp. 198–201, 1995.

[4] K. B. Davis, M. O. Mewes, M. R. Andrews, N. J. van Druten, D. S. Durfee, D. M. Kurn, and W. Ketterle, "Bose-Einstein condensation in a gas of Sodium atoms," *Phys. Rev. Lett.*, vol. 75, pp. 3969–3973, Nov 1995.

[5] M. Andrews, C. Townsend, H.-J. Miesner, D. Durfee, D. Kurn, and W. Ketterle, "Observation of interference between two Bose condensates," *Science*, vol. 275, no. 5300, pp. 637–641, 1997.

[6] M. Albiez, R. Gati, J. Fölling, S. Hunsmann, M. Cristiani, and M. K. Oberthaler, "Direct observation of tunneling and nonlinear self-trapping in a single bosonic Josephson junction," *Phys. Rev. Lett.*, vol. 95, p. 010402, Jun 2005.

[7] A. J. Leggett, "Macroscopic quantum systems and the quantum theory of measurement," *Progress of Theoretical Physics Supplement*, vol. 69, pp. 80–100, 1980.

[8] M. Arndt and K. Hornberger, "Testing the limits of quantum mechanical superpositions," *Nature Physics*, vol. 10, no. 4, pp. 271–277, 2014.

[9] L. Pezzè, A. Smerzi, M. K. Oberthaler, R. Schmied, and P. Treutlein, "Quantum metrology with nonclassical states of atomic ensembles," *Rev. Mod. Phys.*, vol. 90, p. 035005, Sep 2018.

[10] C. Gross, T. Zibold, E. Nicklas, J. Estève, and M. K. Oberthaler, "Nonlinear atom interferometer surpasses classical precision limit," *Nature*, vol. 464, pp. 1165–1169, Mar. 2010.

[11] C. D. Hamley, C. S. Gerving, T. M. Hoang, E. M. Bookjans, and M. S. Chapman, "Spin-nematic squeezed vacuum in a quantum gas," *Nature Physics*, vol. 8, pp. 305–308, feb 2012.

[12] B. Lucke, M. Scherer, J. Kruse, L. Pezze, F. Deuretzbacher, P. Hyllus, O. Topic, J. Peise, W. Ertmer, J. Arlt, L. Santos, A. Smerzi, and C. Klempt, "Twin matter waves for interferometry beyond the classical limit," *Science*, vol. 334, pp. 773–776, Oct. 2011.

[13] D. Linnemann, H. Strobel, W. Muessel, J. Schulz, R. J. Lewis-Swan, K. V. Kheruntsyan, and M. K. Oberthaler, "Quantum-enhanced sensing based on time reversal of nonlinear dynamics," *Phys. Rev. Lett.*, vol. 117, p. 013001, Jun 2016.

[14] D. Linnemann, J. Schulz, W. Muessel, P. Kunkel, M. Prüfer, A. Frölian, H. Strobel, and M. K. Oberthaler, "Active SU(1,1) atom interferometry," *Quantum Science and Technology*, vol. 2, p. 044009, aug 2017.

[15] H. Strobel, W. Muessel, D. Linnemann, T. Zibold, D. B. Hume, L. Pezze, A. Smerzi, and M. K. Oberthaler, "Fisher information and entanglement of non-gaussian spin states," *Science*, vol. 345, pp. 424–427, July 2014.

[16] A. Omran, H. Levine, A. Keesling, G. Semeghini, T. T. Wang, S. Ebadi, H. Bernien, A. S. Zibrov, H. Pichler, S. Choi, *et al.*, "Generation and manipulation of Schrödinger cat states in Rydberg atom arrays," *Science*, vol. 365, no. 6453, pp. 570–574, 2019.

[17] B. Keimer and J. Moore, "The physics of quantum materials," *Nature Physics*, vol. 13, no. 11, pp. 1045–1055, 2017.

[18] I. Bloch, J. Dalibard, and S. Nascimbene, "Quantum simulations with ultracold quantum gases," *Nature Physics*, vol. 8, no. 4, pp. 267–276, 2012.

[19] M. Lewenstein, A. Sanpera, V. Ahufinger, B. Damski, A. Sen, and U. Sen, "Ultracold atomic gases in optical lattices: mimicking condensed matter physics and beyond," *Advances in Physics*, vol. 56, no. 2, pp. 243–379, 2007.

[20] I. Bloch, "Ultracold quantum gases in optical lattices," *Nature physics*, vol. 1, no. 1, pp. 23–30, 2005.

[21] M. Greiner, O. Mandel, T. Esslinger, T. W. Hänsch, and I. Bloch, "Quantum phase transition from a superfluid to a Mott insulator in a gas of ultracold atoms," *nature*, vol. 415, no. 6867, pp. 39–44, 2002.

[22] Y.-J. Lin, R. L. Compton, K. Jiménez-García, J. V. Porto, and I. B. Spielman, "Synthetic magnetic fields for ultracold neutral atoms," *Nature*, vol. 462, no. 7273, pp. 628–632, 2009.

[23] Y.-J. Lin, K. Jiménez-García, and I. B. Spielman, "Spin–orbit-coupled Bose–Einstein condensates," *Nature*, vol. 471, no. 7336, pp. 83–86, 2011.

[24] J. Dalibard, F. Gerbier, G. Juzeliūnas, and P. Öhberg, "Colloquium: Artificial gauge potentials for neutral atoms," *Reviews of Modern Physics*, vol. 83, no. 4, p. 1523, 2011.

[25] C. Chin, R. Grimm, P. Julienne, and E. Tiesinga, "Feshbach resonances in ultracold gases," *Reviews of Modern Physics*, vol. 82, no. 2, p. 1225, 2010.

[26] L. Pitaevskii and S. Stringari, *Bose-Einstein Condensation*. Oxford Science Publication.

[27] W. S. Bakr, J. I. Gillen, A. Peng, S. Fölling, and M. Greiner, "A quantum gas microscope for detecting single atoms in a Hubbard-regime optical lattice," *Nature*, vol. 462, no. 7269, pp. 74–77, 2009.

[28] D. M. Stamper-Kurn and M. Ueda, "Spinor Bose gases: Symmetries, magnetism, and quantum dynamics," *Rev. Mod. Phys.*, vol. 85, pp. 1191–1244, Jul 2013.

[29] Y. Kawaguchi and M. Ueda, "Spinor Bose–Einstein condensates," *Physics Reports*, vol. 520, pp. 253–381, Nov. 2012.

[30] L. E. Sadler, J. M. Higbie, S. R. Leslie, M. Vengalattore, and D. M. Stamper-Kurn, "Spontaneous symmetry breaking in a quenched ferromagnetic spinor Bose–Einstein condensate," *Nature*, vol. 443, pp. 312–315, Sept. 2006.

[31] J.-y. Choi, W. J. Kwon, and Y.-i. Shin, "Observation of topologically stable 2d skyrmions in an antiferromagnetic spinor bose-einstein condensate," *Physical review letters*, vol. 108, no. 3, p. 035301, 2012.

[32] R. Loudon, *The quantum theory of light*. OUP Oxford, 2000.

[33] G. I. Mias, N. R. Cooper, and S. M. Girvin, "Quantum noise, scaling, and domain formation in a spinor Bose-Einstein condensate," *Phys. Rev. A*, vol. 77, p. 023616, Feb 2008.

[34] J. Guzman, G.-B. Jo, A. N. Wenz, K. W. Murch, C. K. Thomas, and D. M. Stamper-Kurn, "Long-time-scale dynamics of spin textures in a degenerate $f = 1$ ^{87}Rb spinor Bose gas," *Phys. Rev. A*, vol. 84, p. 063625, Dec 2011.

[35] D. M. Stamper-Kurn and M. Ueda, "Spinor Bose gases: Symmetries, magnetism, and quantum dynamics," *Rev. Mod. Phys.*, vol. 85, pp. 1191–1244, Jul 2013.

[36] D. Jacob, L. Shao, V. Corre, T. Zibold, L. De Sarlo, E. Mimoun, J. Dalibard, and F. Gerbier, "Phase diagram of spin-1 antiferromagnetic Bose-Einstein condensates," *Phys. Rev. A*, vol. 86, p. 061601, Dec 2012.

[37] T. Zibold, V. Corre, C. Frapolli, A. Invernizzi, J. Dalibard, and F. Gerbier, "Spin-nematic order in antiferromagnetic spinor condensates," *Phys. Rev. A*, vol. 93, p. 023614, Feb 2016.

[38] E. M. Bookjans, A. Vinit, and C. Raman, "Quantum phase transition in an antiferromagnetic spinor Bose-Einstein condensate," *Phys. Rev. Lett.*, vol. 107, p. 195306, Nov 2011.

[39] P. Nozieres and D. Saint James, "Particle vs. pair condensation in attractive bose liquids," *Journal de Physique*, vol. 43, no. 7, pp. 1133–1148, 1982.

[40] T.-L. Ho and S. K. Yip, "Fragmented and single condensate ground states of spin-1 Bose gas," *Phys. Rev. Lett.*, vol. 84, pp. 4031–4034, May 2000.

[41] M. Koashi and M. Ueda, "Exact eigenstates and magnetic response of spin-1 and spin-2 Bose-Einstein condensates," *Phys. Rev. Lett.*, vol. 84, pp. 1066–1069, Feb 2000.

[42] E. J. Mueller, T.-L. Ho, M. Ueda, and G. Baym, "Fragmentation of Bose-Einstein condensates," *Phys. Rev. A*, vol. 74, p. 033612, Sep 2006.

[43] Y. Castin and C. Herzog, "Bose–Einstein condensates in symmetry breaking states," *Comptes Rendus de l'Académie des Sciences - Series IV - Physics*, vol. 2, pp. 419–443, Apr. 2001.

[44] A. J. Leggett, "Bose-Einstein condensation in atomic gases: some fundamental concepts," *Rev. Mod. Phys.*, vol. 73, p. 307, 2001.

[45] B. Evrard, A. Qu, K. Jiménez-García, J. Dalibard, and F. Gerbier, "Relaxation and hysteresis near Shapiro resonances in a driven spinor condensate," *Physical Review A*, vol. 100, no. 2, p. 023604, 2019.

[46] C. Cohen-Tannoudji, B. Diu, and F. Laloë, *Mécanique quantique vol.2*. EDP-Sciences.

[47] C. Samuelis, E. Tiesinga, T. Laue, M. Elbs, H. Knöckel, and E. Tiemann, "Cold atomic collisions studied by molecular spectroscopy," *Phys. Rev. A*, vol. 63, p. 012710, Dec 2000.

[48] C. K. Law, H. Pu, and N. P. Bigelow, "Quantum spin mixing in spinor Bose-Einstein condensates," *Phys. Rev. Lett.*, vol. 81, p. 5257, 1998.

[49] S. Yi, O. E. Müstecaplıoğlu, C. P. Sun, and L. You, "Single-mode approximation in a spinor-1 atomic condensate," *Phys. Rev. A*, vol. 66, p. 011601, Jul 2002.

[50] R. Barnett, J. D. Sau, and S. Das Sarma, "Antiferromagnetic spinor condensates are quantum rotors," *Phys. Rev. A*, vol. 82, p. 031602, Sep 2010.

[51] C. Cohen-Tannoudji, B. Diu, and F. Laloë, *Mécanique quantique vol.1*. EDP-Sciences.

[52] V. Corre, *Magnetism in spin-1 Bose-Einstein condensates with antiferromagnetic interactions*. Theses, Ecole normale supérieure - ENS PARIS, Dec. 2014.

[53] K. Jiménez-García, A. Invernizzi, B. Evrard, C. Frapolli, J. Dalibard, and F. Gerbier, "Spontaneous formation and relaxation of spin domains in antiferromagnetic spin-1 condensates," *Nature Communications*, vol. 10, Mar. 2019.

[54] A. Invernizzi, *Phase separation and spin domains in quasi-1D spinor condensates*. Theses, PSL Research University, Nov. 2017.

[55] W. Zhang, S. Yi, and L. You, "Mean field ground state of a spin-1 condensate in a magnetic field," *New Journal of Physics*, vol. 5, pp. 77–77, jun 2003.

[56] D. Jacob, L. Shao, V. Corre, T. Zibold, L. De Sarlo, E. Mimoun, J. Dalibard, and F. Gerbier, "Phase diagram of spin-1 antiferromagnetic Bose-Einstein condensates," *Phys. Rev. A*, vol. 86, p. 061601, Dec 2012.

[57] E. M. Bookjans, A. Vinit, and C. Raman, "Quantum phase transition in an antiferromagnetic spinor Bose-Einstein condensate," *Phys. Rev. Lett.*, vol. 107, p. 195306, Nov 2011.

[58] M.-S. Chang, Q. Qin, W. Zhang, L. You, and M. S. Chapman, "Coherent spinor dynamics in a spin-1 Bose condensate," *Nature Physics*, vol. 1, p. 111, 2005.

[59] J. Kronjäger, C. Becker, P. Navez, K. Bongs, and K. Sengstock, "Magnetically tuned spin dynamics resonance," *Phys. Rev. Lett.*, vol. 97, p. 110404, Sep 2006.

[60] A. T. Black, E. Gomez, L. D. Turner, S. Jung, and P. D. Lett, "Spinor dynamics in an antiferromagnetic spin-1 condensate," *Phys. Rev. Lett.*, vol. 99, p. 070403, Aug 2007.

[61] Y. Liu, E. Gomez, S. E. Maxwell, L. D. Turner, E. Tiesinga, and P. D. Lett, "Number fluctuations and energy dissipation in Sodium spinor condensates," *Phys. Rev. Lett.*, vol. 102, p. 225301, Jun 2009.

[62] C. Klempt, O. Topic, G. Gebreyesus, M. Scherer, T. Henninger, P. Hyllus, W. Ertmer, L. Santos, and J. J. Arlt, "Multiresonant spinor dynamics in a Bose-Einstein condensate," *Phys. Rev. Lett.*, vol. 103, p. 195302, Nov 2009.

[63] C. Klempt, O. Topic, G. Gebreyesus, M. Scherer, T. Henninger, P. Hyllus, W. Ertmer, L. Santos, and J. J. Arlt, "Parametric amplification of vacuum fluctuations in a spinor condensate," *Phys. Rev. Lett.*, vol. 104, p. 195303, May 2010.

[64] B. Lücke, M. Scherer, J. Kruse, L. Pezzé, F. Deuretzbacher, P. Hyllus, O. Topic, J. Peise, W. Ertmer, J. Arlt, L. Santos, A. Smerzi, and C. Klempt, "Twin matter waves for interferometry beyond the classical limit," *Science*, vol. 334, no. 6057, pp. 773–776, 2011.

[65] C. D. Hamley, C. S. Gerving, T. M. Hoang, E. M. Bookjans, and M. S. Chapman, "Spin-nematic squeezed vacuum in a quantum gas," *Nat. Phys.*, vol. 8, pp. 305–308, 2012.

[66] D. Linnemann, H. Strobel, W. Muessel, J. Schulz, R. J. Lewis-Swan, K. V. Kheruntsyan, and M. K. Oberthaler, "Quantum-enhanced sensing based on time reversal of nonlinear dynamics," *Phys. Rev. Lett.*, vol. 117, p. 013001, Jun 2016.

[67] X.-Y. Luo, Y.-Q. Zou, L.-N. Wu, Q. Liu, M.-F. Han, M. K. Tey, and L. You, "Deterministic entanglement generation from driving through quantum phase transitions," *Science*, vol. 355, no. 6325, pp. 620–623, 2017.

[68] T. Ohmi and K. Machida, "Bose-Einstein condensation with internal degrees of freedom in alkali atom gases," *Journal of the Physical Society of Japan*, vol. 67, pp. 1822–1825, June 1998.

[69] T. Kim, O. Pfister, M. J. Holland, J. Noh, and J. L. Hall, "Influence of decorrelation on Heisenberg-limited interferometry with quantum correlated photons," *Phys. Rev. A*, vol. 57, pp. 4004–4013, May 1998.

[70] L. Amico, R. Fazio, A. Osterloh, and V. Vedral, "Entanglement in many-body systems," *Rev. Mod. Phys.*, vol. 80, pp. 517–576, May 2008.

[71] V. Vedral, "The role of relative entropy in quantum information theory," *Rev. Mod. Phys.*, vol. 74, pp. 197–234, Mar 2002.

[72] R. Islam, R. Ma, P. M. Preiss, M. E. Tai, A. Lukin, M. Rispoli, and M. Greiner, "Measuring entanglement entropy in a quantum many-body system," *Nature*, vol. 528, pp. 77–83, Dec. 2015.

[73] M. Gessner and A. Buchleitner, "On the reduced dynamics of a subset of interacting bosonic particles," *Annals of Physics*, vol. 390, pp. 192–213, Mar. 2018.

[74] O. Penrose and L. Onsager, "Bose-Einstein condensation and liquid helium," *Phys. Rev.*, vol. 104, pp. 576–584, Nov 1956.

[75] H. M. Wiseman and J. A. Vaccaro, "Entanglement of indistinguishable particles shared between two parties," *Phys. Rev. Lett.*, vol. 91, p. 097902, Aug 2003.

[76] P. Kunkel, M. Prüfer, H. Strobel, D. Linnemann, A. Frölian, T. Gasenzer, M. Gärttner, and M. K. Oberthaler, "Spatially distributed multipartite entanglement enables EPR steering of atomic clouds," *Science*, vol. 360, pp. 413–416, Apr. 2018.

[77] M. Fadel, T. Zibold, B. Décamps, and P. Treutlein, "Spatial entanglement patterns and Einstein-podolsky-rosen steering in Bose-Einstein condensates," *Science*, vol. 360, pp. 409–413, Apr. 2018.

[78] K. Lange, J. Peise, B. Lücke, I. Kruse, G. Vitagliano, I. Apellaniz, M. Kleinmann, G. Tóth, and C. Klempt, "Entanglement between two spatially separated atomic modes," *Science*, vol. 360, pp. 416–418, Apr. 2018.

[79] J. Hu, L. Feng, Z. Zhang, and C. Chin, "Quantum simulation of unruh radiation," *Nature Physics*, vol. 15, pp. 785–789, May 2019.

[80] M. D. Barrett, J. A. Sauer, and M. S. Chapman, "All-optical formation of an atomic Bose-Einstein condensate," *Phys. Rev. Lett.*, vol. 87, p. 010404, Jun 2001.

[81] E. Mimoun, *Bose-Einstein condensate of Sodium in a mesoscopic trap*. Theses, Université Pierre et Marie Curie - Paris VI, Sept. 2010.

[82] D. Jacob, *Spin-1 Bose-Einstein condensates : experimental study with Sodium atoms in an optical dipole trap*. Theses, Université Pierre et Marie Curie - Paris VI, May 2012.

[83] E. Mimoun, L. D. Sarlo, J.-J. Zondy, J. Dalibard, and F. Gerbier, "Sum-frequency generation of 589 nm light with near-unit efficiency," *Opt. Express*, vol. 16, pp. 18684–18691, Nov 2008.

[84] E. Mimoun, L. D. Sarlo, D. Jacob, J. Dalibard, and F. Gerbier, "Fast production of ultracold Sodium gases using light-induced desorption and optical trapping," *Phys. Rev. A*, vol. 81, p. 023631, Feb 2010.

[85] D. Jacob, E. Mimoun, L. D. Sarlo, M. Weitz, J. Dalibard, and F. Gerbier, "Production of Sodium Bose–Einstein condensates in an optical dimple trap," *New Journal of Physics*, vol. 13, p. 065022, jun 2011.

[86] A. Qu, B. Evrard, J. Dalibard, and F. Gerbier, "Probing entanglement in a spinor condensate near the single atom level," *arXiv preprint arXiv:2004.09003*, 2020.

[87] J. Dalibard, *Atomes ultra-froids*. Notes de cours.

[88] D. Steck, *Alkali D line Data*.

[89] K. W., D. D.S., and S.-K. D.M., "Making, probing and understanding Bose-Einstein condensates," *Proceedings of the International School of Physics Enrico Fermi*, vol. 140, no. Bose-Einstein Condensation in Atomic Gases, p. 67–176, 1999.

[90] S. J. M. Kuppens, K. L. Corwin, K. W. Miller, T. E. Chupp, and C. E. Wieman, "Loading an optical dipole trap," *Phys. Rev. A*, vol. 62, p. 013406, Jun 2000.

[91] C. Frapolli, *Thermodynamics and magnetism of antiferromagnetic spinor Bose-Einstein condensates*. Theses, PSL Research University, Mar. 2017.

[92] G. Reinaudi, T. Lahaye, Z. Wang, and D. Guéry-Odelin, "Strong saturation absorption imaging of dense clouds of ultracold atoms," *Opt. Lett.*, vol. 32, pp. 3143–3145, Nov 2007.

[93] Y. Castin and R. Dum, "Bose-Einstein condensates in time dependent traps," *Phys. Rev. Lett.*, vol. 77, pp. 5315–5319, Dec 1996.

[94] D. B. Hume, I. Stroescu, M. Joos, W. Muessel, H. Strobel, and M. K. Oberthaler, "Accurate atom counting in mesoscopic ensembles," *Phys. Rev. Lett.*, vol. 111, p. 253001, Dec 2013.

[95] W. Muessel, H. Strobel, M. Joos, E. Nicklas, I. Stroescu, J. Tomkovič, D. B. Hume, and M. K. Oberthaler, "Optimized absorption imaging of mesoscopic atomic clouds," *Applied Physics B*, vol. 113, pp. 69–73, Oct 2013.

[96] E. W. Streed, A. Jechow, B. G. Norton, and D. Kielpinski, "Absorption imaging of a single atom," *Nature Communications*, vol. 3, Jan. 2012.

[97] S. Chu, L. Hollberg, J. E. Bjorkholm, A. Cable, and A. Ashkin, "Three-dimensional viscous confinement and cooling of atoms by resonance radiation pressure," *Phys. Rev. Lett.*, vol. 55, pp. 48–51, Jul 1985.

[98] W. D. Phillips, J. V. Prodan, and H. J. Metcalf, "Laser cooling and electromagnetic trapping of neutral atoms," *J. Opt. Soc. Am. B*, vol. 2, pp. 1751–1767, Nov 1985.

[99] T. W. Hodapp, C. Gerz, C. Furtlehner, C. I. Westbrook, W. D. Phillips, and J. Dalibard, "Three-dimensional spatial diffusion in optical molasses," *Applied Physics B*, vol. 60, pp. 135–143, Feb 1995.

[100] C. F. Ockeloen, A. F. Tauschinsky, R. J. C. Spreeuw, and S. Whitlock, "Detection of small atom numbers through image processing," *Phys. Rev. A*, vol. 82, p. 061606, Dec 2010.

[101] C. Frapolli, T. Zibold, A. Invernizzi, K. Jiménez-García, J. Dalibard, and F. Gerbier, "Stepwise Bose-Einstein condensation in a spinor gas," *Phys. Rev. Lett.*, vol. 119, p. 050404, Aug 2017.

[102] W. Zhang, D. L. Zhou, M.-S. Chang, M. S. Chapman, and L. You, "Coherent spin mixing dynamics in a spin-1 atomic condensate," *Phys. Rev. A*, vol. 72, p. 013602, Jul 2005.

[103] J. Kronjäger, C. Becker, M. Brinkmann, R. Walser, P. Navez, K. Bongs, and K. Sengstock, "Evolution of a spinor condensate: Coherent dynamics, dephasing, and revivals," *Phys. Rev. A*, vol. 72, p. 063619, Dec 2005.

[104] B. Josephson, "Possible new effects in superconductive tunnelling," *Physics Letters*, vol. 1, no. 7, pp. 251 – 253, 1962.

[105] S. Shapiro, "Josephson currents in superconducting tunneling: The effect of microwaves and other observations," *Phys. Rev. Lett.*, vol. 11, pp. 80–82, Jul 1963.

[106] G. P. A. Barone, *Physics and Applications of the Josephson Effect*. New York: John Wiley and Sons, 1982.

[107] R. L. Kautz, "Noise, chaos, and the Josephson voltage standard," *Reports on Progress in Physics*, vol. 59, no. 8, p. 935, 1996.

[108] S. V. Pereverzev, A. Loshak, S. Backhaus, J. C. Davis, and R. E. Packard, "Quantum oscillations between two weakly coupled reservoirs of superfluid 3He," *Nature*, vol. 388, p. 449, July 1997.

[109] O. Avenel, Y. Mukharsky, and E. Varoquaux, "Josephson effect and a π-state in superfluid 3He," *Nature*, vol. 397, p. 484, Feb. 1999.

[110] R. W. Simmonds, A. Marchenkov, J. C. Davis, and R. E. Packard, "Observation of the superfluid Shapiro effect in a ^{3}He weak link," *Phys. Rev. Lett.*, vol. 87, p. 035301, Jun 2001.

[111] K. Sukhatme, Y. Mukharsky, T. Chui, and D. Pearson, "Observation of the ideal Josephson effect in superfluid ^{4}He," *Nature*, vol. 411, p. 280, May 2001.

[112] D. Sarchi, I. Carusotto, M. Wouters, and V. Savona, "Coherent dynamics and parametric instabilities of microcavity polaritons in double-well systems," *Phys. Rev. B*, vol. 77, p. 125324, Mar 2008.

[113] I. A. Shelykh, D. D. Solnyshkov, G. Pavlovic, and G. Malpuech, "Josephson effects in condensates of excitons and exciton polaritons," *Phys. Rev. B*, vol. 78, p. 041302, Jul 2008.

[114] M. Abbarchi, A. Amo, V. Sala, D. Solnyshkov, H. Flayac, L. Ferrier, I. Sagnes, E. Galopin, A. Lemaitre, G. Malpuech, and J. Bloch, "Macroscopic quantum self-trapping and Josephson oscillations of exciton polaritons," *Nature Physics*, vol. 09, pp. 275–279, May 2013.

[115] S. Levy, E. Lahoud, I. Shomroni, and J. Steinhauer, "The a.c. and d.c. Josephson effects in a Bose-Einstein condensate," *Nature*, vol. 449, pp. 579–583, 10 2007.

[116] L. J. LeBlanc, A. B. Bardon, J. McKeever, M. H. T. Extavour, D. Jervis, J. H. Thywissen, F. Piazza, and A. Smerzi, "Dynamics of a tunable superfluid junction," *Phys. Rev. Lett.*, vol. 106, p. 025302, Jan 2011.

[117] C. Ryu, P. W. Blackburn, A. A. Blinova, and M. G. Boshier, "Experimental realization of Josephson junctions for an atom SQUID," *Phys. Rev. Lett.*, vol. 111, p. 205301, Nov 2013.

[118] G. Valtolina, A. Burchianti, A. Amico, E. Neri, K. Xhani, J. A. Seman, A. Trombettoni, A. Smerzi, M. Zaccanti, M. Inguscio, and G. Roati, "Josephson effect in Fermionic superfluids across the BEC-BCS crossover," *Science*, vol. 350, no. 6267, pp. 1505–1508, 2015.

[119] M. Pigneur, T. Berrada, M. Bonneau, T. Schumm, E. Demler, and J. Schmiedmayer, "Relaxation to a phase-locked equilibrium state in a one-dimensional Bosonic Josephson junction," *Phys. Rev. Lett.*, vol. 120, p. 173601, Apr 2018.

[120] T. M. Hoang, C. S. Gerving, B. J. Land, M. Anquez, C. D. Hamley, and M. S. Chapman, "Dynamic stabilization of a quantum many-body spin system," *Phys. Rev. Lett.*, vol. 111, p. 090403, Aug 2013.

[121] T. M. Hoang, M. Anquez, B. A. Robbins, X. Y. Yang, B. J. Land, C. D. Hamley, and M. S. Chapman, "Parametric excitation and squeezing in a many-body spinor condensate," *Nature Communications*, vol. 7, p. 11233, Apr. 2016.

[122] L. D. Landau and E. M. Lifshitz, *Mechanics*, vol. 1. Pergamon Press, 1st ed., 1960.

[123] R. Citro, E. G. D. Torre, L. D'Alessio, A. Polkovnikov, M. Babadi, T. Oka, and E. Demler, "Dynamical stability of a many-body Kapitza pendulum," *Annals of Physics*, vol. 360, pp. 694 – 710, 2015.

[124] M. Rigol, V. Dunjko, and M. Olshanii, "Thermalization and its mechanism for generic isolated quantum systems," *Nature*, vol. 452, pp. 854–858, Apr. 2008.

[125] A. Polkovnikov, K. Sengupta, A. Silva, and M. Vengalattore, "*Colloquium* : Nonequilibrium dynamics of closed interacting quantum systems," *Rev. Mod. Phys.*, vol. 83, pp. 863–883, Aug 2011.

[126] J. Eisert, M. Friesdorf, and C. Gogolin, "Quantum many-body systems out of equilibrium," *Nature Physics*, vol. 11, p. 124, Feb. 2015.

[127] A. Lazarides, A. Das, and R. Moessner, "Equilibrium states of generic quantum systems subject to periodic driving," *Phys. Rev. E*, vol. 90, p. 012110, Jul 2014.

[128] L. D'Alessio and M. Rigol, "Long-time behavior of isolated periodically driven interacting lattice systems," *Phys. Rev. X*, vol. 4, p. 041048, Dec 2014.

[129] F. Peronaci, M. Schiró, and O. Parcollet, "Resonant thermalization of periodically driven strongly correlated electrons," *Phys. Rev. Lett.*, vol. 120, p. 197601, May 2018.

[130] T. Mori, T. Kuwahara, and K. Saito, "Rigorous bound on energy absorption and generic relaxation in periodically driven quantum systems," *Phys. Rev. Lett.*, vol. 116, p. 120401, Mar 2016.

[131] D. A. Abanin, W. De Roeck, W. W. Ho, and F. m. c. Huveneers, "Effective hamiltonians, prethermalization, and slow energy absorption in periodically driven many-body systems," *Phys. Rev. B*, vol. 95, p. 014112, Jan 2017.

[132] T. Mori, "Floquet prethermalization in periodically driven classical spin systems." arXiv:1804.02165, 2018.

[133] T. Lahaye, C. Menotti, L. Santos, M. Lewenstein, and T. Pfau, "The physics of dipolar bosonic quantum gases," *Reports on Progress in Physics*, vol. 72, no. 12, p. 126401, 2009.

[134] S. Yi, O. E. Müstecaplıoğlu, C. P. Sun, and L. You, "Single-mode approximation in a spinor-1 atomic condensate," *Phys. Rev. A*, vol. 66, p. 011601, Jul 2002.

[135] R. Barnett, J. D. Sau, and S. Das Sarma, "Antiferromagnetic spinor condensates are quantum rotors," *Phys. Rev. A*, vol. 82, p. 031602, Sep 2010.

[136] Y. Kawaguchi and M. Ueda, "Spinor Bose-Einstein condensates," *Physics Reports*, vol. 520, no. 5, pp. 253 – 381, 2012.

[137] S. Knoop, T. Schuster, R. Scelle, A. Trautmann, J. Appmeier, M. K. Oberthaler, E. Tiesinga, and E. Tiemann, "Feshbach spectroscopy and analysis of the interaction potentials of ultracold Sodium," *Phys. Rev. A*, vol. 83, p. 042704, Apr 2011.

[138] T.-L. Ho, "Spinor Bose condensates in optical traps," *Phys. Rev. Lett.*, vol. 81, pp. 742–745, Jul 1998.

[139] M. Ueda, "Many-body theory of dilute Bose-Einstein condensates with internal degrees of freedom," *Phys. Rev. A*, vol. 63, p. 013601, Dec 2000.

[140] S. Uchino, M. Kobayashi, and M. Ueda, "Bogoliubov theory and Lee-Huang-Yang corrections in spin-1 and spin-2 Bose-Einstein condensates in the presence of the quadratic zeeman effect," *Phys. Rev. A*, vol. 81, p. 063632, Jun 2010.

[141] S. Kohler and F. Sols, "Chemical potential standard for atomic Bose–Einstein condensates," *New Journal of Physics*, vol. 5, no. 1, p. 94, 2003.

[142] S. H. Strogatz, *Nonlinear Dynamics And Chaos*. 1994.

[143] A. Eckardt, "Colloquium: Atomic quantum gases in periodically driven optical lattices," *Rev. Mod. Phys.*, vol. 89, p. 011004, Mar 2017.

[144] L. W. Clark, A. Gaj, L. Feng, and C. Chin, "Collective emission of matter-wave jets from driven Bose-Einstein condensates," *Nature*, vol. 551, p. 356, Nov. 2017.

[145] J. Cheng, "Chaotic dynamics in a periodically driven spin-1 condensate," *Phys. Rev. A*, vol. 81, p. 023619, Feb 2010.

[146] J. Kronjäger, K. Sengstock, and K. Bongs, "Chaotic dynamics in spinor Bose–Einstein condensates," *New Journal of Physics*, vol. 10, no. 4, p. 045028, 2008.

[147] C. Gross, H. Strobel, E. Nicklas, T. Zibold, N. Bar-Gill, G. Kurizki, and M. K. Oberthaler, "Atomic homodyne detection of continuous-variable entangled twin-atom states," *Nature*, vol. 480, pp. 219–223, 12 2011.

[148] Y.-Q. Zou, L.-N. Wu, Q. Liu, X.-Y. Luo, S.-F. Guo, J.-H. Cao, M. K. Tey, and L. You, "Beating the classical precision limit with spin-1 Dicke states of more than 10,000 atoms," *Proceedings of the National Academy of Sciences*, 2018.

[149] J. P. Wrubel, A. Schwettmann, D. P. Fahey, Z. Glassman, H. K. Pechkis, P. F. Griffin, R. Barnett, E. Tiesinga, and P. D. Lett, "Spinor Bose-Einstein-condensate phase-sensitive amplifier for SU(1,1) interferometry," *Phys. Rev. A*, vol. 98, p. 023620, Aug 2018.

[150] J. Tomkovič, W. Muessel, H. Strobel, S. Löck, P. Schlagheck, R. Ketzmerick, and M. K. Oberthaler, "Experimental observation of the poincaré-birkhoff scenario in a driven many-body quantum system," *Phys. Rev. A*, vol. 95, p. 011602, Jan 2017.

[151] "A gravitational wave observatory operating beyond the quantum shot-noise limit," *Nature Physics*, vol. 7, pp. 962–965, Sept. 2011.

[152] H. Grote, K. Danzmann, K. L. Dooley, R. Schnabel, J. Slutsky, and H. Vahlbruch, "First long-term application of squeezed states of light in a gravitational-wave observatory," *Phys. Rev. Lett.*, vol. 110, p. 181101, May 2013.

[153] M. Kitagawa and M. Ueda, "Squeezed spin states," *Phys. Rev. A*, vol. 47, pp. 5138–5143, Jun 1993.

[154] D. J. Wineland, J. J. Bollinger, W. M. Itano, and D. J. Heinzen, "Squeezed atomic states and projection noise in spectroscopy," *Phys. Rev. A*, vol. 50, pp. 67–88, Jul 1994.

[155] A. S. Sørensen and K. Mølmer, "Entanglement and extreme spin squeezing," *Phys. Rev. Lett.*, vol. 86, pp. 4431–4434, May 2001.

[156] G. Vitagliano, I. Apellaniz, M. Kleinmann, B. Lücke, C. Klempt, and G. Tóth, "Entanglement and extreme spin squeezing of unpolarized states," *New Journal of Physics*, vol. 19, p. 013027, jan 2017.

[157] B. Lücke, J. Peise, G. Vitagliano, J. Arlt, L. Santos, G. Tóth, and C. Klempt, "Detecting multiparticle entanglement of Dicke states," *Phys. Rev. Lett.*, vol. 112, p. 155304, Apr 2014.

[158] X.-Y. Luo, Y.-Q. Zou, L.-N. Wu, Q. Liu, M.-F. Han, M. K. Tey, and L. You, "Deterministic entanglement generation from driving through quantum phase transitions," *Science*, vol. 355, pp. 620–623, Feb. 2017.

[159] M. Gabbrielli, L. Pezzè, and A. Smerzi, "Spin-mixing interferometry with Bose-Einstein condensates," *Phys. Rev. Lett.*, vol. 115, p. 163002, Oct 2015.

[160] P. Grassberger, "Entropy estimates from insufficient samplings," 2003.

[161] P. D. Nation, J. R. Johansson, M. P. Blencowe, and F. Nori, "Colloquium: Stimulating uncertainty: Amplifying the quantum vacuum with superconducting circuits," *Rev. Mod. Phys.*, vol. 84, pp. 1–24, Jan 2012.

[162] P. M. Anisimov, G. M. Raterman, A. Chiruvelli, W. N. Plick, S. D. Huver, H. Lee, and J. P. Dowling, "Quantum metrology with two-mode squeezed vacuum: Parity detection beats the Heisenberg limit," *Phys. Rev. Lett.*, vol. 104, p. 103602, Mar 2010.

[163] A. Evrard, V. Makhalov, T. Chalopin, L. A. Sidorenkov, J. Dalibard, R. Lopes, and S. Nascimbene, "Enhanced magnetic sensitivity with non-gaussian quantum fluctuations," *Phys. Rev. Lett.*, vol. 122, p. 173601, May 2019.

[164] L. D'Alessio, Y. Kafri, A. Polkovnikov, and M. Rigol, "From quantum chaos and eigenstate thermalization to statistical mechanics and thermodynamics," *Advances in Physics*, vol. 65, no. 3, pp. 239–362, 2016.

[165] M. Rigol, V. Dunjko, and M. Olshanii, "Thermalization and its mechanism for generic isolated quantum systems," *Nature*, vol. 452, pp. 854–858, Apr. 2008.

[166] J. M. Deutsch, "Quantum statistical mechanics in a closed system," *Phys. Rev. A*, vol. 43, pp. 2046–2049, Feb 1991.

[167] M. Srednicki, "Chaos and quantum thermalization," *Phys. Rev. E*, vol. 50, pp. 888–901, Aug 1994.

[168] M. Prüfer, P. Kunkel, H. Strobel, S. Lannig, D. Linnemann, C.-M. Schmied, J. Berges, T. Gasenzer, and M. K. Oberthaler, "Observation of universal dynamics in a spinor Bose gas far from equilibrium," *Nature*, vol. 563, pp. 217–220, Nov. 2018.

[169] M. Anquez, B. A. Robbins, H. M. Bharath, M. Boguslawski, T. M. Hoang, and M. S. Chapman, "Quantum kibble-zurek mechanism in a spin-1 Bose-Einstein condensate," *Phys. Rev. Lett.*, vol. 116, p. 155301, Apr 2016.

[170] Y. Liu, E. Gomez, S. E. Maxwell, L. D. Turner, E. Tiesinga, and P. D. Lett, "Number fluctuations and energy dissipation in Sodium spinor condensates," *Phys. Rev. Lett.*, vol. 102, p. 225301, Jun 2009.

[171] A. M. Kaufman, M. E. Tai, A. Lukin, M. Rispoli, R. Schittko, P. M. Preiss, and M. Greiner, "Quantum thermalization through entanglement in an isolated many-body system," *Science*, vol. 353, pp. 794–800, Aug. 2016.

[172] T. Kinoshita, T. Wenger, and D. S. Weiss, "A quantum newtons cradle," *Nature*, vol. 440, pp. 900–903, Apr. 2006.

[173] T. Langen, S. Erne, R. Geiger, B. Rauer, T. Schweigler, M. Kuhnert, W. Rohringer, I. E. Mazets, T. Gasenzer, and J. Schmiedmayer, "Experimental observation of a generalized gibbs ensemble," *Science*, vol. 348, pp. 207–211, Apr. 2015.

[174] S. P. Kelly, E. Timmermans, and S. w. Tsai, "Thermalization and its breakdown for a large nonlinear spin.," 2019.

[175] I. Lovas, J. Fortágh, E. Demler, and G. Zaránd, "Entanglement and entropy production in coupled single-mode Bose-Einstein condensates," *Phys. Rev. A*, vol. 96, p. 023615, Aug 2017.

[176] M. A. Garcia-March, S. van Frank, M. Bonneau, J. Schmiedmayer, M. Lewenstein, and L. F. Santos, "Relaxation, chaos, and thermalization in a three-mode model of a Bose–Einstein condensate," *New Journal of Physics*, vol. 20, p. 113039, nov 2018.

[177] C. B. Dağ, S.-T. Wang, and L.-M. Duan, "Classification of quench-dynamical behaviors in spinor condensates," *Phys. Rev. A*, vol. 97, p. 023603, Feb 2018.

[178] P. Nozières, "Some comments on Bose-Einstein condensation," *Bose-Einstein Condensation*, pp. 15–30, 1995.

[179] K. Madison, F. Chevy, W. Wohlleben, and J. Dalibard, "Vortex formation in a stirred Bose-Einstein condensate," *Physical review letters*, vol. 84, no. 5, p. 806, 2000.

[180] N. R. Cooper, "Rapidly rotating atomic gases," *Advances in Physics*, vol. 57, no. 6, pp. 539–616, 2008.

[181] N. R. Cooper, N. K. Wilkin, and J. Gunn, "Quantum phases of vortices in rotating Bose-Einstein condensates," *Physical review letters*, vol. 87, no. 12, p. 120405, 2001.

[182] A. J. Leggett, "Bose-Einstein condensation in the alkali gases: Some fundamental concepts," *Rev. Mod. Phys.*, vol. 73, pp. 307–356, Apr 2001.

[183] S. Ashhab and A. J. Leggett, "Measurement theory and interference of spinor Bose-Einstein condensates," *Phys. Rev. A*, vol. 65, p. 023604, Jan 2002.

[184] Y. Castin and J. Dalibard, "Relative phase of two Bose-Einstein condensates," *Phys. Rev. A*, vol. 55, pp. 4330–4337, Jun 1997.

[185] R. Barnett, H.-Y. Hui, C.-H. Lin, J. D. Sau, and S. Das Sarma, "Quantum rotor theory of spinor condensates in tight traps," *Phys. Rev. A*, vol. 83, p. 023613, Feb 2011.

[186] A. I. Lvovsky and M. G. Raymer, "Continuous-variable optical quantum-state tomography," *Rev. Mod. Phys.*, vol. 81, pp. 299–332, Mar 2009.

[187] G. M. D'Ariano, M. G. Paris, and M. F. Sacchi, "Quantum tomography," *Advances in Imaging and Electron Physics*, vol. 128, pp. 206–309, 2003.

[188] G. Breitenbach, S. Schiller, and J. Mlynek, "Measurement of the quantum states of squeezed light," *Nature*, vol. 387, no. 6632, pp. 471–475, 1997.

[189] J. Peise, I. Kruse, K. Lange, B. Lücke, L. Pezzè, J. Arlt, W. Ertmer, K. Hammerer, L. Santos, A. Smerzi, and C. Klempt, "Satisfying the Einstein–podolsky–rosen criterion with massive particles," *Nature Communications*, vol. 6, Nov. 2015.

[190] A. I. Lvovsky, "Iterative maximum-likelihood reconstruction in quantum homodyne tomography," *Journal of Optics B: Quantum and Semiclassical Optics*, vol. 6, pp. S556–S559, may 2004.

[191] V. Bužek, G. Drobný, G. Adam, R. Derka, and P. L. Knight, "Reconstruction of quantum states of spin systems via the jaynes principle of maximum entropy," *Journal of Modern Optics*, vol. 44, no. 11-12, pp. 2607–2627, 1997.

[192] D. Guéry-Odelin, A. Ruschhaupt, A. Kiely, E. Torrontegui, S. Martínez-Garaot, and J. G. Muga, "Shortcuts to adiabaticity: Concepts, methods, and applications," *Rev. Mod. Phys.*, vol. 91, p. 045001, Oct 2019.

[193] L. D. Sarlo, L. Shao, V. Corre, T. Zibold, D. Jacob, J. Dalibard, and F. Gerbier, "Spin fragmentation of Bose–Einstein condensates with antiferromagnetic interactions," *New Journal of Physics*, vol. 15, p. 113039, nov 2013.

[194] A. Sala, D. L. Núñez, J. Martorell, L. De Sarlo, T. Zibold, F. Gerbier, A. Polls, and B. Juliá-Díaz, "Shortcut to adiabaticity in spinor condensates," *Physical Review A*, vol. 94, no. 4, p. 043623, 2016.

[195] E. Demler and F. Zhou, "Spinor bosonic atoms in optical lattices: Symmetry breaking and fractionalization," *Physical review letters*, vol. 88, no. 16, p. 163001, 2002.

[196] S. Yip, "Dimer state of spin-1 bosons in an optical lattice," *Physical review letters*, vol. 90, no. 25, p. 250402, 2003.

[197] A. Imambekov, M. Lukin, and E. Demler, "Spin-exchange interactions of spin-one bosons in optical lattices: Singlet, nematic, and dimerized phases," *Physical Review A*, vol. 68, no. 6, p. 063602, 2003.

[198] M. Boll, T. A. Hilker, G. Salomon, A. Omran, J. Nespolo, L. Pollet, I. Bloch, and C. Gross, "Spin-and density-resolved microscopy of antiferromagnetic correlations in Fermi-Hubbard chains," *Science*, vol. 353, no. 6305, pp. 1257–1260, 2016.

[199] M. F. Parsons, A. Mazurenko, C. S. Chiu, G. Ji, D. Greif, and M. Greiner, "Site-resolved measurement of the spin-correlation function in the Fermi-Hubbard model," *Science*, vol. 353, no. 6305, pp. 1253–1256, 2016.

[200] M. J. Holland and K. Burnett, "Interferometric detection of optical phase shifts at the Heisenberg limit," *Phys. Rev. Lett.*, vol. 71, pp. 1355–1358, Aug 1993.

[201] P. Bouyer and M. A. Kasevich, "Heisenberg-limited spectroscopy with degenerate Bose-Einstein gases," *Phys. Rev. A*, vol. 56, pp. R1083–R1086, Aug 1997.

RÉSUMÉ

Dans cette thèse, nous présentons des expériences réalisé avec des gaz d'atome de sodium ultrafroids, piégés à l'intersection de deux faisceaux laser. A très basse température, discrétisation de l'énergie et indiscernabilité des particules conduisent à un nouvel état de la matière, un condensat de Bose-Einstein. Ce phénomène remarquable à d'abords été décrit pour un gaz idéal, c'est à dire sans interaction entre ses constituants. Ici, nous nous intéressons aux effets des interactions entre atomes. Plus précisément, nos atomes possèdent un spin 1, et nous nous interessont à l'état spinoriel collectif, dans un régime ou les degrées de liberté spatiaux sont gelés.
Deux résultats importants que nous présentons ont été obtenus en plongeant le condensat dans un champ magnétique quasi-nul. Dans ce régime, les interactions dominent et favorisent l'émergence d'états fortement corrélés. Dans une première série d'expériences, le champ est soudainement réduit, et le système se retrouve hors-équilibre. Il s'ensuit une dynamique de relaxation, qui mène à un état stationnaire bien décrit par un ensemble de Gibbs. Dans une seconde expérience, le champ est progressivement réduit, de façon à suivre l'état fondamental du système. Nous réalisons ainsi un condensat fragmenté, dont une remarquable propriété est l'invariance sous rotations des spins. La restauration de cette symétrie, toujours brisée par les condensat "simple" (i.e. non-fragmenté), se fait grâce à l'appariement des atomes en état singulet.

MOTS CLÉS

Atomes ultrafroids, condensat de Bose-Einstein spinoriel, fragmentation

ABSTRACT

In this thesis, we present some experiments realized with ultracold gases of sodium atoms, trapped at the intersect between two laser beams. At very low temperature, the discretization of energy and the indistinguishability of particles, lead to a new state of matter, a Bose-Einstein condensate. This remarkable phenomenon was initially introduced to describe an ideal gas, that is to say with no interactions between its constituents. Here, we are interested in the effects of the interactions between the atoms. More precisely, our atoms carry a spin 1, and we focus on the collective spin state, in a regime where the spatial degrees of freedom are frozen. Two important results that we present were obtained by embedding the condensate in a nearly vanishing magnetic field. In that regime, interactions dominate and favor the emergence of strongly correlated states. In a first series of experiment, the magnetic field is suddenly decreased to bring the system out-of-equilibrium. The ensuing relaxation dynamics leads to a stationnary state that can be well described by a Gibbs ensemble. In a second experiment, the field is slowly reduced, in order to follow the ground state of the system. We thereby produce a fragmented condensate, which possesses the remarkable feature of being invariant upon spin rotations. The restoration of this symmetry, always broken by single (i.e. non-fragmented) condensates, is driven by the pairing of atoms in singlet states.

KEY WORDS

Ultracold Atoms, Spinor Bose-Einstein condensates, Fragmentation